PhD Dissertation

High-resolution algorithms for the reconstruction of the equivalent currents of an antenna by means of modal theory and a priori information

Universidad Politécnica de Valencia

Departamento de Comunicaciones

Author

Daniel Sánchez Escuderos

Advisor

Prof. Dr. Mariano Baquero Escudero

Valencia, July 2009

To my parents and sister.

Agradecimientos

Han pasado muchos años desde que comencé esta tesis y muchas personas me han ayudado a llevarla a cabo. Algunos han estado desde el principio y otros llegaron más tarde. A todos ellos quiero dedicar esta primera parte de la tesis para darle las gracias por todo su apoyo.

Mi primer agradecimiento es para mi director de tesis, Mariano Baquero. Empezamos a trabajar juntos hace más de cinco años y desde entonces siempre ha estado ahí para ayudarme con el proyecto final de carrera, con la tesina de máster y, por supuesto, con esta tesis. A él mi más sincero agradecimiento por toda su ayuda y todo su apoyo. Espero seguir trabajando con él en el futuro, con sus enseñanzas y sus consejos.

En segundo lugar quiero dar las gracias a Miguel Ferrando por su dirección del grupo durante todos estos años y su apoyo en los múltiples congresos a los que hemos asistido. También quiero agradecerle su ayuda a Alejandro Valero. Siempre que he tenido dudas ha estado ahí para resolvérmelas y ayudarme. Tampoco me puedo olvidar de Vicent Miquel Rodrigo, del que nunca me ha faltado la ayuda cuando se la he pedido.

También quiero darle las gracias a todos mis compañeros y amigos durante estos años empezando, por supuesto, por Esperanza. Con ella empecé mi andadura por esta tesis y hemos pasado por todos los tramos juntos: los congresos nacionales, los internacionales, las tesinas, los cursos, etc. Me ha ayudado durante todo este tiempo y me ha animado cuando las cosas no venían bien dadas. Por eso quiero agradecerle todo su apoyo y ánimo.

Quiero agradecerle también de forma muy especial su ayuda a Eva, por sus consejos durante todos estos años y su decidido compromiso para que el trabajo y el grupo salieran adelante. Asimismo quiero darle las gracias a Jose Ignacio, por brindarme su ayuda cuando la he necesitado, y a Marta, por su apoyo durante todos estos años.

Por supuesto, también tengo que agradecerle su ayuda y colaboración a Toni y Bernat. Sin su trabajo en el laboratorio esta tesis no hubiera sido posible. Pero además, su ayuda y apoyo fuera de él ha sido inigualable así que mi más sincero agradecimiento por todo.

No puedo olvidarme tampoco de Dani, David y Felipe. Los tres están o han estado cerca durante todos estos años en los que he estado haciendo esta tesis. A los tres, gracias por vuestros consejos y ayuda, y por hacerme pasar mejor los momentos difíciles.

Finalmente quiero agradecer su amistad a Marko, Michele, y Carlos. Aunque los he conocido durante poco tiempo, siempre me han prestado su ayuda cuando la he necesitado.

Y, por supuesto, gracias a los que siempre estuvieron cerca: Vicente, Ariana, Miguel, Cristina, Denis, Juanma, Emilio, Jorge, Fulvio, Ana, ..., y a mis compañeros de viaje durante todos estos años: Rubén y Dani.

En último lugar, y no por ello menos importante, quiero dar las gracias a mis padres, José y Ramona, y a mi hermana, Elena. Sin ellos, estoy seguro de que esta tesis hubiera sido imposible de realizar. Gracias por la ayuda, el apoyo, la paciencia, el ánimo ... gracias por todo.

Abstract

The aim of the antenna diagnosis is the detection of errors in manufactured antennas. Since this diagnosis is quite hard to carry out by just observing field measurements, the diagnosis is done by using the reconstructed equivalent currents on a surface close to the antenna. This thesis describes different possibilities to perform this reconstruction on a flat surface from spherical near-field measurements. Specifically, the modal expansion techniques are extensively studied and applied to practical situations.

The main problem of the modal techniques is the limitation in the resolution of the reconstructed equivalent currents. The reason for this limitation is the small region available in the plane wave spectrum (whose Fourier transform are the equivalent currents). In this thesis this problem is studied and several examples are shown. Moreover, the possibilities to improve the resolution are described. Among these possibilities, the use of an extrapolation technique is proposed. By using this technique, the non-visible spectrum is estimated from the known region (the visible spectrum) and additional information about the antenna, e.g. the size of the antenna.

Among the different extrapolation techniques, the most commonly used techniques are described and compared. Firstly, the iterative Papoulis-Gerchberg algorithm is applied by using the size and shape of the antenna. Then, the direct versions of this algorithm, i.e., the extrapolation matrix by rows and columns, and the generalized extrapolation matrix, are described. Finally, the PDFT transformation is studied and compared to the previous algorithms. All these techniques are applied to real situations with a significant improvement of resolution.

The last chapter of this thesis deals with the probe calibration procedures. These procedures are especially important in antenna diagnosis since they allow to take into account the effect of the probe in the field measurement. Thus, the best diagnosis of the antenna under study may be carried out. In this thesis, the iterative probe calibration algorithm proposed by Hansen is described. In addition, several alternatives to this algorithm for three different situations are proposed. These techniques are verified in real situations with quite good results.

Resumen

El objetivo del diagnóstico de antenas es la detección de errores en antena fabricadas. Dado que este diagnóstico es difícil de realizar simplemente observando medidas de campo, el diagnóstico se realiza usando las corrientes equivalentes reconstruidas en una superficie próxima a la antena. Esta tesis describe diferentes posibilidades de realizar esta reconstrucción en una superficie plana a partir de medidas esféricas en campo próximo. En concreto, se estudian extensivamente, y se aplican a situaciones reales, las técnicas de la expansión modal.

El problema principal de las técnicas modales es la limitación en la resolución de las corrientes equivalentes. La razón de esta limitación es la pequeña región disponible del espectro de ondas planas (cuya transformada de Fourier son las corrientes equivalentes). En esta tesis se estudia este problema, se muestran varios ejemplos y se describen las posibilidades de mejorar la resolución. De entre estas posibilidades, se propone el uso de una técnica de extrapolación con la que estimar el espectro no visible a partir de la región conocida (el espectro visible) y de información adicional sobre la antena como, por ejemplo, el tamaño de la antena.

Entre las diferentes técnicas de extrapolación, se describen y comparan las técnicas más usadas comúnmente. En primer lugar, se aplica el algoritmo iterativo de Papoulis-Gerchberg usando el tamaño y la forma de la antena. Después se describen las versiones directas de este algoritmo, es decir la matriz de extrapolación por filas y columnas y la matriz de extrapolación generalizada. Finalmente, se estudia la transformación PDFT y se compara con los algoritmos anteriores. Todas estas técnicas son aplicadas en situaciones reales con una importante mejora en la resolución.

El último capítulo de esta tesis trata de los procedimientos de calibración de sonda. Estos procedimientos son especialmente importantes en el diagnóstico de antenas ya que permiten tener en cuenta el efecto de la sonda en la medida de campo. De este modo, se puede llevar a cabo el mejor diagnóstico de la antena bajo estudio. En esta tesis se describe el algoritmo iterativo de calibración de sondas propuesto por Hansen. Además se proponen varias alternativas a este algoritmo para tres situaciones diferentes. Estas técnicas son verificadas en situaciones reales con resultados bastante buenos.

Resum

L'objectiu del diagnòstic d'antenes és la detecció d'errors en antenes fabricades. Donat que aquest diagnòstic és prou difícil de realitzar simplement observant mesures de camp, el diagnòstic es realitza utilitzant els corrents equivalents reconstruïts en una superficie próxima a l'antena. Esta tesi descriu diferents possibilitats per a realitzar aquesta reconstrucció en una superificie plana a partir de mesures esfériques de camp pròxim. En concret, s'estudien extensivament, i s'apliquen a situacions reals, les técniques de l'expansió modal.

El problema principal de les técniques modals és la limitació en la resolució dels corrents equivalents. La raó d'aquesta limitació es la reduïda regió disponible de l'espectre d'ones planes (la transformada de Fourier del qual són els corrents equivalents). En aquesta tesi s'estudia aquest problema, es mostren diversos exemples i es descriuen les possibilitats per millorar la resolució. D'entre aquestes possibilitats, es proposa l'ús d'una técnica d'extrapolació amb la qual estimar l'espectre no visible a partir de la regió coneguda (l'espectre visible) i d'informació adicional sobre l'antena, com per exemple, les dimensions de l'antena.

Entre les diferents técniques d'extrapolació existents, es descriuen i comparen les técniques més usades comunment. En primer lloc, s'aplica l'algoritme d'extrapolació de Papoulis-Gerchberg usant les dimensions i la forma de l'antena. Després es descriuen les versions directes d'aquest algoritme, es a dir, la matriu d'extrapolació per files i columnes, i la matriu d'extrapolació generalitzada. Finalment, s'estudia la transformació PDFT i es compara amb els algoritmes anteriors. Totes aquestes técniques són aplicades en situacions reals amb una important millora en la resolució.

L'últim capítol d'aquesta tesi tracta del procediments de calibració de la sonda. Aquests procediments són especialment importants en el diagnòstic d'antenes perquè permeten tindre en compte l'efecte de la sonda en la mesura del camp. D'aquesta manera, es pot portar a terme el millor diagnòstic de l'antena en estudi. En aquesta tesi es descriu l'algoritme iteratiu de calibració de sondes propost per Hansen. A més a més es proposen diverses alternatives a aquest algoritme per a tres situacions diferents. Aquestes técniques són verificades en situacions reals amb resultats prou bons.

Table of contents

List of Figures

List of Tables

Chapter 1

Introduction

The design of an antenna involves several steps. Firstly, the specifications of the antenna are established according to both the application in which the antenna must be used and the parameters that characterize the antenna [1]. Secondly, a study is carried out in order to find out the kind of antenna (an array antenna, a patch antenna, a reflector, etc.) that best fits the specifications stated in the first step. Finally, the physical dimensions of the selected antenna are determined according to the specifications.

After the design process, an analysis of the resulting antenna is carried out. The aim of this analysis is to check if the antenna satisfies the specifications. There are several methods of analysis, e.g. the Method of Moments (MoM) [2], the Finite Difference Time Domain method (FDTD) [3] or the Finite-Element method (FEM) [3], which may be implemented by own codes or by commercial software [4]-[6]. If the result of the analysis does not satisfy exactly the desired specifications, an optimization algorithm, e.g. a genetic algorithm (GA) [7] or the particle swarm optimization (PSO) [8], may be applied. Thus, the design is optimized so that the designed antenna satisfies the specifications in the most accurate way.

Once the design, analysis and optimization have been carried out, the antenna is manufactured. This is one of the most difficult steps since the result does not depend on who is manufacturing the antenna, but on the precision of the manufacturing instrument. The tolerance of this instrument is known a priori, however, this knowledge may not be enough. If the tolerance is large, the manufactured antenna may be quite different from the designed antenna. Consequently, the resulting antenna may not satisfy the specifications. In addition, it is worth to mention that the tolerance is a physical term. Thus, the higher the frequency is, the worse the tolerance in electrical terms is. Hence, at high frequencies, the manufacturing problems may rise.

The simplest way to avoid the manufacturing problems consists in taking into account the tolerance of the manufacturing instrument during the design and optimization processes [9]. Thus, the bad behavior of the manufacturing instrument is prevented and corrected.

Nevertheless, even though the above technique is employed, the manufactured antenna must be always checked. This check determines, first, if the physical dimensions of the antenna agree with the design and, then, if the antenna satisfies the specifications. To do this second part, the radiation pattern of the antenna, as well as the S_{11} parameter, are normally measured.

If the above measurements are within the margins of variation of the specifications, the antenna behaves as it was desired and, hence, the antenna may be used in the desired application. However, if the above measurements are not within these margins, another process must be started. The aim of this process, which is known as *antenna diagnosis*, is to find out the source of the error, either in the design or in the manufacture, that has caused the bad behavior of the antenna.

The antenna diagnosis is done from measurements of the field radiated by the antenna. If these measurements are taken far from the antenna, a problem arises. Whereas these measurements allow to determine whether the specifications of the antenna are satisfied or not, they do not allow the errors to be easily located. To do this location in an easy way, the field on points close to the antenna must be used. By using this field, the location of the errors of the antenna is immediate.

The problem of this option lies in the difficulty of measuring the field on points close to the antenna. In [10] this problem is studied and the use of small-loop probes placed on the surface where the field must be known is proposed. Nevertheless, even though this set-up is used, reflections and couplings may take place between the probes and the antenna.

For this reason, instead of measuring the field on points close to the antenna, the radiated field is measured far from the antenna, where reflections and couplings do not take place. Later, this field is backpropagated (from the field measured far from the antenna to the field on a surface close to the antenna) to carry out the antenna diagnosis. This transformation is known as the *inverse problem* and constitutes the basis of this thesis.

Once the tangential field to the surface of interest is known a simply transformation may be carried out. This transformation consists in obtaining the equivalent currents on this surface. The aim of this transformation is to locate in an easy way the errors of the antenna by using the physical connotations of the equivalent currents. Hence, from now on, the aim of the inverse problem will be the determination of the equivalent currents on a surface close to the antenna.

The inverse problem may be solved by an *integral equation* method [11], [12] or by a *modal expansion* method [13], [14]. In this thesis, though a brief description of the integral equation methods is done to compare some results and the complexity of both methods, the attention is focused on the modal expansion methods. For this reason, firstly, a review of the expansions for the main coordinate systems, namely, planar, cylindrical and spherical, is done. In addition, the modal expansion for the oblate spheroidal coordinate system is presented and the way to compute the spheroidal coefficients and the spheroidal wave functions is described.

The first step of the inverse problem must be always to establish the coordinate system in which the measurements are taken, and the coordinate system in which it is described the surface where the currents are desired. The application of the above methods strongly depends on these definitions and, hence, these definitions must be done at the beginning of the solution of the inverse problem.

On the one hand, in this thesis the attention is focused on antennas whose main radiating surface is flat. Thus, the aim is to obtain the currents on a plane close to the antenna. For this reason, a planar coordinate system is the most suitable coordinate system to express the equivalent currents for the antenna diagnosis.

On the other hand, one of the most used measurement systems is the spherical measurement system since it allows a complete sphere around the antennas to be measured. Thus, no loss of information is produced while measuring the radiated field. In addition, the anechoic chamber of the electromagnetic radiation group (grupo de radiación electromagnética, GRE), where this thesis has been developed, includes a spherical measurement system so that, by studying this kind of measurements, real measurement may be used to test the techniques studied in this thesis. Therefore, a spherical measurement will be assumed from now on.

The radiated field may be measured either in the far-field region or in the near-field region [15]. For the integral equation methods, this difference does not entail any change in the derivation of the solution. However, for the modal expansion methods, the fact of measuring in the near-field region or in the far-field region, may lead to different algorithms.

The reason for this difference lies in the information present in both field regions. Whereas the *evanescent waves*, and the information they contain, are not present in the far-field region, the near-field region may include these evanescent waves. Hence, if the field is measured in the near-field region (and quite close to the antenna) the information present in these waves might be considered during the inverse algorithm. By doing so, the resolution of the equivalent currents might be improved.

Thus, if the field is measured in the far-field region, and a modal expansion method is used, the microwave holographic technique [16]-[18] may be directly applied. The aim of this technique is to determine the plane wave spectrum, whose Fourier transform is the field on a plane (except by a phase correction due to the position of this plane). The advantage of having the far field is the easy transformation of this field into the plane wave spectrum. Thus, the equivalent currents on the surface of interest may be easily obtained by using the field in the far-field region.

Nevertheless, if the field is measured in the near-field region, two different possibilities arise. Firstly, it may be assumed that the evanescent waves have been measured. In this case, in order to take into account the information present in these waves, a direct transformation technique [13],[19] must be applied. This transformation, which is known as SWE-to-PWE transformation, computes the plane wave spectrum from the spherical near-field measurement. Thus, no loss of information is produced during the backpropagation.

Secondly, it may be assumed that the evanescent waves have not been measured or, even though these waves have been measured, it may be assumed that the information of these waves may be ruled out. In this case, the inverse transformation may be carried out in two steps. First, the near-field measurement is transformed into far-field by means of a near-field to far-field transformation in spherical coordinates [20]. Then, by using the microwave holographic technique over the computed far-field [14], the equivalent currents may be determined on the surface of interest.

In this last case, the most difficult part lies in the transformation of the near-field measurement into far-field. This transformation has been widely studied in literature [20]-[22] for several coordinate systems[23]. Specifically for spherical near-field measurements, the transformation is extensively described and studied by Hansen in [20].

One of the most important problems regarding the near-field to far-field transformation is the probe correction [24], which considers the effect of the probe in the measurement. In [20] the transformation is proposed by assuming first-order probe correction, e.g. an open-waveguide excited by the TE_{11} mode. This correction entails an additional problem: the determination of the probe receiving coefficients (which characterize the probe in reception), what is normally known as probe calibration. This probe calibration is also studied in this thesis due to the strong effect of the receiving coefficients in the transformation of the near-field into far-field.

By looking at both ways to reconstruct the equivalent currents, it may be conclude that the first way is the most suitable if the field is measured in the near-field region. However, it is worth to mention that the evanescent waves are strongly attenuated at short distances. Thus, in order to measure these waves, the measurement must be taken quite close to the antenna. Many times

this is not possible due to the geometry of the measurement system or the coupling between the probe and the antenna under test (AUT). Hence, the most common situation is normally closer to the second situation, i.e., when it is assumed that the evanescent waves are not present in the measurement. Thus, instead of using the measured near-field, the far field (which does not include the information of the evanescent waves) may be considered in the inverse problem.

From the point of view of the microwave holographic technique, the consequence of just considering the far field may be observed in the computed plane wave spectrum. By using the far field, just a small region of the spectrum (a circle of radius k, where k is the wavenumber) is available. This region is known as *visible spectrum* and the consequence of just knowing a small region of this spectrum is the restriction in the resolution of the equivalent currents.

Since the plane wave spectrum is related to the equivalent currents by a Fourier transform (actually the Fourier transform relation is between the spectrum and the field on the surface of interest, but this field is directly related to the equivalent currents), if a small region of the spectrum is known, the resolution of the equivalent currents is limited to a certain value, even though the spectrum is extended with zeros. Specifically, considering that just the visible spectrum is known, the resolution that may be achieved is of just 1 λ in the equivalent currents. In this thesis several examples are shown.

In order to improve the resolution, the region of the plane wave spectrum beyond the circle of radius k, the so-called *non-visible spectrum*, must be determined. To do this, the use of an extrapolation technique [25] is proposed in this thesis. The aim of these techniques is to determine a signal from a known segment of this signal and a priori information.

The most widely used extrapolation technique is the Papoulis-Gerchberg algorithm [26]-[28], which implements the extrapolation iteratively by using a band-limitation in the transformed domain. By using this technique interesting results are obtained, as this thesis shows. However, the Papoulis-Gerchberg algorithm has several drawbacks, e.g. the application of the extrapolation by iterations and the low speed of convergence. For this reason the acceleration of the algorithm has also been studied [29] with the aim of achieving the same estimate in a lower number of iterations.

Moreover, direct versions of the iterative Papoulis-Gerchberg algorithm have been presented to be able to extrapolate signals with a high number of iterations. These techniques form the so-called *extrapolation matrix* [30] to perform the extrapolation by multiplying this matrix by the known segment of the signal. For 2-D signals, two different versions of the extrapolation matrix have been proposed: the extrapolation matrix by rows and columns [31] and the generalized extrapolation matrix [32]. In this thesis, both versions are described and several examples are shown.

Beside the iterative Papoulis-Gerchberg algorithm, other useful extrapolation algorithms have been proposed [33]-[35]. Among these algorithms, one of the most interesting techniques is the Prior discrete Fourier transform (PDFT) [36]. This technique performs the extrapolation in a single step, similarly to the extrapolation matrix. The application of this technique to a real situation offers quite good results and even better than those obtained with the iterative Papoulis-Gerchberg algorithm. In this thesis, the PDFT is also presented and applied to several situations.

By using the previous extrapolation algorithms, the resolution in the equivalent currents is improved, from 1 λ with just the visible spectrum, up to 0.3-0.4 λ in the estimate obtained with the extrapolation techniques. Thus, by using these improved equivalent currents, the antenna diagnosis may be done more accurately and, hence, the errors of the antenna can be easier detected.

Finally, it must be pointed out that this thesis has been developed in the Grupo de Radiación Electromagnética (GRE), which is part of the Instituto de Telecomunicaciones y Aplicaciones Multimedia (ITEAM) in the Universidad Politécnica de Valencia (UPV). In addition, this work has been supported by the Spanish Ministry of Education and Science (Ministerio de Educación y Ciencia) under the FPI research fellowship program TEC2004-04866-C04-01, which is co-financed by the European Social Fund (ESF), and under the project TEC2007-6698-C04-03.

1.1 Objectives of the thesis

The objectives of this thesis are:

1. Describe the main techniques to determine the equivalent currents on a flat surface close to an antenna from spherical near-field measurements. As commented above, these techniques may be divided into two main groups: the integral equation techniques, and the modal expansion techniques. In this thesis, both techniques are described paying special attention to the modal expansion techniques. Specifically, the spherical wave expansion is used to reconstruct the equivalent currents either with a direct transformation of by using the far field as an intermediate step.

   In addition, the possibility of using the oblate spheroidal wave expansion is proposed and the algorithm to reconstruct the equivalent currents by using this expansion and spherical measurements is described.

2. Describe the limitation in resolution of the equivalent currents by using measurements taken at far distances. The aim is to determine the resolution that may be achieved in the limit case, in which case just the visible spectrum is available, and show several examples.

3. Present several methods to improve the resolution in the reconstructed equivalent currents of an antenna. Since the low resolution is due to the limited known region of the plane wave spectrum, several algorithms are reviewed and, other, proposed, with the aim of increasing the resolution. These methods are based on extrapolation techniques and apply additional information to achieve the improvement in resolution.

4. Propose several techniques for the probe calibration. The main aim of the probe calibration is to determine the receiving coefficients of the probe used in the spherical near-field measurement. By knowing these coefficients, an accurate probe correction may be applied in the determination of the spherical coefficients. Thus, the reconstruction of the equivalent currents by means of the spherical wave expansion may be done in the most accurate way. This thesis proposes three different techniques to determine the probe receiving coefficients.

1.2 Structure of the thesis

This thesis is organized as follows:

Chapter 2 reviews the solution of the vector wave equation in a source-free region. The solution is described in four different coordinate systems, namely, planar, cylindrical, spherical and oblate spheroidal coordinate system. In addition, this chapter describes the algorithms that must be applied to determine the coefficients of the modal expansions in the planar and spherical coordinate systems. Special attention is paid to this last case due to the extensive use of this transformation in later chapters.

Chapter 3 describes the main techniques to carry out the reconstruction of the equivalent currents of an antenna from spherical near-field measurements. Among the presented techniques, special attention is focused on the modal expansion techniques and, specially, in the technique that makes use of the far field as an intermediate step. Several examples with simulated and real antennas are shown and compared. Finally, the reconstruction of the equivalent currents on a flat surface is proposed by using the oblate spheroidal wave expansion. The way in which the spheroidal vector functions are computed is explained in detail in Appendix D and the transformation of the spherical coefficients into the spheroidal coefficients is described in the actual chapter.

Chapter 4 studies the resolution achieved by using measurements taken at several distances. The attenuation of the evanescent waves is determined and depicted. Moreover, the limit case, in which no evanescent wave is measured, i.e., just the visible plane wave spectrum is available, is considered. For this case the resolution is determined and several examples are shown. Finally, the possibilities to improve this resolution are detailed and compared.

Chapter 5 presents several techniques to improve the resolution by estimating the non-visible plane wave spectrum with an extrapolation technique. In this chapter, these techniques are defined, and a review of the state of the art is done. Then, one of the most widely used extrapolation techniques, the Papoulis-Gerchberg algorithm, is applied to the extrapolation of the plane wave spectrum. Later, the direct versions of this algorithm, the so-called extrapolation matrices, are studied and applied to both, simulated and real situations. Finally, another direct technique, the prior discrete Fourier transform, is described and applied.

Chapter 6 proposes several algorithms to carry out the probe calibration for first-order probes. As a result, the receiving coefficients of the probe under study are determined, which allow the probe correction to be applied. Thus, the transmitting coefficients of an antenna may be accurately obtained by removing the effect of the probe in the spherical measurement. Three different situations, depending on the possibilities of the laboratory, are studied: when 2 identical antennas are available, when just 2 different antennas are available but the gain of one of them is known, and when previous situation are not possible and, hence, three different antennas are required but an a priori knowledge about the antennas is not necessary.

Chapter 2

Field modal expansions

The introduction has established the general aims of this thesis. All these aims deal with the way on how the radiated field of an antenna is treated in order to get as much information as possible of the behavior of the antenna, either on a surface closed to the antenna or in the far-field region. It is, then, important to start with a review of the basic theory related to the electromagnetic fields, from the Maxwell's equations to the expression of the electric field as a modal expansion.

This chapter carries out this review in the main coordinate systems (planar, cylindrical and spherical) paying specific attention to the spherical wave expansion, which will be widely used the rest of this thesis. Furthermore, this chapter also introduces the wave expansion in an oblate spheroidal coordinate system, which will be used in future chapters as an important resource for back-propagation on planes.

Finally, this chapter explains the way in which the weights of the modal expansions can be computed from the radiated field measurements in planar and spherical coordinates. In this last case, a practical example is shown in order to verify the accuracy and the usefulness of the method.

2.1 Maxwell's equations

Time-harmonic fields [37] may be expressed as [38]:

$$E(x, y, z, t) = E(x, y, z)e^{-j\omega t}. \tag{2.1}$$

By assuming this dependence, the Maxwell's equations in a homogeneous, isotropic and linear medium can be expressed in the following way [37]:

$$\nabla \times \vec{E} = -j\omega\mu\vec{H} \tag{2.2}$$

$$\nabla \times \vec{H} = j\omega\varepsilon\vec{E} + \vec{J} \tag{2.3}$$

$$\nabla \cdot \vec{E} = \rho/\varepsilon \tag{2.4}$$

$$\nabla \cdot \vec{H} = 0 \tag{2.5}$$

where $\vec{E}$ and $\vec{H}$ are the the electric and magnetic field vector respectively, $\vec{J}$ is the volume current density, ρ is the volume charge density, ε is the permittivity tensor and μ is the permeability tensor. For a general case both, the permittivity and the permeability, can be matrices. However, in this thesis, just isotropic medias are considered and, hence, ε and μ are just scalar quantities.

In the Maxwell's equations, electric and magnetic field vectors are coupled together. In order to decouple these vectors another equation, which is known as *continuity equation* must be used. This equation may be expressed, assuming time-harmonic fields (2.1), as follows:

$$\nabla\vec{J} = -j\omega\rho \tag{2.6}$$

By using this equation, a new expression, the so-called *wave equation*, is obtained for both, the electric and magnetic field vectors [11].

The wave equation for the electric field vector can be derived by taking the curl of expression (2.2) and substituting (2.3) on the result of this operation. Then, using (2.6), the wave equation is obtained with no dependence with regard to ρ. If some additional vector identities are applied [11], the resulting equation may be expressed as:

$$\nabla^2\vec{E} + k^2\vec{E} = j\omega\mu\vec{J} - \frac{\nabla\nabla\cdot\vec{J}}{j\omega\varepsilon}, \tag{2.7}$$

where k is the wavenumber expressed as $k = \omega\sqrt{\varepsilon\mu}$.

For the magnetic field vector, similar operations can be carried out which lead to the following wave equation:

$$\nabla^2\vec{H} + k^2\vec{H} = -\nabla \times \vec{J}. \tag{2.8}$$

As can be observed, the electric and magnetic wave equations depend on the currents. However, if these equations are solved in a source-free region, this dependence disappears and the wave equations are expressed as:

$$\nabla^2\vec{E} + k^2\vec{E} = 0, \tag{2.9}$$

$$\nabla^2 \vec{H} + k^2 \vec{H} = 0. \tag{2.10}$$

These expressions are the vector wave equations in a source-free region, which are also known as *vector Helmholtz equations*. They will be used in next sections to derive the electric field in this kind of regions (the magnetic field may be derived in the same way, hence, it is not detailed).

Before proceeding, it is worth to mention that the election of the sign in the exponential of the time-harmonic fields (2.1) is arbitrary. Hence, the obtained results are valid for both cases, $e^{j\omega t}$ and $e^{-j\omega t}$. However, it must be pointed out the common election in engineering is $e^{-j\omega t}$, whereas the election in (2.1) is $e^{j\omega t}$, which is more common in physics. Thus, the choice must be taken into account when dealing with the formulation derived in this thesis. Indeed, special care must be taken when combining the results from this thesis with the results obtained from other sources, which might follow the common definition in engineering $e^{-j\omega t}$. The reason for such election is the use of a main reference [20], which chooses $e^{j\omega t}$. For the sake of simplicity, it has been decided to follow this definition, adapting the formulation from other sources to this choice.

2.2 Solution of the wave equation: modal expansion

A general solution to the vector Helmholtz equation can be implemented as a weighted sum of orthogonal vector wave functions. A detailed description on how this is achieved can be found in [37] and [39]. Basically, the procedure followed to derive the general solution is divided in two parts. The first one consists of solving the *scalar Helmholtz equation* (2.11) in order to obtain the generating function ψ.

$$\nabla^2 \psi + k^2 \psi = 0. \tag{2.11}$$

Solution of (2.11) is carried out, first, expressing the Laplacian operator (∇^2) in the coordinates in which the solution is desired. Then, the separation of variables technique [37] is applied in order to obtain the final solution. The main drawback of this technique is that the separation of variables technique cannot be applied for any existing coordinate system. It is just possible in the following 11 orthogonal coordinate systems [40]:

1. Rectangular (or cartesian, or planar)
2. Circular cylinder (or cylindrical)

3. Elliptic cylinder
4. Parabolic cylinder
5. Spherical
6. Conical
7. Parabolic
8. Prolate spheroidal
9. Oblate spheroidal
10. Ellipsoidal
11. Paraboloidal

In this thesis, however, just rectangular, circular cylinder, spherical, and prolate and oblate spheroidal coordinate systems are used. Hence, the scalar Helmholtz equation can be solved applying the separation of variables technique for all the cases dealt with in this thesis.

Once the scalar Helmholtz equation has been solved, the result is used to obtain the transverse electric (TE) and magnetic (TM) solutions with regard to the main direction of propagation. These solutions constitute an orthogonal and complete set of solutions and, thus, the field in the source-free region of interest can be expressed as a weighted sum of (TE) and (TM) fields.

In order to achieve the TE and TM solutions from (2.9) and (2.10), the electric (F) and magnetic (A) vector potential are used. How these potentials are derived is beyond the scope of this thesis. For a detailed description, see [37]. However, for our purpose, it is important to note that the solution, as the solution to the scalar Helmholtz equation, depends on the coordinate system. For instance, if TE and TM solutions transversal to z axis are considered, it can be deduced [37] that the TE electric field (E^{TE}) and the TM electric field (E^{TM}) have the following expressions:

$$E^{TE} = -\nabla \times (\hat{z}\psi) \tag{2.12}$$

$$E^{TM} = \frac{1}{j\omega\varepsilon}\nabla \times \nabla \times (\hat{z}\psi), \tag{2.13}$$

where ψ is the solution of the scalar Helmholtz equation (2.11) in the desired coordinate system and the operator nabla (∇) must be expressed in this coordinate system.

Although similar solutions can be found for other coordinate systems, it must be taken into account that some coordinate systems do not support orthogonal vector wave solutions. Specifically, just the first six coordinate systems [40] of the previous list of 11 coordinate systems that allow separation of variables for the scalar Helmholtz equation support these kinds of solutions. Therefore, special attention will have to be paid when dealing with solutions for the spheroidal coordinate systems in future sections. For the moment, however, attention is going to be focused on the three main coordinate systems (namely rectangular, circular cylinder and spherical) since these systems offer easy mechanical scanning surfaces [24] as well as simple orthogonal functions.

Summing up, the process needed to obtain a general solution to the vector wave equation starts from the solution to the scalar Helmholtz equation (2.11) in the desired coordinate system. Then, this solution is used to compute the orthogonal vector wave functions (TE and TM), which are solutions of the vector wave equation (2.9). Finally, a weighted sum of the vector TE and TM fields, which is known as *wave expansion* or *modal expansion*, is established to completely express the field in the source-free region.

Since the procedure and results depend on the coordinate system, the next sections briefly show the solution in the main coordinate systems as well as in the oblate spheroidal coordinate system. Among all the solutions, special attention is focused on the spherical coordinate systems, since this system is extensively used the rest of this thesis.

2.2.1 Plane wave expansion (PWE)

The solution of vector Helmholtz equation in a rectangular coordinate system (defined in Fig. 2.1), has been widely studied, e.g. [37], [39], though the deepest study was done by Clemmow in [41]. As commented above, the first step to derive this solution consists of solving the scalar Helmholtz equation (2.11). Particularly for the rectangular coordinate system, this is a straightforward step since each term derived form the separation of variables depends on just one coordinate. This leads to a solution formed by harmonic functions:

$$\psi = e^{jk_x x} e^{jk_y y} e^{jk_z z} \tag{2.14}$$

where the constants k_x, k_y and k_z are related to the wave number (k) in the following way:

$$k_x^2 + k_y^2 + k_z^2 = k^2 \tag{2.15}$$

In addition, it can be proved that not only (2.14) is solution of the scalar wave equation (2.11), but also a linear combination of this expression. This combination can be expressed as

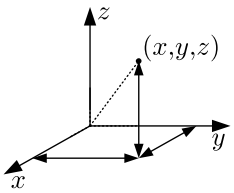

Figure 2.1: Rectangular coordinate system: definition.

$$\psi = \int_{-\infty}^{\infty}\int_{-\infty}^{\infty} f(k_x, k_y) e^{jk_x x} e^{jk_y y} e^{jk_z z} dk_x dk_y. \tag{2.16}$$

Once the scalar equation has been solved, the TE and TM solutions must be obtained. These solutions may be deduced with regard to any axis, however, in this thesis the transversal functions with regard to the z axis are of special interest. Hence, the expression (2.12) must be used to derive the electric field components (E_x, E_y, E_z). By doing so, if the solution (2.16) is considered, the obtained field can be expressed as a linear combination of plane waves in the following way:

$$\vec{E}(x, y, z) = \int_{-\infty}^{\infty}\int_{-\infty}^{\infty} \vec{A}_E(k_x, k_y) e^{jk_x x} e^{jk_y y} e^{jk_z z} dk_x dk_y. \tag{2.17}$$

Expression (2.17) is the electric field modal expansion in rectangular coordinates, which is normally known as *plane wave expansion (PWE)*. In this expression two different parts can be clearly distinguished. The first one are the vector wave functions ($e^{jk_x x}$, $e^{jk_y y}$, $e^{jk_z z}$), i.e., the plane waves, and the second one are the planar coefficients $\vec{A}_E(k_x, k_y)$. These coefficients are normally known as *plane wave spectrum* and will be extensively used in future chapters.

2.2.2 Cylindrical wave expansion (CWE)

The circularly cylinder coordinate system shown in Fig. 2.2, from now on *cylindrical coordinate system* for simplicity, is widely used because its scanning surface for radiation measurements can be mechanically implemented in an easy way. For this reason, the solution of the vector Helmholtz equation in this coordinate system has also been extensively studied. For instance, this solution was described by Harrington [37] and Stratton [39]; deeper, by Leach in his thesis [42] and, later, in a related work [43], and by Romeu also in his thesis [44].

As can be seen in all the mention works, the solution of the scalar wave equation in cylindrical coordinates can be written as follows:

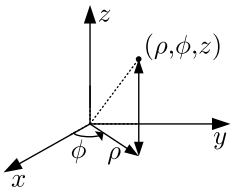

Figure 2.2: Cylindrical coordinate system: definition.

$$\psi = Z_n^{(c)}(k_\rho \rho) e^{jn\phi} e^{jk_z z} \tag{2.18}$$

where constants k_ρ, k_z and k are related in the following way

$$k_\rho^2 + k_z^2 = k^2 \tag{2.19}$$

and where $Z_n^{(c)}(k_\rho \rho)$ is the bessel function of order n (see Appendix A). Depending on the parameter c this function corresponds to the bessel function of first kind ($J_n(k_\rho \rho)$) if $c = 1$; the bessel function of second kind ($N_n(k_\rho \rho)$), or Neumann function, if $c = 2$; or the Hankel function of first ($H_n^{(1)}(k_\rho \rho)$) or second ($H_n^{(2)}(k_\rho \rho)$) kind if $c = 3$ or $c = 4$ respectively.

In order to choose the most suitable bessel function, the behavior of the waves must be considered. To do this, it must be taken into account that, whereas the bessel functions of first and second kind indicate standing waves, the Hankel functions represent outward and inward traveling waves. Thus, since in this thesis transmitted field is being studied, what means outgoing waves from the origin, Hankel functions are going to be considered. Specifically, if dependence of field with regard to time established in equation (2.1) is assumed, the Hankel function that must be chosen is the function of first kind, which represents outward traveling waves.

Once the bessel function has been chosen, the scalar solution (2.18) must be used to solve the vector Helmholtz equation. With this purpose, as in the rectangular coordinate system, the solution is going to be split into TE and TM solutions with regard to z direction. In this case, however, though equations (2.12) and (2.13) can also be applied, the solution is not as straightforward as in planar coordinates because the extension of the nabla operator (∇) must be carried out in cylindrical coordinates. By doing so, the exact E_ρ, E_ϕ and E_z components of field for the TE^z and TM^z solutions are obtained.

However, it can be considered that, not only the expression (2.18) is solution of the scalar Helmholtz equation, but also a weighted sum of these functions. This sum can be done over n and k_ρ, or over n and k_z, but not over k_ρ and k_z

since they are interrelated [37]. For this thesis the second option is considered and, thus, the weighted sum of solutions is expressed as:

$$\psi = \sum_{n=-\infty}^{\infty} \int_{-\infty}^{\infty} f_n(k_z) H_n^{(1)}(k_\rho \rho) e^{jn\phi} e^{jk_z z} dk_z \tag{2.20}$$

where $f_n(k_\rho)$ are the weights and the Hankel function of first kind has been assumed.

If the solution expressed in (2.20), instead of the one from (2.18), is considered to solve the vector Helmholtz equation, the *cylindrical wave expansion* may be expressed as follows [43]:

$$\vec{E}(\rho, \phi, z) = \sum_{s=1}^{2} \sum_{n=-\infty}^{\infty} \int_{-\infty}^{\infty} a_{sn}(k_z) \vec{M}_{snk_z}(\rho, \phi, z) dk_z \tag{2.21}$$

where $a_s n(k_z)$ are the *cylindrical wave coefficients*, and $\vec{M}_{snk_z}(\rho, \phi, z)$ are the *cylindrical wave functions* whose expressions are:

$$\vec{M}_{1nk_z}(\rho, \phi, z) = \left(\frac{jnH_n^{(1)}(k_\rho \rho)}{\rho} \hat{\rho} - \frac{\partial H_n^{(1)}(k_\rho \rho)}{\partial \rho} \hat{\phi} \right) e^{jn\phi} e^{jk_z z} \tag{2.22}$$

$$\vec{M}_{2nk_z}(\rho, \phi, z) = \left(-\frac{jk_z}{k} \frac{\partial H_n^{(1)}(k_\rho \rho)}{\partial \rho} \hat{\rho} + \left(\frac{nk_z}{k\rho} \hat{\phi} + \frac{k_\rho^2}{k} \hat{z} \right) H_n^{(1)}(k_\rho \rho) \right) e^{jn\phi} e^{jk_z z} \tag{2.23}$$

Thus, a general solution to the vector wave equation (2.9) has been obtained in cylindrical coordinates using a wave expansion technique. When dealing with the radiation of an antenna, this field will represent the radiated field by the antenna outside its minimum enclosing cylinder. The reason for such limitation is the fact that the wave equation has been solved in a source-free region and the region inside this cylinder contains the antenna, i.e., a source.

2.2.3 Spherical wave expansion (SWE)

The spherical coordinate system, defined in Fig. 2.3, has become one of the most used in antenna measurements. The main reason for this election is the fact that the spherical coordinate system is the simplest measurement system allowing the measurement of the radiated field on a canonical surface (with r constant) enclosing completely the antenna. This is an important fact since, only measuring the field in the whole surface enclosing the antenna, all the information is considered. Other coordinate systems, such as rectangular or

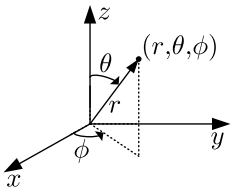

Figure 2.3: Spherical coordinate system: definition.

cylindrical, need two canonical surfaces to describe a surface enclosing completely the antenna, what normally means harder work on field measurement.

Being one of the most used coordinate systems, the solution of the vector wave equation in a spherical coordinate system has been extensively studied by many authors, e.g. Harrington [37], Stratton [39] or Hansen [20]. This last publication offers a specially detailed formulation about the solution in spherical coordinates, and deals with problems related with spherical measurements. Hansen's book assumes the dependence with regard to time assumed at the beginning of this chapter (2.1).

From [20], the solution to the scalar wave equation applying the separation of variables technique in the spherical coordinate system can be expressed as follows:

$$\psi = z_n^{(c)}(kr) L_n^m(\cos\theta) e^{jm\phi} \tag{2.24}$$

where $z_n^{(c)}(kr)$ are the *spherical Bessel functions* of order n (see Appendix A), and $L_n^m(\cos\theta)$ are the *associated Legendre function* of degree n and order m (see Appendix B). There are two types of Legendre functions, the first and second kind functions. However, in order to guarantee ψ finite from $\theta = 0$ to $\theta = \pi$, first kind functions ($P_n^m(\cos\theta)$) must be chosen as well as integer values for degree n [37].

The spherical Bessel functions can be computed from the Bessel functions with the following expression:

$$z_n^{(c)}(kr) = \sqrt{\frac{\pi}{2kr}} Z_{n+1/2}^{(c)}(kr) \tag{2.25}$$

where $Z_n^{(c)}(kr)$ are the Bessel functions explained previously for the cylindrical wave expansion. In this case, the same parameter c appears, with the same meaning as in the cylindrical case. Therefore, since outward traveling waves are also desired for the spherical case, $c = 3$ must be the election ($z_n^{(3)}(kr)$), i.e. the *spherical Hankel function of first kind* ($h_n^{(1)}(kr)$).

In the spherical coordinate system, like in previous systems, a weighted sum of the solution of the scalar wave equation is also solution of the scalar wave

equation. The difference with regard to other coordinate systems is that, now, the sum is performed with a double sum, instead of an integral. Thus, the weighted sum is expressed as:

$$\psi = \sum_n \sum_m q_{mn} h_n^{(1)}(kr) P_n^m(\cos\theta) e^{jm\phi} \tag{2.26}$$

where q_{mn} are the coefficients of the weighted sum.

Once the scalar equation has been solved, the vector Helmholtz equation may be solved. To do this, the first option consists of expressing the solution by means of transversal solutions with regard to z direction (TE^z and TM^z solutions [37], as in previous coordinate systems). However, a simpler solution can be found if transversal solutions with regard to the r direction, i.e., TE^r and TM^r solutions, are considered. A detailed explanation on how this is carried out and its particularities can be found in [37].

Before detailing the expressions for the TE^r and TM^r fields, it must be pointed out that, as commented above, Hansen's notation [20] is applied in this thesis. The use of this notation implies a somewhat different solution to the scalar wave equation. The reason for this change is a power-normalization in the spherical waves that makes an outgoing wave with amplitude 1 radiate 1/2 watt. Thus, the normalized solution to the scalar wave equation is expressed, in general (considering all inward, outward or standing waves), as follows:

$$F_{mn}^{(c)}(r,\theta,\phi) = \frac{1}{\sqrt{2\pi}} \frac{1}{\sqrt{n(n+1)}} \left(-\frac{m}{|m|}\right)^m z_n^{(c)}(kr) \bar{P}_n^{|m|}(\cos\theta) e^{jm\phi} \tag{2.27}$$

where $\bar{P}_n^{|m|}(cos(\theta))$ are the *normalized associated Legendre functions* and factor $(-m/|m|)^m$ is 1 for m=0.

Hence, instead of considering (2.24), the expression of the normalized solution must be used. If this is done, the TE^r and TM^r fields that are derived are the same as in [20], and the final solution, the so-called *spherical wave expansion*, is expressed in the following way:

$$\vec{E}(r,\theta,\phi) = \frac{k}{\sqrt{\eta}} \sum_{smn} Q_{smn}^{(c)} \vec{F}_{smn}^{(c)}(r,\theta,\phi), \quad \text{for} \quad r > r_0 \tag{2.28}$$

where η is the admittance of medium ($\eta = \sqrt{\epsilon/\mu}$), r_0 is the radius of the minimum sphere enclosing the antenna, $Q_{smn}^{(c)}$ are the *spherical wave coefficients* and $\vec{F}_{smn}^{(c)}(r,\theta,\phi)$ are the *spherical wave functions* expressed as follows:

$$\vec{F}_{1mn}^{(c)}(r,\theta,\phi) = \frac{1}{\sqrt{2\pi}}\frac{1}{\sqrt{n(n+1)}}\left(-\frac{m}{|m|}\right)^m \left[z_n^{(c)}(kr)\frac{jm\bar{P}_n^{|m|}(\cos\theta)}{\sin\theta}e^{jm\phi}\hat{\theta} - z_n^{(c)}(kr)\frac{d\bar{P}_n^{|m|}(\cos\theta)}{d\theta}e^{jm\phi}\hat{\phi}\right] \tag{2.29}$$

$$\vec{F}_{2mn}^{(c)}(r,\theta,\phi) = \frac{1}{\sqrt{2\pi}}\frac{1}{\sqrt{n(n+1)}}\left(-\frac{m}{|m|}\right)^m \left[\frac{n(n+1)}{kr}z_n^{(c)}(kr)\bar{P}_n^{|m|}(\cos\theta)e^{jm\phi}\hat{r} + \frac{1}{kr}\frac{d}{d(kr)}\{krz_n^{(c)}(kr)\}\frac{d\bar{P}_n^{|m|}(\cos\theta)}{d\theta}e^{jm\phi}\hat{\theta} - \frac{1}{kr}\frac{d}{d(kr)}\{krz_n^{(c)}(kr)\}\frac{jm\bar{P}_n^{|m|}(\cos\theta)}{\sin\theta}e^{jm\phi}\hat{\phi}\right] \tag{2.30}$$

As commented above, in previous expressions it must be chosen $c = 3$, i.e., the spherical Hankel functions of first kind, in order to just consider outward traveling waves. By doing so, the only remaining step to obtain the radiated field by an antenna is the way in which the spherical wave coefficients are computed. Section 2.3.2 will explain this procedure.

2.2.4 Spheroidal wave expansion (SoWE)

The spheroidal coordinates [45], [46] are less used than previous coordinates. They are not as intuitive as planar, cylindrical and spherical, and the formulation derived from these new coordinates is somewhat more difficult. However, these kind of systems offer interesting applications, as it will be seen in future chapters. For this reason, the solution of the vector Helmholtz equation in these coordinates is studied in this section.

There are two kinds of spheroidal systems: the *prolate spheroidal coordinate system* and the *oblate spheroidal coordinate system*. Both are depicted in Fig. 2.4, where d is the focal distance and η, ξ and ϕ are the spheroidal coordinates. As can be observed in this figure, the spheroidal systems are formed by rotating an ellipse around the z axis. Depending on the positions of the ellipse focuses, a prolate (if they are in the z axis) or an oblate (if they are in the x or y axis, or in general in the XY plane) spheroidal coordinate system is formed.

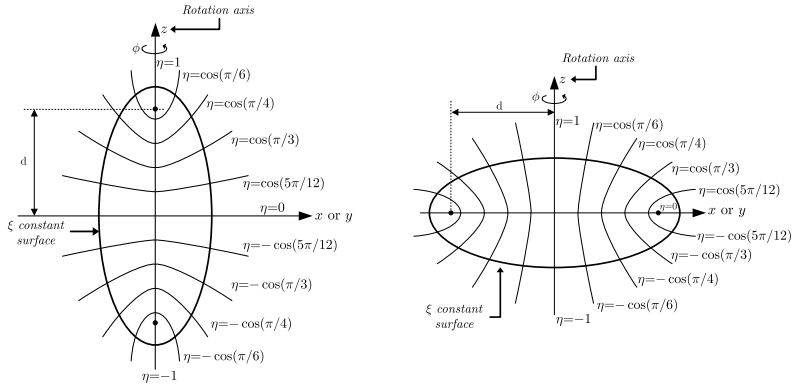

(a) Prolate. (b) Oblate.

Figure 2.4: Spheroidal coordinate systems.

The prolate and oblate spheroidal coordinate systems are similar, but different. This means that, despite both start from a rotated ellipse, the resulting canonical surface, i.e., a surface with ξ constant, is not the same. Whereas in the prolate coordinates the resulting surface is similar to a rugby ball, in the oblate coordinates, this surface is quiet similar to an Olympic discus. The immediate consequence of this fact is that formulation derived from these two coordinate systems is different and, therefore, they must be studied independently.

For the sake of simplicity, in this thesis just the oblate spheroidal coordinate system is considered. The reason for this election is related to the aim of currents reconstruction in the XY plane raised in the introduction. As it will be seen in future chapters, the oblate coordinates offer the possibility of computing the field on a surface close to a flat surface in the XY plane, thus the currents can be obtained at points close to the desired plane.

The solution of the scalar Helmholtz equation in the oblate spheroidal coordinates, though being one of the coordinates systems which allow the separation of variables [40], has not been as widely studied as the solution in previous coordinates systems. However, recently Li et al. [47] published an extensive study about the spheroidal coordinates and the solution of the wave equation in these coordinates.

From [47], if the dependence with regard to the time is changed to that of the expression (2.1) (in [47] the usual definition is considered), the solution to the scalar Helmholtz equation in the oblate spheroidal coordinate system can be expressed as:

$$\psi = S_{mn}^{(p)}(-jc,\eta)R_{mn}^{(q)}(-jc,j\xi)e^{jm\phi} \tag{2.31}$$

where $c = kd$, and $S_{mn}^{(p)}(-jc,\eta)$ and $R_{mn}^{(q)}(-jc,j\xi)$ are the *spheroidal angular functions* and the *spheroidal radial functions*, respectively. For the detailed expressions of these functions and a detailed explanation on how they are computed, see Appendix D.

Regarding to indices p and q, on the one hand, the index p is used to select the first or second order spheroidal angular functions, which depend on the associated Legendre functions of first and second kind, respectively. As in the spherical case, the first kind functions must always be chosen in the case dealt with in this thesis [48], thus $p = 1$ is assumed from now on. On the other hand, the index q has the same meaning as the index c of the bessel functions in cylindrical and spherical wave functions. Therefore, since the main interest in this thesis is focused on the outward traveling waves and the dependence of (2.1) is assumed, $q = 3$ must be chosen.

Of course, as in other coordinate systems, a weighted sum of the simple solution of the scalar equation is also solution. Thus, instead of (2.31), the following solution, where the desired indices are already indicated and α_{mn} are the weights of the sum, may be considered:

$$\psi = \sum_m \sum_n \alpha_{mn} S_{mn}^{(1)}(-jc,\eta)R_{mn}^{(3)}(-jc,j\xi)e^{jm\phi} \tag{2.32}$$

Once the scalar Helmholtz equation has been solved, the solution to the vector Helmholtz equation must be derived. However, as it was commented above, the spheroidal coordinate systems are not among the six coordinate systems in which the vector Helmholtz equation solution can be expressed as transverse solutions to a coordinate surface [40]. The reason for this problem is that the spheroidal radial functions are not orthogonal [47] and, therefore, the TE and TM field with regard η, ξ or ϕ cannot be deduced.

In [47] it is explained the way the previous drawback is overcome. This procedure is similar to the one suggested by Harrington [37] as an alternative for the spherical solution. It consists of obtaining transversal solutions with regard to a component of a coordinate systems among the six coordinate systems in which this is possible, e.g. $\hat{x}$, $\hat{y}$, $\hat{z}$ or $\hat{r}$, instead of the spheroidal components. Thus, transversal solutions, for instance TE^z and TM^z if they are with regard to $\hat{z}$, are derived using the solution to the scalar Helmholtz equation (2.31). Thus, the solution is expressed in spheroidal coordinates, but in cartesian components.

Once this solution has been deduced, a transformation of cartesian components into spheroidal components is done by applying transformation formulas of Appendix D, what leads to a solution of the wave equation in spheroidal components and coordinates.

When the previous procedure is applied [47], the following expressions for the vector wave functions using TE^z and TM^z solutions and (2.31) can be stated:

$$\vec{M}_{1mn}(\eta,\xi,\phi) = \nabla \times (\psi\hat{z}) \tag{2.33}$$

$$\vec{M}_{2mn}(\eta,\xi,\phi) = \frac{1}{k}\nabla \times \nabla \times (\psi\hat{z}) \tag{2.34}$$

The solution of previous equations and the transformation into spheroidal components can be performed by using the expressions of Appendix D. If this is done, the *spheroidal vector wave functions* are obtained. The expressions for these functions are:

$$\begin{aligned}\vec{M}_{1mn}(\eta,\xi,\phi) =& \frac{jm\eta S_{mn}R_{mn}}{\sqrt{(\xi^2+\eta^2)(1+\xi^2)}}e^{jm\phi}\hat{\xi} \\ &+\frac{jm\xi S_{mn}R_{mn}}{\sqrt{(\xi^2+\eta^2)(1-\eta^2)}}e^{jm\phi}\hat{\eta} \\ &-\frac{\sqrt{(1+\xi^2)(1-\eta^2)}}{(\xi^2+\eta^2)}\left[\eta S_{mn}\frac{\partial R_{mn}}{\partial\xi}+\xi R_{mn}\frac{\partial S_{mn}}{\partial\eta}\right]e^{jm\phi}\hat{\phi}\end{aligned} \tag{2.35}$$

$$\begin{aligned}\vec{M}_{2mn}(\eta,\xi,\phi) =& \\ &\frac{\sqrt{1+\xi^2}}{kd\sqrt{\xi^2+\eta^2}}\left[\frac{m^2\xi S_{mn}R_{mn}}{(\xi^2+\eta^2)(1-\eta^2)}\right. \\ &\left.-\frac{\partial}{\partial\eta}\left(\frac{(1-\eta^2)}{(\xi^2+\eta^2)}\left[\eta S_{mn}\frac{\partial R_{mn}}{\partial\xi}+\xi R_{mn}\frac{\partial S_{mn}}{\partial\eta}\right]\right)\right]e^{jm\phi}\hat{\xi} \\ &+\frac{\sqrt{1-\eta^2}}{kd\sqrt{\xi^2+\eta^2}}\left[-\frac{m^2\eta S_{mn}R_{mn}}{(\xi^2+\eta^2)(1-\eta^2)}\right. \\ &\left.+\frac{\partial}{\partial\xi}\left(\frac{(1+\xi^2)}{(\xi^2+\eta^2)}\left[\eta S_{mn}\frac{\partial R_{mn}}{\partial\xi}+\xi R_{mn}\frac{\partial S_{mn}}{\partial\eta}\right]\right)\right]e^{jm\phi}\hat{\eta} \\ &+\frac{jm\sqrt{(1+\xi^2)(1-\eta^2)}}{kd(\xi^2+\eta^2)}\left[\frac{S_{mn}}{(1-\eta^2)}\frac{\partial\xi R_{mn}}{\partial\xi}-\frac{R_{mn}}{(1+\xi^2)}\frac{\partial\eta S_{mn}}{\partial\eta}\right]e^{jm\phi}\hat{\phi}\end{aligned} \tag{2.36}$$

where, for the sake of simplicity, $S_{mn}^{(1)}(-jc,\eta)$ has been denoted as S_{mn}, and $R_{mn}^{(3)}(-jc,j\xi)$ as R_{mn}.

Finally, the general solution to the vector Helmholtz equation is expressed as a weighted sum of both previous spheroidal vector wave functions in the following way:

$$\vec{E}(\eta,\xi,\phi)=\sum_{smn}\alpha_{smn}\vec{M}_{smn}(\eta,\xi,\phi) \tag{2.37}$$

As pointed out above, the previous result is only valid for the oblate spheroidal coordinates. If the solution in the prolate spheroidal coordinate system is desired, a similar procedure might be carried out [47], what would lead to similar, though different, spheroidal vector wave functions.

2.3 Wave coefficients determination

In the first section of this chapter it has been shown that the field present in a source-free region can be obtained by solving the vector Helmholtz equation. Later, in the second section, a general solution of this equation in four different coordinate systems has been found. This solution is expressed as a weighted sum of the vector wave functions expressed on each coordinates. The applied weights are known as *wave coefficients* and characterize the field that is being studied. For instance, the wave coefficients may be used to characterize the radiated field by an antenna. In addition, by doing so, the coefficients not only characterize the field, but also the antenna. Hence, the same coefficients may be used to compute the field at any spatial point outside the minimum canonical surface enclosing the antenna.

The main problem concerning the wave coefficients is the way in which they are computed. For simple cases, an analytical solution can be deduced, as is done for the spherical wave coefficients of the electric and magnetic Hertzian dipole in [20]. However, for complex situations, or real antennas, this is not possible, and the wave coefficients must be computed from field measurements. Although it is not specifically necessary, it is advisable to perform the transformation of field measurements into wave coefficients from measurements in a coordinate surface. For instance, if spherical wave coefficients must be obtained, measurements on a sphere mesh are recommended.

Therefore, the available measurement system determines the wave coefficients that can be easily obtained. For this thesis the available facility includes an anechoic chamber with a spherical measurement system. For this reason the algorithm used for computing the spherical coefficients from spherical measurements is going to be explained. Furthermore, though a planar measurement

system is not available, transformation of planar measurements into planar coefficients is also going to be detailed since it will be used in next chapters.

2.3.1 Planar coefficients

As mentioned above, in order to compute planar coefficients, the most suitable election is to use planar measurements. This kind of measurement systems performs tangential measurements on a plane like the one depicted in Fig. 2.5. The position of the plane measurement with regard to the cartesian axes depends on the application. For the purpose dealt with in this thesis, the most suitable choice is a plane with z component constant, i.e., the plane shown in Fig. 2.5.

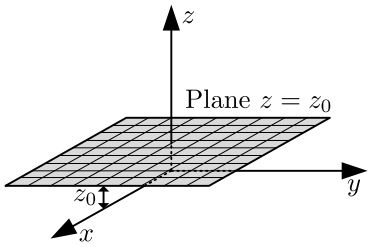

Figure 2.5: Rectangular coordinate system: canonical surface.

Once the tangential components of the electric field to the plane of Fig. 2.5 have been measured, i.e. $E_x(x, y, z_0)$ and $E_y(x, y, z_0)$, the planar coefficients can be computed. These coefficients, as commented Section 2.2.1, are known as *plane wave spectrum* ($\vec{A}_E(k_x, k_y)$) and just depend on the spectral variables (k_x, k_y). The way this spectrum is obtained is by means of the following Fourier transform (FT) [23],[49]:

$$\vec{A}_E(k_x, k_y) = \int_{-\infty}^{\infty} \int_{-\infty}^{\infty} \vec{E}(x, y, z_0) e^{-jk_x x} e^{-jk_y y} e^{-jz_0\sqrt{k^2 - k_x^2 - k_y^2}} dxdy, \quad (2.38)$$

where, as can be observed, just an inversion of (2.17) has been carried out.

Of course, though expressed as continuous inverse Fourier transform, in practice the transformation of plane measurements into plane wave spectrum is performed by means of a discrete Fourier transform (DFT). Thus, the integrals are expressed as follows:

$$\vec{A}_E(k_x,k_y)=\sum_{n=-N_x}^{N_x}\sum_{m=-N_y}^{N_y}\vec{E}(n\Delta x,m\Delta y,z_0)e^{-jn\Delta xk_x}e^{-jn\Delta yk_y}e^{-jz_0\sqrt{k^2-k_x^2-k_y^2}} \tag{2.39}$$

where $(2N_x+1)$ and $(2N_y+1)$ are the number of measurement points in the x and y axes, and Δx and Δy are the spacing for the mesh measurement in the x and y axes, respectively.

Once $\vec{A}_E(k_x,k_y)$ has been obtained, the computation of the field is a straightforward step since just expression (2.17) must be applied. At this point, however, one limitation must be taken into account. Since solution has been derived for a source-free region, the field computed with (2.17) will only be valid for this kind of regions. This means that, for instance, if an antenna is placed in $z<0$ and close to the XY plane, the field can only be computed with (2.17) in $z>0$, i.e., the region without sources.

2.3.2 Spherical coefficients

The spherical coefficients are not computed as straightforward as the planar coefficients. The formulas to express the coefficients $Q_{smn}^{(c)}$ as a function of the spherical measurement ($\vec{E}(r,\theta,\phi)$) does not just consists of a Fourier transform, but requires a more complex algorithm.

Furthermore, the complexity is increased with regard to the planar coefficients because, now, real measurements taken with real probes are considered. Previously, when computing the planar coefficients from plane measurements, the use of real probes has not been considered because planar measurements have not been available for this thesis. However, now, since the available facility includes a spherical measurement system, real measurements are used and, hence, the effect of the probe, especially in those measurements taken in the near-field region, must be taken into account.

The way in which the effect of the probe is considered is known as *probe correction* and has been widely studied for a general case, e.g. by Paris [50] or Yaghjian [24] and, specifically for the spherical coordinate system, by Larsen [51]. Inclusion of probe correction in the algorithm for computing the spherical coefficients is a hard task. For this reason, in [52], Larsen introduced an improved algorithm to easily consider the influence of the probe in the measurements. Later, Hansen [20] summarized this algorithm and its related formulation.

There are two levels of probe correction: first-order probe correction [51],[20] and high-order probe correction [53]-[57]. Whereas the first-order just considers low-order probe receiving modes, i.e., general probe behavior, the high-order carries out a complete correction considering all the modes necessary for this

purpose. Of course, the high-order is more accurate than the first-order; however, in this thesis, not much accuracy is needed and, hence, only the first-order probe correction is going to be considered.

The first consequence of taking into account the probe correction is the fact that the algorithm does not take as data the electric field ($\vec{E}$) present on the measurement points, but the amplitude of the received signal (ω) in the probe on each point. Of course these both quantities are not the same because of the effect of probe in measurements. In order to correct this difference, probe correction incorporates the knowledge of the incoming modes to the probe (receiving coefficients).

Once it has been established the kind of probe correction to apply, it must be described the points where the measurements must be taken in order to compute the spherical coefficients. The algorithm [20] requires measurements on the points depicted in Fig. 2.6. As can be observed, these points form a spherical surface where the measurement points are equispaced in θ and ϕ, and placed at $r = A$ from the origin of the spherical coordinate system. In addition, the algorithm requires measurements with two different orthogonal polarizations ($\chi = 0$ and $\chi = \pi/2$) on each point. Therefore, two different measurements (or one if both polarizations are measured at the same time) must be carried out.

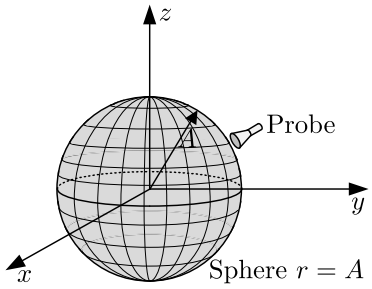

Figure 2.6: Rectangular coordinate system: canonical surface.

The previous measurements ($w(A, \chi, \theta, \phi)$) are related to the outgoing spherical waves $Q^{(3)}_{smn}$ by means of the *transmission formula* [20]. This formula, however, does not determines the coefficients $Q^{(3)}_{smn}$, but the so-called *transmitting coefficients* (T_{smn}), which are related to $Q^{(3)}_{smn}$ by [20]:

$$Q^{(3)}_{smn} = vT_{smn} \tag{2.40}$$

where v is the amplitude of the incoming wave to the local port of the antenna under test. From now on this notation will be assumed and, hence, the aim will be the determination of the transmitting coefficients.

By using these coefficients, the transmission formula can be expressed as follows:

$$w(A,\chi,\theta,\phi) = \frac{v}{2}\sum_{\substack{smn\\ \mu}} T_{smn} e^{jm\phi} d^n_{\mu m}(\theta) e^{j\mu\chi} P_{s\mu n}(kA) \tag{2.41}$$

In (2.41), $d^n_{\mu m}(\theta)$ are the *rotation coefficients* (whose complete expressions can be found in Appendix C), and $P_{s\mu n}(kA)$ are the *probe response constants*. These constants depend on the spherical coefficients characterizing the antenna in reception, i.e. the coefficients for the incoming modes to the probe. These coefficients, which are known as *receiving coefficients* ($R_{\sigma\mu\nu}$), are used to eliminate the effect of the probe in the spherical measurement. These coefficients are employed to compute the probe response constants as follows:

$$P_{s\mu n}(kA) = \frac{1}{2}\sum_{\sigma\nu} C^{sn(3)}_{\sigma\mu\nu}(kA) R_{\sigma\mu\nu} \tag{2.42}$$

where $C^{sn(3)}_{\sigma\mu\nu}(kA)$ are the *translation coefficients* whose expressions can be found in Appendix C.

From [20], the derivation of an equation to express in an easy way the transmitting coefficients (T_{smn}) as a function of the measurement $w(A,\chi,\theta,\phi)$ can be achieved by means of a three-fold integral transform. First, the function $w_\mu(A,\theta,\phi)$ is computed with the following Fourier transform:

$$w_\mu(A,\theta,\phi) = \frac{1}{2\pi}\int_{\chi=0}^{2\pi} w(A,\chi,\theta,\phi) e^{-j\mu\chi} d\chi \tag{2.43}$$

Then, $w_\mu(A,\theta,\phi)$ is used to obtain the function $w_{\mu m}(A,\theta)$ by means of another Fourier transform in ϕ:

$$w_{\mu m}(A,\theta) = \frac{1}{2\pi}\int_{\phi=0}^{2\pi} w_\mu(A,\theta,\phi) e^{-jm\phi} d\phi \tag{2.44}$$

Finally, the function $w^n_{\mu m}(A)$ is computed applying the following integral to the previous function:

$$w^n_{\mu m}(A) = \frac{2n+1}{2}\int_{\theta=0}^{\pi} w_{\mu m}(A,\theta) d^n_{\mu m}(\theta) sin\theta d\theta \tag{2.45}$$

The ways in which the previous integrals are done in practice are beyond the scope of this thesis. For a detailed explanation on this issue see [20].

Once the previous three-fold integral transform has been derived, a relation between the transmitting coefficients, the functions $w^n_{\mu m}(A)$ and the probe response constants $P_{s\mu n}(kA)$ must be established. By assuming first-order probes, e.g. an open-ended circular waveguide excited by the TE_{11} mode [20],

just the receiving coefficients with $\mu = \pm 1$ must be considered since these coefficients are the only coefficients that are not negligible in the first-order probes receiving coefficients. Consequently, only the probe response constants $P_{s\pm 1n}(kA)$ must be taken into account and, hence, the transmitting coefficients may be obtained as:

$$T_{1mn} = \frac{1}{v}\left(\frac{P_{21n}(kA)w^n_{-1m}(A) - P_{2,-1n}(kA)w^n_{1m}(A)}{P_{21n}(kA)P_{1,-1n}(kA) - P_{11n}(kA)P_{2,-1n}(kA)}\right) \tag{2.46}$$

$$T_{2mn} = \frac{1}{v}\left(\frac{P_{11n}(kA)w^n_{-1m}(A) - P_{1,-1n}(kA)w^n_{1m}(A)}{P_{2,-1n}(kA)P_{11n}(kA) - P_{21n}(kA)P_{1,-1n}(kA)}\right) \tag{2.47}$$

Unfortunately, when applying (2.46) and (2.47) in practice one problem arises. Since probe response constants are necessary, and the probe receiving coefficients must be used to compute these constants, these receiving coefficients must be available to obtain the transmission coefficients. However, this is not always possible since special algorithms and additional measurements must be carried out in order to compute the probe receiving coefficients. These algorithms are part of a more general procedure, which is known as *probe calibration*, and will be deeply studied in Chapter 6. Until then, it will be considered that the probe receiving coefficients are known, and therefore, the transmission coefficients will be determined with no problems.

Hence, the determination of the spherical coefficients is not as straightforward as for the planar case, but can be easily achieved by using (2.46) and (2.47). Once this has been carried out, the antenna under test is characterized in transmission by the transmitting coefficients and its radiated field can be computed with (2.40) and (2.28).

Finally, it must commented that, normally, the field is required in the far-field region, i.e., at points with $r > 2D^2/2$, where D is the diameter of the antenna. In this region it can be considered that the shape of the radiation pattern does not change and just an attenuation of the pattern takes place. Mathematically this fact is achieved by using the approximation of Hankel functions for $r \to \infty$ (see Appendix A) in the spherical wave functions (2.29), (2.30). By doing so, the electric field can be expressed as follows:

$$\vec{E}(r,\theta,\phi)|_{_{FF}} \to \frac{k}{\sqrt{\eta}}\frac{1}{\sqrt{4\pi}}\frac{e^{jkr}}{kr}v\vec{K}(\theta,\phi) \tag{2.48}$$

where $\vec{K}(\theta,\phi)$ is the normalized far-field pattern obtained in the following way:

$$\vec{K}(\theta,\phi) = \sum_{smn} T_{smn}\vec{K}_{smn}(\theta,\phi) \tag{2.49}$$

In this expression, $\vec{K}_{smn}(\theta,\phi)$ are the spherical wave functions in the far-field region derived from the particularization of the spherical wave functions (2.29), (2.30) for $r \to \infty$. From [20], these far-field functions can be expressed as:

$$\begin{aligned}\vec{K}_{1mn}(\theta,\phi) =& \sqrt{\frac{2}{n(n+1)}}\left(-\frac{m}{|m|}\right)^m (-j)^{n+1} e^{jm\phi} \\ & \left[\frac{jm\bar{P}_n^{|m|}(\cos\theta)}{\sin\theta}\hat{\theta} - \frac{d\bar{P}_n^{|m|}(\cos\theta)}{d\theta}\hat{\phi}\right]\end{aligned} \tag{2.50}$$

$$\begin{aligned}\vec{K}_{2mn}(\theta,\phi) =& \sqrt{\frac{2}{n(n+1)}}\left(-\frac{m}{|m|}\right)^m (-j)^{n} e^{jm\phi} \\ & \left[\frac{d\bar{P}_n^{|m|}(\cos\theta)}{d\theta}\hat{\theta} + \frac{jm\bar{P}_n^{|m|}(\cos\theta)}{\sin\theta}\hat{\phi}\right]\end{aligned} \tag{2.51}$$

Therefore, the field in the far-field region can be computed applying (2.48), which just requires the computation of the far-field wave functions (2.50) and (2.51), instead of the much more complicated was functions (2.29) and (2.30).

Practical results In order to verify the described algorithm, an antenna was measured and its transmitting coefficients were computed. Then, the radiated field was obtained at the same distance where the measurements had been done to test the accuracy of the method. Finally, the field in the far-field region was also computed in order to show all the possibilities of the algorithm.

The measured antenna was a slot-array antenna at 36.85 GHz. In the upper part of each slot, a passive dipole was placed in order to obtain a circularly polarized field. Fig. 2.7(a) shows the lower part of the substrate placed over the feeding waveguide, and Fig. 2.7(b) shows the upper part of the substrate with the passive dipoles. The position of the dipoles with regard to the slots is depicted in Fig. 2.8. In addition, in this figure it is shown the position of the antenna with regard to the coordinate system in the measurement facility. It must be pointed out that, in Fig. 2.8, for the sake of simplicity just some elements have been drawn. As shown in pictures of Fig. 2.7, the antenna is formed by 40 elements, but just 16 have been drawn.

The slot-array antenna was measured on the spherical mesh shown in Fig. 2.6 and at a 0.92 m of distance, i.e., in the near-field region. Once this measurement had been carried out, the transmitting coefficients of the antenna were computed, firstly, determining the probe response constants (2.42) by means of

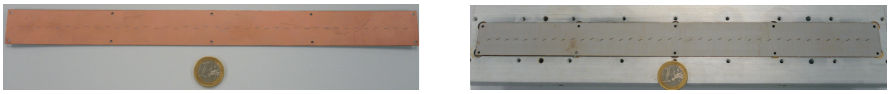

(a) Lower part of the substrate: slots.

(b) Upper part of the substrate: dipoles.

Figure 2.7: Picture of the measured slot array antenna with passive dipoles at 36.85 GHz

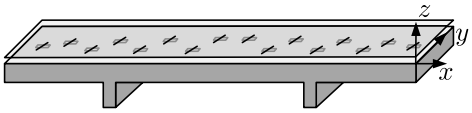

Figure 2.8: Diagram of the measured slot array antenna with passive dipoles at 36.85 GHz

the probe receiving coefficients (which had been previously computed as will be described in Chapter 6), and, then by applying (2.46) and (2.47). Finally, the field at the same measurement distance was obtained with (2.40) and (2.28).

Fig. 2.9 shows a comparison between the measured near field at 0.92 m on the XZ plane (Fig. 2.9(a)) and on the YZ plane (Fig. 2.9(b)), and the computed field at the same distance using the spherical wave expansion (2.28). As can be observed, both fields are quite similar and just a few points are different in amplitude. This fact confirms the accuracy of the method for computing the transmitting coefficients as well as the radiated field.

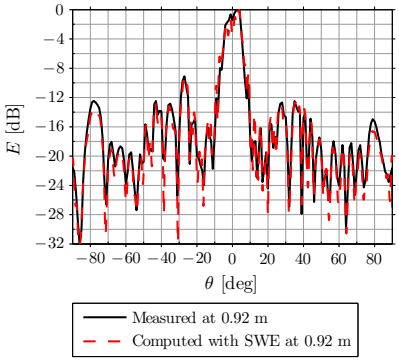

(a) Field on the XZ plane (AZIMUTH)

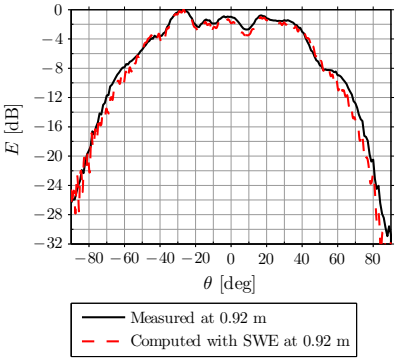

(b) Field on the YZ plane (ELEVATION)

Figure 2.9: Comparison of the measured and computed near-field on the main planes of the slot-array antenna at 36.85 GHz.

Finally, the field in the far-field region was computed by applying (2.48). Fig. 2.10 shows this field on the main planes. Here it can be seen that, in the far-field region, the antenna has a high directivity, as it should be in an antenna formed by many (40) elements. In this case no other data is available in order to verify wether the computed far field is correct or not. However, since the computed field at the same measurement distance (Fig. 2.9) is quiet accurate, it can be concluded that the way in which the far field was computed is correct. Thus, this algorithm will be used in future chapters to compute the far field from near-field measurements.

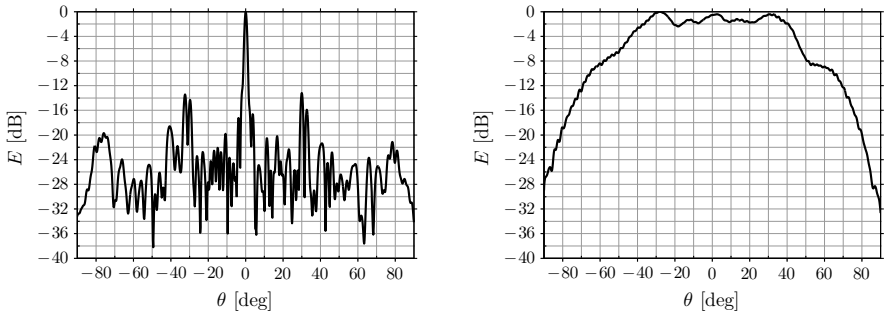

(a) Field on the XZ plane (AZIMUTH)

(b) Field on the YZ plane (ELEVATION)

Figure 2.10: Computed field in the far-field region on the main planes of the slot-array antenna at 36.85 GHz.

Chapter 3

Equivalent currents

The design or manufacturing processes of an antenna may be affected by errors. The location of these errors is carried out by the so-called *antenna diagnosis* procedure, which utilize the information of field measurements. By observing these measurements, however, the errors are hard to detect. For this reason, the equivalent currents on a surface close to the antenna are employed. The way in which these equivalent currents are obtained is one of the objectives stated in the introduction. This chapter describes several methods to obtain the equivalent currents and shows several real results.

3.1 Introduction

The equivalent currents of an antenna are defined by means of the field equivalence principle. The first section of this chapter reviews this principle and describes the most important cases for this thesis. By now, however, it is important to note that the determination of the equivalent currents on a surface is done from the electric or magnetic field on this surface.

To determine this field, the first option consists in measuring the field directly on the surface close to the antenna where the currents are needed. For this purpose, small-loop probes may be placed close to the antenna which allow the field to be measured on the surface of interest [10]. The drawback of this technique is the reflection and coupling that may take place between the probes and the antenna. This effect may lead to non-correct field measurements and, hence, to wrong equivalent currents. For this reason, this option is normally ruled out and other techniques are adopted.

The second option computes the field on the surface of interest from field measurements taken far from the antenna. This backpropagation is part of a more general topic known as *inverse problem*. This problem has been studied

in many areas, e.g. X-rays, seismic waves, atomic structures. It is defined, in the most general of cases, as the determination of the cause of a phenomenon from measurements of this phenomenon [58]. Specifically in the electromagnetic branch, the inverse problem may be defined as the determination of the source characteristics (the antenna) from measurements of the field radiated by the source [58],[59].

In order to solve the inverse problem, several techniques may be applied. These techniques can be divided into two main groups: *integral equation* (IE) methods [11], [12] and *modal expansion* methods [13], [14]. On the one hand, the aim of the integral equation methods is to obtain the equivalent sources that radiate the same field that has been measured. To do this, the solution of the wave equation in a source region is used and an integral equation is solved by means of a numerical method, e.g. the method of moments (MoM) [60] or the finite difference time domain technique (FDTD) [61].

On the other hand, the aim of the modal expansion methods is to obtain the field on the surface of interest by backpropagation and, later, the equivalent currents by means of the equivalence principle. By doing so, the solution of the wave equation in a source-free region, described in Chapter 2, can be applied.

A comparison of both kind of techniques can be found in [62] and also in [63], where the integral equation method is referred as *Sources reconstruction method* (SRM). In this thesis the attention is focused on the modal expansion techniques, though a briefly review of the integral equation methods is also done.

No matter the method is chosen, the solution always depends on the coordinate system in which measurements are taken and on the surface where the equivalent currents are desired. The study of every specific case is beyond the scope of this thesis. The aim is rather the study of one of the most common situations. This situation consists in obtaining the equivalent currents on a flat surface from spherical near-field measurements. Many antennas present a plane radiating part so that the equivalent currents must be determined on a flat surface. Furthermore, one of the most important measurement systems is the spherical measurement system since it allows for complete sphere measurements which do not entail loss of information. For the sake of generality, near-field measurements may be considered to obtain the best result.

Regarding the modal expansion methods, by using spherical near-field measurements, the spherical wave expansion must be used and, hence, the spherical coefficients must be obtained. This fact leads to a restriction: since the solution of the wave equation in a source-free region expressed by means of the spherical wave expansion is only valid outside the minimum sphere enclosing the antenna, the field cannot be obtained on the desired flat surface close to the antenna. For this reason, a change in the coordinate system must be carried out.

This change is normally done from spherical coordinates to planar coordinates by using the plane wave spectrum (PWE) as an intermediate step. The transformation of the plane wave spectrum into the field on a plane is performed by means of a Fourier transform, as described in Section 2.3.1. Since the field in spherical coordinates is considered to be in the near-field region, two different ways exits to perform the above transformation: compute the PWE directly from the measurements [13], [64], or compute firstly the far-field and, later, by applying this field, determine the PWE, what is normally known as the *microwave holographic technique* [16]-[18]. In this chapter both methods are described.

If a more general transformation is desired, the spherical coefficients may be transformed into oblate spheroidal coefficients. By doing so, the field is expressed by means of the oblate spheroidal wave expansion, described in Section 2.2.4. The advantage of this expansion lies in the fact that it is valid at points outside the minimum spheroid enclosing the antenna, even on a extremely flat spheroid surrounding the antenna.

This chapter is organized as follows: first the equivalence principle is reviewed and, then, the integral equation methods are described. Later, the modal expansion techniques are studied and, finally, the transformation of the spherical coefficients to spheroidal coefficients is described.

3.2 Field equivalence principle

The *field equivalence principle* [11],[12] allows a source (e.g. an antenna) to be replaced by an equivalent source. This last source is equivalent within a region because they produce the same field in this region than the original source. Electrically, sources are represented by current densities (electric J and magnetic M) and, hence, the equivalent sources may be named as *equivalent currents*. The significance of these currents arises when they are obtained on a surface enclosing an antenna. In this case, the radiated field by the antenna outside the enclosing surface can be computed by using the equivalent currents instead of the original antenna.

For this thesis the equivalent currents are required on a plane surface (it is supposed the radiating part of the antenna is mainly flat). In this case, the equivalence principle works as depicted in Fig. 3.1. As can be observed, in the original problem (Fig. 3.1(a)) the source, i.e., the antenna, is radiating the field $\vec{E}_1$ and $\vec{H}_1$ inside and outside the infinite surface enclosing the source formed by the infinite flat surface S and the infinite surface S_∞, i.e., in the volumes V_1 and V_2.

In Fig. 3.1(b) the original problem is substituted by the equivalent problem. In this situation, the source has been replaced by the equivalent currents on

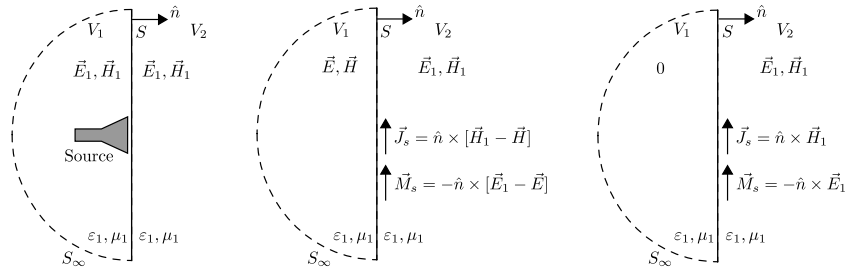

(a) Original problem. (b) Equivalent problem. (c) Love's equivalent.

Figure 3.1: Principle of equivalence.

the surface S, which are noted as $\vec{J}_s$ and $\vec{M}_s$. These currents radiate the same field outside the infinite surface enclosing the source (V_2), though the field radiated inside this volume (V_1) is different ($\vec{E}$ and $\vec{H}$). This characteristic, however, entails an advantage. Since the region inside the infinite surface is not of interest, the field in this region can be anything. Thus, $\vec{E}$ and $\vec{H}$ can be set to zero. This situation, depicted in Fig 3.1(c), is known as *Love's equivalent*. As can be observed, in this case, the equivalent currents can be computed from just the field in the region of interest as follows:

$$\vec{J}_s = \hat{n} \times \vec{H}_1 \tag{3.1}$$

$$\vec{M}_s = -\hat{n} \times \vec{E}_1 \tag{3.2}$$

Beside the Love's equivalent problem, two additional equivalence principles may be stated by taking in advantage that the inner zone to the infinite surface (V_1), and the field in this region, are not of interest. The first equivalent problem is the one depicted in Fig. 3.2. In this case, a *perfect electric conductor* (PEC) is placed inside the volume V_1. By doing so, the electric equivalent currents on the surface vanish and, hence, just the magnetic currents must be considered (see Fig. 3.2(a)). This other problem may become harder than the Love's equivalence since the presence of the conductor must be considered when computing the radiated field by the equivalent currents. However, since the magnetic currents are on a flat surface, the image theory may be applied to simplify the problem. The resulting problem is depicted in Fig. 3.2(b) where, as can be observed, the equivalent currents are:

$$\vec{M}_s = -2\hat{n} \times \vec{E}_1 \tag{3.3}$$

The advantage of the equivalent problem depicted in Fig. 3.2(b) lies in the fact that the magnetic currents (3.3) radiate in an unbounded medium and,

hence, the radiated field may be computed easier than in the problem with the PEC.

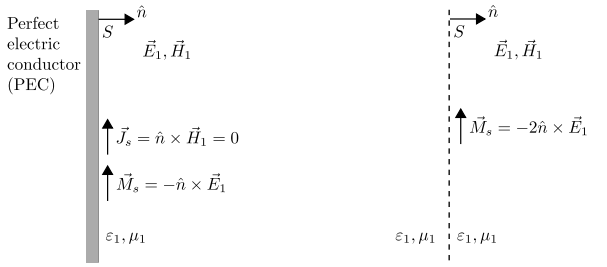

(a) Equivalent problem with PEC.

(b) Equivalent problem with PEC from image theory.

Figure 3.2: Principle of equivalence for the case of a perfect electric conductor.

The third equivalent problem, depicted in Fig. 3.3, places a *perfect magnetic conductor* (PMC) in the region where the radiated field is not of interest (V_1). As can be observed in Fig. 3.3(a), now the equivalent magnetic currents on the surface vanish and, hence, just the electric currents must be considered. In this case, as in the above problem, the image theory may be applied. By doing so, the problem is simplified as shown in Fig. 3.3(b), where the equivalent problem is formed by just the equivalent electric currents of (3.4) radiating in an unbounded medium.

$$\vec{J}_s = 2\hat{n} \times \vec{H}_1 \tag{3.4}$$

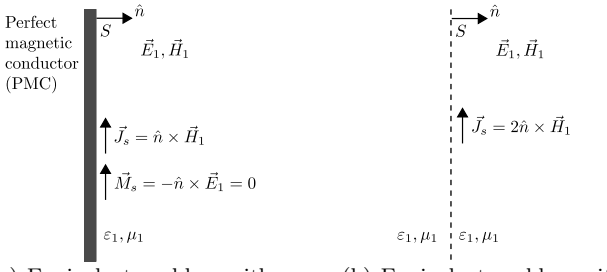

(a) Equivalent problem with PMC.

(b) Equivalent problem with PMC from image theory.

Figure 3.3: Principle of equivalence for the case of a perfect magnetic conductor.

3.3 Integral equation methods

The aim of the integral equation methods applied to the inverse problem is to find the sources that produce the same field that has been measured. To do this, the wave equation is solved in a source region what leads to an integral equation. The solution of this equation is achieved by means of a numerical method [3]. Among the existing methods, the *Finite Difference Time Domain* method (FDTD) [61], [65], the *Finite-Element method* (FEM) [66], and, specially, the *Method of Moments* (MoM) [2] are widely employed in literature.

The solution of the wave equation with arbitrary sources is a hard problem with a high computational cost. For this reason, the equivalence principle is first applied so that the wave equation is solved by just considering the equivalent currents. The shape and position of the surface where the equivalent currents are determined must be chosen in such a way that a great amount of information is obtained but without increasing the complexity of the problem. Recently several works have been presented with the aim of solving the inverse problem on arbitrary three-dimensional surfaces [63],[67]. To do this, the love's equivalence principle (see Fig. 3.1(c)) is applied and the electric and magnetic equivalent currents are obtained by means of the method of moments.

Nevertheless, an easier situation may rise if attention is focused on the radiating part of the antenna. By doing so, flat equivalent surfaces may be applied, e.g. near the aperture of a horn [68] or on the surface of a plane array [69]. The advantage of considering flat surfaces arises because the second and third equivalent problems, depicted in Fig. 3.2 and Fig. 3.3, respectively, may be applied. Thus, just one kind of equivalent currents, which characterize the whole problem, must be considered. It is worth to mention that, though both solutions are completely correct, the result might be interpreted more intuitively by choosing one approach or another, depending on the specific situation. For instance, if the antenna were formed by slots, it might be convenient to use the equivalent magnetic approach to be closer to the real situation.

The equivalent magnetic approach from planar measurements [60],[70] or from spherical measurements [68] considers the situation of Fig. 3.2(b). By doing so, the wave equation may be easily solved [11] by just using the electric vector potential $\vec{F}$. Thus, the radiated electric field $\vec{E}$ can be obtained from the vector $\vec{F}$ as follows:

$$\vec{E} = -\frac{1}{\varepsilon}\nabla \times \vec{F}. \tag{3.5}$$

Since the electric vector potential $\vec{F}$ is related to the magnetic currents $\vec{M}$ by means of the convolution of these currents and the Green's function, the relation between the radiated electric field $\vec{E}$ and the equivalent magnetic currents $\vec{M}$ using the equivalent magnetic approach is given by:

$$\vec{E}(\vec{r}) = -\frac{1}{4\pi}\nabla \times \iint_{S_0} \vec{M}(\vec{r}')G(\vec{r},\vec{r}')dS' \tag{3.6}$$

where $\vec{r}'$ are the points of the surface where the equivalent currents are desired, $\vec{r}$ are the points where the electric field is measured, S_0 is the surface of interest, and $G(\vec{r},\vec{r}')$ is the three-dimensional Green's function expressed as follows:

$$G(\vec{r},\vec{r}') = \frac{e^{jk|\vec{r}-\vec{r}'|}}{|\vec{r}-\vec{r}'|}. \tag{3.7}$$

Similarly for the equivalent electric approach [22], the wave equation may be solved considering the problem depicted in Fig. 3.3(b). In this case, the general solution of the wave equation in a source region by means of the potential vectors [11] may be also applied. By doing so, since the magnetic currents are not present, the electric field can be expressed as a function of the magnetic vector potential $\vec{A}$ in the following way:

$$\vec{E} = -j\omega\mu\vec{A} + \frac{1}{j\omega\varepsilon}\nabla(\nabla\cdot\vec{A}). \tag{3.8}$$

The relation between the potential $\vec{A}$ and the electric currents $\vec{J}$ is the convolution of these currents and the three-dimensional Green's function (3.7) expressed as follows:

$$\vec{A}(\vec{r}) = \frac{1}{4\pi}\iint_{S_0} \vec{J}(\vec{r}')G(\vec{r},\vec{r}')dS' \tag{3.9}$$

where $\vec{r}'$, $\vec{r}$ and S_0 have the same meaning as in (3.6). Substituting (3.9) into (3.8) the field $\vec{E}(\vec{r})$ is found.

The solution of (3.6) and (3.9) may be deduced by applying the method of moments with point matching [22] or Galerkin's type solution [70]. Whichever option is chosen, the result is an equation system that must be solved to obtain the desired currents. This step normally becomes the most difficult step because, at first, the number of unknowns and equations may not be the same. Hence, the *method of least squares* [71] must be applied to be able to solve the system. Furthermore, the equation system is normally ill-conditioned and, therefore, must be solved by, for instance, the *Singular Value Decomposition* (SVD) method (considering the most significant singular values) [71], the *Conjugate Gradient* (CG) method [72],[73] or the *Generalized Minimal Residual* (GMRES) method [72],[73].

In addition, the equation system may require regularization, e.g. the Tikhonov regularization technique [74],[75], to obtain faithful results. These kinds of techniques, however, present some drawbacks, such as the election of the

suitable parameters to obtain the best results without losing information [76], what enhances the difficulty in finding accurate results.

The study in depth of all the previous approaches (electric and magnetic) and the different possibilities for the solution of the equation system is beyond the scope of this thesis. It is worth, however, to show how the solution for a specific case might be obtained.

3.3.1 Equivalent magnetic approach

In this section, the case of an antenna with a planar radiating surface parallel to the XY plane and mainly radiating towards z positive is studied. Fig. 3.4(a) depicts a diagram of this situation if the antenna were a horn. In this case, the aperture of the horn is not exactly on the XY plane, but extremely close to this plane so that the computation of the equivalent currents on a flat surface in the XY plane contributes valuable information about the field on the aperture.

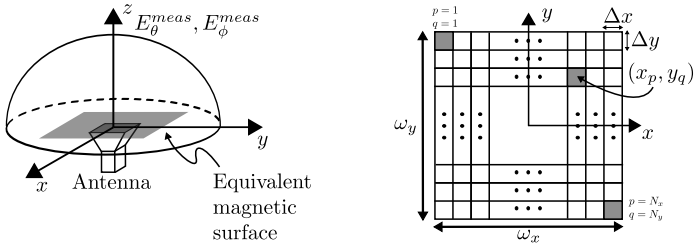

(a) Diagram of the problem.

(b) Discretization of the equivalent magnetic surface.

Figure 3.4: Equivalent magnetic approach.

The application of the equivalence principle in Fig. 3.4(a) by using a flat equivalence surface on the XY plane, and the insertion of a PEC (see Fig. 3.2), leads to a simplified equivalent problem. In this problem neither the antenna nor the PEC are present and, hence, just the magnetic equivalent currents on the equivalent magnetic surface must be considered.

In order to faithfully follow the general aim of this thesis, spherical near-field measurements (E_θ^{meas},E_ϕ^{meas}) are considered [68] for the solution of the equivalent magnetic approach, as depicted in Fig. 3.4(a).

The solution of the problem is achieved by solving the vector wave equation in a source region. Since the equivalent magnetic approach is being considered, only the equivalent magnetic currents (3.3) must be obtained and, hence, the integral equation that must be solved is the one depicted in equation (3.6).

To do this, the method of moments with point matching is applied [68]. For this purpose, the first step consists in discretizing the surface of interest as

depicted in Fig. 3.4(b). Thus, the discrete points where the equivalent currents must be obtained can be expressed as:

$$x_p = -\frac{\omega_x}{2} - \frac{\Delta x}{2} + p\Delta x \tag{3.10a}$$

$$y_q = -\frac{\omega_y}{2} - \frac{\Delta y}{2} + q\Delta y \tag{3.10b}$$

By considering the previous discretization, the equivalent magnetic currents may be expressed as follows:

$$M_x(x', y') = \sum_{p=1}^{N_x}\sum_{q=1}^{N_y} a_{pq}\Delta x\Delta y\delta(x' - x_p, y' - y_q) \tag{3.11a}$$

$$M_y(x', y') = \sum_{p=1}^{N_x}\sum_{q=1}^{N_y} b_{pq}\Delta x\Delta y\delta(x' - x_p, y' - y_q) \tag{3.11b}$$

where (x',y') are the points of the surface where the equivalent magnetic currents must be obtained, N_x and N_y are the number of discrete points in the x and y axes, respectively, a_{pq} and b_{pq} are the weights of M_x and M_y, respectively, and $\delta(x, y)$ is the *Dirac delta function* [46].

The advantage of the discretization stated in (3.11) arises when evaluating the integral of (3.6). The use of the function $\delta(x, y)$ allows the integral to be replaced by their integrand evaluated at the positions of the function $\delta(x, y)$.

Once the integrals have been evaluated, one step still remains. Since the result of the integral is in cartesian coordinates and the measurement is in spherical coordinates, a change of coordinate system must be carried out. This is an easy step that may be done by applying the following formulas, where the r component has been neglected:

$$E_\theta = \cos\theta\cos\phi E_x + \cos\theta\sin\phi E_y - \sin\theta E_z \tag{3.12a}$$

$$E_\phi = -\sin\phi E_x + \cos\phi E_y \tag{3.12b}$$

The spherical near-field measurements are known at discrete points on a sphere around the antenna. Hence, a point matching procedure [2] may be applied what leads to express the solution by the following equation system:

$$\begin{bmatrix} E_\theta^{meas}(\theta,\phi) \\ E_\phi^{meas}(\theta,\phi) \end{bmatrix} = \begin{bmatrix} L_{11} & L_{12} \\ L_{21} & L_{22} \end{bmatrix} \begin{bmatrix} M_x \\ M_y \end{bmatrix}. \tag{3.13}$$

where the vectors M_x and M_y are just the weights of the equivalent currents in the discretization stated in (3.11), i.e., a_{pq} and b_{pq}, and the block-matrices L_{11}, L_{12}, L_{21} and L_{22} are obtained as follows:

$$L_{11} = \frac{\Delta x \Delta y}{4\pi} \frac{e^{jkR_{mn}}}{R_{mn}^2} \left(-jk + \frac{1}{R_{mn}}\right) \left(\cos\theta_m \sin\phi_m z_m^f + \sin\theta_m (y_m^f - y_n^c)\right) \tag{3.14a}$$

$$L_{12} = -\frac{\Delta x \Delta y}{4\pi} \frac{e^{jkR_{mn}}}{R_{mn}^2} \left(-jk + \frac{1}{R_{mn}}\right) \left(\cos\theta_m \cos\phi_m z_m^f + \sin\theta_m (x_m^f - x_n^c)\right) \tag{3.14b}$$

$$L_{21} = \frac{\Delta x \Delta y}{4\pi} \frac{e^{jkR_{mn}}}{R_{mn}^2} \left(-jk + \frac{1}{R_{mn}}\right) \left(\cos\phi_m z_m^f\right) \tag{3.14c}$$

$$L_{22} = \frac{\Delta x \Delta y}{4\pi} \frac{e^{jkR_{mn}}}{R_{mn}^2} \left(-jk + \frac{1}{R_{mn}}\right) \left(\sin\phi_m z_m^f\right) \tag{3.14d}$$

where (θ_m,ϕ_m) are the mth measurement points (which transformed into cartesian coordinates are noted as (x_m^f,y_m^f,z_m^f)), the points (x_n^c,y_n^c) are the nth current points in the coordinate system (x',y') and R_{mn} is the distance between the field points and the current points computed as:

$$R_{mn} = \sqrt{(x_m^f - x_n^c)^2 + (y_m^f - y_n^c)^2 + (z_m^f)^2}. \tag{3.15}$$

As stated above, the solution of the equation system requires special algorithms because of the ill-conditioning of the problem. For this thesis, the GMRES method has been chosen, though depending on the specific case, other method might become more accurate or faster.

Simulated results

The solution for equivalent magnetic approach described above was tested with the antenna shown in Fig. 3.5. As can be observed, the antenna is formed by two $\hat{x}$-directed slots placed along the x axis and separated by 0.8 λ (one in $x = 0.4\lambda$ and the other one in $x = -0.4\lambda$) at the operating frequency (300 MHz).

The spherical near-field radiated by the antenna was simulated with FEKO [4] at $R = 1$ λ. This field was used to solve the equation system derived from the integral equation technique for the equivalent magnetic approach (3.13) what allowed the equivalent magnetic currents to be obtained on the XY Plane.

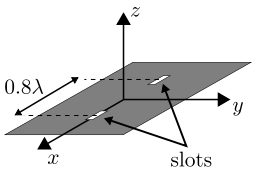

Figure 3.5: Simulated slot-array antenna.

Fig. 3.6 shows the result in linear scale. As it was expected, the y component of the equivalent currents is negligible and just the x component is significant. This behavior rises because the slots are oriented in the x direction and, hence, the main component of the real magnetic current is M_x.

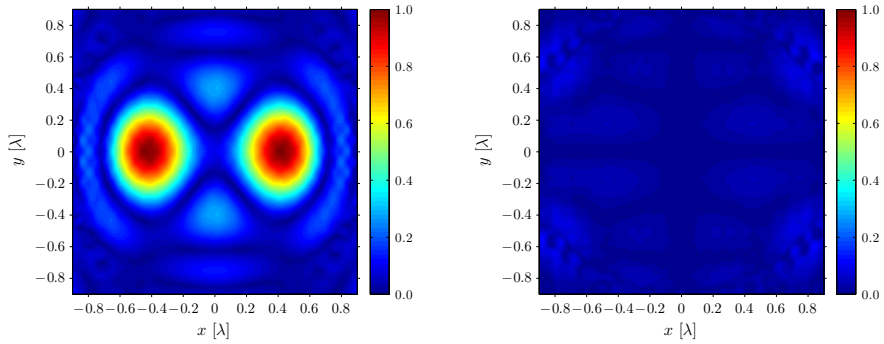

(a) x component (M_x). (b) y component (M_y).

Figure 3.6: Equivalent magnetic currents for the slot-array antenna obtained with the integral equation method.

In order to verify the accuracy of the method in placing the maximum of the currents on the correct position, i.e., where the slots are, the section of the x component (M_x) at $y = 0$ has been represented in logarithmic scale in Fig. 3.7. As can be observed in this figure, the maximum of the currents are correctly placed on the positions where the slots where placed for the simulation. Therefore it can be concluded that the described approach and the solution of the equation system by the GMRES method are correct.

3.4 Modal expansion methods

In Chapter 2 the solution of the vector wave equation in a source-free region was derived. This solution was implemented for each coordinate system by means

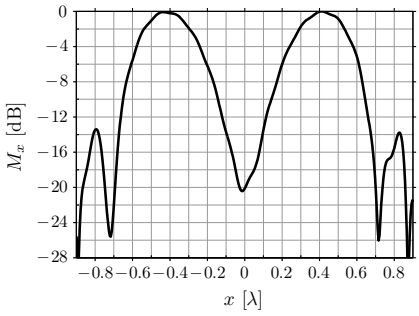

Figure 3.7: Section of the x component (M_x) at $y = 0$.

of a weighted sum of orthogonal basis functions, which were also noted as *modal expansions* or *wave expansions*. The way in which these weights (or coefficients) are computed from radiated field measurements is described in Section 2.3 for the planar and spherical wave expansion. By doing so, the coefficients characterize the antenna and, hence, the radiated field can be computed in other points by just inserting the computed coefficients into the weighted sum.

Regarding the inverse problem, the modal expansion technique presents a major drawback. Since the solution is derived in a source-free region, this solution does not allow the equivalent currents to be directly obtained as in the integral equation methods. For this reason, a different approach must be considered.

This other approach requires to back-propagate the field, from the measurement points to the points on the surface where the equivalent currents are desired. By determining the field on this surface, the equivalence principle (see Section 3.2) can be applied, what leads to the desired equivalent currents.

This second approach entails an additional problem. The modal expansion is only valid outside the minimum surface enclosing the antenna. The problem arises when the radiating surface, close to which the equivalent currents must be obtained, is different from the measurement system, as it is the case of this thesis. In this case, the closest points to the antenna where the field can be computed by means of the modal expansion may be too far from the radiating surface and, hence, they may not contribute valuable information for the antenna diagnosis.

Specifically for this thesis, a spherical measurement system is considered, and the radiating surface is supposed to be plane. Hence, the equivalent currents must be obtained on a flat surface close to this radiating surface in order to obtain valuable information about the antenna. However, the spherical measurement (either in the far-field or in the near-field region) allows the spherical

coefficients to be easily computed and, therefore, the spherical wave expansion is applied. This expansion is only valid outside the minimum sphere enclosing the antenna, as indicated in (2.28). This minimum sphere is far from the desired surface, as depicted in Fig. 3.8, and, hence, the field on this sphere cannot be used to perform an accurate antenna diagnosis.

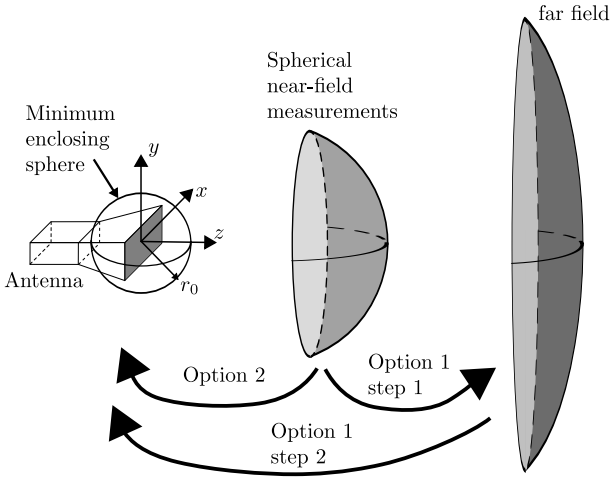

Figure 3.8: Options for the modal expansion technique using spherical near-field measurements.

In order to obtain the field on the desired flat surface, a coordinate system change (from a spherical coordinate system to a planar coordinate system) may be applied. This change is normally performed by means of the plane wave spectrum, which is related to the field on a plane surface by a Fourier transform (2.17) [41],[23].

Assuming spherical near-field measurements, the transformation of these measurements (or the computed spherical coefficients) into the plane wave spectrum may be done in two different ways. Both ways are depicted in Fig. 3.8. As can be observed, one way (*Option 1*) makes use of the far field as an intermediate step to, later, back-propagate the field to the surface close to the antenna. The other way (*Option 2*) directly computes the field on the surface of interest from the spherical near-field measurements. Next, both options are described and several results are shown.

3.4.1 Option 1: Microwave holographic technique

The first option applies the so-called *Microwave holographic technique* (MHT) [16], [17], [18], which is used in many applications, e.g. in reflector antennas diagnosis [77] or in location of defective elements in array antennas [78].

The MHT obtains the field distribution on a plane surface close to the antenna from far-field measurements by means of a Fourier transform. To do this, two steps are carried out. Firstly, the plane wave spectrum is obtained from far-field measurements and, later, the computed plane wave spectrum is used to determine the field on the surface of interest by means of a Fourier transform (2.17). This second step has been previously described (see Section 2.2.1), thus, the point of interest now is the way in which the plane wave spectrum and the far-field measurements are related.

To obtain this relation, the asymptotic expansion for $kz \gg 1$ of the electric field (2.17) must be derived by the method of steepest descent [12]. This asymptotic expansion can be represented as [23]:

$$\vec{E}^{FF}(R,\theta,\phi) = \frac{jk\cos\theta e^{jkR}}{R}\vec{A}_E(k_x,k_y) \tag{3.16}$$

where $\vec{E}^{FF}(R,\theta,\phi)$ is the far field in spherical components (θ,ϕ), R is the measurement distance, $\vec{A}_E(k_x,k_y)$ is the plane wave spectrum and, k_x and k_y are the spectral points given by:

$$k_x = k\sin\theta\cos\phi \tag{3.17a}$$

$$k_y = k\sin\theta\sin\phi \tag{3.17b}$$

Hence, from (3.16), the plane wave spectrum can be easily computed from the spherical far-field. The spectral points (k_x,k_y) where the spectrum is obtained are determined from the spatial points (θ,ϕ) where the far field is known by (3.17a) and (3.17b). These relations, however, entail a major problem. By observing them, it can be deduced that equispaced spatial points lead to a non-equispaced spectral grid. Therefore, the Fourier transform of the plane wave spectrum required for the computation of the field on the surface of interest (2.17) cannot be performed by the traditional *Fast Fourier Transform* (FFT) algorithm [79], which can only be applied on functions at equispaced points.

For this reason, other algorithms must be used. For instance, one possibility might be the application of an interpolation procedure to the plane wave spectrum to obtain the spectrum on an equispaced spectral grid. Another possibility might consist in directly computing the Fourier transform by means of the *Discrete Fourier transform* (DFT) or, in a faster way, the *Non-Uniform Fast Fourier Transform* (NUFFT) algorithm [80]-[81].

In this thesis, however, another solution is adopted. Since the transmitting coefficients are available, the far field can be computed at any spatial point. For this reason, instead of an equispaced spatial grid, a equispaced spectral grid is chosen. By doing so, the far field is computed in the non-equispaced spatial grid (θ,ϕ) determined according to the following expressions, derived from (3.17a) and (3.17b):

$$\theta = \arcsin\left(\frac{\sqrt{k_x^2 + k_y^2}}{k}\right) \tag{3.18a}$$

$$\phi = \arctan\left(\frac{k_y}{k_x}\right). \tag{3.18b}$$

Hence, no matter the region where the measurement is taken (far-field or near-field region), firstly the transmitting coefficients T_{smn} are determined from the spherical measurement as described in Section 2.3.2. Later, the far field is obtained in the suitable points by applying (2.28) or the asymptotic expression (2.48). If the first expression is used, the distance at which the field is determined must be chosen according to the antenna size so that the field is computed in the far-field region.

Therefore, the steps that must be carried out to obtain the equivalent currents from spherical near-field measurements by using the microwave holographic technique are [14]:

1. The spherical wave coefficients T_{smn} are computed from the spherical near-field measurement.

2. The points (θ,ϕ) where the far field must be determined are obtained from a equispaced grid (k_x,k_y) and the expressions (3.18a) and (3.18b).

3. The coefficients T_{smn} are used to obtain the field in the far field region $\vec{E}^{FF}(R, \theta, \phi)$.

4. The far field is applied in (3.16) to determine the plane wave spectrum $\vec{A}_E(k_x, k_y)$.

5. The tangential field $\vec{E}(x, y)$ on the surface of interest (according to Fig. 3.8, this surface is a plane parallel to the XZ plane) is obtained by means of the Fourier transform of the spectrum (2.17).

6. The equivalent currents are determined from the tangential field obtained in the previous step by applying the equivalence principle.

Next sections show the result obtained by applying this algorithm to several antennas. By doing so, the accuracy and usefulness of the method will be shown. In addition, the aim of the next examples is to show the advantages of knowing the equivalent currents for the antenna diagnosis.

Practical results 1

In this first example, the above algorithm was tested with the X-band slot-array antenna shown in Fig. 3.9. As can be observed, the antenna is formed by 7 $\hat{x}$-directed slots, fed in phase, and placed along the x axis at different y positions to obtain a cosine distribution. The separation between slots is 1.98 cm, i.e., 0.66 λ at the operating frequency (10 GHz) as shown in Fig. 3.9.

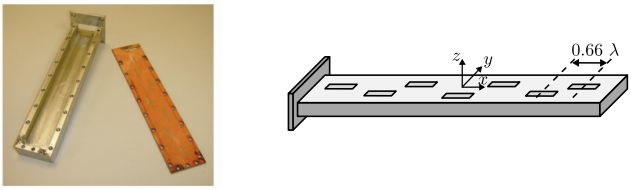

(a) Picture. (b) Diagram.

Figure 3.9: Measured X-band slot-array antenna.

The spherical field measurement of the antenna was taken at 2.70 m (90 λ at 10 GHz). Hence, taken into account the antenna dimensions (number of slots and separation between slots), the field was measured in the far-field region. This field was used to carry out the algorithm described above, from the computation of the transmitting coefficients to the determination of the equivalent currents.

Fig. 3.10 shows the computed far field pattern on the main planes by using the transmitting coefficients computed in the first step. As can be observed, both patterns are quite similar to their respective ideal patterns (beside the slightly higher sidelobes than in the ideal pattern in the XZ plane). In addition, though it cannot be seen in Fig. 3.10(a), the antenna is not exactly pointing towards $\theta = 0^\circ$ as it was designed.

Fig. 3.11 shows the absolute value in linear scale of the x and y components of the resulting equivalent currents determined in the sixth step of the above algorithm, as well as a black box to indicate where the antenna was located. As can be observed, the currents are all completely inside the radiating part of the antenna (the slots) and an oscillatory behavior can be observed due to the different position of the slots in the y axis along the x axis (see Fig. 3.9(b)).

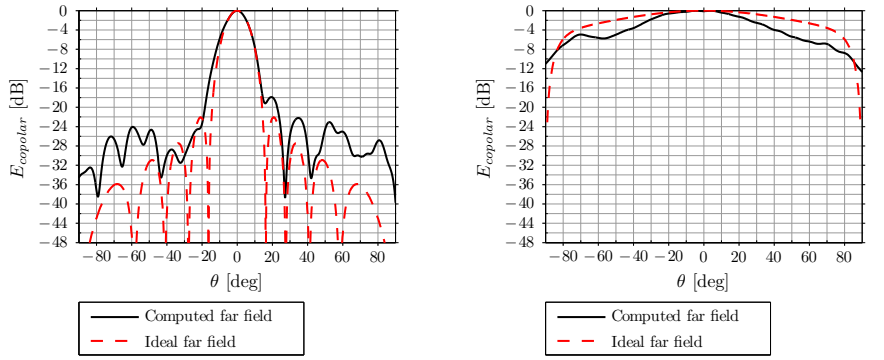

(a) Field on the XZ plane (AZIMUTH). (b) Field on the YZ plane (ELEVATION).

Figure 3.10: Computed far field of the X-band slot-array antenna at 10 GHz obtained by means of the spherical wave expansion.

Furthermore, the x component has a higher level, as it must be since the slots are $\hat{x}$-directed slots whose main magnetic current is in this direction.

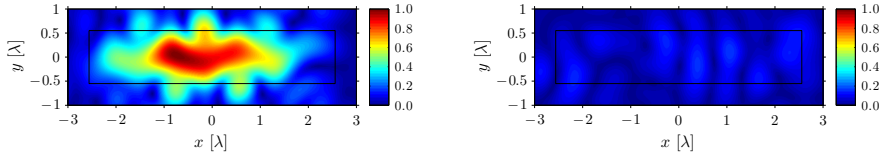

(a) Absolute value of M_x. (b) Absolute value of M_y.

Figure 3.11: Absolute value of the equivalent magnetic currents for the X-band slot-array antenna at 10 GHz obtained with the Microwave holographic technique.

The design of the antenna was done to feed all the slots in phase. Thus, a constant phase should be observed on reconstructed equivalent currents. In order to verify this fact, the phase of these currents has been represented in Fig. 3.12. As can be observed, the x component Fig. 3.12(a) has an almost constant phase along the x axis. The y component Fig. 3.12(b), is not constant, however, this phase is not significant since the absolute value Fig. 3.11(b) has a low level because of the direction of the slots, and, hence, this phase may be considered as noise.

The behavior of the absolute value and phase may be better observed in Fig. 3.13. Here, the equivalent currents have been represented on the exact position where the slots are and, hence, the values of the currents are indicated

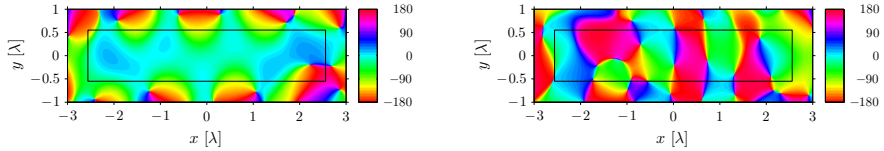

(a) Phase in degrees of M_x.

(b) Phase in degrees of M_y.

Figure 3.12: Phase of the equivalent magnetic currents for the X-band slot-array antenna at 10 GHz obtained with the Microwave holographic technique.

with regard of the 7 slots. Fig. 3.13(a) shows the absolute value in dB compared to the ideal envelope of the slots amplitude and Fig. 3.13(b) shows the phase in degrees compared with the ideal constant phase of the currents. From these figures it may be concluded (beside the value inside the slot, which cannot be exactly observed) that the envelope of the absolute value is correct. In addition, the phase has a variation of 50°, caused by the incorrect position of the slots along the y axis. This variation is the reason because the antenna is not exactly pointing towards $\theta = 0°$, as commented above.

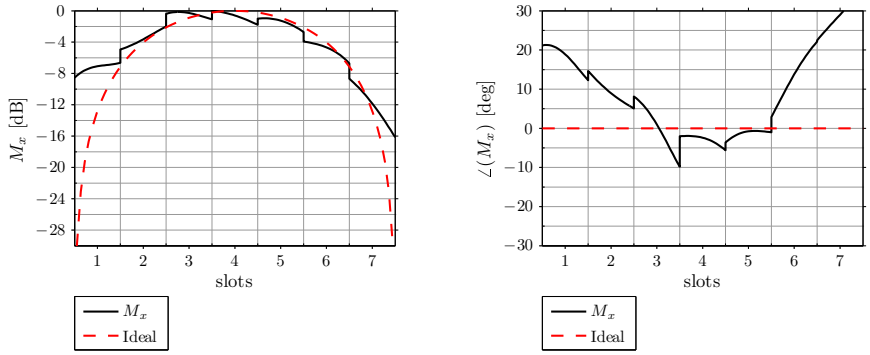

(a) Absolute value of M_x in dB.

(b) Phase of M_x in degrees.

Figure 3.13: Equivalent magnetic currents on the slots positions for the X-band slot-array antenna at 10 GHz obtained with the Microwave holographic technique.

Practical results 2

The MHT was also applied to the antenna studied in the example of Section 2.3.2. As described there, this antenna is a slot-array antenna with passive dipoles above each slot to obtain a circularly-polarized field. Fig. 2.7 shows a picture of the main sides of the antenna, and Fig. 2.8 shows a diagram of the antenna.

As commented in that example, a spherical near-field measurement was taken at 36.85 GHz to, later, compute the transmitting coefficients. Thus, the first step of the algorithm described above was already done and the far field in the suitable points (θ,ϕ) (obtained from a equispaced spectral grid (k_x,k_y) by (3.18a) and (3.18b)) could be obtained. Later, the rest of the algorithm was applied and, finally, the equivalent electric currents were obtained.

Fig. 3.14 shows the absolute value of the equivalent electric currents on a plane close to the XY plane (where the passive dipoles are placed). As can be observed, the currents appear just where the radiating part of the antenna is (indicated by a black square). Furthermore, a different level on the x component (J_x in Fig. 3.14(a)) and on the y component (J_y in Fig. 3.14(b)) can be observed. This difference is the reason for the high maximum axial ration (4.41 dB) of the antenna (it was design for 0 dB).

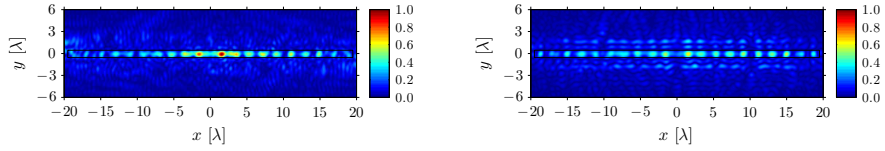

(a) Absolute value of J_x.

(b) Absolute value of J_y.

Figure 3.14: Absolute value of the equivalent electric currents for the slot-array antenna with dipoles at 36.85 GHz obtained with the microwave holographic technique.

Although it has not been commented above, the slots of the antenna are separated $\lambda_g/2$ (where λ_g is the wavelength in the waveguide) to feed the slots in phase. To verify if the slots are correctly placed, the phase of the equivalent electric currents for the x and y components is shown in Fig. 3.15. As can be seen, a constant phase is obtained in both components and, hence, it may be concluded that the slots were placed correctly with regard to the x axis on the waveguide.

Fig. 3.16 shows the section of the equivalent electric currents at $y = 0$ compared with the ideal distribution. Fig. 3.16(a) shows the section for the absolute value in logarithmic scale and Fig. 3.16(b) shows the section for the

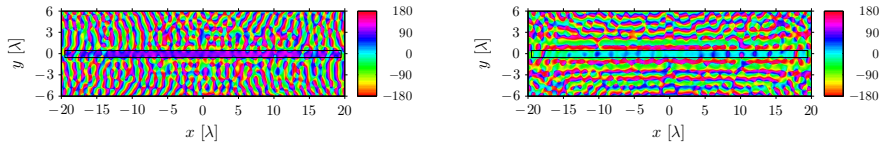

(a) Phase in degrees of J_x.

(b) Phase in degrees of J_y.

Figure 3.15: Phase of the equivalent electric currents for the slot-array antenna with dipoles at 36.85 GHz obtained with the microwave holographic technique.

phase of each component compared to the ideal phase of the x component (the ideal phase of the y component is the phase of the x component shifted 90°).

By observing Fig. 3.16(a), an important problem with regard to the assembly of the antenna can be detected. As can be observed, just 20 peaks can be detected, however, the antenna is formed by 40 elements. Hence, just half of the elements are excited, what justifies the high lobes at 30° in the XZ plane of the far field depicted in Fig. 2.10(a).

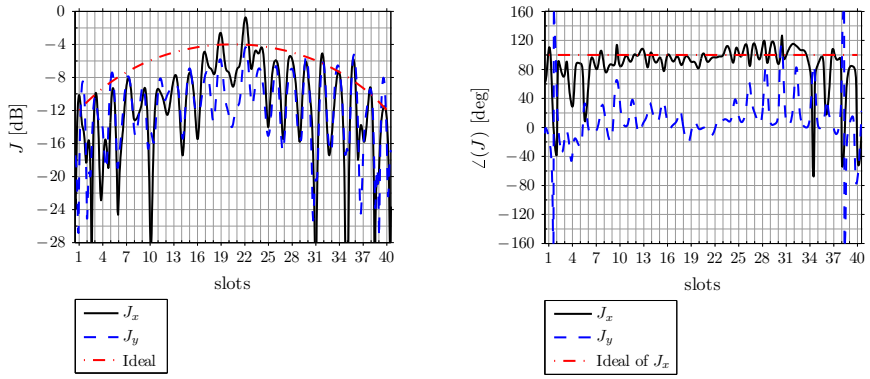

(a) Section of the absolute value in dB.

(b) Section of the phase in degrees.

Figure 3.16: Section of the equivalent electric currents at y=0 for the slot-array antenna with dipoles at 36.85 GHz obtained with the microwave holographic technique.

Therefore, this example shows the accuracy of the algorithm depicted above for reconstructing the equivalent currents of an antenna. Furthermore, the example shows the usefulness of knowing the equivalent currents of an antenna to locate errors.

Practical results 3

The equivalent currents reconstruction algorithm by the MHT was also tested in another practical case. In this case, the antenna under study was the antenna depicted in Fig. 3.17, where the position with regard to the coordinate system has been indicated. The antenna is a 2D slot-array antenna with, as in the previous example, passive dipoles to obtain a circularly-polarized field. The operating frequency was 36.85 GHz and the spherical measurement was taken at 1.86 m (229.63 λ). Considering the size of the antenna, which diameter is 36.22 cm, the measurement was taken in the near-field region.

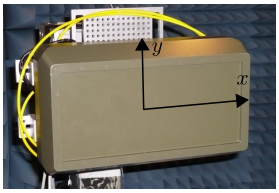

Figure 3.17: 2D array antenna measured at 36.85 GHz.

Firstly, the transmitting coefficients were obtained and, then, the far field was computed. Fig. 3.18 shows the co-polar component of this field on the main planes (XZ and YZ) compared to the ideal field. As can be observed, the field on XZ plane (Fig. 3.18(a)) agrees very well with the ideal field, however, the field on the YZ plane differs from the ideal field. In order to find out the error that had caused this difference, the equivalent currents were reconstructed.

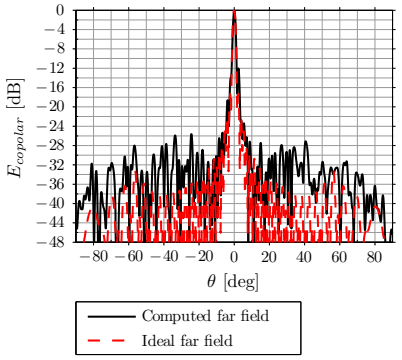

(a) Field on the XZ plane (AZIMUTH).

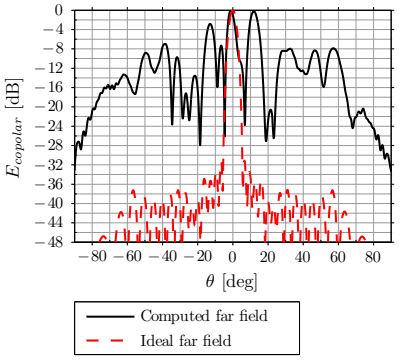

(b) Field on the YZ plane (ELEVATION).

Figure 3.18: Computed far field of the 2D array antenna at 36.85 GHz obtained by means of the spherical wave expansion.

To do this, the algorithm described above, from the computation of the coefficients T_{smn} to the determination of the equivalent magnetic currents ($\vec{M}_s$), was applied. Fig. 3.19 shows the absolute value in linear scale of the reconstructed equivalent electric currents. Several conclusions may be adopted from this figure. Firstly, the antenna is only radiating in the part where the radiating elements, namely slots and passive dipoles, are. Secondly, the amplitude of the y component is higher than the amplitude of the x component. And, finally, the lower part ($y < 0$) of antenna has a higher amplitude than the upper part ($y > 0$). These considerations allow the antenna to be improved for the manufacturing of the next prototype.

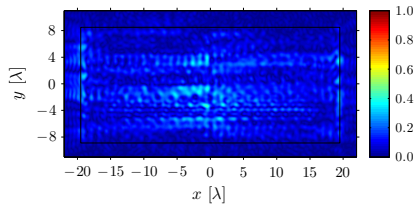

(a) Absolute value of J_x.

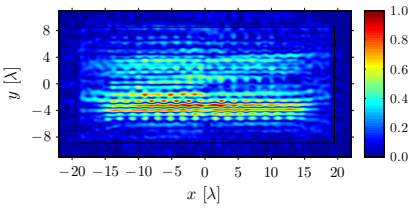

(b) Absolute value of J_y.

Figure 3.19: Absolute value of the equivalent electric currents for the 2D array antenna at 36.85 GHz obtained with the microwave holographic technique.

Fig. 3.20 shows the phase in degrees of the reconstructed currents. In order to be able to interpret this phase it must be taken into account that the antenna was design to have all the elements in phase. Thus, by observing Fig. 3.20 it is clear that this aim was not achieved since every row of elements has a random phase.

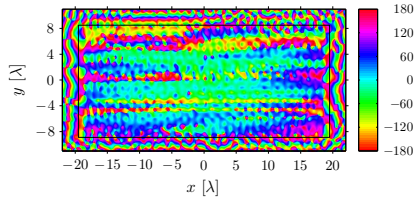

(a) Phase in degrees of J_x.

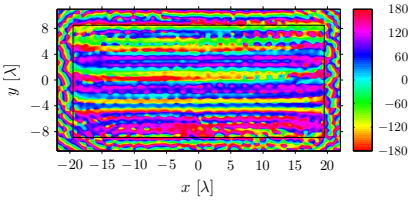

(b) Phase in degrees of J_y.

Figure 3.20: Phase of the equivalent electric currents for the 2D array antenna at 36.85 GHz obtained with the microwave holographic technique.

The differences with regard to the ideal distributions of the absolute value and phase may be better observed in Fig. 3.21. In this figure, the section of the

y component (the component with higher amplitude) at $x = 5\lambda$ and $x = -5\lambda$ (at both sides of the antenna) of the reconstructed currents is represented and compared to the ideal distributions. By looking at this figure it can be concluded that the major problem lies in the phase distribution (Fig. 3.21(b)) along the y axis of the antenna, which is quite different from the ideal case. The absolute value distribution (Fig. 3.21(a)), though different from the ideal, does not differ enough to cause the high sidelobes of the radiation pattern in elevation (Fig. 3.18(b)).

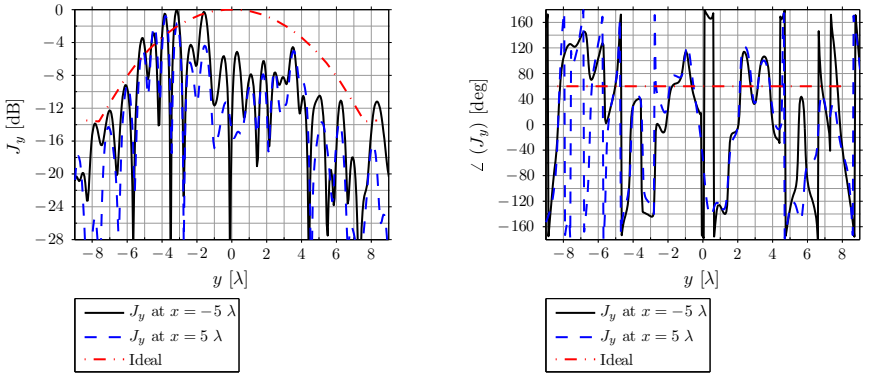

(a) Section of the absolute value in dB.

(b) Section of the phase in degrees.

Figure 3.21: Section of the equivalent electric currents at $x = 5$ λ and $x = -5$ λ for the 2D array antenna at 36.85 GHz obtained with the microwave holographic technique.

Due to the bad phase distribution in the y component along the y axis, a correction of the antenna was carried out in order to obtain a better phase distribution. After this correction, the antenna was measured again and, later, the equivalent currents were obtained once again. Fig. 3.22 shows the distribution along the y axis, at $x = 5\lambda$ and $x = -5\lambda$, of the antenna after correction. As can be observed, now, the distribution looks like the ideal distribution in both, absolute value and phase.

Fig. 3.23 shows the computed far-field pattern of the antenna after correction on the main planes. Now, not only the XZ plane looks like the ideal pattern, but also the YZ plane. Of course, there are still small differences with regard to the ideal pattern. However, comparing Fig. 3.18(b) and Fig. 3.23(b) it can be concluded that a great improvement was achieved by using the reconstructed equivalent currents and improving the antenna suitably.

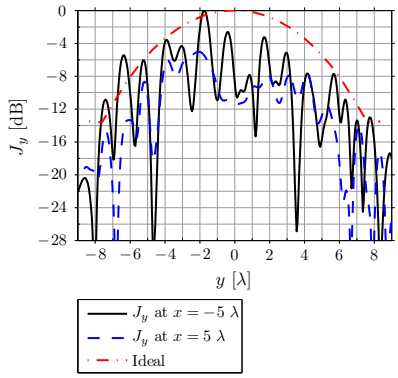

(a) Section of the absolute value in dB.

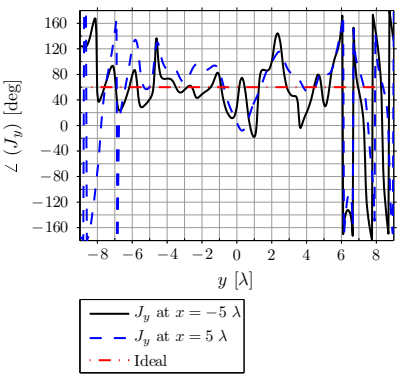

(b) Section of the phase in degrees.

Figure 3.22: Section of the equivalent electric currents at $x = 5$ λ and $x = -5$ λ for the 2D array antenna after correction at 36.85 GHz obtained with the microwave holographic technique.

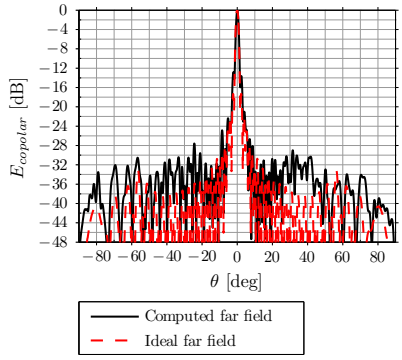

(a) Field on the XZ plane (AZIMUTH).

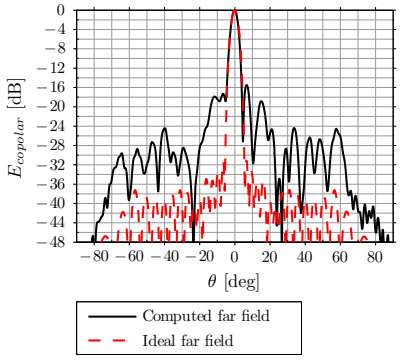

(b) Field on the YZ plane (ELEVATION).

Figure 3.23: Computed far field of the 2D array antenna after correction at 36.85 GHz obtained by means of the spherical wave expansion.

3.4.2 Option 2: SWE to PWE transformation

The second option performs a direct transformation, from the spherical near-field measurement to the near-field on the surface of interest, without employing the far field. By doing so, the information present on the evanescent modes (which are present in the near field, but not in the far field) can be used. Thus, a higher accuracy may be achieved on the reconstructed equivalent currents.

This direct technique is known as *Spherical wave expansion-to-Planar wave expansion* (SWE-to-PWE) transformation. It has been recently proposed by Cappelllin [13],[19], and applied to the diagnosis of an offset reflector antenna [64] with quite good results. In this section a briefly review of this technique is carried out.

The aim of the SWE-to-PWE transformation is to obtain the plane wave spectrum ($\vec{A}_E(k_x, k_y)$) directly from the transmitting coefficients (T_{smn}) (which must be previously computed from the spherical near-field measurement). In order to determine this relation, first the spherical wave functions ($\vec{F}^{(3)}_{smn}(\vec{r})$) are expressed as an expansion of plane waves (e^{jkz}) in the following way [82] (valid only for $z > 0$):

$$\vec{F}^{(3)}_{1mn}(\vec{r}) = \frac{(-j)^n}{2\pi\sqrt{n(n+1)}} \int_{-\pi}^{\pi} \int_{C_+} \vec{Y}^m_n(\alpha, \beta) e^{jk\hat{s}\cdot\vec{r}} \sin\alpha \, \mathrm{d}\alpha \, \mathrm{d}\beta \tag{3.19}$$

$$\vec{F}^{(3)}_{2mn}(\vec{r}) = \frac{j(-j)^n}{2\pi\sqrt{n(n+1)}} \int_{-\pi}^{\pi} \int_{C_+} \hat{s} \times \vec{Y}^m_n(\alpha, \beta) e^{jk\hat{s}\cdot\vec{r}} \sin\alpha \, \mathrm{d}\alpha \, \mathrm{d}\beta. \tag{3.20}$$

The vector $\hat{s}$ is related to the unitary cartesian vectors as:

$$\hat{s} = \sin\alpha\cos\beta\hat{x} + \sin\alpha\sin\beta\hat{y} + \cos\alpha\hat{z} \tag{3.21}$$

where $\beta \in [-\pi, \pi]$ and α is a complex variable which domain is the contour C_+ shown in Fig. 3.24.

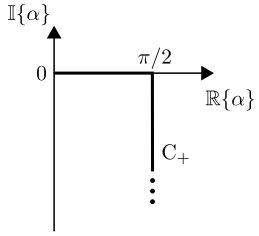

Figure 3.24: Domain of the variable α (C_+).

In (3.19) and (3.20), the basis functions $\vec{Y}^m_n(\alpha, \beta)$ are given by [83]:

$$\begin{aligned} \vec{Y}^m_n(\alpha, \beta) = &- j\frac{1}{\sqrt{(2\pi)}} \left(-\frac{m}{|m|}\right)^m \left(\frac{\partial}{\partial\alpha}\bar{P}^{|m|}_n(\cos\alpha) e^{jm\beta}\hat{\beta}\right. \\ &\left. -\frac{1}{\sin\alpha}\bar{P}^{|m|}_n(\cos\alpha) jm e^{jm\beta}\hat{\alpha}\right) \end{aligned} \tag{3.22}$$

where $\bar{P}_n^m(\cos\alpha)$ is the normalized associated Legendre functions (see Appendix B) and the vectors $\hat{\alpha}$ and $\hat{\beta}$ are expressed, from the unitary cartesian vectors, as:

$$\hat{\alpha} = \cos\alpha\cos\beta\hat{x} + \cos\alpha\sin\beta\hat{y} - \sin\alpha\hat{z} \tag{3.23a}$$

$$\hat{\beta} = -\sin\beta\hat{x} + \cos\beta\hat{y}. \tag{3.23b}$$

By substituting (3.19) and (3.20) into the spherical wave expansion (2.28), the field may be expressed for $z > r_0$ (being r_0 the radius of the minimum sphere enclosing the antenna) as follows [13]:

$$\vec{E}(\vec{r}) = \frac{jk}{8\pi^2}\int_{\pi}^{\pi}\int_{C_+}\hat{E}(\hat{s})e^{jk\hat{s}\cdot\vec{r}}\sin\alpha\,\mathrm{d}\alpha\,\mathrm{d}\beta \tag{3.24}$$

where the spectrum $\hat{E}(\hat{s})$ is given by:

$$\hat{E}(\hat{s}) = \sum_{n=1}^{\infty}\sum_{m=-n}^{n}\frac{(-j)^n 4\pi}{\sqrt{\eta}\sqrt{n(n+1)}}\left[T_{2mn}\hat{s}\times\vec{Y}_n^m(\alpha,\beta) - jT_{1mn}\vec{Y}_n^m(\alpha,\beta)\right] \tag{3.25}$$

The comparison of the field expressed by (3.24) and the field expressed by means of the plane wave spectrum (2.17) allows to establish the following relation [13] between the spectrum in the (α,β)-domain ($\hat{E}(\hat{s})$) and the spectrum in the (k_x,k_y)-domain (the plane wave spectrum ($\vec{A}_E(k_x,k_y)$)):

$$\vec{A}_E(k_x,k_y)e^{jk_z z} = \frac{1}{4\pi k_z}\hat{E}(\hat{s})e^{jk\cos\alpha z} \tag{3.26}$$

In the previous relation, it must be taken into account that, from (3.21), the spectral variables (k_x,k_y) and the vector $\hat{s}$ may be related by $\hat{s} = \vec{k}/k$, where $\vec{k} = k_x\hat{x} + k_y\hat{y} + k_z\hat{z}$.

The significance of (3.25) lies in the way the spherical near-field measurement is directly related to the plane wave spectrum.

In order to clarify the way this direct transformation is done, the following list describes the steps that must be carried out to perform the SWE-to-PWE transformation:

1. The transmitting coefficient (T_{smn}) are determined from the spherical near-field measurement.

2. The spatial points (θ, ϕ) are determined from the equispaced grid (k_x,k_y) and the expressions (3.18a) and (3.18b). Then, the points (α, β) are obtain by substituting θ by α and ϕ by β.

3. The spectrum in the (α, β)-domain $(\hat{E}(\hat{s}))$ is computed with (3.25).

4. The plane wave spectrum $(\vec{A}_E(k_x, k_y))$ is obtained by inserting $\hat{E}(\hat{s})$ into (3.26).

5. The field close to the antenna is computed from the spectrum $\vec{A}_E(k_x, k_y)$ by (2.17).

6. The equivalence principle is applied to determine the equivalent currents.

Practical results

The SWE-to-PWE technique was tested with the antenna studied in the first example of the previous section. Specifically, the antenna was the X-band slot-array antenna shown in Fig. 3.9. As commented in that example, a spherical far-field measurement was taken at 2.7 m (90 λ at the operating frequency, 10 GHz). As in that case, the MHT might have been directly applied to the far-field measurements. However, it was a good test to check the whole algorithm in a known situation. In addition, the application of the SWE-to-PWE to this antenna allows the MHT and the SWE-to-PWE techniques to be compared in the same situation.

To obtain the equivalent magnetic currents, the algorithm described above was carried out. Fig. 3.25 shows the absolute value of these currents as well as a black box to show where the antenna is placed. As can be observed, the amplitude of the x component (Fig. 3.25(a)) is the only significant component (the y component (Fig. 3.25(b)) is negligible) and a oscillatory behavior due to the different position of the elements in the y axis may be observed.

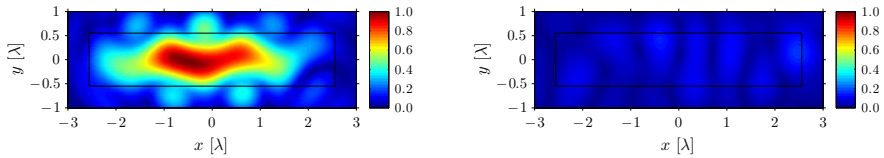

(a) Absolute value of M_x.

(b) Absolute value of M_y.

Figure 3.25: Absolute value of the equivalent magnetic currents for the X-band slot-array antenna at 10 GHz obtained with the SWE-PWE technique.

Fig. 3.26 shows the phase of the computed equivalent currents. In this case, a constant phase is again obtained since the slots where placed to feed all of them in phase. Thus, a result close to the ideal is obtained. The y component Fig. 3.26(b) is not considered because the absolute value has a extremely low level and, hence, this component may be considered noise.

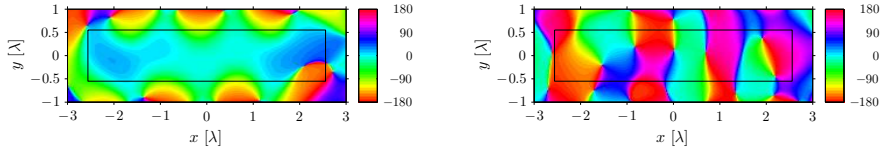

(a) Phase in degrees of M_x.

(b) Phase in degrees of M_y.

Figure 3.26: Phase of the equivalent magnetic currents for the X-band slot-array antenna at 10 GHz obtained with the SWE-PWE technique.

The value of the equivalent magnetic currents on the positions of the slots is shown in Fig. 3.27 in both, absolute value in dB (Fig. 3.27(a)) and phase in degrees (Fig. 3.27(b)). As can be observed, the absolute value is quite similar to the envelope of the ideal distribution, and the phase presents a variation of 50° around the ideal distribution.

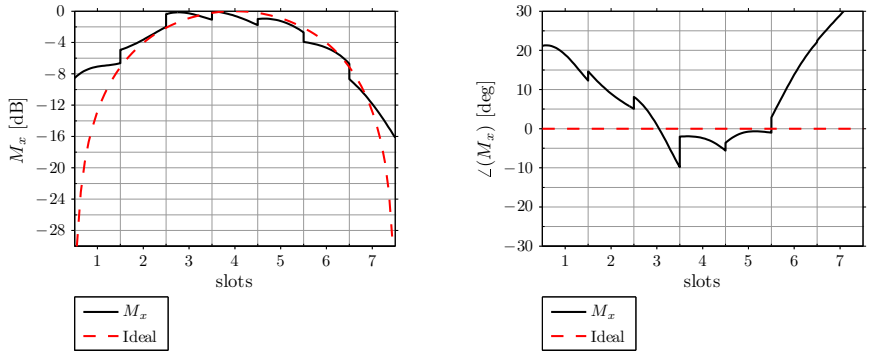

(a) Absolute value of M_x in dB.

(b) Phase of M_x in degrees.

Figure 3.27: Equivalent magnetic currents on the slots positions for the X-band slot-array antenna at 10 GHz obtained with the SWE-PWE technique.

Therefore, looking at all these results, and comparing them to the results obtained with MHT (see Fig. 3.11, Fig. 3.12 and Fig. 3.13), it can be concluded that the same result is obtained with the SWE-to-PWE transformation

and the microwave holographic technique. The advantage of the SWE-to-PWE technique arises with near-field measurements. In these cases, the information present in the evanescent modes may be considered and, hence, a better resolution may be achieved.

Regarding the computation time, no great differences were detected on computing the previous example with the MHT or the SWE-to-PWE transformation. Specifically, the computation of the transmitting coefficients (required in both techniques) took around 10 seconds, and the computation the basis functions (quite similar in both cases) took around 30 seconds. Then, the spectrum was obtained in around 5 seconds, and the FFT algorithm was applied to the computed spectrum, what did not take almost time due to the fast FFT algorithm implemented in MATLAB.

3.5 Equivalent currents by means of the spheroidal wave expansion

The aim of the current chapter is to obtain the equivalent currents on a flat surface from spherical near-field measurements. In previous section, the solution has been the transformation of the spherical coefficients to a planar coordinate system by the plane wave spectrum. By doing so, the field could be determined on the flat surface of interest. There is, however, another option which has not been mention up to now.

This option consists in using a spheroidal oblate coordinate system to determine the field and, hence, the equivalent currents, near the plane of interest. Recently, this coordinate system has been applied in several applications, e.g. in near to far-field transformations [48] or in inverse problems [84],[85]. This last case is of special interest for this thesis.

The advantage of the spheroidal oblate coordinate system lies in the different shapes the canonical surface can adopt. By varying the spheroidicity parameter (see Appendix D) and the radial component ξ, the resulting surface with ξ-component constant may become extremely flattened spheroids. In the extreme case, these spheroids may become a plane so that the field can be obtained even on a flat surface. Fig. 3.28 shows several spheroids for different ξ components and $c = 1$ (the spheroidicity parameter).

Regarding the validity of the wave expansion, it is worth to mention that the solution derived Section 2.2.4 for the spheroidal oblate coordinate system (the spheroidal wave expansion) is only valid in a source-free region. The advantage now is that the source-free region in a spheroidal oblate coordinate system is the region outside the minimum flattened spheroid enclosing the antenna. This minimum spheroid might be the one depicted in Fig. 3.28(a), so that

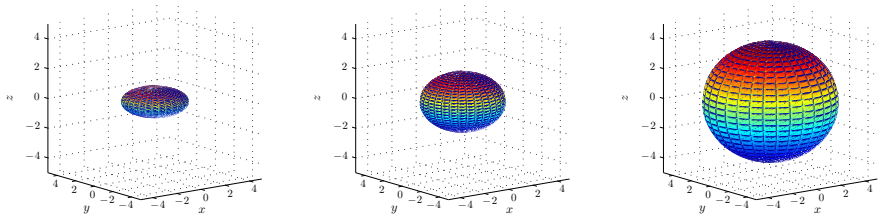

(a) $\xi = 0.5$ (b) $\xi = 1$ (c) $\xi = 2$

Figure 3.28: Flattened spheroids resulting from the oblate spheroidal coordinate system with $c = 1$ and several ξ.

this surface is quite close to the source and, hence, the field on this surface contributes valuable information about the antenna.

Fig. 3.29 compares the cross sections the minimum enclosing surface in a spherical coordinate system and the minimum enclosing surface in a spheroidal oblate coordinate. As can be observed, there is a great advantage in using the spheroidal oblate coordinate system instead of the spherical coordinate system.

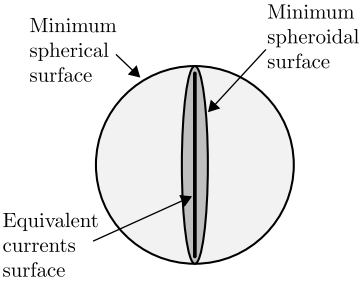

Figure 3.29: Comparison of the minimal enclosing sphere and the minimal enclosing spheroid.

In order to obtain the field in a spheroidal oblate coordinate system, two different parts may be distinguished. The first one consists in obtaining the oblate spheroidal coefficients. This computation might require measurements on an oblate measurement system and the solution of a transmission formula in spheroidal coordinates, as in the spherical case. However, the spheroidal coordinate system is hard to implement mechanically and, hence, this possibility is not normally used. In addition, for this thesis, the only available measurements are taken in a spherical system, which allow the transmitting coefficients (T_{smn}) to be easily determined.

Therefore it must be established the way the oblate spheroidal coefficients (α_{smn}) are determined from the transmitting coefficients (T_{smn}). In [86] the formulas to carry out this transformation are derived. If the suitable corrections are done to express this relation assuming the time variation stated for this thesis (2.1), the transformation can be expressed as follows:

$$T_{smk}(-j)^k = \sum_n \alpha_{smn}(-j)^k d_{k-|m|}^{|m|n}(-jc) \tag{3.27}$$

where $d_k^{mn}(-jc)$ are the expansion coefficients (see Appendix D).

As can be observed in (3.27), the transformation of spherical coefficients into spheroidal coefficients is performed by solving an equation system. Furthermore, the transformation depends on the spheroidicity parameter (c). The election of this parameter depend on the size of the surface where the equivalent currents must be obtained since it restricts the minimum surface with ξ constant enclosing the antenna.

The second part computes the field on the surface of interest by means of the spheroidal wave expansion (2.37) and the spheroidal coefficients computed with (3.27). Appendix D describes in detail the way in which the spheroidal vector wave functions (required in the computation of the spheroidal wave expansion) are obtained, from the spheroidal angular and radial functions to the secondary parameters (the spheroidal eigenvalues and the expansion coefficients).

Summing-up, the steps that must be carried out to determine the field and, in turn, the equivalent currents on points close to the antenna by means of the spheroidal wave expansion are:

1. The transmitting coefficients (T_{smn}) are computed from the spherical near-field measurements as described in previous sections.
2. The spheroidicity parameter (c) is determined so that the minimum surface with ξ-component constant encloses the antenna.
3. The transmitting coefficients are transformed into the oblate spheroidal coefficients (α_{smn}) by (3.27).
4. The field on the minimum flattened spheroid is computed by means of the coefficients computed in the previous step and the spheroidal wave expansion described in Section 2.2.4.
5. The equivalent currents are determined by applying the equivalence principle.

The transformation into spheroidal coordinates allows to compute the field on closed points to the antenna without using the far field. Hence, it works similarly to the direct transformation (SWE-to-PWE) described in Section 3.4.2 (in

both cases the measurements in the near-field region are directly transformed into the near-field on closed points to the antenna). The difference of both methods lies in the difficulty of computing the basis functions. Whereas the basis functions for the SWE-to-PWE transformation (3.22) are easily computed, the computation of the spheroidal vector wave functions (see Appendix D) may become a hard task. For this reason, the SWE-to-PWE technique might be preferable to the spheroidal technique.

However, it must be pointed out an interesting advantage may be found in the using of the spheroidal coordinate system. This technique might be applied in a wider range of cases than the SWE-to-PWE transformation. For instance, not only currents on flat surfaces may be determined, but also on elliptic surfaces and on spherical surfaces. Moreover, this is done with a uniform notation for all, plane, ellipse and sphere surfaces.

Chapter 4

Visible spectrum

As described above, the equivalent currents of an antenna can be obtained from near-field or far-field measurements. The use of near-field measurements may lead to obtain the equivalent currents with a higher resolution than with far-field measurements. This chapter explains the reasons for this higher resolution and describes the limitations of this possibility in a real situation. In addition, the behavior of the plane wave spectrum by considering near-field or far-field measurements and the resolution achieved on each case are described.

4.1 Introduction

The reconstruction of the equivalent currents is known, in general, as the *inverse source problem* [59]. As proved in [58], this problem has a non-unique solution due to the presence of the so-called *non-radiating sources* [87]. As a consequence, the resolution of the reconstructed equivalent currents is limited to a certain value which cannot be overcome even though measurements at very short distances are done.

These very close measurements, however, may be done to recover the so-called *radiating sources*. Unfortunately, these kinds of measurements are hard to perform in practice due to the coupling between the probe and the AUT, and the limitations of the measurement facility. For these reasons, the measurements are taken, at least, at few wavelengths from the AUT. The problem arises because the so-called *evanescent waves* are exponentially attenuated. Therefore, these waves cannot be normally measured and, hence, the information they contain is not considered in the reconstruction of the equivalent currents, what reduces the resolution of these currents.

In the limit case, no evanescent wave is measured and only the propagating waves are considered. Regarding the plane wave spectrum, this situation means

that just a small region of the spectrum, which is known as *visible spectrum*, can be used. This region allows to establish a maximum resolution of 1 λ in the reconstructed equivalent currents.

To improve this resolution, the plane wave spectrum in the spectral points outside the visible region must be determined. To do this, the radiated field must be measured as close to the antenna as possible and the SWE-to-PWE transformation may be applied. However, in some cases, this is not possible and just far-field measurements are available. In these cases, additional techniques must be applied to improve the resolution. Next chapter studies in depth these other techniques.

The chapter is organized as follows. First the inverse source problem and the non-radiating sources are described and defined, respectively. Then, the behavior of the evanescent waves is depicted. Later, the resolution as a function of the available region of the plane wave spectrum is determined. Finally, the options to improve the resolution of the equivalent currents are studied.

4.2 The inverse source problem and the non-radiating sources

As described in previous chapter, the inverse problem is defined as the determination of the cause of a phenomenon from measurements of the phenomenon [58]. This problem is investigated in many areas, e.g. in spectroscopy, X-ray crystallography or seismology. Through these investigations it has been found that, in most of the cases, the inverse problem is *ill-posed*.

The concept of ill-posedness, referred to the inverse problem, involves two characteristics: the non-uniqueness of the solution and the ill-conditioning of the problem. To explain these concepts, the direct problem shown in Fig. 4.1 may be observed. In this direct problem, the *objects* in the *currents space* are transformed into the *images* in the *field space* by means of the operator A. As can be observed, the direct problem does not entail any problem (every objet is transformed into a single image). However, the inverse problem (A^{-1}) has the previous two characteristics. On the one hand, the solution of the inverse problem is non-unique because one image lead to two different objects. Thus, when applying the inverse (A^{-1}) to this image, two different solutions can be obtained. On the other hand, it can be observed in Fig. 4.1 that two close images lead to two far objects. This is known as ill-conditioning because a little error, e.g. produced by noise, in the image (which is the measured space in the inverse problem) may lead to two quite different solutions.

In [58], a solution for the non-uniqueness of the inverse problem is proposed. It consists in adding prior knowledge of the sources to the inverse problem. As depicted in Fig. 4.2, this prior knowledge allows the solution to be limited to

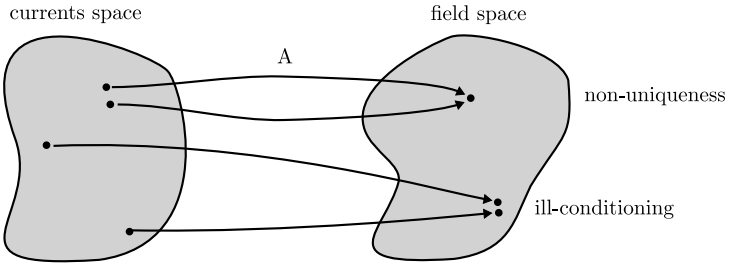

Figure 4.1: Direct problem whose inverse problem is ill-posed

just a small region. By doing so, the non-uniqueness problem may be solved as well as the ill-conditioning of the problem.

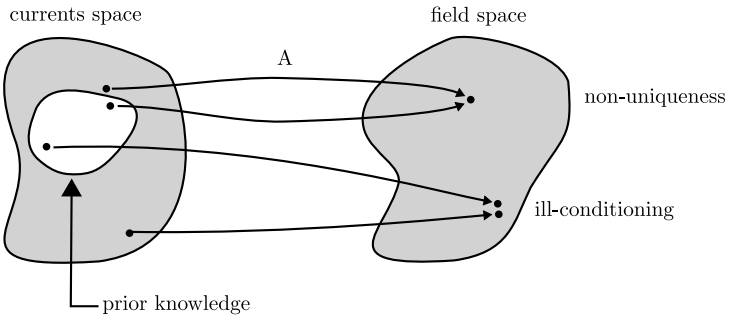

Figure 4.2: Application of prior knowledge to the solution of the inverse problem

There are several kinds of inverse problems. Concerning to this thesis, the inverse problem of interest is the *inverse source problem*. This problem is specifically defined as the determination of the properties of an antenna from the measurements of the radiated field by that antenna [58], i.e., the reconstruction of the equivalent currents. In this case, the non-uniqueness of the solution may be explained from the point of view of the *non-radiating* (NR) sources.

NR sources are defined as those sources that generate a field that vanishes identically at every point outside the support region of the antenna [88]. Over the past years, several publications have proposed methods to specify these sources by forcing boundary conditions on the surface of the support of the antenna. For instance, in [89] and [90] two methods are proposed to specify non-radiating scalar sources with or without spherical symmetry, respectively.

Similarly, in [84] a method is proposed to specify the NR sources in a vectorial form.

Regarding the problem dealt with in this chapter, it must be emphasized that the field generated by the NR sources vanishes, i.e., it is not simply exponentially attenuated [87]. Also, it must be pointed that another characteristic of the NR sources is that their Fourier transform also vanishes [88]. Hence, the plane wave spectrum does not contain information about the NR sources.

From the above explanation two conclusions arise. Firstly, if far-field measurements are used to obtain the equivalent currents, an approximate solution is always obtained. The reason lies in the non-contribution of some part of the currents (the NR sources) to the plane wave spectrum, which is directly related to the far field.

Secondly, even though near-field measurements are taken, the NR sources cannot be recovered because the NR sources do not radiate beyond the support region of the antenna. The only possibility of recovering all the sources consists in measuring the field inside the support region. Nevertheless, these measurements cannot be performed with a spherical measurement system and, in addition, if this measurement would be possible, a lot of drawbacks should be overcome (such as the coupling between the probe and the AUT).

Therefore, no matter the distance at which the radiated field is measured in a spherical measurement system, some sources (the NR sources) cannot be recovered by just using the field measurement. Consequently, the resolution of the reconstructed equivalent currents is limited to a certain value which cannot be overcome.

Assuming this limitation, this thesis is focused on achieving this maximum resolution by recovering the radiating sources. In general, these sources as well as the non-radiating sources form part of any antenna. However, for the sake of simplicity, from now on it will be assumed that the antenna is formed by just the radiating sources. Thus, by obtaining the equivalent currents of an antenna, the radiating sources will be determined.

4.3 Evanescent waves

The waves radiated by the radiating sources may be classified as: *propagating waves* and *evanescent waves*. The difference between them lies in the behavior of the wavenumber. To describe this fact, the following plane wave may be considered:

$$E(x,y,z) = E_0 e^{jk_x x} e^{jk_y y} e^{jk_z z} \tag{4.1}$$

where the constants k_x, k_y and k_z are related, from (2.15), as follows:

$$k_z = \sqrt{k^2 - k_x^2 - k_y^2}. \tag{4.2}$$

Assuming k_x and k_y reals, this relation allows two different situations to be clearly distinguished. These two situations depend on the condition stated in the following expression:

$$k_x^2 + k_y^2 \leq k^2 \tag{4.3}$$

In the first situation, (k_x,k_y) satisfy the above condition and, hence, the constant k_z in (4.2) is *real*. Thus, the plane wave is considered to be a propagating wave because the exponentials in (4.1) are all imaginary.

In the second situation, the constants (k_x,k_y) do not satisfy the condition stated in (4.3) and, hence, the constant k_z in (4.2) is *imaginary*. The insertion of this imaginary constant in (4.1) produces a real exponential (i.e., since $k_z = ja$, the field in (4.1) behaves as $E \propto e^{-az}$). Thus, the wave vanishes exponentially with z forming the so-called evanescent wave.

In general, this behavior may be seen from the point of view of the plane wave spectrum ($\vec{A}_E(k_x, k_y)$). From its definition, the spectrum are the weights of the plane waves propagating in different directions whose integral, according to (2.17), allows the electric field to be computed. Therefore, instead of considering just one plane wave, all the waves included in the plane wave spectrum must be studied. By doing so, two different regions can be established in the plane wave spectrum according to the different situations depicted above. These two regions are shown in Fig. 4.3.

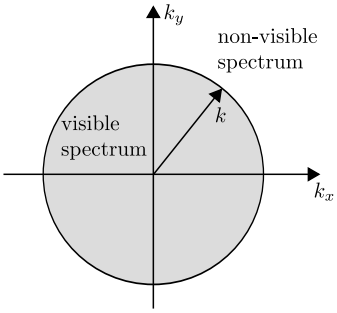

Figure 4.3: Regions in the plane wave spectrum

As can be observed in Fig. 4.3, the points of the spectrum (k_x,k_y) satisfying the condition (4.3) form the so-called *visible spectrum* (also known as *visible region*). However, the points (k_x,k_y) that do not satisfy (4.3) form the so-called *non-visible spectrum* (also known as *invisible spectrum* or *invisible region*).

The term *visible* refers to the possibility of obtaining the waves from the far field. From (3.16) it can be seen that there is a direct relation between the spectrum in the spectral points (k_x,k_y) and the far field in the spatial points (θ,ϕ). The relation between (k_x,k_y) and (θ,ϕ) is stated by (3.17a) and (3.17b). As can be observed, just the points (k_x,k_y) satisfying the condition (4.3) produce real angles (θ,ϕ). Hence, from the far field (either measured or computed from near-field measurements) just the visible spectrum can be obtained.

Physically, this characteristic arises because the plane waves in the invisible spectrum are exponentially attenuated and, hence, they are not present in the far-field region. Thus, in this region, just the propagating waves can be measured and used. In order to show this behavior, Fig. 4.4 represents the attenuation produced by the exponential ($e^{jk_z z}$) for several k_r (being $k_r = \sqrt{k_x^2 + k_y^2}$) at different distances z. As can be observed, after 10 wavelengths, the evanescent waves are attenuated by more than 100 dB. Furthermore, it must be taken into account that the waves that have been represented are those close to the circle of radius k. If waves placed far from this circle had been considered, the attenuation would have been higher than the observed in Fig. 4.4 since, as depicted in this figure, the higher k_r is, the faster the evanescent wave is attenuated.

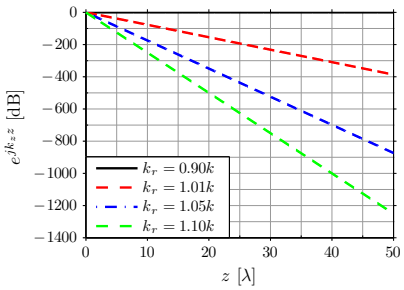

Figure 4.4: Attenuation of the evanescent waves.

Therefore, two conclusions may be adopted from the behavior of the waves radiated by the antenna. Firstly, if the field in the far-field region (either measured or computed) is considered, just the propagating waves, i.e., the visible spectrum, can be computed.

Secondly, near-field measurements might be considered to reconstruct directly the equivalent currents of the antenna. However, it must be taken into account that the waves that may be present in the near-field region but not in the far-field region are only the evanescent waves. These waves, as depicted in Fig. 4.4, are exponentially attenuated with the distance and, hence, very

close measurements to the antenna must be performed in order to be able to measure them.

4.4 Visible spectrum: resolution in the equivalent currents

So far, the waves radiated by the radiating sources have been classified in evanescent and propagating waves. Thus, it is worth to study the effect in the reconstructed equivalent currents if all these waves (propagating and evanescent) are measured or if just the propagating waves, which can always be measured (whichever the measurement distance is), are taken into account. To do this, the relation between the plane wave spectrum and the equivalent currents must be considered.

From previous chapters, this relation is stated by a Fourier transform of the plane wave spectrum. If only the propagating waves are considered, just the visible spectrum is used to reconstruct the equivalent currents. However, if the evanescent waves are considered, the non-visible spectrum is also used. Of course, due to the exponentially attenuation of the evanescent waves, not all the evanescent waves can be measured, but some of them and, specifically, those waves with (k_x,k_y) close to the circle of radius k. Hence, there is a limit on the maximum region of the plane wave spectrum applied to reconstruct the equivalent currents. From the Fourier transform properties [79], the limits in the k_x axis ($\pm k_{x_{max}}$) and in the k_y axis ($\pm k_{y_{max}}$) of the plane wave spectrum, and the precision in the equivalent currents are related as follows:

$$\Delta x = \frac{\pi}{k_{x_{max}}} \tag{4.4a}$$

$$\Delta y = \frac{\pi}{k_{y_{max}}} \tag{4.4b}$$

where Δx and Δy are the spatial precision in the x and y axis, respectively.

In the limit case, in which just the visible spectrum can be applied ($\pm k_{x_{max}} = \pm k_{y_{max}} = k$), the precision becomes:

$$\Delta x = \frac{\lambda}{2} \tag{4.5a}$$

$$\Delta y = \frac{\lambda}{2} \tag{4.5b}$$

As commented above, the evanescent waves are hard to measured, thus, their information is not normally used. For this reason, the most typical situation is the last one, in which just the visible spectrum is applied. To illustrate the resolution achieved in this situation, the antenna formed by 2 $\hat{x}$-directed slots (also studied in the previous chapter) was simulated again. In this case, however, the field was computed in the far-field region. In addition, four different cases with four different separations between the slots were considered. Fig. 4.5 shows the diagram with the variable Sep_x indicating the separation between the slots, which positions are: $-Sep_x/2$ and $Sep_x/2$ in the x axis.

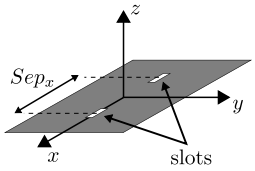

Figure 4.5: Diagram of the antenna formed by 2 slots with several separations between the slots.

Once the far field was simulated with FEKO [4], the microwave holographic technique (see Section 3.4.1), which just uses the far-field information, was applied. As a result, the equivalent currents were obtained on a surface close to the XY plane. Fig. 4.6 shows the x component of the resulting equivalent magnetic currents for the different separations (the y component is negligible). As can be observed, the closer the elements are, the harder it is to distinguish them.

Fig. 4.7 shows the cross section at $y = 0$ of the reconstructed equivalent currents for all the separations depicted in Fig. 4.6. By looking at these cross sections, it can be observed how the positions of the maximums, which correspond to the positions of the slots, are correctly placed. However, for the case of a separation of 0.8 λ and 0.4 λ, the maximums are not clearly distinguished, and, hence, the slots are not detected.

To explain this situation, the concepts of precision and resolution must be reviewed. On the one hand, the precision is the distance between two consecutive points in the spatial domain. On the other hand, the resolution is the ability to distinguish the spectral response of two or more signals [91]. Thus, for this thesis, the resolution is the minimum separation that must exist between two consecutive elements to be clearly distinguished.

The main difference between these two concepts lies in the possibility of improving each one. Whereas the precision can be easily increased, the improvement of the resolution is hard to be obtained.

In order to increase the precision, a zero padding technique may be applied to the spectral signal [91]. This technique adds zeros beyond the known region

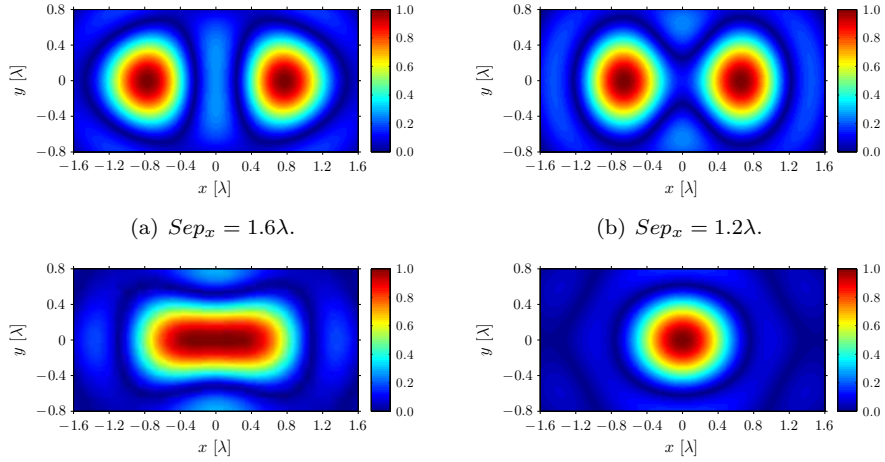

(a) $Sep_x = 1.6\lambda$.

(b) $Sep_x = 1.2\lambda$.

(c) $Sep_x = 0.8\lambda$.

(d) $Sep_x = 0.4\lambda$.

Figure 4.6: Reconstructed equivalent currents from far-field measurements using the microwave holographic technique for the antenna formed by 2 slots with several separations between the slots.

on points were the spectral signal is not known. Thus, smoother spatial signals are obtained due to the interpolation produced in the spatial domain [91]. In the above examples, if the zero padding technique were not applied, i.e., if just the visible spectrum were used, the currents would be obtained on samples separated $\lambda/2$ (4.5), i.e., the precision would be $\lambda/2$.

Nevertheless, as can be observed in Fig. 4.6 and Fig. 4.7, the currents are depicted on closer points. This is because the zero padding technique was applied to improve the precision up to $\lambda/4$. The resulting plane wave spectrums from this zero padding are shown in Fig. 4.8.

By looking at the above results, it can be observed how the zero padding increases the precision but not the resolution. Thus, even though more zeros would had been added to the spectrum, the slots separated 0.8 λ and 0.4 λ could not have been distinguished.

Hence, the improvement of resolution is not achieved by just adding zeros in the non-visible spectrum, but the exact value of the spectrum in this region must be known. Furthermore, it is also important the window employed for the spectrum. In this thesis, a rectangular window [79] is used, which is the best window regarding the resolution. However, other windows, e.g. a hamming or a triangular window, might have been applied to decrease the sidelobes. In

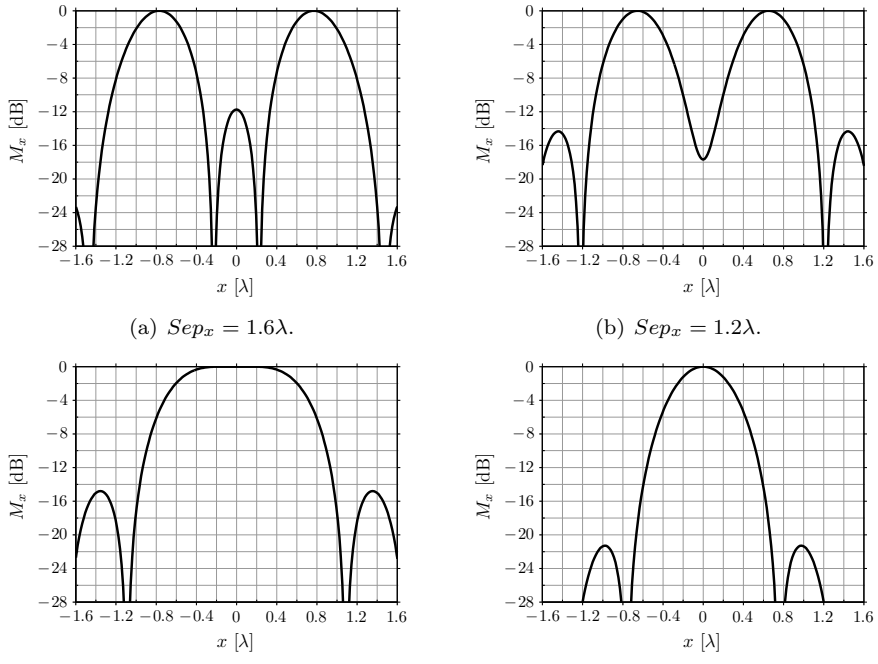

(a) $Sep_x = 1.6\lambda$.

(b) $Sep_x = 1.2\lambda$.

(c) $Sep_x = 0.8\lambda$.

(d) $Sep_x = 0.4\lambda$.

Figure 4.7: Section at $y = 0$ of the reconstructed equivalent currents from far-field measurements using the microwave holographic technique for the antenna formed by 2 slots with several separations between the slots.

this thesis, this problem is not dealt with and, hence, the rectangular window is applied to the known spectrum.

By using the beamwidth at -3 dB of the rectangular window ($\Delta_{-3dB} = 2/\delta_k$) [91],[79], and the width of the visible spectrum ($\delta_k = 2k$), see Fig. 4.3, it may be deduced that the maximum resolution that can be achieved by just using the visible spectrum is 1 λ. Next section deals with the ways in which this resolution can be improved.

4.5 Improvement of resolution

The improvement of resolution in the reconstructed equivalent currents consists, basically, in obtaining the non-visible spectrum. The information of this part of the spectrum is present in the evanescent waves, whose measurement depends on the measurement distance and on the dynamic range of the net-

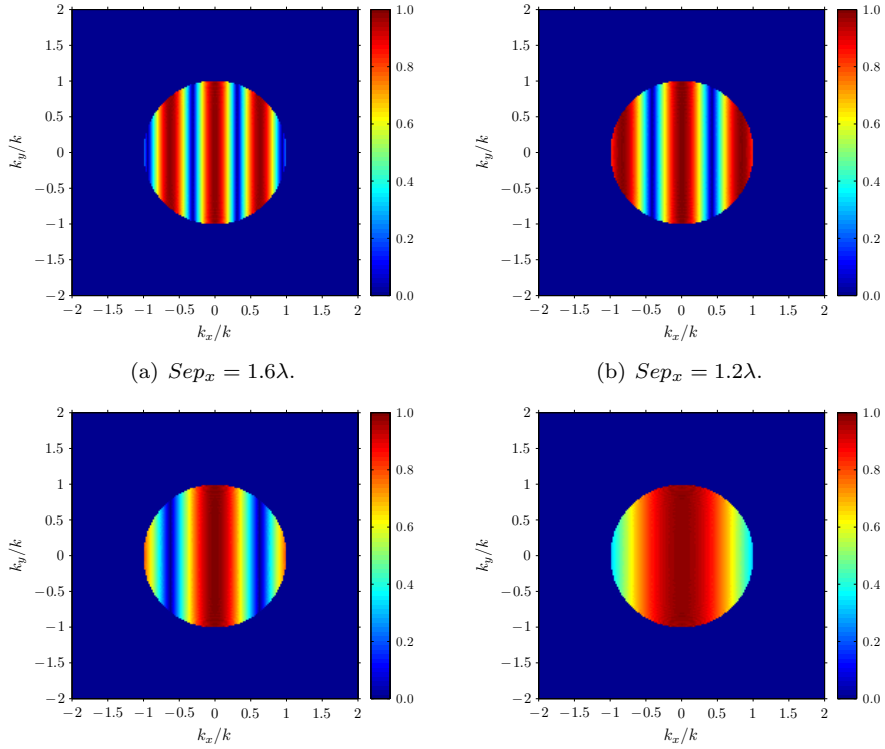

(a) $Sep_x = 1.6\lambda$.

(b) $Sep_x = 1.2\lambda$.

(c) $Sep_x = 0.8\lambda$.

(d) $Sep_x = 0.4\lambda$.

Figure 4.8: Visible region with zero padding of the y component of the plane wave spectrum for the antenna formed by 2 slots with several separations between the slots.

work analyzer. Thus, if the measurement is taken at a quite short measurement distance so that the network analyzer can measure some part of these waves, the non-visible spectrum can be directly computed.

In these cases, the use of the microwave holographic technique (see Section 3.4.1) would eliminate this information since this technique just considers the visible spectrum. To avoid this problem the SWE-to-PWE transformation (see Section 3.4.2) may be used. This technique applies the information of the measured evanescent waves to obtain the non-visible spectrum.

To illustrate the advantages of this technique, the SWE-to-PWE transformation was applied to reconstruct the equivalent currents of the slot-array antenna formed by 2 elements and separated 0.8 λ (see Fig. 4.5). In this case,

instead of simulating the radiated field in the far-field region, the field was obtained in the near-field region, at 1 λ, as in the example of Section 3.3. By doing so, the field was simulated close enough to include several evanescent waves.

Once the spherical near-field measurement was obtained, the transmitting coefficients were determined and the algorithm described in Section 3.4.2 was carried out. As a result, the plane wave spectrum was not only computed in the visible region, but also in the invisible region on points satisfying the condition: $\sqrt{k_x^2 + k_y^2} \leq 1.5k$ (from this limit, the resolution allows the elements separated 0.8 λ to be distinguished). Fig. 4.9 shows this spectrum. As can be observed, the obtained region was greater than the visible region, though a problem arose in the circle of radius k. The spectrum on this circle could not be obtained due to the constant k_z in the denominator of the expression (3.26). In the circle of radius k the constant k_z is 0 and, hence, by applying (3.26), a singularity is produced at these points. In [64] a solution to this problem is proposed by means of the Weyl identity [92].

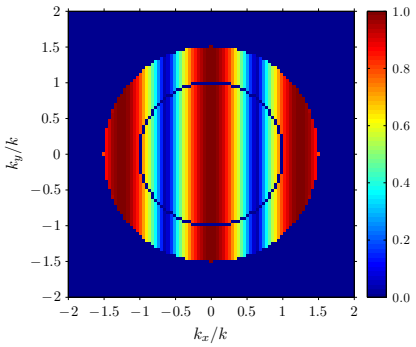

Figure 4.9: y component of the plane wave spectrum from near-field measurements using the SWE-to-PWE transformation for the antenna formed by 2 slots separated 0.8 λ

Moreover, it must be pointed out that the number of modes applied to the computation of the plane wave spectrum was higher than the usual limit of $N = kr_0 + 10$ proposed in [20]. As described in [13], a higher number of modes are required to achieve the convergence in the non-visible spectrum. Specifically, the number of modes used in this example was $N = kr_0 + 40$.

By applying the plane wave spectrum of Fig. 4.9 to reconstruct the equivalent currents, a better resolution was obtained in these currents. Fig. 4.10(a) shows the 2D representation of the x component of the equivalent magnetic currents and Fig. 4.10(b) shows the cross section of these currents at $y = 0$. As

can be observed, the use of the non-visible spectrum enhances the resolution so that, now, both slots are clearly distinguished.

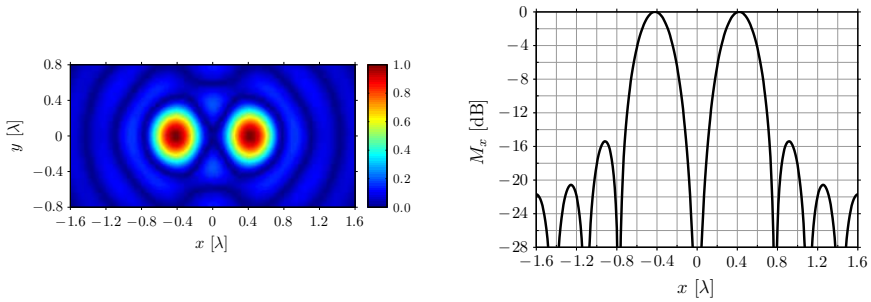

(a) $M_x(x, y)$. (b) M_x at $y = 0$.

Figure 4.10: Reconstructed equivalent currents from near-field measurements using the SWE-to-PWE transformation for the antenna formed by 2 slots separated 0.8 λ.

From previous results it can be seen that the non-visible spectrum is required to improve the resolution in the reconstructed equivalent currents. The problem arises on choosing the technique to compute the non-visible spectrum. If just the modal expansion methods are considered, the above technique (SWE-to-PWE transformation) offers quite good results for near-field measurements. However, several drawbacks can be found.

First of all, the near-field measurement must be taken extremely close to the antenna in order to be able to measure the evanescent waves. For instance, the previous example required to simulate the near-field at 1 λ to include the information of the evanescent waves up to $k_r = 1.5k$ in the plane wave spectrum. Nevertheless, this was not a realistic situation since, in practice, this measurement would have entailed serious coupling problems between the probe and the antenna.

In addition, the dynamic range of the network analyzer and the noise level must be also taken into account. These factors limit the minimum measurable radiated field power and, hence, the evanescent waves that can be measured. For instance, for the real antennas studied in Section 3.4.1 with MHT, it was not possible to achieve the convergence with the SWE-to-PWE transformation though the measurement was taken in the near-field region and quite close to the antenna. For these cases, the dynamic range of the network analyzer should have been larger than 50 dB. Furthermore, at these levels, the reflectivity of the anechoic chamber also affects the measurement and, hence, may mask the evanescent waves.

Moreover, as described in [13], the number of modes required to achieve the convergence in the non-visible spectrum is higher than the typical $N = kr_0 + 10$ limit. To increase this limit, the number of sample points in the measurement grid must be enhanced, what entails a longer measurement time and a higher computational cost, specially for electrically large antennas.

Therefore, in many cases, the non-visible spectrum cannot be obtained with just near-field measurements, e.g. because the near-field measurement cannot be taken close enough to the antenna, or because the dynamic range of the network analyzer is not wide enough. All these reasons lead normally to just be able to consider the visible spectrum.

In these cases, other techniques must be applied. Next chapter deals with these techniques which, basically, add prior knowledge of the antenna to obtain the non-visible spectrum. By doing so, part of the evanescent waves is recovered. Thus, the resolution is enhanced in the reconstructed equivalent currents.

Chapter 5

High-resolution algorithms

The plane wave spectrum used to reconstruct the equivalent currents of an antenna is restricted to a limited region. In the limit case, just the visible spectrum is available, what limits the resolution to just 1 λ in the spatial domain. To improve this resolution, the non-visible spectrum must be determined. This chapter describes and introduces several techniques to carry out the computation of the non-visible spectrum by using prior information about the antenna.

5.1 Introduction

The determination of the non-visible spectrum from the visible spectrum may be done by an *extrapolation technique* [25]. The general goal of this technique is to estimate a signal $f(t)$ from a limited known segment $g(t)$ of this signal and *a priori* information about the signal $f(t)$, either in the actual domain (t) or in the transformed domain (f).

To achieve an accurate estimate of $f(t)$, several methods have been proposed to perform the extrapolation. The most common methods are: the *maximum entropy method* [34] and *minimum error energy method* [26]-[33]. The main difference between these methods is the non-linearity of the maximum entropy method in front of the linearity of the minimum error energy method. For this reason the minimum error energy method has become the most widely used technique.

Specifically, the *Papoulis-Gerchberg algorithm*, which implements a minimum error energy method, has been the most widely used algorithm. Interesting applications can be found in literature, e.g. to reduce the truncation errors in near-field measurements [93],[94] or to locate surface distortions in large reflector antennas [95]. The most important problem of this technique is that the extrapolation is done by means of an iterative algorithm whose stop criterion

has not been found up to date. Furthermore, the speed of convergence of the iterative technique is low and, hence, a long computation time is required to obtain an accurate estimate.

To accelerate the convergence of the Papoulis-Gerchberg algorithm an acceleration constant was proposed in [29]. Also, direct versions of the algorithm, the so-called *extrapolation matrix* for 1-D signals [30] or 2-D signals [31],[32] have been proposed. The aim of these techniques is to obtain the same result that would be obtained with the Papoulis-Gerchberg algorithm after a specific or an infinite number of iterations.

In addition, an interesting direct technique, the so-called *Prior discrete Fourier transform* [36], has been proposed. The criterion of extrapolation of this technique is the *minimum weighted norm*, which is slightly different from the criterions used in the above methods. The advantage of the Prior discrete Fourier transform lies in that it offers quite good results [96] in the reconstruction of the equivalent currents for real antennas.

The chapter describes all these techniques as follows: First a review of the most important extrapolation techniques is done. Then, the Papoulis-Gerchberg algorithm is described in its iterative version by applying all the available information about the antenna. Later, the extrapolation matrix in 1-D and 2-D of the Papoulis-Gerchberg algorithm is presented. Finally, the prior discrete Fourier transform is described and several real results are shown.

Before to proceed, however, it must be pointed out that all the results presented in this chapter have been done with MATLAB® (R2007a). The computer had a processor Pentium® 4 at 3.2 GHz and 2 GB of RAM memory. Thus, all the computation times that are indicated from now on are referred to this computer.

5.2 Extrapolation techniques

The extrapolation techniques estimate a signal $f(t)$ from a segment $g(t)$ of this signal. Fig. 5.1 shows graphically this goal for the 1-D case.

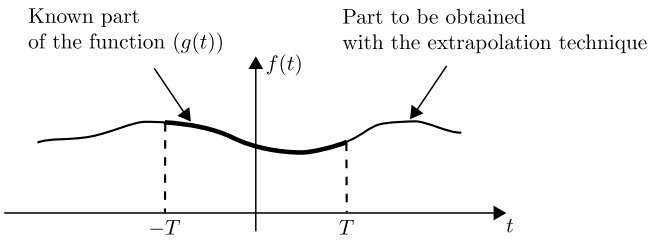

Figure 5.1: Extrapolation technique.

Mathematically, both signals related as:

$$g(t) = \begin{cases} f(t), & |t| \leq T \\ 0, & |t| > T \end{cases} \tag{5.1}$$

The estimate is done by incorporating additional information to the extrapolation procedure. One of the most common data is the band-limitation in the transformed domain. Thus, if a signal in the time domain is limited in the frequency domain by ω_0, the following condition may be imposed in the transformed domain:

$$F(\omega) = 0, \quad |\omega| > \omega_0 \tag{5.2}$$

In general, this band-limitation may be seen as a mask on the transformed domain. If the signal is just band-limited, the mask is a rectangular window. However, more information may be known about the transformed signal, e.g. some knowledge about the shape of the signal or some periodicity in the spectrum. For this reason, a more general way to express the prior information about the transformed signal is the following expression:

$$F_{prior}(\omega) = P(\omega)F(\omega) \tag{5.3}$$

where $P(\omega)$ is the *prior information function*.

The way in which this information is introduced in the extrapolation procedure depends on the specific method applied for the extrapolation. These methods are characterized by the criterion used to find the best estimate. In literature, several useful methods may be found, however, the most common are the *maximum entropy method* and the *minimum error energy method*.

On the one hand, the goal of the maximum entropy method (or *Burg's maximum entropy method*) [34],[35] is to maximize the integral entropy given by:

$$H = \int_{-\pi/\Delta}^{\pi/\Delta} \ln(\hat{f}(t))\mathrm{d}t \tag{5.4}$$

where H is the entropy and $\hat{f}(t)$ is the estimate of the signal obtained with the extrapolation method.

This is the basic definition of the Burg's method and, as can be observed, it is a non-iterative and non-linear method which does not include the incorporation of new information in its primary definition. The main problem of this technique is its tendency to produce spurious when the data is oversampled [97]. To avoid this problem, prior information may be incorporated as a weighting function [97] to the method. By doing so, and considering the

non-linearity of the method, a high degree of resolution may be obtained in the extrapolated signal.

On the other hand, the minimum error energy method is based on minimizing the error energy (E) of the estimated signal $\hat{f}(t)$ with regard to the ideal signal $f(t)$. This energy may be expressed as:

$$E = \int_{-\infty}^{\infty} |f(t) - \hat{f}(t)|^2 \mathrm{d}t. \tag{5.5}$$

The most important algorithm that applies this method is the so-called *Papoulis-Gerchberg algorithm*. This algorithm was first proposed in 1973 by Papoulis [26] and, independently, in 1974 by Gerchberg [27]. Later, Papoulis proved the convergence of the method in 1975 [28].

The Papoulis-Gerchberg algorithm is applied on band-limited signals (5.2). The estimation is performed iteratively, by replacing the known part in the time domain and filtering in the transformed domain. Though in [28] the convergence of the algorithm was proved, no general stop criterion has been established. Nevertheless, the stop criterion has been studied for special cases. For instance, in [98] a stop criterion was proposed for the application of the method in the reduction of truncation errors in near-field measurements. Also, in [99] a study of the number of iterations to achieve accurate results in the reconstruction of the equivalent currents was done.

An accelerate version of the Papoulis-Gerchberg algorithm was proposed in [29] and a non-iterative version based on the extrapolation matrix in [30],[31]. This last version allows the estimate to be obtained after a specific number of iterations or after an infinite number of iterations, i.e., the result towards which the iterative algorithm converges.

Apart from the Papoulis-Gerchberg algorithm, other methods have been introduced whose goal is to minimize the integral (5.5). Among these methods, one of the most important methods is the method proposed by Cadzow [33] based on alternating orthogonal projections [100]. This method has an iterative and a non-iterative version [101] - [103]. The result of this non-iterative algorithm is the same as the result obtained in [104] by minimum least squares.

Nevertheless, it is worth to mention that other extrapolation criterions have been introduced, though they are less used. The goal of these criterions is to improve the solution in specific cases or extend the applicability of the previous criterions. For instance, in [105] and [106] time domain limitations are applied to improve the extrapolated signal within the region of the signal obtained with the previous methods.

Furthermore, energy constraints can be also applied to improve the extrapolated signal. By doing so, the error done by not measuring the signal on maximum energy positions may be corrected [107]. In addition, a generic

mask (5.3) may be used to indicate an approximate shape of the estimated signal [108], or to compensate the effect of noise on measurements [109].

Another important method is the *Prior discrete Fourier transform* [36], which applies the *minimum weighted norm* criterion to perform the extrapolation. This transformation goes beyond the simply band-limitation (5.2), and is able to apply an arbitrary mask of prior information (5.3). In addition, the extrapolation is non-iterative, what avoids long iterative procedures. However, it is worth to mention that other problems must be faced up to such as the ill-conditioning and the size of the resulting equation systems.

Among all the previous extrapolation methods, this thesis pays special attention to the Papoulis-Gerchberg algorithm. The reason for this election is the linearity of the method and the wide range of applications of algorithm [95],[94]. First of all, the iterative version is reviewed and, then, the direct transformations are also studied. Later, the Prior discrete Fourier transform is fully discussed and applied, since it is a general technique with quite good practical results.

Before study all these algorithms, two comments must be done. Firstly, it must be pointed out that, all these algorithms are normally proposed for 1-D signals and, later, extended to the 2-D case. In this chapter the aim is to extrapolate the visible plane wave spectrum. Hence, the interest lies in the 2-D versions of the algorithms. For this reason, though the 1-D versions may be shortly explained in some cases, the attention is focused on the 2-D versions.

Secondly, a small change must be applied to the common versions of the algorithms. Normally, for 2-D signals, the signal is known (and limited) in the spatial domain and the band-limitation is produced in the spectral domain. However, in the case dealt with in this chapter, the known (and limited) 2-D signal is the visible spectrum, and the band-limitation is done in the spatial domain since this limitation is done from the knowledge of the maximum size of the antenna. Thus, a change is always done in the order of application of the Fourier transforms to adapt the algorithms to the requirements of this chapter.

5.3 Papoulis-Gerchberg algorithm

The Papoulis-Gerchberg algorithm is an extrapolation technique for band-limited signals. The 1-D version of the algorithm starts from the known segment of the signal to extrapolate (5.1). As additional information, the band-limitation of the signal in the transformed domain (5.2) is used. The estimation is done iteratively in such a way that, on each iteration, the error energy of the estimated signal decreases.

Basically, the algorithm works as follows. Firstly, the known segment of the signal ($g(t)$) is transformed into the frequency domain ($G(\omega)$) by means of

a Fourier transform (for discrete signals, the *FFT* algorithm is normally employed). Secondly, the signal $G(\omega)$ is filtered according to the band-limitation of the signal that is being estimated (5.2). As a result, a filtered signal ($F_1(\omega)$) is obtained. Later, this signal is transformed into the time domain ($f_1(t)$) by an inverse Fourier transform (the *IFFT* algorithm for discrete signals). This signal is not exactly the same as the original signal $g(t)$, nor the ideal signal $f(t)$. However, from (5.1), it is known that the estimate $f_1(t)$ must be exactly $g(t)$ between $-T$ and T. For this reason, the values of the signal $f_1(t)$ in $[-T, T]$ are substituted by the values of $g(t)$ in this interval. By doing so, a new signal is obtained ($g_1(t)$) which is the result of the iterative algorithm after the first iteration.

The above algorithm is repeated iteratively so that the signal obtained on each iteration ($g_n(t)$) is a better estimate of the signal $f(t)$ than the estimation in the previous iteration ($g_{n-1}(t)$). Mathematically, the iterative Papoulis-Gerchberg algorithm may be expressed as follows:

$$g_n(t) = w_{n-1}(t) * \frac{\sin Tt}{\pi t} \tag{5.6}$$

where $g_n(t)$ is the estimation of the signal $f(t)$ in the n-th iteration, the symbol $*$ indicates convolution, and the signal $w_n(t)$ is given by:

$$w_n(t) = \begin{cases} g(t), & |t| \leq T \\ g_n(t), & |t| > T \end{cases} \tag{5.7}$$

with $g_0(t) = 0$.

The application of the Papoulis-Gerchberg algorithm to 2-D signals requires several modifications. First of all, the Fourier transforms (direct and inverse) must be 2-D transforms. In practice, these transformations are done by first applying the Fourier transform by rows and, later, by columns. For discrete signals the Fourier transform is normally performed by the *Fast Fourier Transform* (FFT) algorithm and the *Inverse Fast Fourier Transform* (IFFT) algorithm [79].

Furthermore, as commented above, the signal to extrapolate in this chapter is a signal in the spectral domain, and the band-limitation is known in the spatial domain (the equivalent currents are limited by the size of the antenna). For this reason, the order of application of the previous Fourier transforms must be on the way round of the algorithm described above for 1-D signals.

Finally, for 2-D signals, the band-limitation in the transformed domain does not just consist in applying a rectangular window. In 2-D, the limitation in the transformed domain may be a square, but also a triangle, a circle, or, in general, any shape. Thus, the band-limitation in the spatial domain may adapt to the shape of the antenna that is being studied. In addition, the known segment of

the spectrum may have any shape, however, for the case under study for this thesis, this shape is always a circle of radius k, i.e., the visible spectrum.

By applying the previous considerations, the 2-D version of the Papoulis-Gerchberg algorithm works as depicted in Fig. 5.2. As can be observed, the algorithm starts from the visible spectrum with zeros outside the circle of radius k (the non-visible region). This spectrum is first transformed into the spatial domain by an inverse Fourier transform. The resulting signal is filtered by applying the known limitation of the signal in the spatial domain (in general, the filter may be any function fitted to the shape of the antenna). Later, the filtered signal is transformed into the spectral domain by a Fourier transform. Finally, the visible spectrum is substituted into the signal obtained after the last transformation, what allows the estimate in the first iteration ($G_1(k_x, k_y)$) to be obtained.

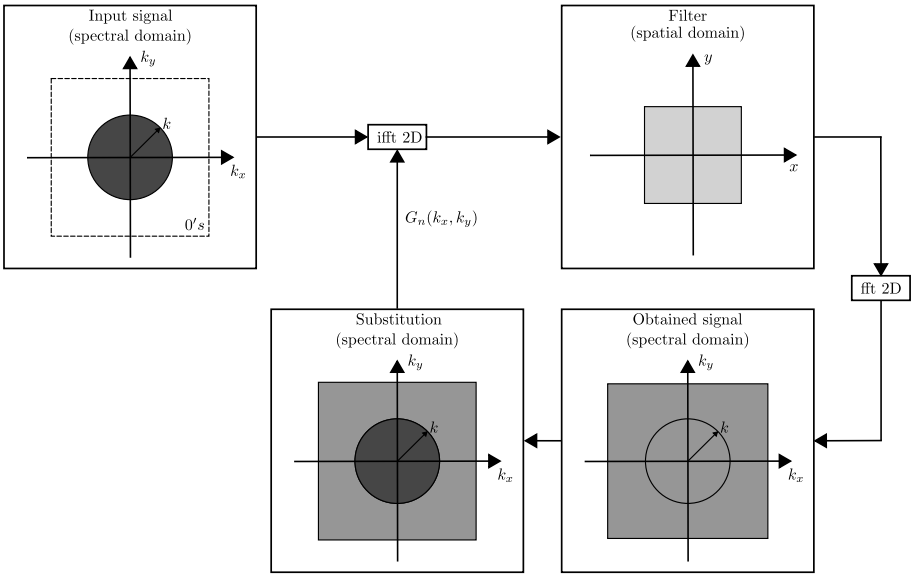

Figure 5.2: 2-D Papoulis-Gerchberg algorithm.

The previous procedure is repeated iteratively, what leads to obtain better estimates of the spectral signal in the non-visible spectrum on each iteration (proof of convergence of this 2-D version can be found in [31],[110]). The last step consists in transforming the resulting spectrum (the known visible region and the estimated non-visible spectrum) into the space domain. By doing so, the equivalent currents are obtained with an improved resolution since the known part of the plane wave spectrum is larger.

Similarly to the 1-D version of the algorithm, the estimation at the n-th iteration $G_n(k_x, k_y)$ of the 2-D Papoulis-Gerchberg algorithm may be expressed as follows:

$$G_n(k_x, k_y) = W_{n-1}(k_x, k_y) * FFT2D\{f(x, y)\} \tag{5.8}$$

where the symbol $*$ indicates 2-D convolution, $FFT2D\{f(x, y)\}$ is the Fourier transform of the generic filter in the spatial domain ($f(x, y)$), and the signal $W_n(k_x, k_y)$, particularized to the case in which the known segment is the visible spectrum, is obtained as:

$$W_n(k_x, k_y) = \begin{cases} G(k_x, k_y), & \sqrt{k_x^2 + k_y^2} \leq k \\ G_n(k_x, k_y), & \sqrt{k_x^2 + k_y^2} > k \end{cases} \tag{5.9}$$

with $G_0(k_x, k_y) = 0$.

The election of the number of iterations that must be applied to obtain a good estimate depends on the case. For this thesis, as pointed out in [99], the adopted stop criterion has been a tradeoff between the number of iterations, the computation time and the improvement achieved on each iteration. Thus, the time used to perform one iteration has been compared to the improvement of the estimate on one iteration. Furthermore, a tendency of both factors has been compared and, from this behavior, a conclusion about the number of iterations to apply has been taken.

Simulated results 1 The Papoulis-Gerchberg algorithm was tested with the slot-array antenna depicted in Fig. 4.5. This antenna is formed by two $\hat{x}$-directed slots placed on the x axis. The separation between the slots was 0.8 λ for this test. As in the example of Section 4.4, the field radiated by the antenna was simulated with FEKO [4] in the far-field region. Later, the Microwave holographic technique was applied to this field what allowed the plane wave spectrum to be obtained.

As can be observed in Fig. 4.8(c), the obtained spectrum only contains information in the visible region. In order to obtain the non-visible spectrum, the iterative algorithm depicted in Fig. 5.2 was applied. As space filter, a square mask of 1.6 λ × 1.6 λ was applied.

The number of iterations was chosen according to the difference between consecutive iterations and the time required to compute one iteration. Fig. 5.3(a) shows the cross section of the y-component of the plane wave spectrum for several number of iterations. In addition, the result is compared with the ideal cross section. As can be observed, the higher the number of iterations is, the more the resulting spectrum seems to the ideal spectrum. However, it can also be seen that the relative improvement between 100 and 1000 iterations is

higher than between 1000 and 5000 iterations. For this reason, the stop number was chosen at 5000 iterations. More iterations could have been employed, however the improvement would not have been significant for the increase on the computation time. Regarding to this computation time, for the case of 5000 iterations, the computation time was of around 20 min, though it must be pointed out this time strongly depends on the computer and on the precision used for the computations.

Fig. 5.3(b) shows the equivalent magnetic currents obtained from the plane wave spectrum obtained after several number of iterations, and a comparison to the ideal distribution. As can be observed, since the known region of the spectrum for a high number of iterations is quite large, the resolution is enhanced. Thus, for the case of 5000 iterations, both slots are clearly distinguished.

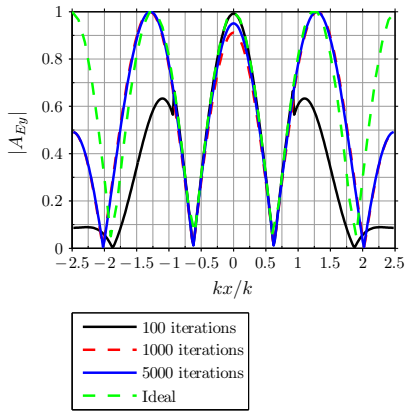

(a) A_{Ey} at $k_y = 0$.

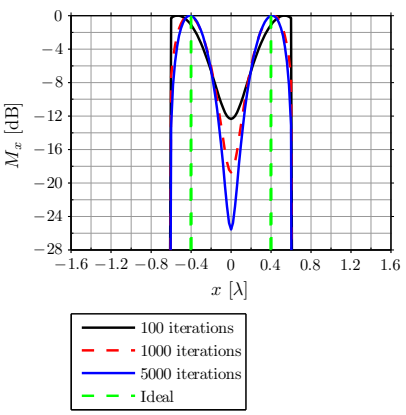

(b) M_x at y=0.

Figure 5.3: Cross sections of the result of the Papoulis-Gerchberg algorithm after several number of iterations for slot-array antenna formed by 2 slots separated 0.8 λ.

In order to show the behavior in 2-D, Fig. 5.4 shows the 2-D representations of the plane wave spectrum (y-component) and the equivalent magnetic currents (x-component) after 5000 iterations. As can be observed, the non-visible region of the plane wave spectrum is partly known, not only in the k_x direction, but also in the k_y direction. As a result, the equivalent currents shown in Fig. 5.4(b) allows the slots to be clearly distinguished.

Simulated results 2 In order to test the Papoulis-Gerchberg algorithm in a more complex situation, the antenna depicted in Fig. 5.5 was simulated with FEKO [4] in the far-field region at 300 MHz. As can be observed, the antenna

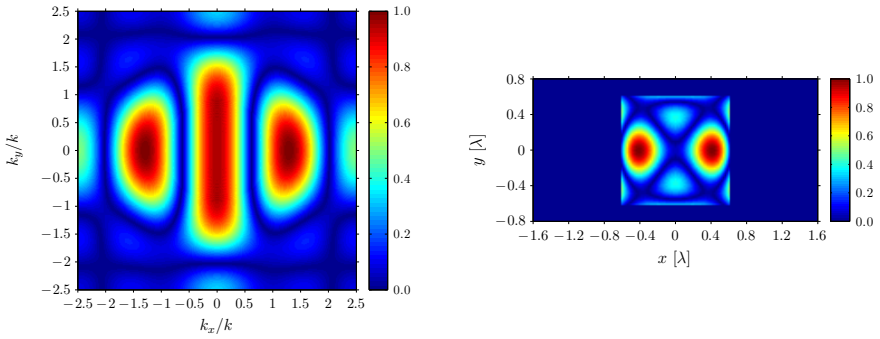

(a) Spectrum (A_{Ey}). (b) Equivalent currents (M_x).

Figure 5.4: Result of the Papoulis-Gerchberg algorithm after 5000 iterations for the slot-array antenna formed by 2 slots separated 0.8 λ.

is formed by 25 $\hat{x}$-directed slots uniformly distributed in 5 rows and 5 columns (a 5×5 slot-array antenna). The separation between elements is 0.4 λ, i.e., the separation is smaller than the maximum resolution achieved with the visible spectrum. In this antenna, one element was not fed so that, the aim of the reconstruction algorithms is to find this slot. In Fig. 5.5 the slot that was not fed is filled with a black color.

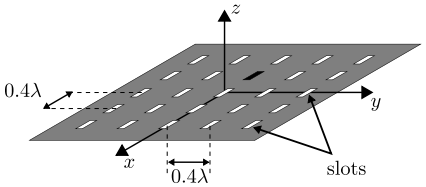

Figure 5.5: 5×5 slot-array antenna with elements uniformly distributed and separated 0.4 λ, and one slot not fed.

Fig. 5.6 shows the result obtained by applying the MHT described in Section 3.4.1 to the simulated far field of the antenna. As can be observed, just the visible spectrum is obtained (see Fig. 5.6(a)). This region just allows a resolution of 1 λ and, hence, the elements of the antenna cannot be distinguished, as shown in Fig. 5.6(b). In addition, if the slot that is not fed were not known, it would not be possible to determine exactly which slot is not fed.

To improve the resolution, the Papoulis-Gerchberg algorithm depicted in Fig. 5.2 was applied to the visible spectrum of Fig. 5.6(a). As a filter, a square mask (with ones inside the mask and zeros outside) of 2 λ × 2 λ centered

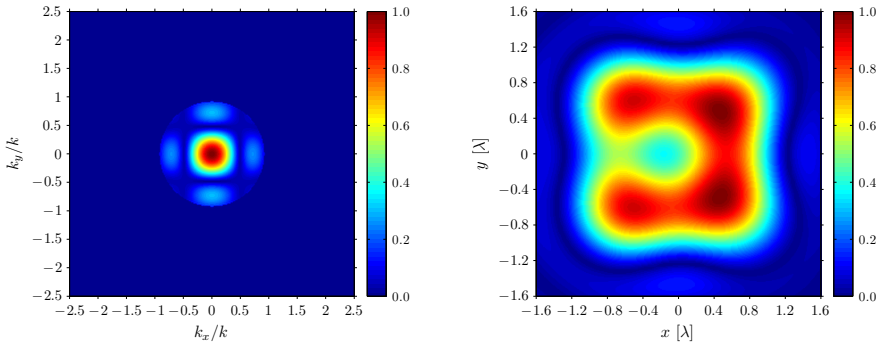

(a) Visible spectrum ($A_{Ey}(k_x, ky_y)$). (b) Equivalent currents ($M_x(x, y)$).

Figure 5.6: Result obtained by applying the MHT to the computed far-field of the 5x5 slot-array antenna at 300 MHz.

at the origin was applied. After 5000 iterations it was detected that the improvement achieved by one iteration did not worth its computation time and, hence, the algorithm was stopped (the 5000 iterations took 20 minutes to be computed). Fig. 5.7(a) shows the spectrum obtained after 5000 iterations and, as can be observed, part of the non-visible spectrum was determined. This new information, however, was not enough in this case to be able to distinguish the slots and detect the slot that was not fed. As can be seen in Fig. 5.7, a small improvement can detected in the reconstructed equivalent current, but it is clearly not sufficient for this antenna. Hence, it can be concluded that, though the iterative algorithm work in many cases, in other cases is may not be enough to use the maximum size of the antenna. Thus, more prior information about the antenna is required to improve the resolution of the equivalent currents.

Practical results The iterative Papoulis-Gerchberg algorithm depicted in Fig. 5.2 was also tested with the X-band slot-array antenna shown in Fig. 3.9. This antenna was measured in the far-field region at 2.70 m. The operating frequency was 10 GHz.

In Section 3.4.1 it is described the way in which the plane wave spectrum was determined. As a result, the visible spectrum shown in Fig. 5.8(a) was obtained, what led to the equivalent magnetic currents shown in Fig. 5.9(a). To improve the resolution of these currents, the iterative algorithm of Fig. 5.2 was applied to the spectrum of Fig. 5.8(a) with a rectangular spatial filter of 5.12 $\lambda \times 2\ \lambda$ centered at the origin.

Fig. 5.8(b) shows the plane wave spectrum after 5000 iterations. As can be observed, part of the non-visible spectrum is obtained. However, some kind of

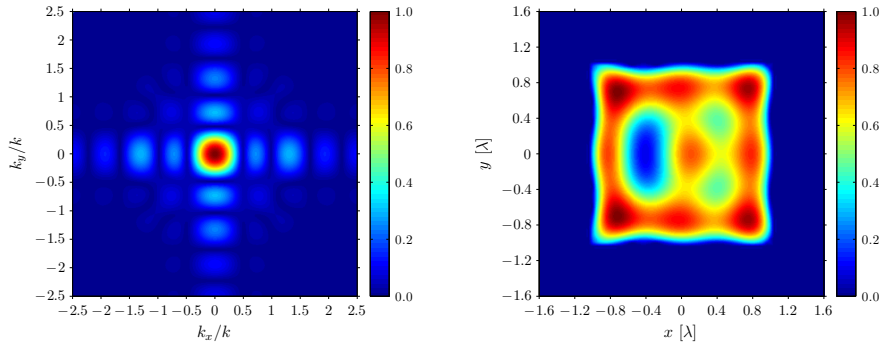

(a) Obtained spectrum ($A_{Ey}(k_x, k_y)$). (b) Equivalent currents ($M_x(x, y)$).

Figure 5.7: Result obtained by applying the MHT to the computed far-field of the 5x5 slot-array antenna at 300 MHz and the Papoulis-Gerchberg algorithm with 5000 iterations.

singularities are observed in the zone of the non-visible spectrum closed to the circle of radius k. The reason of these singularities is the quite big filter used in the iterative algorithm.

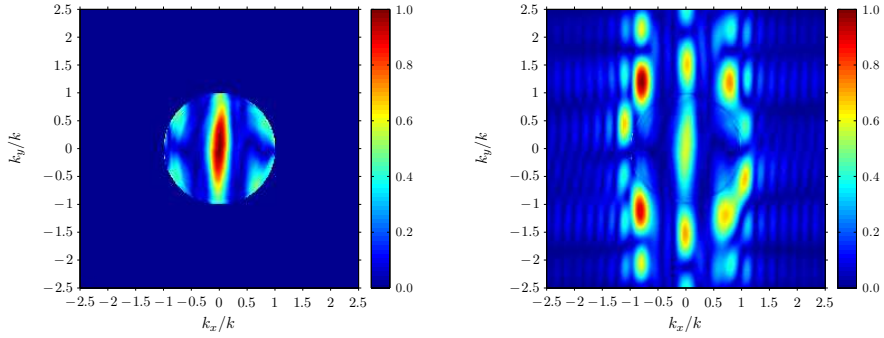

(a) Visible spectrum (A_{Ey}). (b) Spectrum (A_{Ey}).

Figure 5.8: Improvement in the plane wave spectrum of the X-band slot-array antenna formed by 7 slots by applying the Papoulis-Gerchberg algorithm with 5000 iterations.

Fig. 5.9(b) shows the equivalent currents obtained from Fig. 5.8(b). Due to the singularities near the circle of radius k, the result is quite bad. No element

is clearly distinguished and singularities may be observed closed to the edge of the filter.

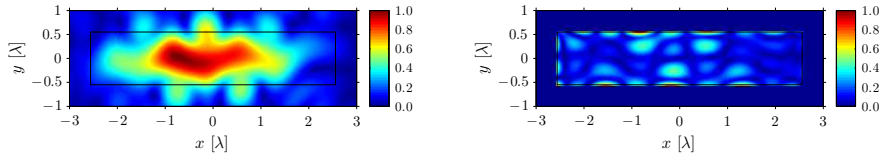

(a) Initial currents (M_x). (b) Final currents (M_x).

Figure 5.9: Improvement in the reconstructed equivalent currents of the X-band slot-array antenna formed by 7 slots by applying the Papoulis-Gerchberg algorithm with 5000 iterations.

In Fig. 5.10 the value on each slot after the application of the Papoulis-Gerchberg is represented and compared to both, the ideal distribution and the currents obtained from just the visible spectrum. By looking at this figure, it can be concluded that, though singularities appear on the edge of the filter, an improvement in the resolution is achieved inside the filter. As can be observed, a certain cosine distribution inside the slot is observed, though the envelope is not preserved after the application of the iterative algorithm. Thus, it can be concluded that the Papoulis-Gerchberg algorithm works correctly, though some little errors are detected. To eliminate these errors, new information is required.

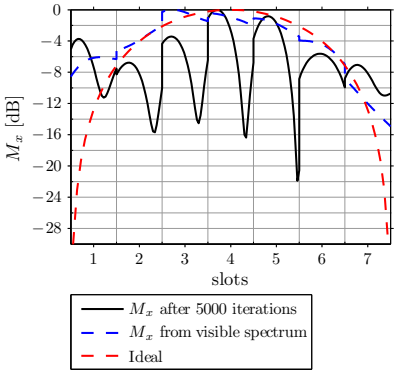

Figure 5.10: Equivalent currents on the positions of the slots of the X-band slot-array antenna formed by 7 slots by applying the Papoulis-Gerchberg algorithm with 5000 iterations.

5.3.1 Spectral periodicity

In order to improve the equivalent currents obtained by means of the Papoulis-Gerchberg algorithm, new information about the antenna must be included. This information consists in indicating, not only the size of the antenna, but also the positions where the equivalent currents can only exist. For instance, if the antenna is an array, it is known a priori that the equivalent currents are only present on the positions where the elements of the array are placed.

The simplest situation arises when the array is formed by small elements distributed uniformly. In this case, the equivalent currents may be considered as a discrete function which points are equispaced. The advantage lies in that, no matter the amplitude of the discrete points, the Fourier transform of this kind of functions is periodic [111]. For instance, the Fourier transform of the discrete function shown in Fig. 5.11(b), which is formed by two equispaced elements, is the function shown in Fig. 5.11(a). As can be observed, this function is periodic and, hence, by just knowing the periodic region, the whole function may be determined by just replying this part on the suitable positions.

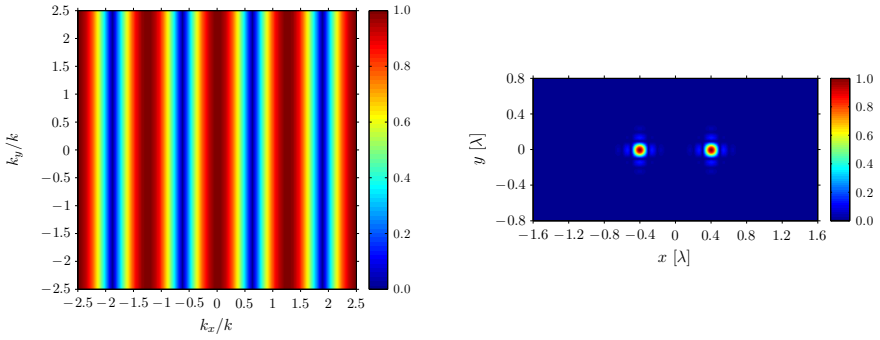

(a) Spectrum.

(b) Discrete signal.

Figure 5.11: Discrete function formed by 2 elements separated 0.8 λ and its spectrum.

The period of the spectral function, i.e., the width of the region to reply in the spectrum, is determined from the separation between elements (Δx and Δy in the x and y axes, respectively). This period, noted as Δk_x and Δk_y, is obtained as follows:

$$\Delta k_x = \frac{2\pi}{\Delta x} \tag{5.10a}$$

$$\Delta k_y = \frac{2\pi}{\Delta y} \tag{5.10b}$$

The width of the replied region determines the positions where the replies must be placed. Since the periodic region is centered in the origin, the positions of the replies ($k_{x_{rep}}$,$k_{y_{rep}}$) are exactly the same as the width of the periodic region. Hence:

$$k_{x_{rep}} = \Delta k_x \tag{5.11a}$$

$$k_{y_{rep}} = \Delta k_y \tag{5.11b}$$

The application of this property to the equivalent currents of array antennas implies an important advantage. Since, from this property, the plane wave spectrum of the antenna is periodic, the whole spectrum may be determined from just the visible spectrum. To do this, the antenna must be formed by equispaced elements. From the separations between these elements, the period of the spectrum is determined by (5.10) and the positions of the spectrum (where the periodic function must be placed) by (5.11).

Example This property may be applied to the 5×5 slot-array antenna shown in Fig. 5.5. Since the elements are separated 0.4 λ, the width of the periodic region of the plane wave spectrum is, from (5.10), $2\pi/0.4$ λ in both axes (k_x and k_y), i.e., 2.5 if the width is normalized with regard to k. The positions of the replies coincide with this value (5.11).

Thus, if the visible spectrum shown in Fig. 5.6(a) is replied according to these values, the obtained plane wave spectrum is the spectrum shown in Fig. 5.12(a). As can be observed, part of the non-visible spectrum is determined by just using the knowledge of the separation between the elements. However, this new information is not enough to distinguish completely all the elements with the correct amplitude. This fact can be observed in the corresponding equivalent currents of this spectrum, shown in Fig. 5.12(b).

The reason for not obtaining the correct equivalent currents are the zeros between the known regions in the spectrum shown Fig. 5.12(a). These regions must be obtained to determine the amplitude of equivalent currents accurately.

The limit case in which the application of this technique allows the whole spectrum to be directly obtained is that in which the elements are separated

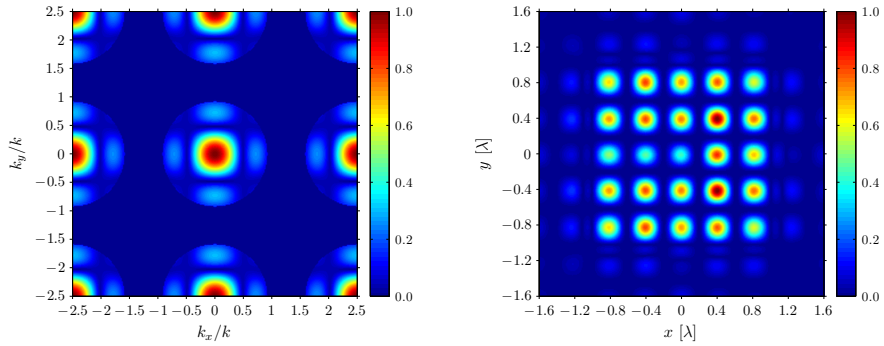

(a) Spectrum ($A_{Ey}(k_x, k_y)$). (b) Equivalent currents ($M_x(x, y)$).

Figure 5.12: Result obtained by applying the MHT to the computed far-field of the 5x5 slot-array antenna at 300 MHz and replying the visible spectrum according to the separation between elements (0.4 λ).

$1/\sqrt{2}$ λ. In that case, the replies of the visible spectrum overlap themselves and, hence, the entire the spectrum is obtained. However, the closer the elements are, the greater is the distance between the replies and, hence, the zero's region between the known part of the spectrum becomes larger, as shown Fig. 5.12(a) for a separation of 0.4 λ.

To obtain the zero's region between the replies of the visible spectrum, the Papoulis-Gerchberg algorithm may be applied. In this case, two different options arise depending on the order of application of each technique. Next, both options are described.

5.3.1.1 Option 1: First PG algorithm and, then, replication of the spectrum

In this first option [112], the Papoulis-Gerchberg algorithm is first applied by using the maximum size of the antenna. By doing so, part of the non-visible spectrum is obtained and, hence, the known part is larger than at the beginning, when just he visible region is known.

Then, the width of the spectrum that must be replied is obtained by using the separation between elements and, finally, by using this width (and the positions of replies) the spectrum is replied. In this case, however, instead of replying the visible spectrum, the spectrum obtained by means of the Papoulis-Gerchberg algorithm is used. Thus, the zero's region between replies is minimized since this part is obtained by the iterative algorithm.

Simulated results The above procedure was tested with the 5×5 slot-array antenna shown in Fig. 5.5. The spectrum obtained after 5000 iterations is shown in Fig. 5.7(a). As commented above, since the separation between elements is 0.4 λ, the width (and the positions of the replies) normalized with regard to k is 2.5 in the k_x and k_y axes. Thus, if the spectrum obtained with the iterative algorithm is replied according the width and positions of replies, the resulting spectrum is the one shown in Fig. 5.13(a).

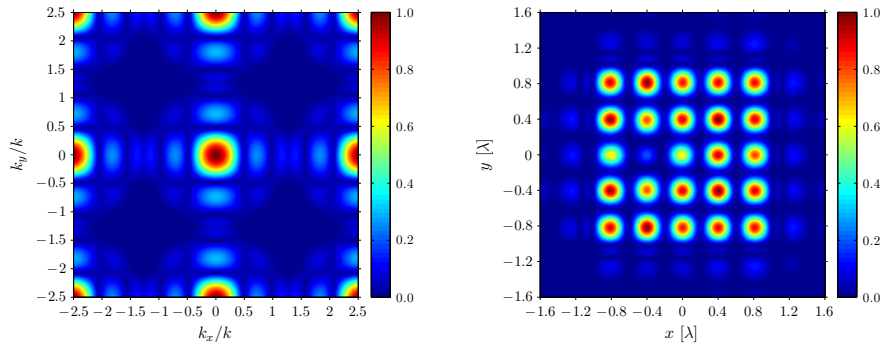

(a) Spectrum ($A_{Ey}(k_x, k_y)$). (b) Equivalent currents ($M_x(x, y)$).

Figure 5.13: Result obtained by applying the MHT to the computed far-field of the 5x5 slot-array antenna at 300 MHz, and the algorithm described in the option 1.

As can be observed in this spectrum, not only the visible region is replied, but also the surrounding points around the circle of radius k, which have been obtained by the iterative algorithm. This improved spectrum leads to the equivalent currents shown in Fig. 5.13(b). In this case, the elements are better distinguished than with the equivalent currents from the visible spectrum and the amplitude of the different elements is closer to the ideal currents (in the ideal currents, all the slots have the same weight, apart from the slot that is not fed). Nevertheless, it must be pointed out that this amplitude is not completely uniform. Certain variations can be observed due to the fact that the iterative algorithm does not obtain a large enough area of the non-visible spectrum. For this reason, the next option proposes a modification to improve the result.

5.3.1.2 Option 2: First replication of the spectrum and, then, PG algorithm

The second option [113],[114] makes use of the spectrum replies during the iterative algorithm so that the replies help to improve the extrapolation per-

formed by the Papoulis-Gerchberg algorithm. To do this, the iterative algorithm (shown in Fig. 5.2) not only substitutes the visible spectrum on each iteration, but also the replies of the visible spectrum present in the non-visible spectrum due to the discrete behavior of the antenna.

Therefore, the modified iterative algorithm for discrete signals works as depicted in Fig. 5.14. As can be observed, the algorithm basically works as the iterative algorithm shown in Fig. 5.2. The difference lies in the substitution of the known part of the spectrum in the iterative algorithm. Now, since the antenna is discrete and the elements are equispaced, it is known a priori that the spectrum is periodic. Hence, the replies of the visible spectrum, which positions are determined according to the separation between elements (5.11), are also substituted.

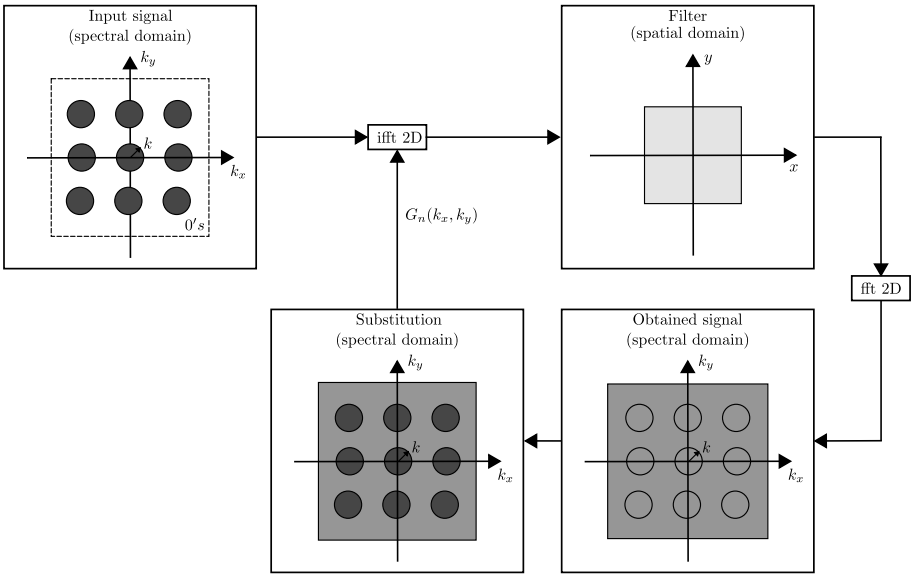

Figure 5.14: 2-D Papoulis-Gerchberg algorithm with replies of the spectrum.

Simulated results The algorithm described above was tested with the 5×5 slot-array antenna depicted in Fig. 5.5. As commented above, according to the 0.4 λ of separation between elements, the width of the spectrum that must be replied is 2.5 (in normalized with regard to k form). This width coincides with the positions of the replies of the visible spectrum.

By using the previous positions of replies, the iterative algorithm depicted in Fig. 5.14 was applied. As a result, the spectrum shown in Fig. 5.15(a) was

obtained after 5000 iterations. By looking at this figure, and comparing this result to the spectrum of Fig. 5.13(a), it can be seen how the spectrum obtained with this second option somewhat better than the result of the first option. Specially, on points where the spectrum of Fig. 5.13(a) is completely zero, the spectrum shown in Fig. 5.15(a) has a correct value. As a proof of this improvement, Fig. 5.15(b) shows the corresponding equivalent currents determined from the spectrum of Fig. 5.15(a). In this case, not only the elements are clearly distinguished, but also the amplitude is more uniform than the amplitude of the currents shown in Fig. 5.13(b).

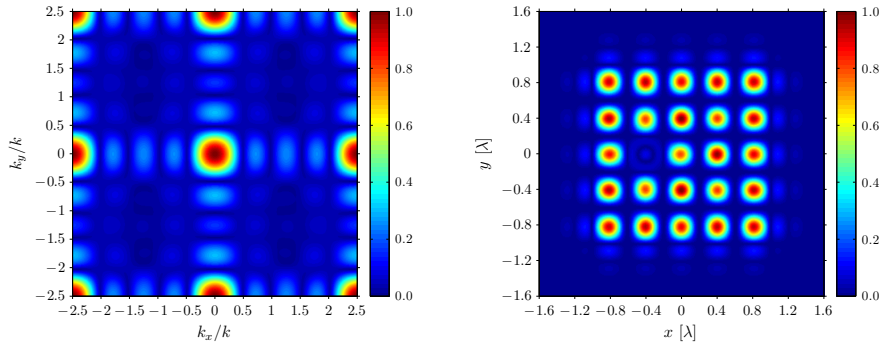

(a) Spectrum ($A_{Ey}(k_x, k_y)$). (b) Equivalent currents ($M_x(x, y)$).

Figure 5.15: Result obtained by applying the MHT to the computed far-field of the 5x5 slot-array antenna at 300 MHz, and the algorithm described in the option 2.

Practical results This second option was also applied to improve the resolution in the equivalent currents of the X-band slot array antenna shown in Fig. 3.9. In this case, the slots are not discrete elements, however it may be assumed that the energy is in the center of the slot and, hence, assume a separation of 0.66 λ in the x axis (i.e., the separation between slots in this axis). In the other axis, the y axis, the elements are not equispaced but a small separation, i.e., the precision used for the simulation (0.01 λ), can be assumed. Thus, the currents may inform about the position of the slots on this axis.

By using the previous separations, the algorithm depicted in Fig. 5.14 was applied. The plane wave spectrum that was obtained is shown in Fig. 5.16(a). By looking at this spectrum it can be seen how the assumed separation between slots in the x axis led to a periodic spectrum in the k_x axis. Consequently, the equivalent currents that were determined were the currents shown

in Fig. 5.16(b). As can be observed, the energy is concentrated on points separated 0.66 λ.

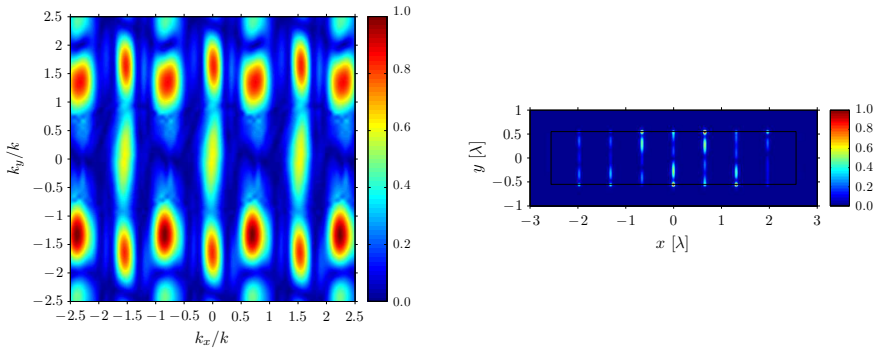

(a) Spectrum ($A_{Ey}(k_x, k_y)$). (b) Equivalent currents ($M_x(x, y)$).

Figure 5.16: Improvement in the plane wave spectrum of the X-band slot-array antenna formed by 7 slots by applying the Papoulis-Gerchberg algorithm with 5000 iterations and replies of the spectrum (option 2).

Fig. 5.17 shows the value of the equivalent currents depicted in Fig. 5.16(b) on the positions of the slots. By looking at this figure it can be concluded that the replication of the spectrum does not lead to a reasonably distribution of the currents in the y axis. Thus, though the 2-D representation indicates some oscillation in this axis, the cross section indicates that some error has been introduced by assuming the previous separations between slots. Next, other kinds of filters are studied.

5.3.2 Restrictive filters

From previous results it can be seen how the Papoulis-Gerchberg in conjunction with the replication of the spectrum may help to the diagnosis of antennas formed by small elements. If the antenna is not formed by small elements, the technique concentrates the energy on discrete points so that the result can be interpreted to perform the diagnosis accurately.

Nevertheless, to improve the result when the antenna is not formed by quite small elements, e.g., the X-band slot-array antenna formed by 7 elements studied previously and shown in Fig. 3.9, a more complex filter may be used during the iterative algorithm. Thus, the filter may consist not only in a square mask according to the maximum size of the antenna, but also a mask with 1's on the positions of the radiating elements and 0's outside. By doing so, the result is constraint to positions where the equivalent currents are supposed

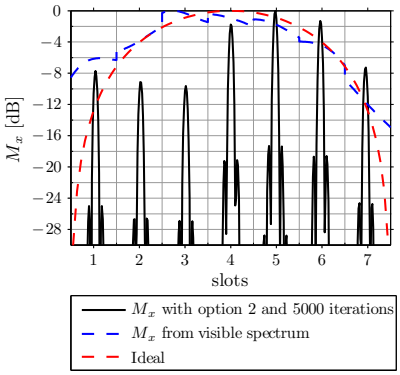

Figure 5.17: Equivalent currents on the positions of the slots of the X-band slot-array antenna formed by 7 slots by applying the Papoulis-Gerchberg algorithm with 5000 iterations and replies of the spectrum (option 2).

to exist. Nevertheless, it must be taken into account that the use of these restrictive filters does not allow the errors outside the radiating areas to be found. Hence, special care must be taken when applying these kinds of filters since the application of a wrong filter might lead to a non-correct diagnosis.

Practical results To test the effect of a restrictive filter, the plane wave spectrum of the X-band slot-array antenna shown in Fig. 3.9 was extrapolated. Fig. 5.8 shows the visible spectrum of this antenna and the spectrum obtained by applying the Papoulis-Gerchberg algorithm with a rectangular spatial filter (including all the slots).

In this section, the applied filter was a mask with ones on the exact positions where the slots are, i.e., on the points where the antenna radiates, and zeros outside. This filter may be observed in Fig. 5.18.

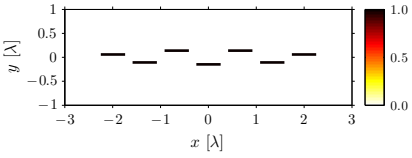

Figure 5.18: Spatial filter restricted to the positions of the slots.

By applying the previous filter in the iterative algorithm, the resulting equivalent currents after 1000 iterations were fitted to just the positions of the slots. Fig. 5.19(b) shows the obtained equivalent currents and, as can be observed,

currents are only present on the points of the filter which value is 1. To obtain these currents, the plane wave spectrum that was determined by the extrapolation algorithm was the spectrum shown in Fig. 5.19(a). Here it can be seen how a wide region of the non-visible spectrum is determined and a certain periodicity is observed, as predicted in previous section due to the equispaced behavior of the slots in the x axis.

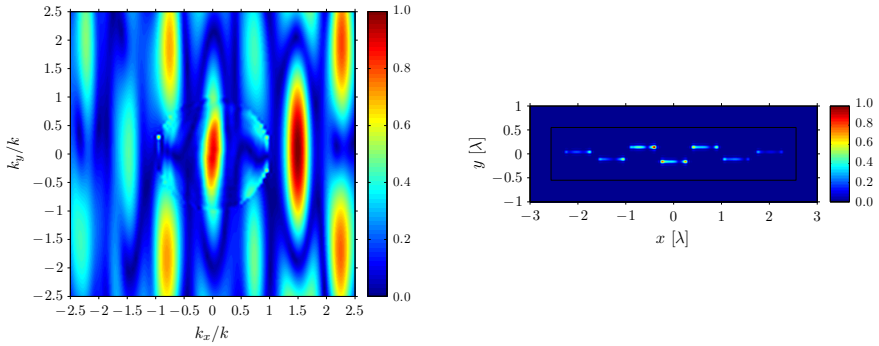

(a) Spectrum ($A_{Ey}(k_x, k_y)$).

(b) Equivalent currents ($M_x(x, y)$).

Figure 5.19: Improvement in the plane wave spectrum of the X-band slot-array antenna formed by 7 slots by applying the Papoulis-Gerchberg algorithm with a restrictive filter and 5000 iterations.

Nevertheless, by looking at Fig. 5.19(b) is can also be concluded that the singularities have been translated from the edge of the large filter (see Fig. 5.9(b)) to the edge of the restrictive filter. This fact can also be seen in the obtained equivalent currents on the positions of the slots shown in Fig. 5.20. In this figure it can be observed that, though certain correct behavior inside the slot can be detected, singularities arise on the edge of the slots. To avoid these singularities, a higher number of iterations might be used, however, this higher number of iterations would increase considerably the computation time. To reduce the computation time, next sections describe and propose several methods.

5.3.3 Acceleration constant

One of the most important drawbacks of the Papoulis-Gerchberg algorithm is its speed of convergence. Though a termination criterion is not available, a great number of iterations are required to achieve a result with a small error. This high number of iterations implies a high computation time, especially for 2-D signals.

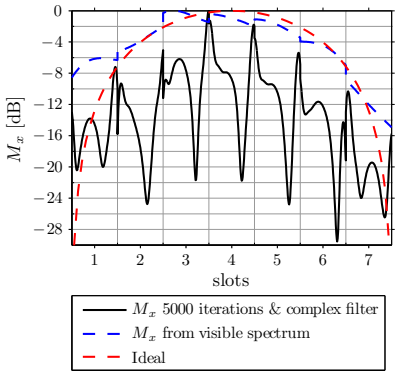

Figure 5.20: Equivalent currents on the positions of the slots of the X-band slot-array antenna formed by 7 slots by applying the Papoulis-Gerchberg algorithm with a restrictive filter.

In [29] a modification of the iterative algorithm is proposed to speed up the algorithm. The modification consists in multiplying the result on each iteration by a factor computed from the result in the previous iteration. By doing so, the convergence is earlier achieved and, hence, with a lower number of iterations, the error becomes quite small to be able to stop the iterative algorithm.

The algorithm is proposed for 1-D signals, however, in this thesis the interest is on 2-D signals (the plane wave spectrum). For this reason, in this section the extension to 2-D is described, as proposed in [115].

The inclusion of an acceleration constant is based on the mathematical representation of the Papoulis-Gerchberg depicted in expression (5.8). As described above, the result on the iteration n is computed from the convolution of the Fourier transform of the spatial filter $FFT2D\{f(x,y)\}$ with the function $W_n(k_x,k_y)$ computed as shown in (5.9). To speed up the iterative algorithm, this function is computed in a different way. In this case, a multiplicative factor A_n is added on each iteration as follows:

$$W_n(k_x,k_y) = \begin{cases} G(k_x,k_y), & \sqrt{k_x^2+k_y^2} \leq k \\ A_n G_n(k_x,k_y), & \sqrt{k_x^2+k_y^2} > k \end{cases} \tag{5.12}$$

with $G_0(k_x,k_y) = 0$.

As can be observed in this expression, the function $W_n(k_x,k_y)$ is computed from the visible spectrum and from the non-visible spectrum (which is obtained on each iteration) multiplied by the constant A_n. The computation of this factor is done so that the error produced on each iteration ($G(k_x,k_y) -$

$A_n G_n(k_x, k_y)$) and the signal obtained on each iteration ($G_n(k_x, k_y)$) are orthogonal. This orthogonal relation is expressed in the following way:

$$\sum_{k_x=-\infty}^{\infty} \sum_{k_y=-\infty}^{\infty} [[G(k_x, k_y) - A_n G_n(k_x, k_y)] - G_n^*(k_x, k_y)] = 0 \tag{5.13}$$

where $G_n^*(k_x, k_y)$ is the complex conjugate of the function $G_n(k_x, k_y)$.

At first, from (5.13), the computation of A_n requires the knowledge of the entire spectrum $G(k_x, k_y)$, which is not known. However, from the derivation of the acceleration constant described in [29], an expression to obtain A_n without the requirement of knowing the correct function in the entire spectrum may be achieved. Thus, in a similar way than in [29], the acceleration constant is given by:

$$A_n = \frac{X_n}{Z_n} \tag{5.14}$$

The functions X_n and Z_n are computed as:

$$Z_n = \sum_{k_x=-\infty}^{\infty} \sum_{k_y=-\infty}^{\infty} |G_n(k_x, k_y)|^2 \tag{5.15}$$

and

$$X_n = X_1 + A_{n-1}(X_{n-1} Y_{n-1}) \tag{5.16}$$

where the function Y_n is computed as follows:

$$Y_n = \sum_{k_x=-k}^{k} \sum_{k_y=-k_{y_{max}}}^{k_{y_{max}}} G(k_x, k_y) G_n^*(k_x, k_y) \tag{5.17}$$

The limits in the summations of the previous expression are chosen so that the ideal function $G(k_x, k_y)$ is only required on the spectral points (k_x,k_y) inside the visible spectrum ($\sqrt{k_x^2 + k_y^2} \leq k$), i.e., the spectrum known at the beginning. Thus, the first summation varies from $k_x = -k$ to $k_x = k$, and the second summation from $k_y = -k_{y_{max}}$ to $k_y = k_{y_{max}}$, where $\pm k_{y_{max}}$ are the limits on the k_y axis within the visible spectrum for the value of k_x taken in the first summation.

The initial values of the functions X_n and Y_n for the computation of X_n in (5.16) are:

$$A_0 = 1 \quad X_0 = 0 \quad Y_0 = 0 \tag{5.18a}$$

and

$$X_1 = \sum_{k_x=-k}^{k} \sum_{k_y=-k_{y_{max}}}^{k_{y_{max}}} |G(k_x, k_y)|^2 \tag{5.18b}$$

where the values $\pm k_{y_{max}}$ are defined as in expression (5.17).

Simulated results The acceleration constant was tested with the 5×5 slot-array antenna depicted in Fig. 5.5. To perform this test, the Papoulis-Gerchberg algorithm was first applied and, then, the spectrum was replied according to the separation between elements. The iterative algorithm was carried out with and without acceleration constant, as described above, for just 5 iterations.

Fig. 5.21 shows a comparison of the plane wave spectrum obtained with and without the acceleration constant. As can be observed, if the acceleration constant is not used (see Fig. 5.21(a)), singularities arise between replies at just 5 iterations and, hence, a higher number of iterations is required to decrease these singularities. However, if the acceleration constant is applied (see Fig. 5.21(b)), the result after 5 iterations is quite good and looks like the result obtained without the acceleration constant after 5000 iterations (see Fig. 5.13(a)).

The equivalent currents obtained from the above plane wave spectrums are shown in Fig. 5.22. As can be observed, if the acceleration constant is not used (Fig. 5.22(a)) the obtained currents are far from the uniform distribution of the ideal antenna. However, by applying this constant on each step of the iterative algorithm, the equivalent currents obtained after just 5 iterations present a quite good uniform amplitude. In addition, these currents allow the not-fed slot to be clearly distinguished.

Unfortunately, though good results are obtained after few iterations, it must be pointed out that the algorithm, with or without acceleration constant, converges to the same result. Thus, if a high accuracy is required, a higher number of iterations will have to be applied in both methods. At this high number of iterations, the advantage of using the acceleration constant in front of not using this constant is minimum and, hence, the same result is obtained in both cases. Moreover, the computation of this factor on each iteration consumes time so that, the same result is obtained in both cases, but the use of the acceleration constant increases the computation time. For these reasons, if a high number of iterations is required, e.g. 1000 iterations, the use of the acceleration constant

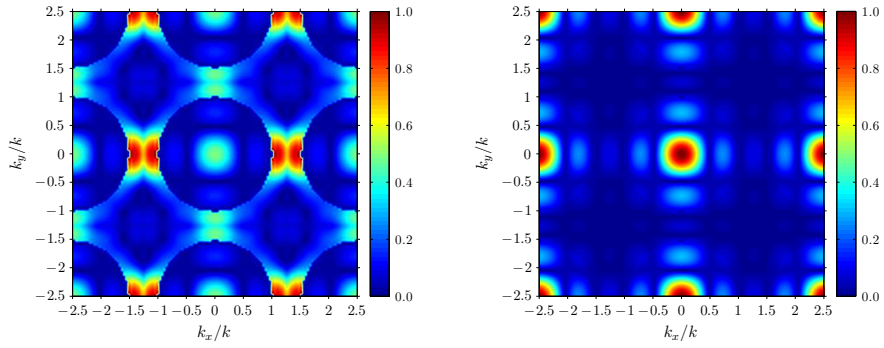

(a) Spectrum ($A_{Ey}(k_x, k_y)$) without An.

(b) Spectrum ($A_{Ey}(k_x, k_y)$) with An.

Figure 5.21: Spectrum obtained by applying the MHT to the computed far-field of the 5x5 slot-array antenna at 300 MHz and the Papoulis-Gerchberg algorithm after 5, with and without the acceleration constant.

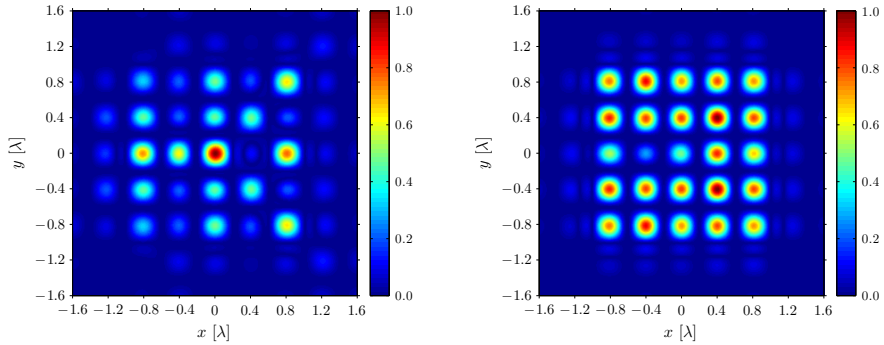

(a) Currents ($M_x(x, y)$) without An.

(b) Currents ($M_x(x, y)$) with An.

Figure 5.22: Currents obtained by applying the MHT to the computed far-field of the 5x5 slot-array antenna at 300 MHz and the Papoulis-Gerchberg algorithm after 5, with and without the acceleration constant.

might not be advisable and other techniques, which perform the extrapolation in a direct step, would be required. Next sections describe these techniques.

5.4 Extrapolation matrix

As commented above, the main drawback of the Papoulis-Gerchberg algorithm is the fact of being an iterative algorithm. In addition, the speed of convergence is quite low and a termination criterion has not been established up to now for a wide range of situations.

To solve these problems, a direct version of the iterative Papoulis-Gerchberg algorithm was also proposed in [30] for 1-D signals and, later, extended to 2-D signals in [31]. These algorithms are based on the formation of a matrix, the so-called *extrapolation matrix*, which, multiplied by the known signal (the visible spectrum for this thesis), leads to the same result as with the iterative algorithm. The extrapolation matrix is formed by using the size of the filter in the transformed domain (i.e., the size of the antenna) and the number of iterations to apply.

Furthermore, under specific conditions, the extrapolation matrix can be computed for an infinite number of iterations. Hence, the same result that would be obtained after an infinite number of iterations with the iterative algorithm (unreachable in a practical situation) is achieved. Thus, the best extrapolation in the sense of the minimum error energy is obtained.

Next, a brief review of the 1-D version of the extrapolation matrix is done. Also, the 2-D extrapolation matrix is described [31] and the drawbacks of this solution are shown. Finally, the 2-D generalized extrapolation matrix, which was proposed recently [32], is described.

5.4.1 1-D Extrapolation matrix

The extrapolation matrix was proposed by Sabri and Steenaart in [30] for 1-D signals. The aim of the extrapolation matrix is to perform, by a single matrix operation, the extrapolation of a band-limited signal which is known in just a segment, as defined in (5.1) and (5.2).

To do this, the iterative algorithm, also expressed in (5.6) and (5.7), must be rewritten as follows:

$$g_n(t) = g(t) + H\{g_{n-1}(t)\} \tag{5.19}$$

where $g_n(t)$ is the extrapolated signal at the n-th iteration, $g(t)$ is the initial signal (5.1) (which is known in the interval $[-T, T]$), $g_{-1} = 0$, and H is an operator given by:

$$H\{\bullet\} = (I - B_t)IFT\{B_f FT\{\bullet\}\} \tag{5.20}$$

In the previous expression, I is the identity matrix, B_t is a time mask with ones inside the interval $[-T, T]$ and zeros outside of this interval, $FT\{\bullet\}$ is

the Fourier transform of the function over which the operand H is applied, i.e., $g_{n-1}(t)$ in (5.19), $IFT\{\bullet\}$ is the inverse Fourier transform, and B_f is the filter in the frequency domain that indicates the band-limitation of the signal in this domain. Thus, the B_f is a mask with ones inside the interval $[-f_0, f_0]$ and zeros outside this interval, being f_0 the limit of the signal in the frequency domain.

The expression (5.19) may be developed for several number of iterations. To do this it must be taken into account that the operands H, $FT\{\bullet\}$, $IFT\{\bullet\}$, B_t and B_f are implemented by matrices multiplied by the functions over which they are applied. Thus, (5.19) can also be written as [30]:

$$g_n(t) = g(t) + Hg(t) + H^2 g(t) + \cdots + H^n g(t) \tag{5.21}$$

Hence, the signal extrapolated after n iterations can also be expressed as:

$$g_n(t) = E_n g(t) \tag{5.22}$$

where E_n is the so-called *extrapolation matrix* given by:

$$E_n = \sum_{k=0}^{n} H^k \tag{5.23}$$

As can be observed, from previous expression the extrapolation of the signal $g(t)$ just consists in computing the operator H by (5.20) and, then, determining the extrapolation matrix E_n by (5.23) for the desired number of iterations. Finally, the multiplication of this matrix by $g(t)$ (5.22) allows the extrapolation of this signal to be performed in a single matrix operation. In this procedure, however, the computation of the summation present in (5.23) implies a drawback since the operand power to all the iterations (H^k) must be determined. To avoid this summation, it must be pointed out that this summation is a geometric series. Thus, instead of performing the summation, the following expression may be used:

$$E_n = (I - H^{n+1})(I - H)^{-1} \tag{5.24}$$

where I is the identity matrix. As can be seen, by applying this other expression, the summation must not be applied and just H^{n+1} must be computed.

Moreover, the extrapolation matrix may be obtained, from (5.24), for an infinite number of iterations ($n = \infty$) as follows [30]:

$$E_\infty = (I - H)^{-1} \tag{5.25}$$

provided that the eigenvalues of H (λ_k) satisfy the following condition:

$$|\lambda_k| < 1, \qquad \text{for all } k \tag{5.26}$$

Therefore, the computation of the extrapolation matrix may be done for a specific number of iterations or even for an infinite number of iterations. In this last case, it is obtained the estimate at which the iterative algorithm tends, i.e., the solution with the minimum error energy.

Regarding the computation of the operator H, in [30], Sabri and Steenaart propose the computation of the operator by means of an intermediate low-pass matrix ($IFT\{B_f FT\{\bullet\}\}$). This matrix may be formed by using the Hilbert transform [116]-[118] or, in an easier way, by using the Discrete Fourier transform matrices [79]. This last formation is used in [30] and in [31] and is somewhat more practical than the application of the Hilbert transform. Thus, from now on, the operator H will be formed by Fourier transform matrices, i.e., by matrices with exponential functions suitably arranged.

Example In order to show the accuracy and advantages of the extrapolation matrix, a cosine signal in the time domain with a frequency of 0.4 Hz was used. The known segment was the interval [-0.5, 0.5] s, i.e., $T = 0.5$ s, and the filter was applied with a cut frequency (f_0) of 0.7 Hz. With these data, the filter B_f and the time mask B_t were formed. In addition, the operators $FT\{\bullet\}$ and $FT^{-1}\{\bullet\}$ were formed as matrices by means of exponential functions. Later, the operator H (5.20) was computed and, with this operator, the extrapolation matrix E_n (5.24) for several number of iterations. Furthermore, since the operator H satisfied the condition stated in (5.26), the extrapolation matrix was also computed for an infinite number of iterations (5.25).

Fig. 5.23 shows the result obtained by applying the computed extrapolation matrix to the known segment of the cosine signal. In Fig. 5.23(a) the estimated signals for 100, 10000, and an infinite number of iterations are shown and compared to the ideal signal. As can be observed, the higher the number of iterations is, the better the obtained signal is. In addition, the best approximation in the sense of the minimum error energy (for $n = \infty$) is determined which, by means of the iterative algorithm cannot be obtained in practice.

The consequence of obtaining a higher part of the signal in the time domain can be seen in Fig 5.23(b). In this figure the signal in the spectral domain is shown and, as can be observed, the higher the number of iterations is, the better the tones at -0.4 Hz and 0.4 Hz are distinguished.

The same extrapolation procedure was carried out but by applying the iterative Papoulis-Gerchberg algorithm. Fig. 5.24 shows the result for the same number of iterations as for the extrapolation matrix (apart from the infinite number of iterations). By comparing these results to the results of the extrapolation matrix is can be concluded that the same estimation is achieved by both algorithms.

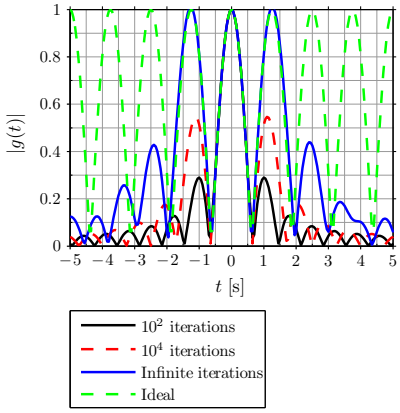

(a) Signal in the time domain.

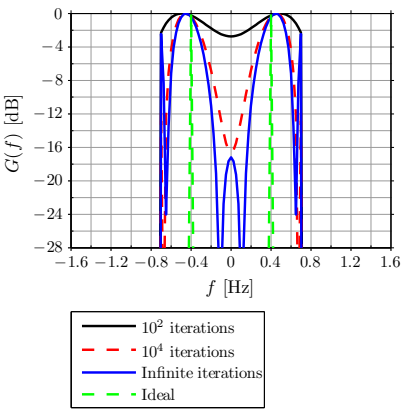

(b) Signal in the spectral domain.

Figure 5.23: Estimated signal from a segment in the time domain of a cosine signal with a frequency of 0.4 Hz by means of the extrapolation matrix.

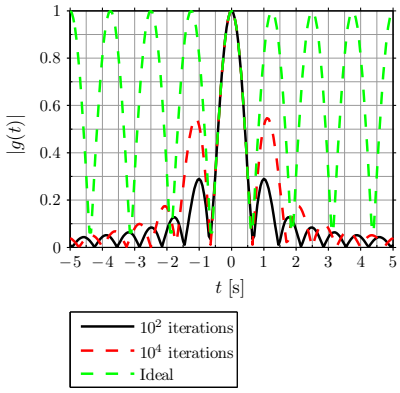

(a) Signal in the time domain.

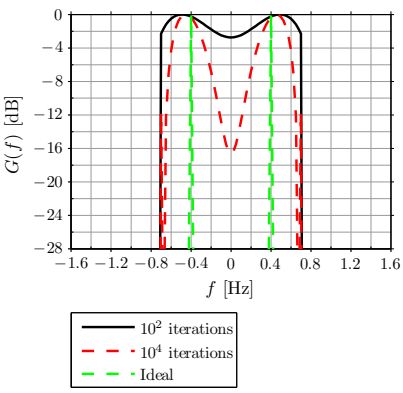

(b) Signal in the spectral domain.

Figure 5.24: Estimated signal from a segment in the time domain of a cosine signal with a frequency of 0.4 Hz by means of the iterative Papoulis-Gerchberg algorithm.

The most important advantage of the extrapolation matrix is its computation time. Fig. 5.25 shows a comparison of the computation times for the iterative algorithm and for the extrapolation matrix. As can be observed, whereas the computation time increases linearly with the number of iterations

for the iterative algorithm, the computation time of the extrapolation matrix keeps practically constant for any number of iterations. Thus, better approximations can be obtained without increasing the computation time. This is the main reason because next sections describe the extension of the extrapolation matrix to 2-D.

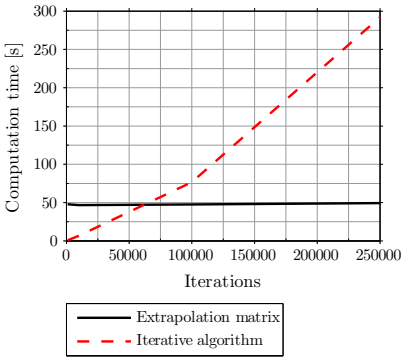

Figure 5.25: Comparison of computation times as a function of the number of iterations for the extrapolation matrix and the iterative algorithm.

5.4.2 2-D Extrapolation matrix: rows and columns

The extrapolation matrix for 2-D signals was proposed in [31] and, later, applied to the improvement of the resolution in the reconstruction of the equivalent currents in [119]. The formation of the extrapolation matrix is done by following the same procedure as in the 1-D case. In this case, however, the way in which the algorithm is applied is the inverse of the algorithm explained for the 1-D case, i.e., the signal is known in a segment of the spectral domain and the band-limitation is in the spatial domain. Thus, the extrapolation procedure estimates a signal $F(k_x, k_y)$ from a segment $G(k_x, k_y)$. For this thesis, this segment is the visible spectrum and, hence, may be expressed as:

$$G(k_x, k_y) = B_{k_x k_y} F(k_x, k_y) \tag{5.27}$$

where $B_{k_x k_y}$ is a mask function given by:

$$B_{k_x k_y} = \begin{cases} 1, & \sqrt{k_x^2 + k_y^2} \leq k \\ 0, & \sqrt{k_x^2 + k_y^2} > k \end{cases} \tag{5.28}$$

With this definition of the signal to extrapolate, the 2-D version of the iterative algorithm may be expressed in the following way:

$$G_n(k_x, k_y) = G(k_x, k_y) + HG_{n-1}(k_x, k_y) \tag{5.29}$$

where H is an operator given by:

$$H = (I - B_{k_x k_y})TF2D\{B_{xy}ITF2D\{\bullet\}\} \tag{5.30}$$

with I the identity matrix; $TF2D\{\bullet\}$ and $ITF2D\{\bullet\}$ the 2-D direct and inverse Fourier transforms, respectively; and B_{xy} a mask function with ones on the positions where the spatial signal may be non-zero and zeros on the positions where it is known a priori that the signal is zero.

In practice, the application of the previous operator is not as straightforward as in the 1-D case. The problem arises in the determination of the 2D Fourier transforms. The simplest form to compute these transforms is by forming two matrices which perform the transformation by 2 matrix multiplications, one on the right and the other one on the left. Thus, one of the matrices (TF_{col}) is multiplied on the left and performs the Fourier transform by columns, and the other matrix (TF_{row}) is multiplied on the right and performs the Fourier transform by rows. These matrices are formed as follows:

$$TF_{col} = \begin{bmatrix} 1 & 1 & 1 & \dots & 1 \\ 1 & W^1 & W^2 & \dots & W^{(N-1)} \\ 1 & W^2 & W^4 & \dots & W^{2(N-1)} \\ \vdots & \vdots & \vdots & \ddots & \vdots \\ 1 & W^{(N-1)} & W^{2(N-1)} & \dots & W^{(N-1)(N-1)} \end{bmatrix} \tag{5.31}$$

$$TF_{row} = \begin{bmatrix} 1 & 1 & 1 & \dots & 1 \\ 1 & Q^1 & Q^2 & \dots & Q^{(M-1)} \\ 1 & Q^2 & Q^4 & \dots & Q^{2(M-1)} \\ \vdots & \vdots & \vdots & \ddots & \vdots \\ 1 & Q^{(M-1)} & Q^{2(M-1)} & \dots & Q^{(M-1)(M-1)} \end{bmatrix} \tag{5.32}$$

where $W = e^{-j\pi/N}$ and $Q = e^{-j\pi/M}$, N is the number of rows of the matrix $G(k_x, k_y)$ and M the number of columns. In case of inverse transforms, W becomes $W = e^{j\pi/N}$ for ITF_{col} and Q becomes $Q = e^{j\pi/M}$ for ITF_{row}.

Therefore, the operator H cannot be applied as it is indicated in (5.30) since the operators $TF2D\{\bullet\}$ and $ITF2D\{\bullet\}$ must be divided into TF_{row} and TF_{col}. By doing so, the operator cannot be grouped at one side of the matrix to extrapolate as for the 1-D case to form a single extrapolation matrix. However,

if the situation is simplified, two different operators H may be formed. This simplification consist in considering just square regions in the spectral ($B_{k_x k_y}$) and the spatial (B_{xy}) domains. Thus, these regions can be split into two parts as follows:

$$B_{k_x k_y} = B_{k_x} B_{k_y} \tag{5.33a}$$

$$B_{xy} = B_x B_y \tag{5.33b}$$

where B_{k_x} and B_x are column vectors and B_{k_y} and B_y are row vectors. In general, these vectors are formed from the limits ($\pm a_{max}$) on each dimension as:

$$B_a = \begin{cases} 1, & |a| \leq a_{max} \\ 0, & |a| > a_{max} \end{cases} \tag{5.34}$$

The previous simplification allows the recursive procedure to be expressed in the following way:

$$G_n(k_x, k_y) = B_{k_x} F(k_x, k_y) B_{k_y} + H_{col} G_{n-1}(k_x, k_y) H_{row} \tag{5.35}$$

where the operators H_{col} and H_{row} are given by

$$H_{col} = (I - B_{k_y}) TF_{col}\{B_y ITF_{col}\{\bullet\}\} \tag{5.36a}$$

$$H_{row} = (I - B_{k_x}) TF_{row}\{B_x ITF_{row}\{\bullet\}\} \tag{5.36b}$$

The iterative expression (5.35) can be developed as for the 1-D case (5.21). The result can be grouped at both sides of the function $G_n(k_x, k_y)$ what leads to express the estimation at the n-th iteration as follows:

$$G_n(k_x, k_y) = E_n^{col} G(k_x, k_y) E_n^{row} \tag{5.37}$$

where E_n^{col} and E_n^{row} are the extrapolation matrices by rows and columns whose expressions are:

$$E_n^{col} = \sum_{k=0}^{n} H_{col}^k \tag{5.38a}$$

$$E_n^{row} = \sum_{k=0}^{n} H_{row}^k \tag{5.38b}$$

Similarly to the 1-D case, the previous geometric series can be faster computed by applying the following expressions:

$$E_n^{col} = (I - H_{col}^{k+1})(I - H_{col})^{-1} \tag{5.39a}$$

$$E_n^{row} = (I - H_{row}^{k+1})(I - H_{row})^{-1} \tag{5.39b}$$

The extrapolation matrices may also be computed for an infinite number of iterations ($n = \infty$) by:

$$E_\infty^{col} = (I - H_{col})^{-1} \tag{5.40a}$$

$$E_\infty^{row} = (I - H_{row})^{-1} \tag{5.40b}$$

As commented above, to be able to apply the previous extrapolation matrices the eigenvalues of H_{col} and H_{row} (λ_k) must satisfy the following condition:

$$|\lambda_k| < 1, \qquad \text{for all } k \tag{5.41}$$

These 2-D extrapolation matrices imply several drawbacks. Firstly, the known segment is limited to a square region. Thus, the extrapolation matrices cannot be applied over the entire visible spectrum, which is a circle od radius k. The known region must be limited to the maximum square region inside the visible region, as shown in Fig. 5.26, since, if a larger region were used, the zeros surrounding the visible region would be assumed as correct values. This fact would lead to a non-correct result. For this reason, the amount of information that can be used for this extrapolation is smaller than with the iterative algorithm since part of the known information must be ruled out.

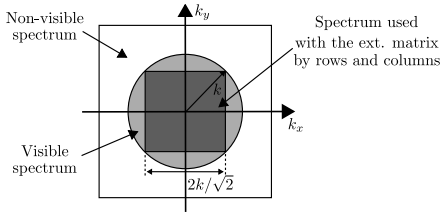

Figure 5.26: Region of the spectrum used by the 2-D extrapolation matrix by rows and columns.

Secondly, the spatial filter must be a square function. This fact limits the shape of the antennas that can be considered with this algorithm. In addition,

it does not allow complex shapes to be taken into account, such as for the X-band slot-array antenna studied above.

Finally, by looking at (5.37), it can be seen how the extrapolation is performed, first by rows and, later, by columns. This is an approximation since the extrapolation by rows does not take into account the result of the extrapolation by columns. Hence, the result is not exactly the same as with the iterative algorithm.

Nevertheless, it must be pointed out that the extrapolation matrices by rows and columns may be useful in many cases. Especially when the visible spectrum near the circle of radius k has a low level, in order to eliminate so little information as possible. In addition, for linear arrays, the technique is quite interesting since the fact of performing the extrapolation by rows and columns separately has a low effect in this kind of antennas.

The most important advantage of this procedure is its low computation time. No matter the number of iterations, the computation time does not grow since the same operations are done for any number of iterations. Hence, a high number of iterations may be applied to improve the estimated signal. Furthermore, if the condition (5.41) is satisfied, the result after an infinite number of iterations may be obtained.

Simulated results 1 The extrapolation matrix by rows and columns was first tested with the array formed by two $\hat{x}$-directed slots placed on the x axis and separated 0.8 λ (see Fig. 4.5). To do this test, a square filter in the spatial domain of 1.6 λ×1.6 λ was applied, i.e., the same filter as in Section 5.3 when the iterative Papoulis-Gerchberg algorithm was applied. The region of the spectrum that was considered, however, was not the entire visible spectrum, but the larger square region inside the circle of radius k (see Fig. 5.26). Thus, all the values of the plane wave spectrum considered in the extrapolation are correct.

With the previous data, the extrapolation matrices by rows and columns were formed (5.39) to estimate the spectrum with 5000 iterations. Fig. 5.27 shows the result of this extrapolation procedure. As can be observed, the non-visible spectrum determined by this technique (see Fig. 5.27(a)) is correct and even better than the result obtained by applying the iterative algorithm (shown in Fig. 5.4(a)). The reason for this behavior is the particular symmetry of this antenna, which makes this technique specially useful for this antenna.

The consequence of the greater region obtained with the extrapolation matrix by rows and columns is the quite good equivalent currents obtained from the estimated spectrum. As can be observed in Fig. 5.27(b), both elements are completely distinguished and correctly placed. This improvement can also be observed in Fig. 5.28, where the cross section of the obtained currents at

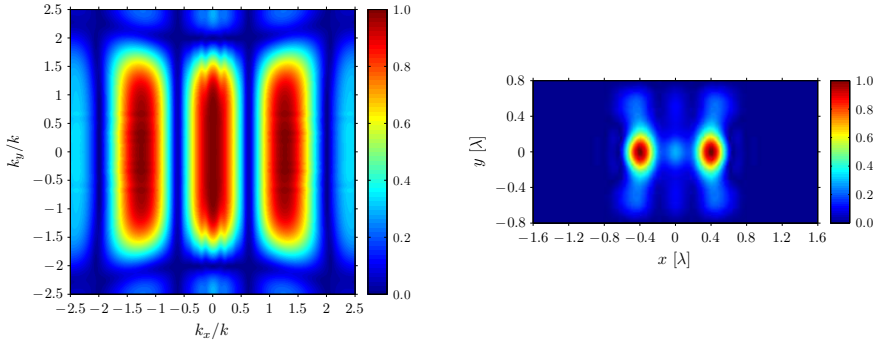

(a) Spectrum ($A_{Ey}(k_x, k_y)$). (b) Equivalent currents ($M_x(x, y)$).

Figure 5.27: Estimate of the non-visible spectrum with 5000 iterations, and its corresponding equivalent currents, by using the extrapolation matrix by rows and columns for the slot-array of 2 elements separated 0.8 λ.

$y = 0$ is compared to the cross section obtained with the iterative algorithm with 5000 iterations (also shown in Fig. 5.3(b)).

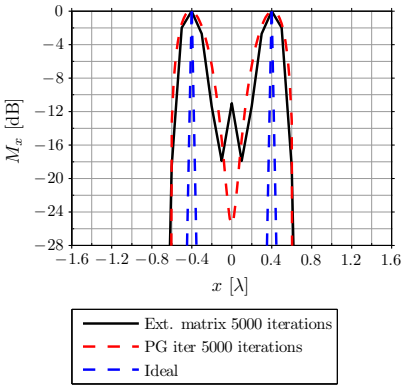

Figure 5.28: Cross section at $y = 0$ of the estimated equivalent currents with 5000 iterations by using the extrapolation matrix by rows and columns and the iterative algorithm for the slot-array of 2 elements separated 0.8 λ.

Nevertheless, the enhancement of resolution is not the main advantage of this technique. The most important improvement lies in the computation time. Whereas the iterative Papoulis-Gerchberg algorithm took 20 minutes to perform the estimation with 5000 iterations, the extrapolation by rows and

columns just took 35 seconds. Furthermore, in this last case, the number of iterations might have been enhanced without increasing the computation time.

Simulated results 2 The second test of the extrapolation matrix by rows and columns was done with the 5×5 slot-array antenna depicted in Fig. 5.5. The spatial filter was a 2 λ×2 λ square mask and, the region of the spectrum that was considered was, as explained above, the larger square inside the circle of radius k as shown in Fig. 5.26.

The extrapolation matrices by rows and columns (5.39) were computed for 5000 iterations. Fig. 5.29(a) shows the estimated spectrum and, as can be observed, similar results to the application of the iterative algorithm are obtained (see Fig. 5.7(a)). Thus, as in the iterative algorithm, the corresponding equivalent currents are correct but without the enough resolution so that all the slots are clearly distinguished (see Fig. 5.29(b)).

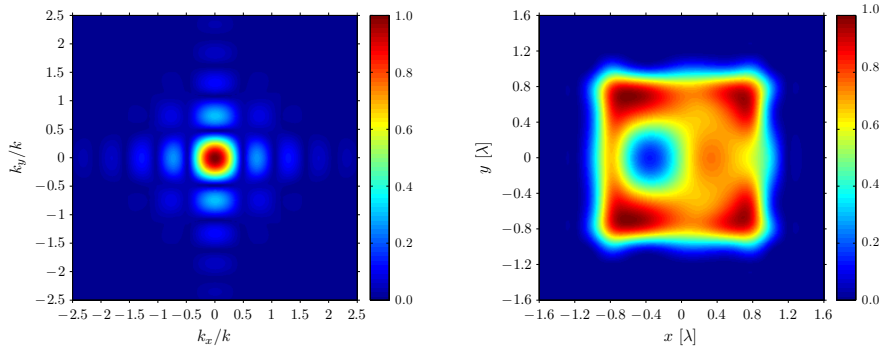

(a) Spectrum ($A_{Ey}(k_x, k_y)$). (b) Equivalent Currents ($M_x(x, y)$).

Figure 5.29: Estimate of the non-visible spectrum with 5000 iterations, and its corresponding equivalent currents, by using the extrapolation matrix by rows and columns for the slot-array of 25 elements separated 0.4 λ with one element not fed.

Of course, as in the previous example, the main advantage of the extrapolation matrix is the computation time (around 35 second) compared to the computation time of the iterative algorithm (around 25 minutes for 5000 iterations). Taking advantage of this situation, the extrapolation matrices were also computed for 1 million of iterations with the purpose of improving the resolution. As a result, the estimated spectrum was the one shown in Fig. 5.30(a). As can be observed, the obtained spectrum is far from the ideal and, hence, the extrapolation matrix by rows and columns does not work for any number

of iterations for this antenna. Of course, the corresponding equivalent currents (shown in Fig. 5.30(b)) are neither correct.

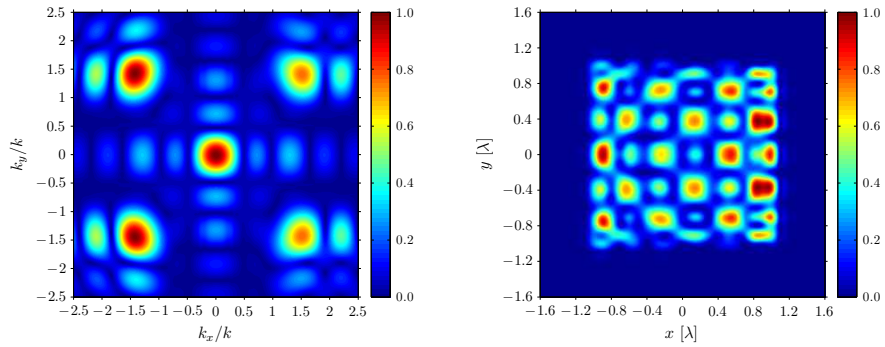

(a) Spectrum ($A_{Ey}(k_x, k_y)$). (b) Equivalent Currents ($M_x(x, y)$).

Figure 5.30: Estimate of the non-visible spectrum with 10^6 iterations, and its corresponding equivalent currents, by using the extrapolation matrix by rows and columns for the slot-array of 25 elements separated 0.4 λ with one element not fed.

The reason for the previous behavior lies in the restriction of the known spectrum to just a square region smaller than the visible spectrum and the application of, first, the extrapolation by rows and, then, the extrapolation by columns. These limitations lead to singularities on the corners of this square region, which produce non-correct currents. In addition, for this specific case, the singularities arise at 1 million of iterations but, in other cases, singularities might arise at lower iterations (if the singularities appear at a certain number of iterations, they also appear at a higher number of iterations). For this reason, a new extrapolation matrix is required so that, no matter the number of iterations, the singularities do not arise and, hence, the best approximation in the way of the minimum error energy may be achieved for any situation.

Practical results The extrapolation matrix by rows and columns was also applied to a real antenna. Specifically, this antenna was the X-band slot-array antenna shown in Fig. 3.9. Fig. 5.31(a) shows the estimated spectrum with 1000 iterations and Fig. 5.31(b) the obtained equivalent currents. As can be observed in these figures, the singularities detected in the above example of the 5×5 slot-array antenna also arise in this case. In addition, this behavior takes place at a low number of iterations (just 1000 iterations) so that no improvement in resolution can be obtained for this antenna with this technique.

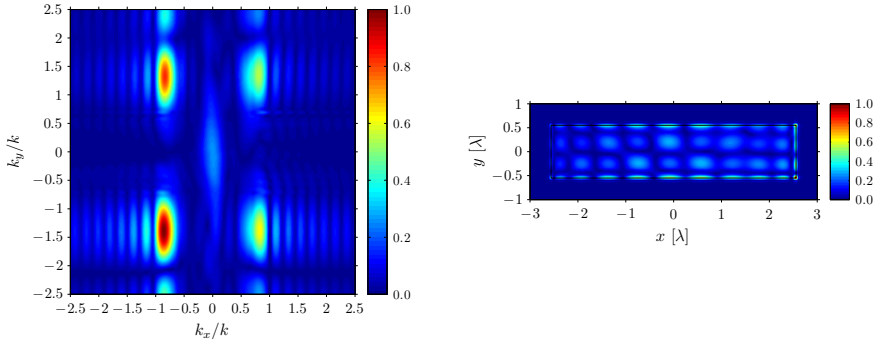

(a) Spectrum ($A_{Ey}(k_x, k_y)$).

(b) Equivalent currents ($M_x(x, y)$).

Figure 5.31: Estimate of the non-visible spectrum with 1000 iterations, and its corresponding equivalent currents, by using the extrapolation matrix by rows and columns for the slot-array of 7 elements.

Furthermore, it must be pointed out that the applied spatial filter was a $5.12\lambda \times 1.1\lambda$ mask. This is the only possibility with this technique since, as commented above, just rectangular filters are allowed with this technique. Thus, no more options exist for this technique applied to the X-band slot-array antenna.

5.4.3 2-D Generalized extrapolation matrix

The previous extension to 2-D of the extrapolation matrix entails serious drawbacks as commented above. To overcome these drawbacks an exact generalization to 2-D signals of the extrapolation matrix was proposed in [32]. The aim of this generalization is to perform the estimation by rows and columns at the same time and, hence, consider the extrapolation as a whole procedure. In addition, the purpose of the generalized extrapolation matrix is to be able to apply any spectral and spatial masks. Thus, the known part of the spectrum may be a circular region, as the visible spectrum, and the filter may be any kind of filter so that this can fit exactly the radiating regions of the antenna.

To determine the generalized extrapolation matrix, the main problem of the above procedure must be taken up again. This problem arises on the division of the operator H into two parts. Thus, the extrapolation matrix is divided into two parts and the spectral and spatial masks limited to just squares. In order to overcome this problem, the aim is to leave all the operands inside the operator H on one side of the signal to extrapolate ($G(k_x, k_y)$).

The first step consists in setting the matrix to extrapolate $G(k_x, k_y)$ in vectorial form. This may be done, for instance, by applying the command $(G(:))$ in MATLAB. In this case, if the matrix $G(k_x, k_y)$ is the given by:

$$G(k_x, k_y) = \begin{bmatrix} G(k_{x1}, k_{y1}) & G(k_{x1}, k_{y2}) & \dots & G(k_{x1}, k_{yM}) \\ G(k_{x2}, k_{y1}) & G(k_{x2}, k_{y2}) & \dots & G(k_{x2}, k_{yM}) \\ \vdots & \vdots & \ddots & \vdots \\ G(k_{xN}, k_{y1}) & G(k_{xN}, k_{y2}) & \dots & G(k_{xN}, k_{yM}) \end{bmatrix}, \tag{5.42}$$

the rearrange $G(:)$ sets the matrix as follows:

$$G(:) = \begin{bmatrix} G(k_{x1}, k_{y1}) \\ G(k_{x2}, k_{y1}) \\ \vdots \\ G(k_{xN}, k_{y1}) \\ G(k_{x1}, k_{y2}) \\ G(k_{x2}, k_{y2}) \\ \vdots \\ G(k_{xN}, k_{y2}) \\ \vdots \\ G(k_{xN}, k_{yM}) \end{bmatrix} \tag{5.43}$$

The second step builds four matrices which, multiplied by $G(:)$ on the left, perform the direct or inverse Fourier transform by rows or columns. The aim is to obtain, for instance, the same result as multiplying TF_{col} (5.31) by $G(k_x, k_y)$ (5.42) on the left, but multiplying the new matrix, noted as A_{col}, on the left of $G(:)$ (5.43). To do this, the new matrix, from (5.31), must be arranged as:

$$A_{col} = \begin{bmatrix} TF_{col} & 0 & \dots & 0 \\ 0 & TF_{col} & \dots & 0 \\ \vdots & \vdots & \ddots & \vdots \\ 0 & 0 & \dots & TF_{col} \end{bmatrix}, \tag{5.44}$$

where TF_{col} is the block matrix depicted in (5.31) and 0 is a block matrix of zeros of the same size as the matrix TF_{col}. The matrix A_{col} is a square matrix so that, the number of blocks in the diagonal is M, i.e., the number of columns of $G(k_x, k_y)$. Thus, the size of the matrix A_{col} is $NM \times NM$.

Similarly, a new matrix A_{row} must be formed to compute the Fourier transform by rows by multiplying this matrix by the vector $G(:)$ (5.43) on the left. The formation of A_{row} must be done in such a way that the multiplication

$A_{row}G(:)$ led to the same result as multiplying the matrix TF_{row} (5.32) by $G(k_x, k_y)$ (5.42) on the right. Thus, the matrix A_{row} must be formed as follows:

$$A_{row} = \begin{bmatrix} I & I & \dots & I \\ I & I * Q^1 & \dots & I * Q^{(M-1)} \\ \vdots & \vdots & \ddots & \vdots \\ I & I * Q^{(M-1)} & \dots & I * Q^{(M-1)(M-1)} \end{bmatrix}, \tag{5.45}$$

where I is the identity matrix of size $N \times N$ and $Q = e^{-j\pi/M}$. The number of blocks is $M \times M$ and, hence, the size of the matrix A_{row} is $NM \times NM$.

The inverse transforms IA_{col} and IA_{row} are formed in a similar way but changing the value of W and Q to: $W = e^{j\pi/N}$ and $Q = e^{j\pi/M}$.

By using the previous matrices, the following relation is satisfied:

$$TF_{col}G(k_x, k_y)TF_{row} = A_{col}A_{row}G(:) \tag{5.46}$$

The difference lies in the organization of the resulting matrix. In the case of the left side of previous expression, the result is a 2-D matrix, whereas in the case of the right side the result is organized as a column vector. However, since the organization is known, a reorganization of the second case allows the matrix to be organized in 2-D, as in the left side.

Before obtaining the operator H with the new organization, the rearrange of the spectral mask $B_{k_x k_y}$ and the spatial filter B_{xy} must be also carried out. At first, these operands are matrices, however, in the case of the extrapolation matrix by rows and columns explained above, these operands are simplified to just vectors (5.33) which, when are applied together, form a square mask or filter.

To overcome the previous limitation, a rearrange of the matrices $B_{k_x k_y}$ and B_{xy} must be done. With this purpose, it must be considered the mask $B_{k_x k_y}$ and the filter B_{xy} as matrices which, multiplied element-by-element by the matrix over which they are applied, offer the desired result. Thus, these matrices may be rearranged as vectors, like the matrix $G(k_x, k_y)$ in (5.43). Once this reorganization is performed, the resulting vector is placed on the diagonal of a $NM \times NM$ matrix of zeros. The new matrices are noted as $B2D_{k_x k_y}$ and $B2D_{xy}$.

By doing the previous modifications, the multiplication of the resulting matrices by a column vector, e.g. $G(:)$, leads to the same result as multiplying element-by-element $B_{k_x k_y}$ and B_{xy} by a 2-D matrix, e.g. $G(k_x, k_y)$.

Using all the described matrices, the recursive algorithm described in (5.29) may be rewritten as follows:

$$G_n(:) = G(:) + H^{2D}G_{n-1}(:) \tag{5.47}$$

where the operator H^{2D} is formed in the following way:

$$H^{2D} = (I - B2D_{k_x k_y})A_{col}A_{row}B2D_{xy}IA_{col}IA_{row} \tag{5.48}$$

As can be observed, now the operator is on just one side of the matrix that must be extrapolated and, hence, the same procedure carried out for the 1-D case can be performed to form a unique extrapolation matrix. Thus, the estimated signal after n iterations may be computed as follows:

$$G_n(:) = E_n^{2D}G(:) \tag{5.49}$$

where E_n^{2D} is the *2-D generalized extrapolation matrix*. This matrix may be computed as a geometric summation of the operator H^{2D} or, as deduced above, in the following easier way:

$$E_n^{2D} = (I - (H^{2D})^{k+1})(I - H^{2D})^{-1} \tag{5.50}$$

Furthermore, as in previous sections, the extrapolation matrix may be determined for an infinite number of iterations as follows:

$$E_\infty^{2D} = (I - H^{2D})^{-1} \tag{5.51}$$

provided that the absolute value of the eigenvalues of H^{2D} (λ_k) are all below 1.

The 2-D generalized extrapolation matrix (E_n^{2D}) has several advantages and drawbacks. Regarding the advantages, it can be seen how this new matrix overcome all the drawbacks of the extrapolation matrix by rows and columns. Thus, the extrapolation is performed by rows and columns at the same time, the spectral mask can adopt any shape, i.e., a circle like the visible spectrum, and the spatial filter can also be any kind of filter so that the shape of the filter can fit the radiating parts of the antenna.

The main drawback of the matrix E_n^{2D} is the computation of the inverse of the matrix $(I - H^{2D})$. This matrix may be ill-conditioned and, hence, the computation of the inverse may become a hard problem. To overcome the ill-conditioning, the Tikhonov regularization technique [74],[75] may be used. In this case, it must be taken into account that the election of the regularization parameter is a hard task [76] and, hence, special care must be taken on its election to obtain accurate results (see Section 5.5.1 for more details).

Moreover, a preconditioner [120] might be applied and inverse may be computed by using the *Singular Value Decomposition* (SVD) method considering the most significant singular values [71] or the *Generalized Minimal Residual* (GMRES) method [72],[73].

Apart from the previous ill-conditioning, a higher problem may arise when dealing with the matrix E_n^{2D}. This matrix is an $NM \times NM$ matrix and, hence,

may become a quite big matrix if the original matrix $G(k_x, k_y)$, whose size is $N \times M$, is large. The problem arises when the matrix E_n^{2D} does not fit in memory. In those cases the aforementioned techniques (preconditioning, SVD and GMRES) cannot be used as they are normally described since they require the whole matrix in memory at the same time to perform the inverse. Thus, other techniques must be applied.

These other techniques must perform the inverse with, at least, part of the matrix in the hard disk, i.e., with the matrix divided in blocks and saved in the hard disk. The inverse of matrices divided in blocks may be done, for instance, by the *SVD-block* algorithm [121] or by using the *QR* decomposition in blocks [122].

However, a faster algorithm has been recently proposed in [123] and improved in [124]. This algorithm computes the inverse of a matrix by the *incomplete LU* (ILU) decomposition by blocks with preconditioning. The results regarding computation time and accuracy are quite good. For this thesis, this algorithm is used to compute $(I - H^{2D})^{-1}$.

Simulated results 1 Firstly, the proposed generalized extrapolation matrix was applied to the slot-array antenna formed by two $\hat{x}$-directed slots placed on the x axis and separated 0.8 λ (see Fig. 4.5). To do this, as in previous examples, a square filter of 1.6 λ×1.6 λ and centered at the origin was applied. With this filter, the matrix $B2D_{xy}$ was built.

The region considered for the extrapolation was the entire visible spectrum. By considering the number of computed samples for this spectrum with the microwave holographic technique and the wavenumber k (since the frequency is 300 MHz, $\lambda = 1$ and, hence, $k = 2\pi$), a spectral mask was formed. This mask had 1's inside the visible region and 0's outside. Later, by using this mask, the matrix $B2D_{k_x k_y}$ was built.

Then, the matrices A_{col}, A_{row}, IA_{col} and IA_{row} were formed according to (5.44) and (5.45). The resulting matrices fit in memory, however, in order to develop a general algorithm for any kind of antenna, these matrices (as well as $B2D_{xy}$ and $B2D_{k_x k_y}$) were divided into blocks. By using these blocks, the operator H^{2D} was computed with (5.48).

Finally, the generalized extrapolation matrix E_n^{2D} was obtained (5.50) with the previous operator H^{2D}. Nevertheless, it must be pointed out that, during the computation of E_n^{2D} it was observed that the denominator $(I - H^{2D})^{-1}$ did not include any singularity. This denominator is, actually, the extrapolation matrix E_n^{2D} for $n = \infty$, i.e., E_∞^{2D} (5.51). In addition, it was observed that the resulting equivalent currents were quite accurate by just considering this extrapolation matrix. For these reasons, the considered extrapolation matrix was the matrix E_∞^{2D} and it was supposed that all the eigenvalues of H^{2D} were below 1. Thus, several operations were avoided, the result was faster ob-

tained and, in addition, with a specific accuracy than with a certain number of iterations.

By using the resulting extrapolation matrix E_{∞}^{2D}, the non-visible spectrum was estimated by (5.49) (the resulting spectrum was organized in a vector form but a rearrangement was applied to leave the spectrum in matrix form). Fig. 5.32 shows the result of both, spectrum and corresponding currents. By looking at the spectrum (see Fig. 5.32(a)) it can be seen how the generalized extrapolation matrix obtains a quite big region of the non-visible spectrum. As a result, the equivalent currents (see Fig. 5.32(b)) are accurately determined since both elements are clearly distinguished and correctly placed. This can also be observed in the comparison shown in Fig. 5.33. Comparing these figures with the result of the extrapolation matrix by rows and columns (see Fig. 5.27 and Fig. 5.28) it can be observed that similar results are obtained. However, the advantage of this new matrix is the possibility of employing different kinds of spatial filters.

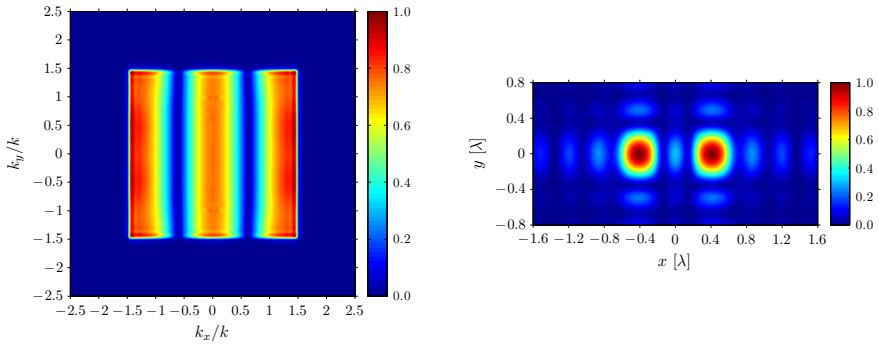

(a) Spectrum ($A_{Ey}(k_x, k_y)$).

(b) Equivalent currents ($M_x(x, y)$).

Figure 5.32: Estimate of the non-visible spectrum with infinite iterations, and its corresponding equivalent currents, by using the generalized extrapolation matrix for the slot-array of 2 elements separated 0.8 λ.

Regarding the computation time, the generalized extrapolation matrix took a longer time than the matrix by rows and columns to be computed and applied. The division into blocks slowed down the process because of the several accesses to the hard disk. Nevertheless, it must be also pointed out that, if a resolution of around 0.4 λ is required, the difference in computation time may be small. For this resolution, the computation time for the generalized extrapolation matrix was of just 2 minutes, whereas, as commented above, the extrapolation matrix by rows and columns took 35 seconds to be computed and applied.

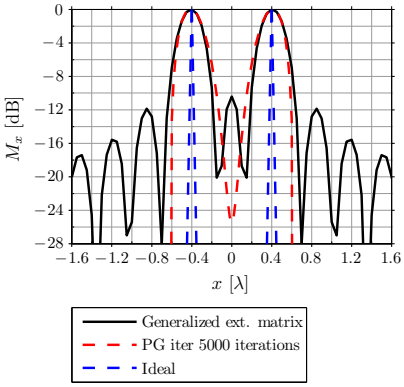

Figure 5.33: Cross section at $y = 0$ of the estimated equivalent currents by using the generalized extrapolation matrix and the iterative algorithm with 5000 iterations for the slot-array of 2 elements separated 0.8 λ.

Simulated results 2 The generalized extrapolation matrix was also tested with the 5×5 slot-array antenna depicted in Fig. 5.5. In this case, the spatial filter was a 2 λ×2 λ square filter and the region of the spectrum considered for the extrapolation was the entire visible spectrum. With these data, the matrices $B2D_{xy}$ and $B2D_{xy}$, as well as A_{col}, A_{row}, IA_{col} and IA_{row} were formed and divided into blocks. Then, the operator H^{2D} was computed by (5.48) by blocks and, finally, the extrapolation matrix E_{∞}^{2D} (5.51) was determined (similar conclusions to those of previous example were reached for the actual example).

The resulting generalized extrapolation matrix was applied to the visible spectrum and, as a result, the plane wave spectrum shown in Fig. 5.34(a) was estimated. In this case, part of the information present in the non-visible spectrum is recovered with this extrapolation so that the equivalent currents (see Fig. 5.34(b)) allows the not fed element to be identified.

In order to distinguish better the different elements of the antenna, the spectral periodicity property, explained in Section 5.3.1., was applied. The resulting plane wave spectrum and the equivalent currents are shown in Fig. 5.35(a) and Fig. 5.35(b), respectively. As can be observed, the slots that is not fed is clearly distinguished due to the non-visible part of the plane wave spectrum estimated with the spectral periodicity and the extrapolation matrix. The rest of the elements have almost the same amplitude, as they were simulated.

The computation time was the same as the one of the previous example. The same region of the non-visible spectrum with the same precision was considered

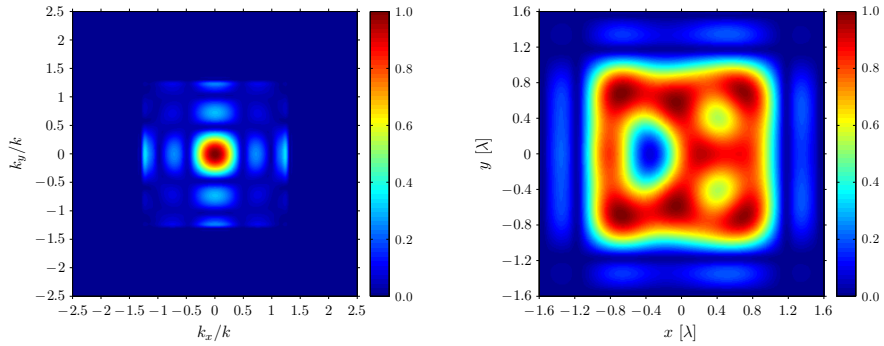

(a) Spectrum ($A_{Ey}(k_x, k_y)$). (b) Equivalent currents ($M_x(x, y)$).

Figure 5.34: Estimate of the non-visible spectrum with infinite iterations, and its corresponding equivalent currents, by using the generalized extrapolation matrix with a wide filter for the 5×5 slot-array antenna with one element not fed.

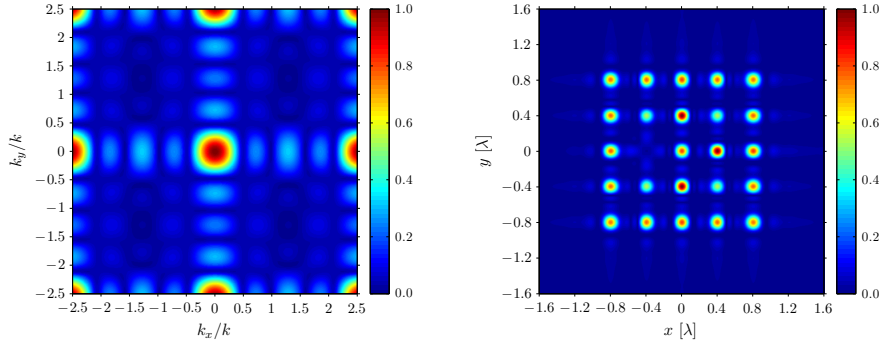

(a) Spectrum ($A_{Ey}(k_x, k_y)$). (b) Equivalent currents ($M_x(x, y)$).

Figure 5.35: Estimate of the non-visible spectrum with infinite iterations, and its corresponding equivalent currents, by using the generalized extrapolation matrix with a wide filter and replying the spectrum for the 5×5 slot-array antenna with one element not fed.

and determined and, hence, the same computation time was required, i.e., around 2 minutes.

Practical results Finally, a real antenna, with a real measurement, was used to test the generalized extrapolation matrix. This antenna was the X-band

slot-array antenna shown in Fig. 3.9. By using this measurement, the visible spectrum was computed with the microwave holographic technique. Later, the same procedure described above was performed to estimate the non-visible spectrum. The spectral mask was a circle of radius k (the visible region) and the spatial filter was a 5.12 $\lambda \times$ 1.1 λ mask (a filter including all the radiating elements).

The resulting matrix E_{∞}^{2D} (again, the computation of the matrix at a specific number of iterations was not done) was applied to the visible spectrum of the antenna. Fig. 5.36 shows the estimated spectrum and the corresponding currents. As can be observed, better results than with the extrapolation matrix by rows and columns under the same conditions (see Fig. 5.31) are obtained. Now, no singularities arise on the corners of the spectral mask (see Fig. 5.36(a)) and, hence, the resulting equivalent currents (see Fig. 5.36(b)) do not have any singularity. In addition, the obtained currents are more accurate than the equivalent currents determined from just the visible spectrum (see Fig. 5.8(a)).

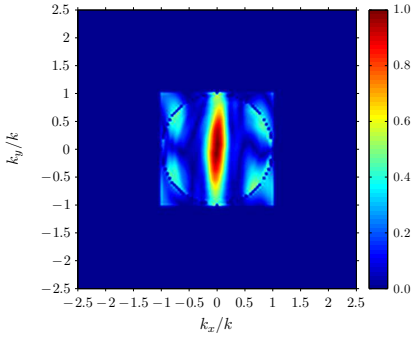

(a) Spectrum ($A_{Ey}(k_x, k_y)$).

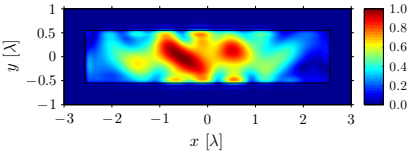

(b) Equivalent currents ($M_x(x, y)$).

Figure 5.36: Estimate of the non-visible spectrum with infinite iterations, and its corresponding equivalent currents, by using the generalized extrapolation matrix with a wide filter for the X-band slot-array antenna of 7 elements.

Furthermore, by using the generalized extrapolation matrix, a more restrictive spatial filter may be used. This advantage was used to apply a filter like the one depicted in Fig. 5.18 (i.e., a filter with 1's on the positions of the slots and 0's outside). The result that was obtained is shown in Fig. 5.37. As can be observed, in this case the currents are confined on the positions of the slots (see Fig. 5.37(b)). Nevertheless, by looking at the exact amplitude of the currents on the positions of the slots shown in Fig. 5.38, it can be seen how the obtained currents are far from the ideal currents. Hence, the algorithm does not work as it was expected for this situation, what makes necessary to adopt a solution.

Next section explains a solution consisting in the application of another direct extrapolation technique, the prior discrete Fourier transform.

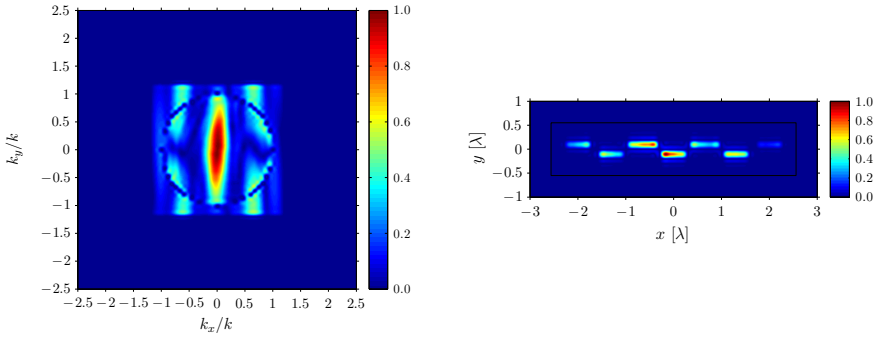

(a) Spectrum ($A_{Ey}(k_x, k_y)$). (b) Equivalent currents ($M_x(x, y)$).

Figure 5.37: Estimate of the non-visible spectrum with infinite iterations, and its corresponding equivalent currents, by using the generalized extrapolation matrix with a restrictive filter for X-band the slot-array antenna of 7 elements.

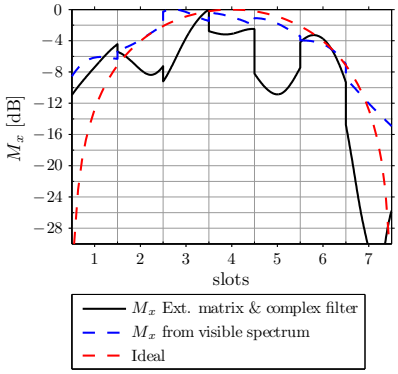

Figure 5.38: Equivalent magnetic currents on the positions of the slots for the X-band slot-array antenna formed by 7 slots by applying the generalized extrapolation matrix.

Regarding the computation time, similar conclusions to those of previous examples may be reached. In this case, to avoid large computation times, a small resolution was adopted as the aim of the technique. If a high resolution is required, the matrix formed for the extrapolation takes a few GBytes of memory and, hence, the computation time grows exponentially.

5.5 Prior discrete Fourier transform

Previous sections have dealt with the Papoulis-Gerchberg algorithm in its iterative and direct versions. The criterion used by this technique to extrapolate a signal from a known segment is to find out the estimation with the minimum error energy. As commented above, other techniques have different criterions and apply other procedures. Among these techniques, an important algorithm is the so-called *Prior discrete Fourier transform* (PDFT).

PDFT was proposed for 1-D signals in [125] and for 2-D signals in [36], and extended to the reconstruction of the equivalent current in [96]. This technique, basically, consists in applying a *prior function* $p(r)$ (containing information about the shape and expected behavior of the antenna) to the extrapolation. By doing so, the technique obtains a *Minimum-weighted-norm* (MWN) estimate, where the squared weighted norm of a function $h(r)$ is defined as [126]:

$$\|h(r)\|^2 = \int |h(r)|^2/p(r)\mathrm{d}r \tag{5.52}$$

The main advantage of the PDFT is the way in which the estimation is directly performed, without iterations. As in previous section, this is an important characteristic since it avoids the use of long iterative algorithms. In addition, it is worth to mention that, as stated in [127], if the prior function just contains the support information of the function to extrapolate, the PDFT estimate has the functional values to which the iterative Papoulis-Gerchberg algorithm converges.

The inverse 2D PDFT technique estimates a signal $F(k_x, k_y)$ from a segment $G(k_x, k_y)$ by applying prior information in the transformed domain (spatial domain in this case). This prior information is expressed by means of a function $p(x, y)$ and can include any information about the spatial signal (the currents for this thesis). If this prior information $p(x, y)$ is just a square mask, the PDFT technique is known as *Modified discrete Fourier transform* (MDFT) [125],[36]. However, this is a particular case and, in general, the function may be any mask, e.g. several separated spots with, even, different amplitudes. In this case, the technique is known as PDFT.

In order to determine the PDFT estimate, first, the expression of the inverse Fourier transform of the signal $G(k_x, k_y)$ after the filtering by the function $p(x, y)$ must be expressed. This transformation is given by:

$$g(x,y)_{filt} = p(x,y) \sum_{m=-\infty}^{\infty} \sum_{n=-\infty}^{\infty} G(m\Delta k_x, n\Delta k_y) e^{jxm\Delta k_x} e^{jyn\Delta k_y} \tag{5.53}$$

where Δk_x and Δk_y are the separation between consecutive points in the k_x and k_y axes, respectively.

The application of the Fourier transform over the signal $g(x,y)_{filt}$ does not lead to the original function $G(k_x,k_y)$. To avoid this difference, the PDFT estimate is introduced. This estimate is obtained as follows:

$$PDFT = p(x,y) \sum_{m=-\infty}^{\infty} \sum_{n=-\infty}^{\infty} \alpha(m,n) e^{jxm\Delta} e^{jyn\Delta} \tag{5.54}$$

where $\alpha(m,n)$ is an intermediate function. To obtain this function it is imposed that the Fourier transform of the PDFT estimate (5.54) must be the known signal $G(k_x,k_y)$. Thus, it can be deduced that the function $\alpha(m,n)$ must be determined by solving the following equation system:

$$G(m\Delta k_x, n\Delta k_y) = \sum_{m=-\infty}^{\infty} \sum_{n=-\infty}^{\infty} \alpha(m,n) P(m\Delta k_x, n\Delta k_y) \tag{5.55}$$

where $P(k_x,k_y)$ is the Fourier transform of the prior function $p(x,y)$.

Therefore, in order to estimate the non-visible spectrum from the visible spectrum, first, the intermediate signal $\alpha(m,n)$ must be determined by (5.55) (Section 5.5.1 deals with the way in which this system may be solved). Then, the PDFT estimate is obtained with (5.54). This estimate is directly the spatial signal and, hence, the equivalent currents with the improved resolution. The Fourier transform of this PDFT estimate is the extrapolated plane wave spectrum. Thus, the goal of the PDFT consists, directly, in improving the resolution of the spatial signal, rather than extrapolate the visible spectrum (what is achieved because of the improvement in spatial resolution).

5.5.1 Regularization

The solution of the equation system (5.55) may become a hard task since, first, the system is quite big so that it must be divided into blocks and, then, the condition number may be high. The first problem may be overcome by using the *incomplete LU* (ILU) decomposition by blocks with preconditioning [123],[124]. The preconditioning helps to improve the condition number of the matrix, however, it may not be enough for the matrix dealt with in the PDFT technique. In these cases the Tikhonov regularization technique (TRT) [74] may be applied [126].

The TRT is used to reduce the sensitivity to noise without losing resolution. Mathematically, this reduction is done by decreasing the condition number of the equation system. To do this, the following general equation system is considered:

$$Ax = b \tag{5.56}$$

By using TRT, the solution of this equation system considering linear least squares is given by [74]:

$$x = (A^T A + \mu M)^{-1} A^T b \tag{5.57}$$

where A^T is the complex conjugate transpose of the matrix A, M is a non-negative semidefinite matrix and μ is the *regularization parameter* which controls the weight of the penalty term in the technique [74].

The election of μ and M determines the accuracy of the solution. In literature, e.g. [74], the matrix M is normally the identity matrix, though some variations are also studied [74]. The election of the parameter μ is rather more difficult. The smaller the parameter is, the higher the condition number is. There are a few techniques to determine this parameter [75], [76], e.g. the *L-curve* [128] or the generalized cross validation (GCV) [129]. For the next examples, the parameter μ has been chosen in the way of the L-curve, so that the election has been a tradeoff between the filtering and the noise in the equivalent currents. As a result, the value used in the examples shown in next sections is 0.1.

Simulated results 1 The PDFT was first tested with the slot-array antenna formed by two $\hat{x}$-directed slots placed on the x axis and separated 0.8 λ, depicted in Fig. 4.5. The spatial filter ($p(x, y)$) was a square of 1.6 λ×1.6 λ centered at the origin, and the region used to perform the extrapolation was the entire visible spectrum.

By using the previous data, firstly the 2D Fourier transform of $p(x, y)$ was done. As a result, the matrix $P(k_x, k_y)$ was obtained on the discrete points $k_x = n\Delta k_x$ and $k_y = n\Delta k_y$. Then, this matrix was rearranged in a column vector, as well as the known spectrum $G(k_x, k_y)$. These two vectors were used to obtain the intermediate function $\alpha(m, n)$ by solving the equation system (5.55) by blocks [123],[124] and with TRT ($\mu = 0.1$).

Later, the obtained function $\alpha(m, n)$ was used to compute the PDFT by means of (5.54). The resulting estimated function can be observed in Fig. 5.39. By looking at Fig. 5.39(a) it can be seen how the estimated non-visible spectrum by PDFT is quite accurate. Proof of this accuracy can be seen in Fig. 5.39(b), where the corresponding equivalent currents are shown. Here, it can be observed how the slots are distinguished and with the correct amplitude. Similar conclusions may be adopted by observing Fig. 5.40, where the cross section of the currents obtained with PDFT and with the iterative algorithm are compared. Nevertheless, it must be pointed out that, in this specific case, the result is not as good as the result obtained with the iterative algorithm or with the above extrapolation matrices.

The computation time, however, is higher than with the previous matrix methods. Whereas, these matrix methods took around 1∼2 minutes to be

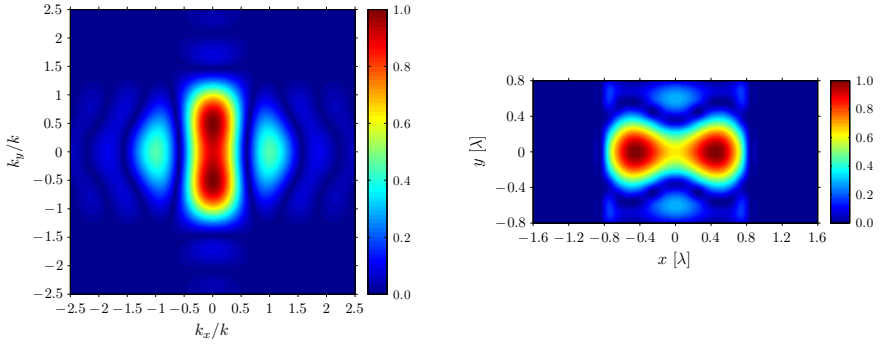

(a) Spectrum ($A_{Ey}(k_x, k_y)$). (b) Equivalent currents ($M_x(x, y)$).

Figure 5.39: Estimate of the non-visible spectrum with infinite iterations, and its corresponding equivalent currents, by using PDFT for the slot-array of 2 elements separated 0.8 λ.

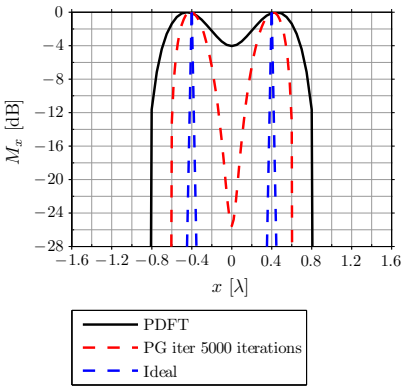

Figure 5.40: Cross section at $y = 0$ of the estimated equivalent currents by using PDFT and the iterative algorithm with 5000 iterations for the slot-array of 2 elements separated 0.8 λ.

computed, the PDFT took more than 7 minutes. In addition, the obtained currents are not as good as the currents obtained with the previous matrix methods (compare Fig. 5.27(b) to Fig. 5.39(b)).

Nevertheless, the obtained currents with PDFT are similar to those obtained with just the Papoulis-Gerchberg algorithm (see Fig. 5.4(b)). Moreover, the computation time of PDFT (7 minutes) is lower than the computation time of the iterative algorithm (20 minutes). Hence, for this specific case, PDFT

obtains better results than the iterative algorithm, but worse results than the matrix methods.

Simulated results 2 The second case in which the PDFT was tested was with the 5×5 slot-array antenna shown in Fig. 5.5. The spatial filter was a 2 λ × 2 λ square filter and the region of the spectrum considered for the extrapolation was the entire visible spectrum. With these data, the procedure followed to obtain the PDFT estimation was the same as described above for the slot-array of 2 elements. The result is shown in Fig. 5.41.

As can be observed in Fig. 5.41(a), the PDFT technique determines part of the non-visible spectrum. However, the estimate of the equivalent currents, shown in Fig. 5.41(b), does not allow the elements of the antenna to be clearly distinguished. To improve this estimate, another spatial filter was applied.

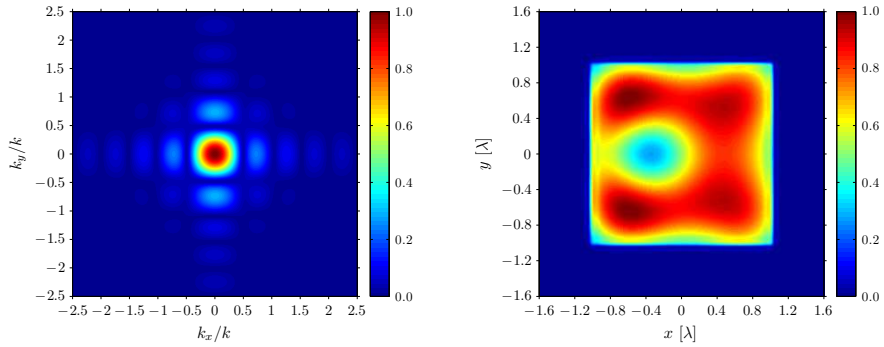

(a) Spectrum ($A_{Ey}(k_x, k_y)$). (b) Equivalent currents ($M_x(x, y)$).

Figure 5.41: Estimate of the non-visible spectrum with infinite iterations, and its corresponding equivalent currents, by using PDFT with a wide filter for the 5×5 slot-array antenna with one element not fed.

This second spatial filter was a mask with ones on the positions of the 25 slots, and zeros outside of these positions. The resulting PDFT estimation is shown in Fig. 5.42(b) where, as can be observed, now, all the elements are distinguished and the element that is not fed is also detected. The corresponding plane was spectrum is shown in Fig. 5.42(a). By looking at this spectrum it can be seen how, by just indicating the discrete positions of the slots with uniform separation, the spectrum behaves like a periodic function, as it was deduced in Section 5.3.1.

Comparing the estimate for this case to the estimate done by the methods explained above (see Fig. 5.15(b), for the iterative algorithm; Fig. 5.30(b) for the extrapolation matrix; and Fig. 5.35(b) for the generalized extrapolation

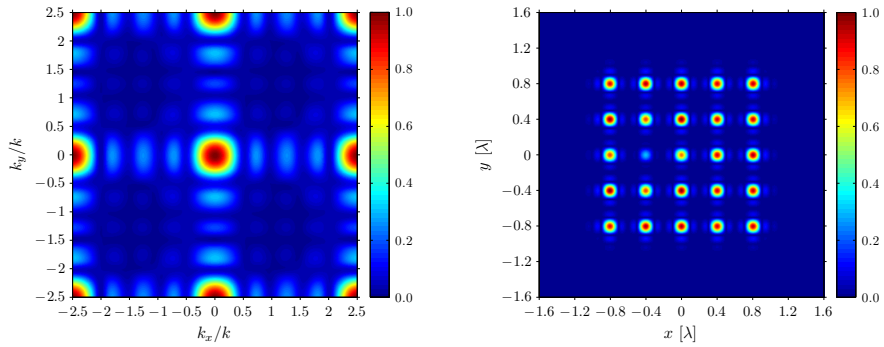

(a) Spectrum ($A_{Ey}(k_x, k_y)$). (b) Equivalent currents ($M_x(x, y)$).

Figure 5.42: Estimate of the non-visible spectrum with infinite iterations, and its corresponding equivalent currents, by using PDFT with a restrictive filter for the 5×5 slot-array antenna with one element not fed.

matrix) it can be concluded that the PDFT estimate performs the best estimation among all the described methods. The computation time (around 7 minutes) is worse than the computation time of the extrapolation matrix (around 1∼2 minutes for both described matrices, by rows and columns and generalized), and better than the iterative algorithm (around 20 minutes for 5000 iterations). However, the quite better results justify the increase of the computation time with regard to the matrix methods.

Practical results Finally, the PDFT was tested with a real case, namely, the X-band slot-array antenna formed by 7 elements depicted in Fig. 3.9. Firstly, the PDFT estimate was obtained by applying a wide filter ($p(x, y)$) including all the slots (i.e., a rectangular filter of $5.12\lambda \times 1.1\ \lambda$). The applied known part of the spectrum was the entire visible region and the procedure was the same as described above for the slot-array of 2 elements.

The PDFT estimate for this filter is shown in Fig. 5.43(b), and the corresponding extrapolated spectrum in Fig. 5.43(a). An improvement with regard to the currents obtained by just using the visible spectrum (see Fig. 5.9(a)) can be observed. However, the resulting currents are far from clarifying which elements are working correctly and which elements are not working.

Fig. 5.44 shows a cross section of the PDFT estimate of Fig. 5.43(b) on the exact positions where the slots are. By looking at this figure it is clear that a minimum improvement is obtained with regard to the currents determined from the visible spectrum. This can also be observed by looking at Fig. 5.43(a), where the extrapolated non-visible part of the spectrum is quite small.

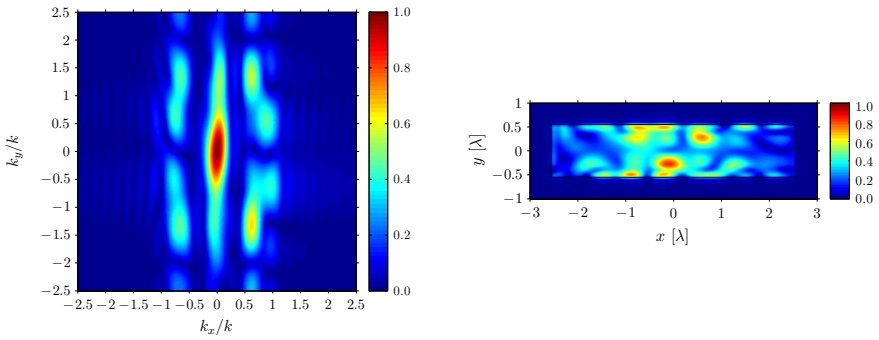

(a) Spectrum ($A_{Ey}(k_x, k_y)$). (b) Equivalent currents ($M_x(x, y)$).

Figure 5.43: Estimate of the non-visible spectrum with infinite iterations, and its corresponding equivalent currents, by using PDFT with a wide filter for the X-band slot-array of 7 elements.

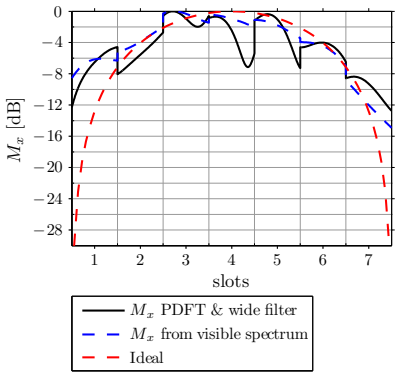

Figure 5.44: Equivalent magnetic currents on the positions of the slots for the X-band slot-array antenna formed by 7 slots by applying PDFT with a wide filter.

To improve the PDFT estimate, the possibility of applying any kind of filter with this technique was used. Thus, the PDFT estimate was again obtained but using the restrictive filter shown in Fig. 5.18. By using this filter, a quite big improvement in the estimation was obtained, as can be seen in Fig. 5.45(b). Here, it can be observed not only the envelope of the currents in the whole array of slots, but also the behavior of the currents inside the slots. This is possible because of the great part of the non-visible spectrum (see Fig. 5.45(a)) determined with the PDFT.

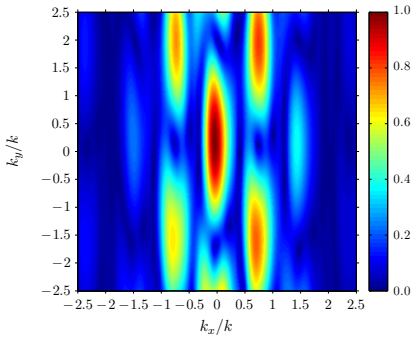

(a) Spectrum ($A_{Ey}(k_x, k_y)$).

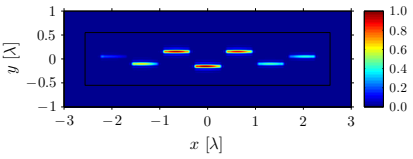

(b) Equivalent currents ($M_x(x, y)$).

Figure 5.45: Estimate of the non-visible spectrum with infinite iterations, and its corresponding equivalent currents, by using PDFT with a restrictive filter for the X-band slot-array of 7 elements.

The estimated equivalent currents by the PDFT can be observed better by looking at Fig. 5.46, where the amplitude of the obtained currents on the positions of the slots is shown. As can be observed, the estimated currents improve the currents obtained by just using the visible spectrum. The envelope of the PDFT estimate follows the ideal distribution but, now, the cosine distribution inside the slots can be observed.

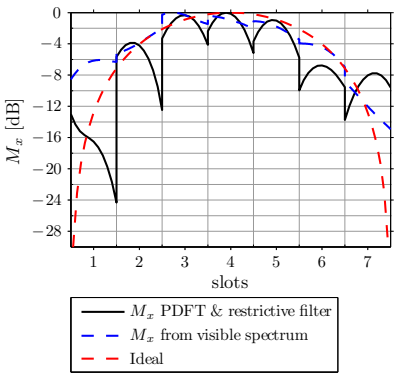

Figure 5.46: Equivalent magnetic currents on the positions of the slots for the X-band slot-array antenna formed by 7 slots by applying PDFT with a restrictive filter.

By looking at the PDFT estimate and comparing these results to the best equivalent currents obtained with the techniques described previously (see Fig. 5.9(b)) for the iterative algorithm with a wide filter; Fig. 5.19(b) for the iterative algorithm with a restrictive filter, Fig. 5.31(b) for the extrapolation matrix by rows and columns; and Fig. 5.37(b) for the generalized extrapolation matrix) it can be concluded that the PDFT is the best extrapolation of all the described techniques. Of course, the computation time (around 7 minutes) is worse than the computation time for the extrapolation matrices (1$\sim$2 minutes), however, the PDFT estimate performs a better extrapolation and the obtained currents look like the ideal currents in all the tests performed with this technique.

Chapter 6

Probe calibration

Throughout this thesis, the equivalent currents of an antenna have been reconstructed from the spherical near-field antenna measurement by means of a modal technique. With this aim, the first step has always been the computation of the spherical coefficients ($Q^{(3)}_{smn}$), which characterize the antenna in transmission (also known as *transmitting coefficients*, T_{smn}). Chapter 2, section 2.3, explained the way in which the transmitting coefficients are computed from the spherical near-field measurement by means of probe-corrected formulas. To do this, the probe receiving coefficients were required, however, it was pointed out that these coefficients were going to be assumed known because of the special algorithms that are required for their exact computation. This chapter describes these special algorithms for first order-probes and shows several examples.

6.1 Introduction

The probe receiving coefficients quantify the effect of the probe in the measurement. This effect may become a heavy-negative influence in the measurement and, as a consequence, in the computed spherical coefficients and in the reconstructed currents. It is, then, of special interest the way in which these coefficients are exactly computed, which is known as *probe calibration*. Thus, the more accurate equivalent currents may be obtained.

Probe calibration algorithms have not been studied as extensively as probe correction techniques, e.g. [24], [52], [130]. The most widely used algorithms have been introduced for first-order probes [52], [20] and consist of a probe's radiated field measurement with an auxiliary probe and the application of transformation techniques in conjunction with the reciprocal relation for obtaining the desired coefficients. The main problem with this technique is that,

since auxiliary probe receiving coefficients are not known, the electric Hertzian dipole coefficients must be applied, which leads to an approximate solution.

The first section of this chapter determines the error introduced by using the electric Hertzian dipole receiving coefficients instead of the correct probe receiving coefficients. As a consequence, the computed transmitting coefficients are not correct in absolute value and, hence, cannot be used when non-normalized radiation patterns are required, as it is the case of gain determination.

The second section of this chapter reviews one of the most important algorithms for first-order probe calibration, which is the iterative algorithm proposed by Hansen [20]. Unfortunately, the restrictions with regard to the required auxiliary probe limit the scope of this algorithm and, hence, many times this algorithm cannot be applied.

As a solution to the previous drawback, the third section of this chapter proposes three different alternatives to the iterative algorithm for first-order probes. These three different procedures depend on the available possibilities in the laboratory when the probe is being calibrated. Thus, the first procedure is applied when two identical antennas are available; the second one when two different antennas are available and, at least, the gain of one of them is known; and the third procedure is applied when the gain of the available antennas are not known and, hence, the second procedure cannot be used. The drawback of the last case is the requirement of three different antennas and four measurements, however, it is the more general procedure since it is the more flexible (there is no restriction about the antennas) and it does not need any information about the antennas involved in the calibration.

Finally, this chapter explains the way the anechoic chamber was characterized for the several results presented in this chapter. This is an extremely important step because transmission formula requires the value of the signal between the input of the AUT and the output of the probe, without the effect of the anechoic chamber, i.e., the effect of the positioners, the connectors, the cables, etc. If this requirement is not satisfied, wrong receiving coefficients are obtained.

6.2 Electric Hertzian dipole receiving coefficients

As stated above, the computation of the transmitting coefficients from the spherical near-field measurement requires prior knowledge of the probe receiving coefficients. If these coefficients are not known, the electric Hertzian dipole receiving coefficients, analytically deduced in [20], are normally applied. The problem arises because these analytical coefficients are ideal. Hence, they are quite different from the receiving coefficients of an arbitrary probe even though

the restriction of first-order probe, i.e., with just modes with $\mu = \pm 1$ different from zero, is satisfied by the arbitrary probe.

For this thesis, these last kind of probes are of interest and, hence, before studying the probe calibration techniques, it is convenient to quantify the error introduced by using the ideal coefficients instead of the correct coefficients of a first-order probe. To do this, the expressions deduced for the solution of the transmission formula must be reviewed. In Chapter 2, section 2.3, the transmitting coefficients are computed, using the result of a three fold transformation of the spherical near-field measurement ($w^n_{\mu m}(A)$) and the probe response constants ($P_{s\mu n}(kA)$) with first-order probe correction, by means of the expressions (2.46) and (2.47). These two expressions can be simplified as follows:

$$T_{smn} = \frac{1}{v} \frac{P_{3-s,1n}(kA) w^n_{-1,m}(A) - P_{3-s,-1n}(kA) w^n_{1,m}(A)}{P_{3-s,1n}(kA) P_{s,-1n}(kA) - P_{s1n}(kA) P_{3-s,-1n}(kA)}. \tag{6.1}$$

From this last equation, the transmitting coefficients T_{smn} can be easily determined since the amplitude of the incoming signal to the AUT (v) is known.

However, a further simplification can be applied to (6.1) by using the following symmetry relation for the probe response constants:

$$P_{s,-1,n}(kA) = (-1)^{s+1} P_{s1n}(kA). \tag{6.2}$$

Thus, if (6.2) is substituted in (6.1), the transmitting coefficients can be expressed as:

$$T_{smn} = \frac{1}{v} \frac{(-1)^{s+1} w^n_{-1,m}(A) + w^n_{1,m}(A)}{2 P_{s1n}(kA)}. \tag{6.3}$$

This last expression is especially useful because, independently of the receiving coefficients applied to compute the transmitting coefficients, the numerator does not vary. Hence, when studying the effect of the receiving coefficients on the transmitting coefficients, the attention may be focused on just the denominator.

Once (6.1) has been simplified, it is easier to determine the difference between the transmitting coefficients computed by applying the electric Hertzian dipole receiving coefficients and the correct transmitting coefficients (which would be obtained using the correct probe receiving coefficients).

On the one hand, from (6.3), if the electric Hertzian dipole receiving coefficients are applied and its response constants are denoted as $P_{s1n}(kA)|_{DIPOLE}$, the computed transmitting coefficients can be expressed as follows:

$$T_{smn}|_{DIPOLE} = \frac{1}{v} \frac{(-1)^{s+1} w^n_{-1,m}(A) + w^n_{1,m}(A)}{2 P_{s1n}(kA)|_{DIPOLE}}, \tag{6.4}$$

On the other hand, if the correct probe receiving coefficients are known and the probe response constants are denoted as $P_{s1n}(kA)|_{CORRECT}$, the computed transmitting coefficients, which are the correct transmitting coefficients, can be expressed, from (6.3), as:

$$T_{smn}|_{CORRECT} = \frac{1}{v}\frac{(-1)^{s+1}w^n_{-1,m}(A) + w^n_{1,m}(A)}{2P_{s1n}(kA)|_{CORRECT}}. \tag{6.5}$$

As can be observed, between the transmitting coefficients of (6.4) and (6.5) there is just a difference in the denominator, since the numerator does not depend on the applied receiving coefficients. This is an important fact because it allows to express the relation between the computed and the correct transmitting coefficients as follows:

$$T_{smn}|_{DIPOLE} = \beta_{sn}(kA)T_{smn}|_{CORRECT}, \tag{6.6}$$

where $\beta_{sn}(kA)$ is, from now on, the *calibration factor*, which can be expressed as:

$$\beta_{sn}(kA) = \frac{P_{s1n}(kA)|_{CORRECT}}{P_{s1n}(kA)|_{DIPOLE}}. \tag{6.7}$$

From (6.6) it may be concluded that an error, which is quantified by the calibration factor (6.7), is produced because of the use of the electric Hertzian dipole receiving coefficients instead of the correct receiving coefficients. Furthermore, the following conclusions with regard to this error may be made from (6.6) and (6.7):

- The error depends on the distance but it does not vanish for large distances. Hence, though the measurement is taken in the far-field region, the use of the electric Hertzian dipole receiving coefficients causes an error in the computed transmitting coefficients.
- The error depends on the indices s and n, but not on the index m. Consequently, the calibration factor may cause mistakes in the computed radiation pattern.
- The error consists of just a multiplicative constant, i.e., no sums, integrals, etc. are needed to compute the correct transmitting coefficients from the computed coefficients. This is a major advantage that will be especially useful later, when removing this error from the computed coefficients.

Nevertheless, although it has been quantified the error caused by the use of the electric Hertzian dipole receiving coefficients, is must be pointed out that,

in several practical situations, the error may become negligible or not detected. Depending on the antenna that is being used as a probe or the application in which the computed transmitting coefficients are applied, it may not be necessary to consider the error quantified by the calibration factor.

For instance, if the probe is an elementary antenna, like an open waveguide or an electrically small horn, both the ideal electric Hertzian dipole receiving coefficients and the correct elementary probe receiving coefficients are quiet similar. Therefore, the calibration factor $\beta_{sn}(kA)$ is almost 1 and, hence, the error is negligible.

In addition, at large measurement distances, an approximation can be applied to the calibration factor (see Section 6.2.1) which allows the error to be considered constant for any combination of s and n. Hence, since $\beta_{sn}(kA)$ is constant, the computed transmitting coefficients and the correct coefficients just differ in a multiplicative factor constant for all the coefficients, what leads to the same normalized computed and correct coefficients. Consequently, when dealing with normalized patterns (computed from normalized transmitting coefficients), no error is detected and the obtained results are completely correct.

The major problem arises in two different situations. The first one is referred to the case in which a near-field measurement is taken, i.e., at a short distance. In this case, the calibration factor is not constant for any combination of s and n and, hence, each computed transmitting coefficient is affected by a different error. Therefore, though normalized coefficients are applied to compute the normalized pattern, an error takes place and the obtained normalized pattern is not the same as the correct normalized pattern. The reason lies in the fact that a different error on each coefficient causes, not only a different scale, but also mistakes in the shape of the radiation pattern which lead to a wrong pattern.

The second situation takes place when the required pattern must be non-normalized. This situation arises, for instance, when the gain must be determined, in which case the non-normalized far-field pattern is needed. Hence, no matter the measurement distance, the error must be removed in order to obtain the desired pattern. The easier case is the case of large measurement distances, in which case just a multiplicative constant must be removed. However, of main interest is the case of short measurement distances since, if the error is removed, the correct transmitting coefficients may be obtained from measurements taken at short measurement distances (even in the near-field region). Consequently, the gain may be determined with just one near-field measurement. This is an interesting application since no far-field measurement is required for the gain determination which, in many cases, is not possible because of the antenna size, the frequency, the anechoic chamber size, etc.

Next sections describe the behavior of the calibration factor for large distances, which will be used in future sections to apply some approximations.

Furthermore, the way in what the gain can be determined by means of the transmitting coefficients is explained in order to show, later, the advantages of determining the correct transmitting coefficients. Finally, some practical results are depicted which show the error produced by the calibration factor when this factor is not removed.

6.2.1 Behavior of the calibration factor at large distances

The calibration factor $\beta_{sn}(kA)$ (6.7) depends on the probe response constants with μ=1, i.e., $P_{s1n}(kA)$, which, in turn, depend on the probe receiving coefficients $R_{\sigma\mu\nu}$ and on the translation coefficients $C^{sn(3)}_{\sigma 1\nu}(kA)$ (2.42). Hence, since the probe receiving coefficients vary for each case, in order to determine the general behavior of β_{sn}, the translation coefficients must be studied.

Appendix C, section C.2, shows the main expressions for the computation of the translation coefficients. Here it can be found both the general expression (C.12) and the asymptotic expression for large distances (C.17). In the present section, it is of main interest the asymptotic expression (C.17b) which allows the translation coefficients with μ=1 to be easily computed for large distances. The interest of (C.17b) lies in the fact that, from this expression, the following two recurrent relations for n and ν may be established:

$$C^{s(n+1)(3)}_{\sigma 1\nu}(kA) = \frac{1}{j}\sqrt{1+\frac{2}{2n+1}}\,C^{sn(3)}_{\sigma 1\nu}(kA); \qquad kA \to \infty \tag{6.8}$$

$$C^{sn(3)}_{\sigma 1(\nu+1)}(kA) = j\sqrt{1+\frac{2}{2\nu+1}}\,C^{sn(3)}_{\sigma 1\nu}(kA); \qquad kA \to \infty \tag{6.9}$$

If these two expressions are applied for the computation of the probe response constants with μ=1 of an arbitrary antenna (2.42), the following formula is obtained:

$$P_{s1n}(kA) = \frac{1}{2}\sum_{\sigma}\left[C^{s1(3)}_{\sigma 11}(kA)\left(\prod_{p=0}^{n-1} a_p^{(1)}\right)\sum_{\nu} R_{\sigma 1\nu}\left(\prod_{k=0}^{\nu-1} a_k^{(2)}\right)\right] \tag{6.10}$$

where

$$a_q^{(r)} = \begin{cases} 1 & ,\text{if} \quad q=0 \\ (-1)^r j\sqrt{1+\frac{2}{2q+1}} & ,\text{if} \quad q\neq 0 \end{cases} \tag{6.11}$$

Of course, (6.10) is somewhat more difficult than (2.42), however, when this expression is applied for the computation of the electric Hertzian dipole

response constants (needed for the computation of the calibration factor (6.7)), it becomes very useful. As it is deduced in [20], the electric Hertzian dipole receiving coefficients have just one non-zero element with μ=1. This coefficient is the one with σ=2 and ν=1, and its value is: $R_{211}|_{DIPOLE} = -\sqrt{2}/2$. Thus, if the calibration factor is computed (6.7), and the recurrent relation (6.10) is applied to compute both, the arbitrary probe and the electric Hertzian dipole response constants, the following expression is obtained for the calibration factor for $kA \to \infty$:

$$\beta_{sn}(kA) = \beta = \frac{\sum_{\sigma\nu} \left(\prod_{k=0}^{\nu-1} a_k^{(2)} \right) R_{\sigma 1 \nu}|_{CORRECT}}{R_{211}|_{DIP}}; \quad kA \to \infty \tag{6.12}$$

As can be observed, at large distances, $\beta_{sn}(kA)$ does not depend on the indices s and n. Therefore, the calibration factor can be considered constant for all the computed transmitting coefficients.

However, one question must be solved: the distance from which the expression (6.12), and the conclusions derived above, can be applied. To determine this distance, it has been compared the result that is obtained with the general expression (C.12) (which is valid for any distance), and the result that is obtained with the asymptotic expression (C.17b) (used previously to deduce (6.8) and (6.9)) valid only for large distances ($kA \to \infty$). Fig. 6.1 shows the quadratic error as a function of the distance made by the asymptotic expression (C.17b) with regard to the general expression (C.12). As can be observed, the error is exponentially decreased for large distances. Thus, if a threshold of 10^{-5} is assumed (practical results have shown that this choice offers quite good results), the error made by the asymptotic expressions may be considered negligible by using measurement distances larger than 50 λ.

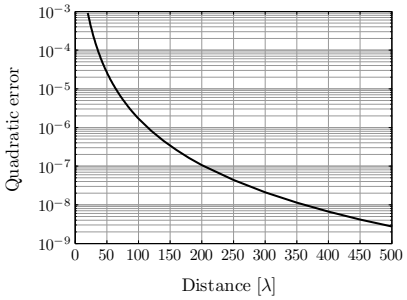

Figure 6.1: Quadratic error of translation coefficients computed with the asymptotic expression

Therefore, for measurement distances larger than 50 λ, the expression (6.12), and the conclusions derived from this expression, can be applied. Hence, the error produced by considering the electric Hertzian dipole receiving coefficients can be considered constant for all the computed transmitting coefficients. This fact will be especially useful later, when describing a an alternate probe calibration procedure for the accurate computation of the receiving coefficients.

6.2.2 Gain determination

The gain is one of the most important parameters of an antenna since it provides information about the efficiency of the antenna. The difference of the gain with regard to other important parameters (e.g. the directivity, the reflection parameter or the beamwidth) is the difficulty to determine it. Whereas the rest of parameters can be easily computed from the spherical near-field measurement, the gain determination normally requires additional measurements and computations. In [131] and [132], Burgos et al. carry out an extensive description of the most important algorithms for the gain determination presented to date. As can be observed in this publication, most of them require far-field measurements and only one of them, also described in [20], can be applied with just near-field measurements.

Unfortunately, many times far-field measurements are not possible because of the operating frequency, the antenna size and the anechoic chamber dimensions. In these cases, just near-field measurements can be carried out and, consequently, the gain must be determined using the gain determination algorithm for near-field measurements described in [20]. The most important drawback of this algorithm is the requirement of several near-field measurements with two auxiliary antennas, what enhances the difficulty and the required time for the gain determination.

As an additional technique, in [20] are also deduced the formulas for the gain determination from just the computed transmitting coefficients. The most important drawback of this technique is the requirement of the exact computation in absolute value of these transmitting coefficients. Nevertheless, if this problem is overcome, the gain may be determined with just one near-field measurement. The way in which these correct transmitting coefficients may be computed will be explained later, however, it is important to describe previously how the gain can be easily determined from the computed transmitting coefficients.

With this aim, first, it must be considered that the gain is defined in the far-field region as the relation between the power radiated per unit solid angle in the direction (θ,ϕ), which can be computed from the transmitting coefficients as:

$$P_{rad\ ant}(\theta,\phi) = \frac{1}{2}\frac{1}{4\pi}\left|\sum_{smn} vT_{smn}\vec{K}_{smn}(\theta,\phi)\right|^2, \tag{6.13}$$

and the power radiated per unit solid angle if the input power accepted by the antenna were radiated isotropically, which is computed by the following expression:

$$P_{acc\ ant} = \frac{1}{2}\frac{1}{4\pi}|v|^2(1-|S_{11}|^2), \tag{6.14}$$

where S_{11} is the reflection parameter. Therefore, the gain is determined as follows:

$$G(\theta,\phi) = \frac{\left|\sum_{smn} T_{smn}\vec{K}_{smn}(\theta,\phi)\right|^2}{1-|S_{11}|^2}. \tag{6.15}$$

This procedure can also be applied to the computation of the directivity. Directivity is defined in the far-field region as the relation between the power radiated per unit solid angle in the direction (θ,ϕ) (6.13), and the power radiated per unit solid angle if the antenna radiated isotropically, which is computed as:

$$P_{iso\ ant} = \frac{1}{2}\frac{1}{4\pi}\sum_{smn}|vT_{smn}|^2. \tag{6.16}$$

Thus, the directivity can also be obtained from the transmitting coefficients by applying the following expression:

$$D(\theta,\phi) = \frac{\left|\sum_{smn} T_{smn}\vec{K}_{smn}(\theta,\phi)\right|^2}{\sum_{smn}|T_{smn}|^2}. \tag{6.17}$$

6.2.3 Practical results

In order to verify the error introduced by considering the electric Hertzian dipole receiving coefficients instead of the correct receiving coefficients, the standard gain horn shown in Fig. 6.2 was measured at 36.85 GHz and 26.40 GHz. As a probe, an identical antenna to that of Fig. 6.2 was used. The measurement distance was 1.49 m, hence, considering the antenna size and the operating frequencies, the spherical measurement was taken in the far-field region at both frequencies.

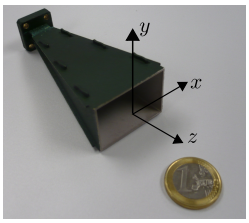

Figure 6.2: Measured standard gain horn and position with regard to the coordinate system of the AUT.

Of course, the horn of Fig. 6.2 is not an ideal first-order probe, but an odd-order probe. However, as Fig. 6.3 shows, the power of high odd-order modes ($\mu = \pm 3, \pm 5, \cdots$) remains 15 dB below the power of modes $\mu = \pm 1$ at both frequencies. Thus the horn of Fig. 6.2 may be considered as a first-order probe without leading to inaccurate results.

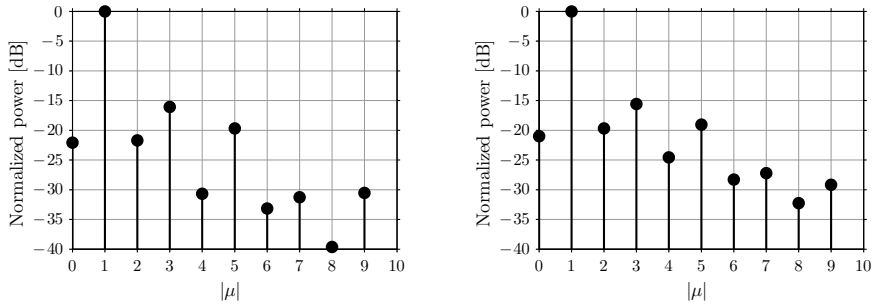

(a) at 26.40 GHz.

(b) at 36.85 GHz.

Figure 6.3: Normalized power of the standard gain horn receiving coefficients for several indices μ.

First of all, using the spherical measurement, the transmitting coefficients were computed using the electric Hertzian dipole receiving coefficients, i.e., applying the expression (6.4). Later the electric far field was computed with the expression (2.48) in the XZ and YZ planes (Fig. 6.2 depicts the position of the antenna with regard to the coordinate system). Fig. 6.4 shows the normalized far-field pattern obtained from the computed transmitting coefficients.

In order to check the validity of this radiation pattern, the transmitting coefficients were also computed by applying the correct probe receiving coefficients (the way these coefficients can be obtained will be explained later). Then, these coefficients were used to compute again the normalized far-field pattern.

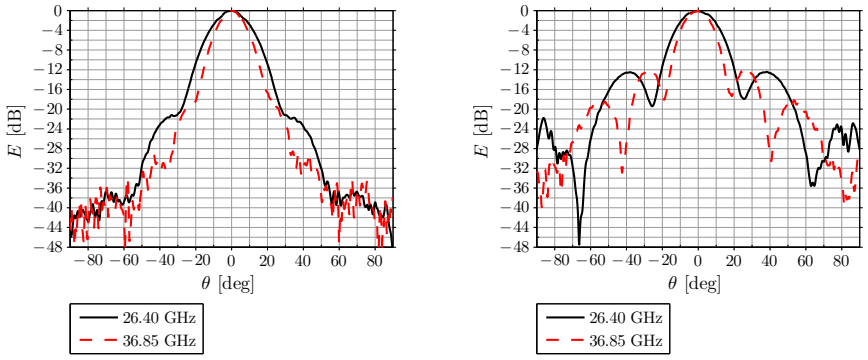

(a) XZ Plane. (b) YZ Plane.

Figure 6.4: Computed far-field of the conical horn at 26.40 GHz and 36.85 GHz using the electric Hertzian dipole receiving coefficients.

Fig. 6.5 shows the difference of this radiation pattern with regard to the radiation pattern of Fig. 6.4, i.e., the pattern computed with the transmitting coefficients obtained using the electric Hertzian dipole receiving coefficients. As can be observed, the error is almost constant for all directions, especially in the maximum radiation directions. The error just becomes significant in low gain directions and, hence, may be considered negligible.

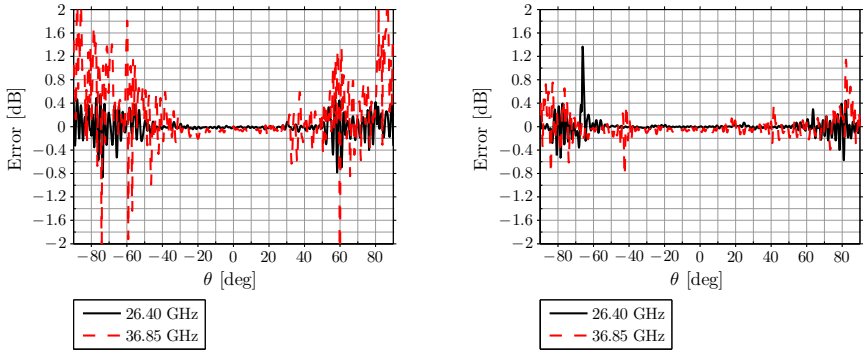

(a) XZ Plane. (b) YZ Plane.

Figure 6.5: Error of the computed far-field of the conical horn at 26.40 GHz and 36.85 GHz using the electric Hertzian dipole receiving coefficients.

Previous results allow to be concluded that, if an error is present, this cannot be observed in normalized values. The reason for this behavior lies in the fact

that the measurement distance (1.49 m) is 184.44 λ at 36.85 GHz and 130.70 λ at 26.40 GHz. Hence, as it is proved in section 6.2.1, the error introduced by the calibration factor can be considered constant for all the coefficients. Thus, the normalized radiation pattern obtained from both the computed and the correct transmitting coefficients are the same and, therefore, the error caused by the use of the electric Hertzian dipole receiving coefficients is not detected.

In order to observe this error, the gain of the antenna of Fig. 6.2 was determined with the expression (6.15). Table 6.1 shows the determined gain as well as the measured S_{11} parameter (which is required for the gain determination (6.15)), the computed directivity (which does not depend on the absolute value of the transmitting coefficients and, hence, is correct) and the gain parameter supplied by the antenna manufacturer (with an accuracy of ± 0.25 dB).

Frequency	**Measured** S_{11}	**Supplied Gain**	**Computed Gain**	**Computed Directivity**
26.40 GHz	-17.62 dB	18.10 dB	**36.54 dB**	18.61 dB
36.85 GHz	-15.00 dB	20.80 dB	**39.34 dB**	20.98 dB

Table 6.1: Determined parameters of the conical horn at 26.40 GHz and 36.85 GHz using the electric Hertzian dipole receiving coefficients.

As can be observed in Table 6.1, there is a big difference between the computed gain and the gain parameter supplied by the manufacturer. This difference arises because the computed transmitting coefficients are not completely correct, as the expression (6.15) requires. The calibration factor causes a change in the level of the computed transmitting coefficients and, hence, though these coefficients are correct in normalized value (as shown in Fig. 6.5), the absolute value is not correct. Next sections deal with the way in which the correct receiving coefficients of an antenna can be accurately computed.

6.3 Probe pattern calibration: iterative algorithm

As it has been observed, the use of the electric Hertzian dipole receiving coefficients does not allow the correct transmitting coefficients to be computed. Therefore, a probe calibration technique must be applied in order to obtain the correct receiving coefficients which, later, are used to obtain the desired correct transmitting coefficients.

One of the most used probe calibration techniques is the iterative algorithm proposed by Hansen [20]. This algorithm computes the correct receiving co-

efficients of an antenna from two sets of measurements. The first one (shown in Fig.6.6(a)) is the measurement of the radiated field of the antenna that is being characterized (antenna A) using an auxiliary probe (antenna B) as a probe. The second one (shown in Fig. 6.6(b) is the inverse measurement, i.e., the measurement of the radiated field of the auxiliary probe (antenna B) using the antenna that is being characterized (antenna A) as a probe.

(a) Measurement M_A.

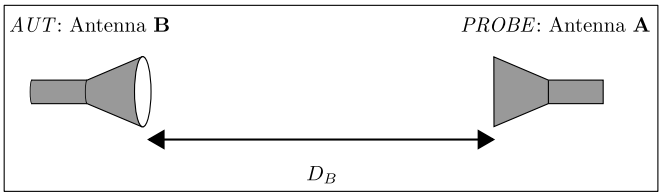

(b) Measurement M_B.

Figure 6.6: Measurements set-ups.

The way the iterative algorithm works is depicted in Fig. 6.7. As can be observed in this figure, the first iteration of the iterative algorithm is the computation of the antenna A transmitting coefficients ($TA_{smn}^{ITER\,1}$) from the measurement M_A by applying the electric Hertzian dipole receiving coefficients R_{dip} (since, at this point, the antenna B receiving coefficients are not known).

Once the coefficients $TA_{smn}^{ITER\,1}$ are known, the antenna A receiving coefficients ($RA_{smn}^{ITER\,1}$) are deduced by means of the transformation of transmitting coefficients into receiving coefficients. The way in which this transformation is carried out is extensively explained in Section 6.3.1. By now, it is going to be assumed that this transformation is obtainable.

In the second iteration, the measurement M_B is used to compute the antenna B transmitting coefficients ($TB_{smn}^{ITER\,2}$). In this case, however, the electric Hertzian dipole receiving coefficients are not used since the antenna A, which is used as a probe in the measurement M_B, receiving coefficients are known from the first iteration ($RA_{smn}^{ITER\,1}$). As a result, the antenna B transmitting coefficients are obtained, which are used to compute the antenna B receiving coefficients ($RB_{smn}^{ITER\,2}$). Later, these coefficients are applied in the third iteration, in which the measurement M_A is used again to compute the

antenna A transmitting coefficients ($TA_{smn}^{ITER\,3}$). Consequently, these last coefficients are more accurate than the coefficients of the first iteration ($TA_{smn}^{ITER\,1}$) since the applied receiving coefficients in this case ($RB_{smn}^{ITER\,2}$) are closer to the correct receiving coefficients of the antenna B than the electric Hertzian dipole receiving coefficients (R_{dip}) applied in the first iteration.

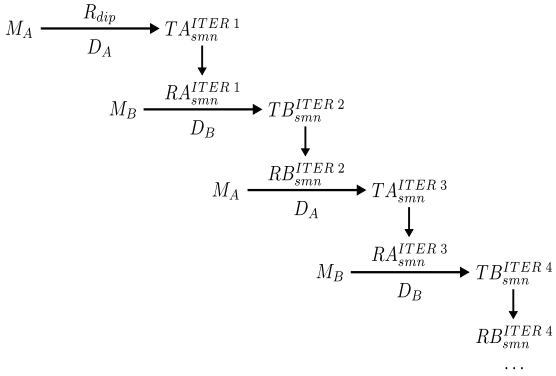

Figure 6.7: Iterative algorithm proposed by Hansen.

As can be observed in Fig. 6.7, the iterative algorithm continues iteration by iteration using the result of the previous iterations. As pointed out by Hansen [20], after several iterations convergence is reached in the computed transmitting coefficients of antennas A and B and, hence, the receiving coefficients of the antenna that is being characterized (antenna A) are obtained accurately.

Nevertheless, it must be taken into account that the convergence of the iterative algorithm depends on the auxiliary antenna (antenna B). As indicated by Hansen [20], the only way to reach the convergence is by using an elementary antenna, e.g. an open waveguide or an electrically small horn, as an auxiliary antenna, otherwise, convergence is not reached. To illustrate this, the measurement of Section 6.2.3 at 36.85 GHz was used to characterize the antenna of Fig. 6.2, which is not an elementary antenna. As it was described there, the measurement was taken using an identical antenna as a probe, hence, both antennas (A and B) are the same and, therefore, they both have the same transmitting and receiving coefficients.

The advantage of this situation is that, in all iterations, the obtained coefficients should be the same if the algorithm converged. To quantify the solution on each iteration, the transmitting coefficients power was calculated using the following expression:

$$P = \sum_{smn} |T_{smn}|^2. \tag{6.18}$$

Fig. 6.8 depicts the computed power for each iteration. As can be observed, the transmitting coefficients do not converge; instead they oscillate for odd and even iterations. Therefore, this example confirms that, when the auxiliary antenna (antenna B) is not an elementary antenna, the iterative algorithm does not converge.

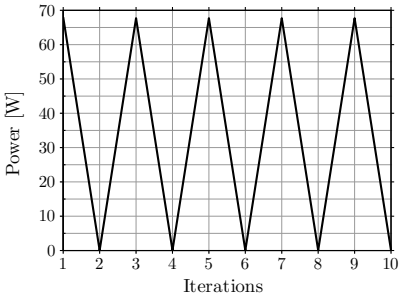

Figure 6.8: Transmitting coefficients power vs number of iterations for the iterative algorithm proposed by Hansen.

This limitation may become a strong drawback because an elementary antenna may not be available when measuring the antenna to be characterized, or because a certain gain may be required in the auxiliary antenna (elementary antennas have a low gain) to reduce the noise present in the received signal. For all these reasons, in this thesis several alternatives to the iterative algorithm proposed by Hansen are introduced. These alternatives are proposed in Section 6.4 for first-order probes and for three different situations.

6.3.1 Transformation of transmitting coefficients into receiving coefficients

For reciprocal antennas, the transformation of transmitting coefficients into receiving coefficients is carried out by just applying the following expression [20]:

$$R_{smn} = (-1)^m T_{s,-m,n}. \tag{6.19}$$

However, when using the resulting receiving coefficients, it must be taken into account that these receiving coefficients are expressed in the same coordinate system as the transmitting coefficients, i.e., the resulting receiving coefficients might not be able to be directly applied in the solution of the transmission formula. Hence, before using the resulting receiving coefficients, it must

be considered the coordinate system in which the transmitting coefficients are expressed and the coordinate system in which the receiving coefficients are required for the solution of the transmission formula.

Concerning to this thesis, several measurements have been taken to calibrate several horns. In all these measurements, the antenna which radiated field has been measured, i.e., the AUT, has been placed with regard to the coordinate system depicted in Fig. 6.9(a). Therefore, the transmitting coefficients computed with the transmission formula are expressed in this coordinate system.

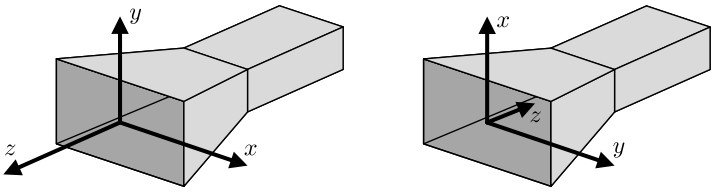

(a) For transmitting coefficients. (b) For receiving coefficients.

Figure 6.9: Antenna position with regard to the coordinate system.

However, as described in [20], the transmission formula is deduced considering that the receiving coefficients are expressed with regard to the coordinate system depicted in Fig. 6.9(b). As can be seen, both, the coordinate system in which the transmitting coefficients are computed (and the receiving coefficients deduced from them by applying (6.19)) and the coordinate system in which the receiving coefficients are required are not the same. Hence, a coordinate system change must be applied to use the computed receiving coefficients in the solution of the transmission formula.

From Fig. 6.9(a) and Fig. 6.9(b), both coordinate systems can be related by means of a rotation of the axes. Specifically, if the rotation is expressed in terms of the Euler angles (described in Fig. C.1), the rotation of the axes may be expressed as:

- $\chi_0 = -90, \quad \theta_0 = 180, \quad \chi_0 = 0;$ or as
- $\chi_0 = 0, \quad \theta_0 = 180, \quad \chi_0 = 90$

To do this rotation of the axes, a rotation of the spherical waves (see Appendix C) can be applied. The general expression (C.1) allows both ingoing waves (receiving coefficients) and outgoing waves (transmitting coefficients) to be rotated. If the rotation of transmitting coefficients is chosen, it can be deduced the following formula for computing the transmitting coefficients in the

rotated coordinate system ($T^{rot}_{\sigma\mu n}$), i.e., the one of Fig. 6.9(b), from the transmitting coefficients in the original coordinate system (T_{smn}), i.e., the one of Fig. 6.9(a):

$$T^{rot}_{\sigma\mu n} = \sum_{m=-n}^{n} e^{jm\phi_0} d^n_{\mu m}(\theta_0) e^{j\mu\chi_0} T_{smn} \tag{6.20}$$

Once the transmitting coefficients are obtained in the appropriate coordinate system, expression (6.19) can be applied. Thus, the receiving coefficients are obtained in the required coordinate system for the solution of the transmission formula.

6.4 Alternative iterative algorithm for probe calibration

In previous section it has been seen that, as pointed out by Hansen [20], the iterative algorithm for probe calibration only converges if an elementary antenna is used as an auxiliary probe. The reason for this behavior can be easily explained by means of the calibration factor deduced in Section 6.2.

As commented above (and depicted in Fig. 6.7), the first iteration of the iterative algorithm makes use of the electric Hertzian dipole receiving coefficients (R_{dip}), since the auxiliary probe receiving coefficients are not known at this point. If the auxiliary probe is an elementary antenna, both, the electric Hertzian dipole receiving coefficients and the auxiliary probe receiving coefficients, are quite similar. Hence, the applied auxiliary probe coefficients (R_{dip}) are essentially correct and the iterative algorithm just has to obtain transmitting coefficients of the probe that is being characterized.

However, if the auxiliary probe is not an elementary antenna, the error quantified by the calibration factor $\beta_{sn}(kA)$ is produced in the first iteration because of the use of the electric Hertzian dipole receiving coefficients. The non-convergence problem arises because this error is not attenuated, but propagated throughout the different iterations.

Next three sections propose alternatives for the iterative algorithm for three different situations. The aim of these alternatives is to remove the calibration factor from the iterative algorithm, what leads to compute the accurate transmitting and receiving coefficients of the antenna that is being characterized.

6.4.1 Case 1: Two identical antennas

In this first case, the antennas involved in the probe calibration algorithm, i.e., the probe that is being characterized (antenna A) and the auxiliary probe

(antenna B), are identical first-order probes. This situation has two advantages: the first one is the reduction in the number of necessary measurements. This is because the measurements M_A and M_B (depicted in Fig. 6.6) are essentially the same, since the exchange of antennas A and B for the measurement M_B produces the same result (the same set-up as in measurement M_A is obtained). Hence, just one spherical measurement needs to be taken, which is used in all the iterations (even and odd). Fig. 6.10 depicts this spherical measurement (M).

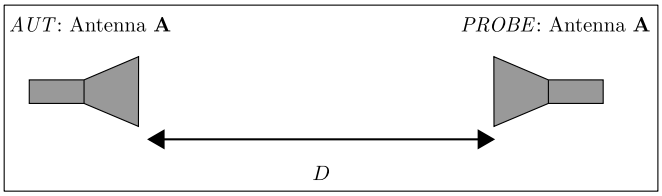

Figure 6.10: Measurement set-up for the case of two identical antennas (Measurement M).

The second advantage is the chance of assuming that the transmitting coefficients of both antennas involved in the measurement M are the same. Since the antennas are identical, their transmitting coefficients are also identical (apart from the manufacturing errors) and, hence, the results obtained in all the iterations must be the same.

Considering previous advantages, the effect of the factor $\beta_{sn}(kD)$ may be easily introduced in the iterative algorithm. To do this, the measurement distance (D, as depicted in Fig. 6.10) must be large enough to consider the error constant for all combinations of s and n. Thus, instead of considering $\beta_{sn}(kD)$, it may be assumed that this factor is just $\beta(kD)$.

By doing the above assumption, the way the iterative algorithm works for this first case can be described as follows: firstly, the AUT transmitting coefficients ($T_{smn}^{ITER\,1}$) are computed from the measurement M by applying the electric Hertzian dipole receiving coefficients (R_{dip}). Therefore, as it was deduced in Section 6.2 (6.6), the resulting transmitting coefficients $T_{smn}^{ITER\,1}$ are the correct AUT transmitting coefficients multiplied by the factor $\beta(kD)$:

$$T_{smn}^{ITER\,1} = \beta(kD) T_{smn}|_{CORRECT}. \tag{6.21}$$

Secondly, the AUT receiving coefficients ($R_{smn}^{ITER\,1}$) are obtained from the computed AUT transmitting coefficients as described in Section 6.3.1. As a result, the obtained receiving coefficients are also the correct coefficients multiplied by the calibration factor. Thus, $R_{smn}^{ITER\,1}$ can be expressed as:

$$R_{smn}^{ITER\,1} = \beta(kD) R_{smn}|_{CORRECT}. \tag{6.22}$$

When these coefficients are applied to compute the AUT transmitting coefficients in the second iteration, first, the probe response constants must be computed. From expression (2.42), it can be deduced that the obtained constants are also the correct probe response constants multiplied by the factor $\beta(kD)$ ($P_{s\mu n}(kD)^{ITER\,1} = \beta(kD) P_{s\mu n}(kD)|_{CORRECT}$), since this factor does not depend on the indices s and n, as stated above. Consequently, if the computed probe response constants are inserted into (6.3), the transmitting coefficients can be expressed as:

$$T_{smn}^{ITER\,2} = \frac{1}{\beta(kD)} T_{smn}|_{CORRECT}. \tag{6.23}$$

As can be observed, in this iteration, the transmitting coefficients $T_{smn}^{ITER\,2}$ are not the correct transmitting coefficients multiplied by $\beta(kD)$, but divided by $\beta(kD)$. Therefore, the receiving coefficients ($R_{smn}^{ITER\,2}$) deduced from these coefficients are also the correct receiving coefficients divided by $\beta(kD)$, i.e., the receiving coefficients in the second iteration are:

$$R_{smn}^{ITER\,2} = \frac{1}{\beta(kD)} R_{smn}|_{CORRECT}. \tag{6.24}$$

From these coefficients, the probe response constants in the second iteration are the correct probe response constants divided by $\beta(kD)$. Hence, if these probe response constants are used to compute the transmitting coefficients in the third iteration (6.3), the resulting coefficients can be expressed as follows:

$$T_{smn}^{ITER\,3} = \beta(kD) T_{smn}|_{CORRECT}. \tag{6.25}$$

Therefore, the computed transmitting coefficients in the first ($T_{smn}^{ITER\,1}$) and third ($T_{smn}^{ITER\,3}$) iterations are the same. If the iterative process continues, it can be observed that the second and fourth iterations behave in the same way, i.e., $T_{smn}^{ITER\,4} = T_{smn}^{ITER\,2}$. In general, this behavior takes place for even and odd iterations, i.e., the computed transmitting coefficients in the odd iterations are always the same, and the computed transmitting coefficients in the even iterations are also the same.

Fig. 6.11 (where, for the sake of simplicity, the dependence of $\beta(kD)$ with regard to kD has not been noted) depicts the procedure commented above. As can be observed in this figure, two sets of solutions are obtained: the solution of the odd iterations and the solution of the even iterations. Of course, the power of the transmitting coefficients of each solution is different, what justifies the oscillatory behavior in the computed power observed in Fig. 6.8 for the example

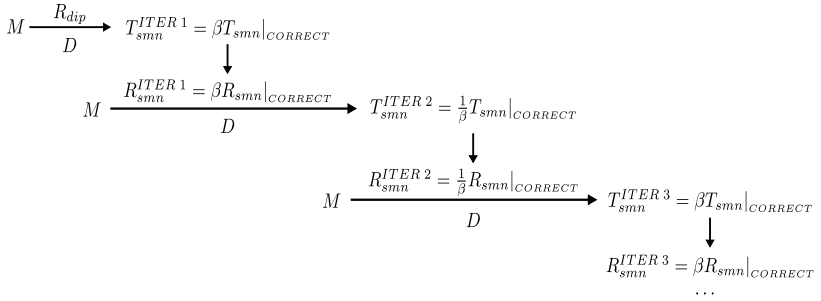

Figure 6.11: Propagation of error throughout the iterative algorithm for the case of two identical antennas.

described in Section 6.3, where the antennas involved in the calibration were two identical first-order probes.

Once it has been studied the way in which the calibration factor is propagated throughout the iterative algorithm, it must be determined how this error can be removed in order to obtain the correct transmitting coefficients. To do this, the solution of the odd and even iterations may be related. Specifically, if the transmitting coefficients computed in an odd iteration ($T_{smn}^{ITER\,odd}$) are divided by the transmitting coefficients computed in an even iteration ($T_{smn}^{ITER\,even}$), the correct transmitting coefficients are eliminated and, hence, the calibration factor can be easily obtained as follows:

$$\beta(kD) = \sqrt{\frac{T_{smn}^{ITER\,odd}}{T_{smn}^{ITER\,even}}}. \tag{6.26}$$

Since $T_{smn}^{ITER\,odd}$ and $T_{smn}^{ITER\,even}$ are known from the iterative algorithm, the calibration factor $\beta(kD)$ can be easily determined. Once this factor is known, one task still remains. This task consists of multiplying the transmitting coefficients obtained in the even iterations by the computed $\beta(kD)$ or dividing the transmitting coefficients of the odd iterations by $\beta(kD)$. No matter the way is chosen, as a result, the correct transmitting coefficients of the antenna that is being characterized ($T_{smn}|_{CORRECT}$) are accurately obtained.

Once the correct transmitting coefficients are known, the computation of the correct receiving coefficients ($R_{smn}|_{CORRECT}$) can be easily done as described in Section 6.3.1. Thus, if the antenna that is characterized by this procedure is used as a probe for measuring the radiated field of another antenna, the obtained correct receiving coefficients will be used to compute accurately the transmitting coefficients of this antenna.

Practical results 1 The described alternative to the iterative algorithm was tested in two different situations. The first one was the same situation as in the example of Section 6.2.3, where the radiated field of the antenna shown in Fig. 6.2 was measured with an identical antenna working as a probe. As described there, the measurement distance was 1.49 m and the operating frequencies were 26.40 GHz and 36.85 GHz. Therefore, in both cases, the electrical measurement distance was larger than 50 λ and, hence, the approximation of the calibration factor (deduced in Section 6.2.1) could be applied.

Firstly, the iterative algorithm was implemented until the eleventh iteration was reached (the election of eleven iterations is due to the fact that it has been observed that a more stable solution is achieved if the solution at high iterations is considered). Then, the calibration factor was determined by means of the expression (6.26).

Later, the computed transmitting coefficients on each iteration were suitably corrected (dividing or multiplying) by the computed calibration factor. As a result, the correct transmitting coefficients in all the iterations were obtained. Fig. 6.12 shows the power of these coefficients at 36.85 GHz and, as can be observed, the oscillatory behavior observed in Fig. 6.8 is not present. Indeed, the power of the computed transmitting coefficients on each iteration tends to a constant value, i.e., the algorithm converges.

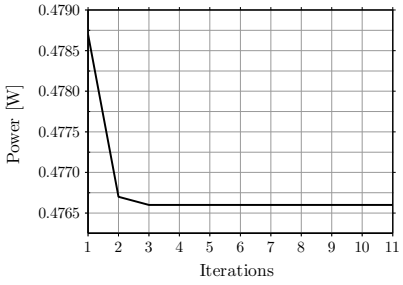

Figure 6.12: Transmitting coefficients power evolution after factor $\beta(kB)$ correction.

In order to verify if the accuracy of the computed transmitting coefficients, the gain was determined using the expression (6.15) and the transmitting coefficients obtained in the iteration 11. Table 6.2 shows the result for the measured S_{11} parameter, the gain supplied by the manufacturer (with a tolerance of ± 0.25 dB), and the computed gain and directivity. As can be observed, the computed gain is, not only close to the value supplied by the manufacturer, but also within the tolerance margin indicated by the manufacturer. Hence, it can be is concluded that the computed transmitting coefficients are completely correct.

Frequency	Measured S_{11}	Supplied Gain	Computed Gain	Computed Directivity
26.40 GHz	-17.62 dB	18.10 dB	**18.25 dB**	18.61 dB
36.85 GHz	-15.00 dB	20.80 dB	**20.87 dB**	20.98 dB

Table 6.2: Determined parameters of the pyramidal horn from the correct transmitting coefficients using the iterative algorithm for two identical antennas.

Practical results 2 In the second situation the wideband horn shown in Fig. 6.13 was measured using an identical antenna as a probe. The measurement was taken at a distance of 1.88 m and at five different frequencies: 11.50 GHz, 11.90 GHz, 12.10 GHz, 12.30 GHz and 12.50 GHz. Hence, again the electrical measurement distance was larger than 50 λ and the approximation of calibration factor constant for all combinations of s and n could be assumed.

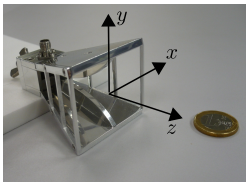

Figure 6.13: Measured wideband horn and position with regard to the coordinate system of the AUT.

Of course, as the above antenna, the horn of Fig. 6.13 is not an ideal first-order probe, but an odd-order probe. Nevertheless, as Fig. 6.14 shows, the power of high odd-order modes ($\mu = \pm 3, \pm 5, \cdots$) remains 13 dB below the power of modes $\mu = \pm 1$ at 12.10 GHz. Thus, by assuming the same behavior at the other frequencies, this horn may be considered as a first-order probe with low error.

As in the first example, the iterative algorithm was applied to the measurements taken at the different frequencies and, after 11 iterations, the calibration factor on each frequency was determined. Then, the transmitting coefficients computed in the eleventh iteration were suitably corrected with the determined factor to obtain the correct transmitting coefficients. As an example, Fig. 6.15 shows the XZ and YZ planes of the normalized far-field pattern at 12.10 GHz computed with the transmitting coefficients at this frequency.

Finally, using the correct transmitting coefficients, the gain and the directivity were computed. Table 6.3 shows these parameters in conjunction with

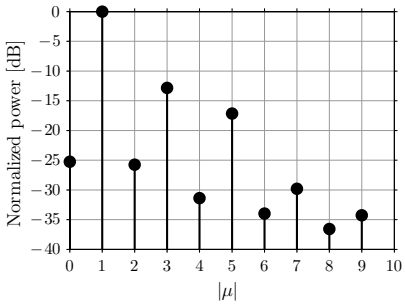

Figure 6.14: Normalized power of the wideband horn receiving coefficients for several indices μ at 12.10 GHz.

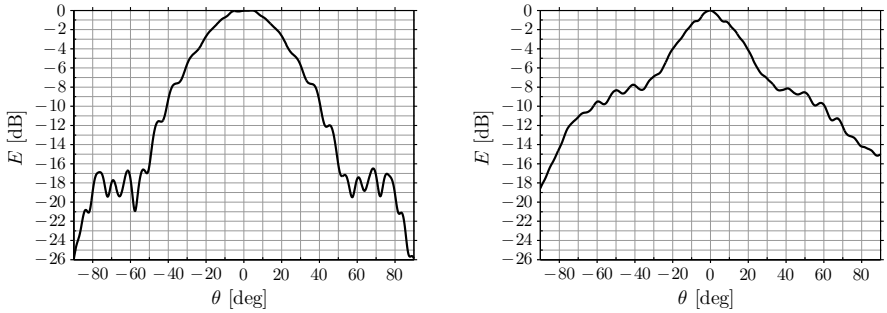

(a) XZ Plane.

(b) YZ Plane.

Figure 6.15: Computed far-field of the wideband horn at 12.1 GHz using the correct transmitting coefficients.

the measured S_{11} parameter and the gain value supplied by the manufacturer. In this case, the manufacturer does not indicate any tolerance for their supplied values. However, as can be observed, the computed values at each frequency are all close to the supplied value what, considering the tolerances of the measurement system used for the calibration and the fact of not been an ideal first-order probe, suggests that the obtained transmitting coefficients are quite accurate.

6.4.2 Case 2: Two different antennas

When two identical first-order probes are not available for the probe calibration, but two different first-order probes, the solution adopted in the case 1 cannot be applied. Of course, the use of the electric Hertzian dipole in the first iteration of

Frequency	**Measured** S_{11}	**Supplied Gain**	**Computed Gain**	**Computed Directivity**
11.50 GHz	-27.72 dB	11.30 dB	**11.50 dB**	12.37 dB
11.90 GHz	-20.73 dB	11.22 dB	**11.45 dB**	12.43 dB
12.10 GHz	-18.39 dB	11.25 dB	**11.52 dB**	12.53 dB
12.30 GHz	-16.58 dB	11.35 dB	**11.74 dB**	12.55 dB
12.50 GHz	-15.74 dB	11.50 dB	**11.80 dB**	12.50 dB

Table 6.3: Determined parameters of the wideband horn from the correct transmitting coefficients using the iterative algorithm for two identical antennas.

the iterative algorithm introduces an error which is propagated throughout the whole iterative algorithm. However, in this case, the advantages of the case 1 are not present. Hence, two different measurements like the ones depicted in Fig. 6.6(a) and Fig. 6.6(b) must be used (since the antennas are different, the exchange of AUT and probe does not lead to the same measurement). In addition, the transmitting coefficients of both antennas are completely different, what causes a different solution in odd and even iterations.

Nevertheless, the behavior of the iterative algorithm considering the propagation of the calibration factor can be studied. Thus, a similar solution to the one of case 1 might be adopted. With this aim, Fig. 6.16 (where, for the sake of simplicity, the dependence of the calibration factor with regard to the distance has not been indicated), depicts the iterative algorithm if the error introduced in the first iteration by $\beta(kD_A)$ (and propagated throughout the whole algorithm) is considered. As in the previous case, it is assumed a measurement distance larger than 50 λ, hence, the factor $\beta(kD_A)$ does not depend on the indices s and n.

As can be observed, the iterative algorithm starts from the measurement M_A (Fig. 6.6(a)). Hence, in the first iteration, the obtained transmitting coefficients are the antenna A transmitting coefficients multiplied by the calibration factor. This calibration factor is the error introduced by considering the electric Hertzian dipole receiving coefficients instead of the antenna B (the probe in measurement M_A) receiving coefficients, i.e., the calibration factor in this case is defined as:

$$\beta_{sn}(kD_A) = \frac{PB_{s1n}(kD_A)|_{CORRECT}}{P_{s1n}(kD_A)|_{DIPOLE}}. \tag{6.27}$$

where $PB_{s1n}(kD_A)|_{CORRECT}$ are the probe response constants of the antenna B.

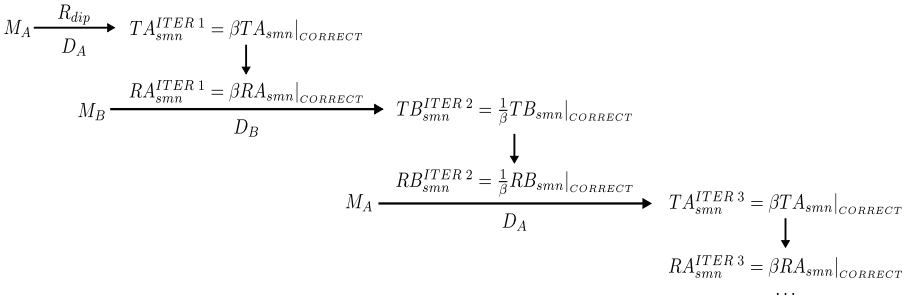

Figure 6.16: Propagation of error throughout the iterative algorithm for the case of two different antennas, starting from the measurement M_A.

In Fig. 6.16, it can be seen that the factor $\beta(kD_A)$ is propagated throughout the iterative algorithm, even when the antenna B transmitting coefficients are computed. However, no error is introduced by the antenna A because the electric Hertzian dipole receiving coefficients are not used at any point instead of the antenna A receiving coefficients. Furthermore, it can be observed in Fig. 6.16 that two sets of solutions are obtained: the antenna A transmitting coefficients multiplied by $\beta(kD_A)$, and the antenna B transmitting coefficients divided by $\beta(kD_A)$. This is a great drawback because, if the same procedure as for the case of two identical antennas is applied to this case, i.e., if the transmitting coefficients computed in odd and even iterations are related, the calibration factor is expressed as follows:

$$\beta(kD_A) = \sqrt{\frac{TA_{smn}^{ITER\,odd} TB_{smn}|_{CORRECT}}{TB_{smn}^{ITER\,even} TA_{smn}|_{CORRECT}}}. \tag{6.28}$$

This expression does not allow the calibration factor to be computed because it requires the knowledge of the correct antenna A and B transmitting coefficients, which, in fact, are the aim of the algorithm. Hence, this algorithm, and the expression (6.28), are not enough to compute the desired correct antenna A transmitting coefficients.

In order to try other possibilities, the iterative algorithm can be started from the measurement M_B. Fig. 6.17, where the dependence of the calibration factor with regard to the distance has not been noted for the sake of simplicity, shows the behavior of the algorithm in this case. As can be observed, the algorithm looks like the previous algorithm (depicted in Fig. 6.16), however, now, the error introduced by the electric Hertzian dipole receiving coefficients is noted as $\alpha(kD_B)$. This is because the error in this case is not the same as in

the previous case. Now, the calibration factor is the error with regard to the antenna A receiving coefficients, i.e., in general, $\alpha_{sn}(kD_B)$ is defined as:

$$\alpha_{sn}(kD_B) = \frac{PA_{s1n}(kD_B)|_{CORRECT}}{P_{s1n}(kD_B)|_{DIPOLE}}. \tag{6.29}$$

where $PA_{s1n}(kD_B)|_{CORRECT}$ are the probe response constants of the antenna A.

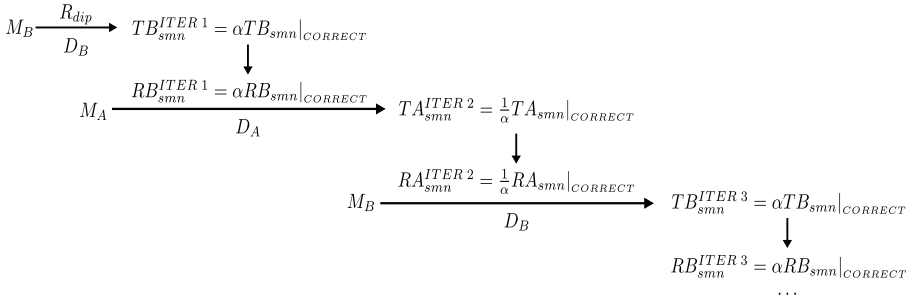

Figure 6.17: Propagation of error throughout the iterative algorithm for the case of two different antennas, starting from the measurement M_B.

Similarly to the previous situation, the transmitting coefficients computed in odd and even iterations can be related to obtain the following factor:

$$\alpha(kD_B) = \sqrt{\frac{TB_{smn}^{ITER\ odd} TA_{smn}|_{CORRECT}}{TA_{smn}^{ITER\ even} TB_{smn}|_{CORRECT}}} \tag{6.30}$$

This expression has the same problem as the expression (6.28), i.e., the correct antenna A and B transmitting coefficients are required to compute $\alpha(kD_B)$. In addition, if expressions (6.28) and (6.30) are related, no way has been found to compute the desired factors ($\beta(kD_A)$ or $\alpha(kD_B)$) without requiring the correct antenna A and B transmitting coefficients.

Therefore, if two identical first-order probes are not available for the probe calibration and, hence, two different measurements are required for the calibration, the same procedure proposed for the case of two identical first-order probes cannot be directly applied. Hence, another procedure must be used in this situation.

In this thesis, two different solutions for two different situations are proposed which aim is the computation of the calibration factor. Next two sections explain both solutions.

6.4.2.1 Application of the supplied gain

The probes used in spherical measurements are normally characterized by the manufacturer or certified by an external laboratory. Among the common parameters that are supplied, the gain is one of the most interesting since it provides valuable information about the antenna. Thus, in this section it is proposed an alternative to the iterative algorithm [133] which makes use of the probe's gain parameter to obtain the correct probe receiving coefficients.

To do this, first it must be expressed the gain determined if the computed transmitting coefficients on each iteration are applied. In principle, no matter the measurement from which the algorithm starts, i.e., it may start from the measurement M_A (Fig. 6.16) or from the measurement M_B (Fig. 6.17). For instance, if the algorithm starting from the measurement M_A is chosen, and the antenna A is the antenna to be characterized, the gain of this antenna may be expressed as follows:

$$G(\theta,\phi)|_{ITER\ odd} = \frac{\left|\sum_{smn} TA_{smn}^{ITER\ odd}\vec{K}_{smn}(\theta,\phi)\right|^2}{1-|S_{11}|^2}, \tag{6.31}$$

where the coefficients $TA_{smn}^{ITER\ odd}$ are the antenna A correct transmitting coefficients multiplied by the calibration factor, i.e., $\beta(kD_A)TA_{smn}|_{CORRECT}$. The way in which these coefficients are obtained is depicted in Fig. 6.16.

Furthermore, it must be pointed out that, if the correct transmitting coefficients were known, the gain could be determined using the following expression:

$$G(\theta,\phi)|_{CORRECT} = \frac{\left|\sum_{smn} TA_{smn}|_{CORRECT}\vec{K}_{smn}(\theta,\phi)\right|^2}{1-|S_{11}|^2}, \tag{6.32}$$

Thus, since the correct coefficients are applied, the gain determined on this way is the correct gain and, hence, is the same as the gain supplied by the manufacturer, i.e., $G(\theta,\phi)|_{CORRECT} = G(\theta,\phi)|_{SUPPLIED}$.

Therefore, from (6.31) and (6.32), the following relation can be established:

$$\frac{G(\theta,\phi)|_{ITER\ odd}}{G(\theta,\phi)|_{SUPPLIED}} = \frac{\left|\sum_{smn} \beta(kD_A)TA_{smn}|_{CORRECT}\vec{K}_{smn}(\theta,\phi)\right|^2}{\left|\sum_{smn} TA_{smn}|_{CORRECT}\vec{K}_{smn}(\theta,\phi)\right|^2}. \tag{6.33}$$

As can be observed in this expression, there are two unknowns: the calibration factor and the antenna A correct transmitting coefficients. However, it is assumed that the measurement distance is larger than 50 λ and, hence, as indicated in (6.33), the calibration factor does not depend on s and n. Thus the factor $\beta(kD_A)$ can be extracted from the sum and, therefore, the expression (6.33) may be simplified. By doing so, the calibration factor can be obtained from just known parameters as follows:

$$|\beta(kD_A)| = \sqrt{\frac{G(\theta,\phi)|_{ITER\ odd}}{G(\theta,\phi)|_{SUPPLIED}}}. \tag{6.34}$$

The described procedure has several drawbacks. Firstly, just the absolute value of the calibration factor can be computed; secondly, the measurements must be taken at distances larger than 50 λ in order to reduce the error introduced by the simplification of calibration factor; and, finally, the gain of the antenna that is being characterized must be known.

However, all drawbacks can, normally, be overcome. With regard to the first drawback, the resulting antenna A receiving coefficients are usually used for the gain determination and, hence, the knowledge of the absolute value of the receiving coefficients may be enough. Concerning to the second drawback, at high frequencies, the restriction of a measurement distance larger than 50 λ may be satisfied in many cases (e.g., at 10 GHz, 50 λ are 1.5 m). Finally, if the antenna has been bought, the gain is probably known since the manufacturer indicates the specifications of the antenna, among which the gain is always included.

In addition, this procedure has the advantage of just requiring one measurement. To do this, the gain $G(\theta,\phi)|_{ITER\ odd}$ must be determined with the transmitting coefficients computed in the first iteration. Thus, the calibration factor is obtained (6.34) with just one iteration and the measurement M_B is not used. Later, the antenna A transmitting coefficients are obtained from the coefficients computed in the first iteration and, with these coefficients, the antenna A receiving coefficients, which are the aim of the probe calibration technique.

Nevertheless, it must be pointed out that it has been observed a convergence behavior towards two sets of solutions after several iterations. Hence, better solutions may be achieved if, instead of the transmitting coefficients of the iteration 1, the transmitting coefficients computed in a higher iteration are used.

Practical results 1 The procedure described above was tested in two different cases. The first one was the same as the first example of Section 6.4.1, i.e., the measurement of the standard gain horn depicted in Fig. 6.2 using an iden-

tical antenna as a probe. As indicated in that section, the measurement was taken at 1.49 m and the operating frequencies were 26.40 GHz and 36.85 GHz.

Of course, the procedure described in this section is not aimed at the measurement with two identical antennas, in which case the technique described in Section 6.4.1 is more accurate. However, it is worth to test if the proposed technique works in a familiar situation. To do this, the gain supplied by the manufacturer (shown in Table 6.2) was used to compute the absolute value of the calibration factor by means of (6.34). The applied transmitting coefficients were the coefficients computed in the eleventh iteration (Fig. 6.16).

Using these data, the absolute value of the obtained calibration factor at 36.85 GHz was: $|\beta(kD)| = 8.44$. It must be pointed out that, in the previous section, where the iterative algorithm for the case of two identical antennas was applied, the obtained calibration factor at 36.85 GHz was: $\beta(kD) = 2.2 - 8.13j$, which absolute value is 8.42. Hence, it can be concluded that this second technique offers a quite good approximation to the correct calibration factor.

Once the calibration factor was known, the correct transmitting coefficients were obtained using the computed coefficients in the eleventh iteration and the obtained factor ($|\beta(kD)| = 8.44$). Table 6.4 shows the gain determined by applying these correct coefficients. As can be seen, the computed gain is close to the supplied gain and just a little variation (caused because of the applied approximations) takes place. Thus, it is confirmed that the proposed technique gives quite good results.

Frequency	**Measured S_{11}**	**Supplied Gain**	**Computed Gain**
26.40 GHz	-17.62 dB	18.10 dB	**18.30 dB**
36.85 GHz	-15.00 dB	20.80 dB	**20.70 dB**

Table 6.4: Determined parameters of the conical horn from the correct transmitting coefficients using the gain supplied by the manufacturer.

Practical results 2 In the second case, the proposed technique was applied for the calibration of the pyramidal horn depicted in Fig. 6.18(a) (antenna A). In this case an identical antenna was not available and, hence, a different antenna was used as a probe. Specifically, the probe antenna was the corrugated conical horn shown in Fig. 6.18(b) (antenna B). Since both antennas (A and B) were different, the measurements M_A and M_B of Fig. 6.6(a) and Fig. 6.6(b), respectively, were taken. The measurement distance was 3.26 m in the measurement M_A and 3.15 m in the measurement M_B, and the operating frequency was 12.1 GHz. Hence, in both cases, the measurement distance was larger than 50 λ and the approximation of the calibration factor could be applied.

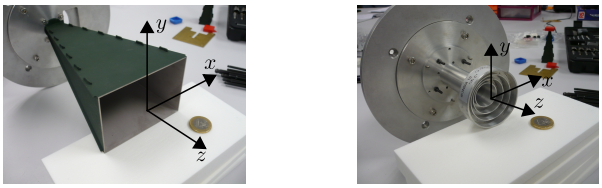

(a) Pyramidal horn. (b) Corrugated horn.

Figure 6.18: Measured antennas at 12.1 GHz.

As the algorithm for two identical antennas, the algorithm proposed in this section is aimed at first-order probes. On the one hand, the pyramidal horn of Fig. 6.18(a) is not a first-order probe, but an odd-order probe. Nevertheless, as depicted in Fig. 6.19(a), the power of the high odd-order modes ($\mu = \pm 3, \pm 5, \cdots$) remains 15 dB below the power of modes $\mu = \pm 1$. Thus, it may be assumed that this horn is a first-order probe with a small error.

On the other hand, the antenna of Fig. 6.18(b) is a rotationally symmetric horn and is excited by a circular waveguide with the TE_{11} mode propagating. Hence, as Fig. 6.19(b) shows, this antenna is an ideal first-order probe and, hence, no approximations must be done with regard to this antenna.

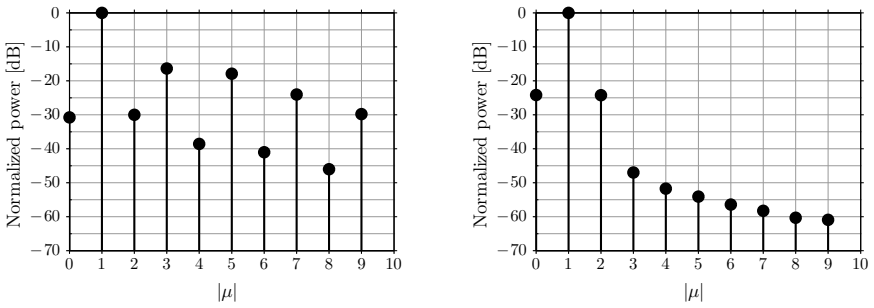

(a) Pyramidal horn. (b) Corrugated conical horn.

Figure 6.19: Normalized power of the pyramidal and conical horn receiving coefficients for several indices μ at 12.10 GHz.

Once the measurements M_A and M_B were taken, the iterative algorithm depicted in Fig. 6.16, i.e., the algorithm which starts from the measurement M_A, was applied for 11 iterations. Then, the antenna A transmitting coefficients computed in the eleventh iteration were used to determine the gain of the antenna A. Later, this gain, and the gain supplied by the manufacturer

(19.96 dB), were used to obtain the calibration factor by means of the expression (6.34). As a result, the obtained calibration factor was: $|\beta(kD_A)| = 3.60$.

Finally, the transmitting coefficients computed on each iteration of the iterative algorithm were corrected and, thus, the correct antenna A and B transmitting coefficients were obtained.

In order to verify if the computed transmitting coefficients were really correct, firstly, the far field was computed. Fig. 6.20 shows the main planes of the normalized far-field pattern for both measured antennas. As can be observed, no big mistakes are detected. Moreover, if the beamwidth supplied by the manufacturer of the pyramidal horn is considered (18° in the XZ plane and 18.75° in the YZ plane), it can be concluded that a quite good far-field pattern was obtained. Of course, being $\beta(kD_A)$ constant, the same normalized pattern would have been obtained if the non-corrected transmitting coefficients had been applied, as pointed out in Section 6.2. However, it is worth to test that, not only specific parameters are correct, but also the pattern computed from the transmitting coefficients.

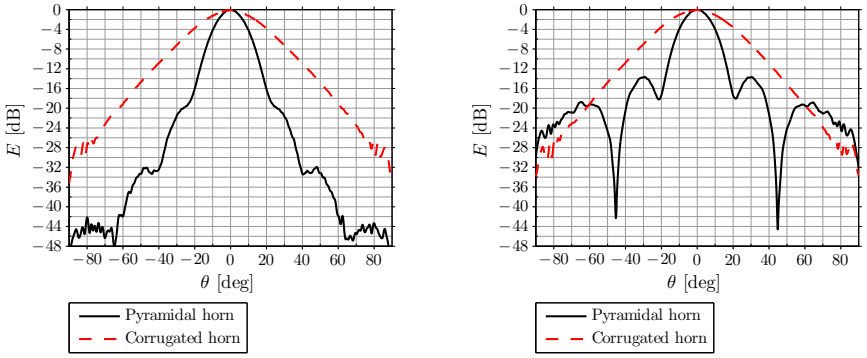

(a) XZ Plane. (b) YZ Plane.

Figure 6.20: Computed far-field of the horns measured at 12.1 GHz using the correct transmitting coefficients.

Secondly, the gain of both antennas was determined applying the computed correct transmitting coefficients. Table 6.5 shows the result for the pyramidal horn. As can be observed, the computed gain is very close to the gain value supplied by the manufacturer, which has a tolerance of ±0.25 dB.

Concerning the corrugated horn, the gain was also computed and the result is shown in Table 6.6. In this case the manufacturer did not supply the gain of the antenna and, hence, it has not been included in the table to compare this value to the computed gain. However, it may be commented that the

Frequency	Measured S_{11}	Supplied Gain	Computed Gain	Computed Directivity
12.10 GHz	-20.80 dB	19.96 dB	**19.90 dB**	20.48 dB

Table 6.5: Determined parameters of the pyramidal horn at 12.1 GHz from the correct transmitting coefficients using the gain supplied by the manufacturer

computed gain is lower than the directivity. Hence, the computed gain is in the valid variation margin.

Frequency	Measured S_{11}	Computed Gain	Computed Directivity
12.10 GHz	-20.80 dB	**13.39 dB**	13.74 dB

Table 6.6: Determined parameters of the corrugated horn at 12.1 GHz from the correct transmitting coefficients of the corrugated horn using the gain supplied by the manufacturer.

6.4.2.2 Use of an additional antenna

Sometimes, the drawbacks of the solution described in previous section cannot be overcome. For instance, if the gain of, at least, one of the antennas involved in the calibration procedure is not known, the described technique cannot be applied. Consequently, another technique must be applied.

This section proposes an alternative procedure for the probe calibration for first-order probes. This new method does not require two identical antennas nor the gain of one of the antennas involved in the calibration. Nevertheless, an additional antenna is required, i.e., the new method employs three different antennas, as well as two more measurements, i.e., altogether four spherical measurements must be taken. As a result, the obtained transmitting coefficients are correct, not only in absolute value, but also in phase, since the complex value of the calibration factor is obtained.

Before describing the way the new technique works, the measurements to be carried out must be detailed. Considering that the antenna A is the antenna to be characterized and the antenna B is the auxiliary probe, the first two measurements are exactly the same as the ones depicted in Fig. 6.6, i.e., the measurements M_A and M_B. To do the rest of measurements, an additional antenna, from now on *Antenna C*, must be used. No special restrictions with

regard to this antenna must be taken into account; however it must guaranteed that the antenna works correctly at the operating frequency.

Once the antenna C has been chosen, the spherical measurements depicted in Fig. 6.21 must be carried out. As can be observed, in both cases the radiated field of the antenna C is measured. However, in the first case (Fig. 6.21(a)), the probe is the antenna A and, in the second case (Fig. 6.21(b)), the probe is the antenna B. It is important to note that the measurement distances of these measurements must be exactly the same as the measurement distances of M_A and M_B. Specifically, the measurement distance of M_{CA} must be the same as the measurement distance of M_B, i.e., D_B, and the measurement distance of M_{CB} must be the same as the measurement distance of M_A, i.e., D_A. This aspect is necessary later to deduce the formulas to compute the calibration factor.

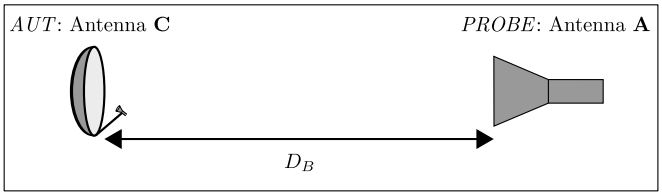

(a) Measurement M_{CA}.

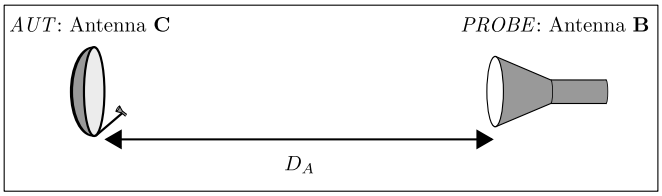

(b) Measurement M_{CB}.

Figure 6.21: Measurements set-ups for the additional antenna.

Being all the necessary measurements available, the next step can be carried out. To do this, first the iterative algorithms depicted in Fig. 6.16 and Fig. 6.17 must be applied using the measurements M_A and M_B. Then, the antenna C transmitting coefficients must be computed, as depicted in Fig. 6.22, from both, the measurements M_{CA} and M_{CB}, using the electric Hertzian dipole receiving coefficients. As can be observed, the error introduced by considering the dipole coefficients ($\beta(kD_A)$ and $\alpha(kD_B)$) is the same as the error propagated throughout the iterative algorithms, since the probes and the measurement distances in measurements M_A and M_{CB} are the same, as well as in the measurements M_B and M_{CA}.

$$M_{CB} \xrightarrow[D_A]{R_{dip}} TC_{smn}^{M_{CB}} = \beta(kD_A)TC_{smn}|_{CORRECT} \qquad M_{CA} \xrightarrow[D_B]{R_{dip}} TC_{smn}^{M_{CA}} = \alpha(kD_B)TC_{smn}|_{CORRECT}$$

(a) Using measurement M_{CB}. (b) Using measurement M_{CA}.

Figure 6.22: Computation of the antenna C transmitting coefficients using the electric Hertzian dipole receiving coefficients.

Therefore, at this moment, several sets of coefficients are available: the coefficients from the iterative algorithms of Fig. 6.16 and Fig. 6.17, and the coefficients depicted in Fig. 6.22. The advantage is that all these coefficients are affected by just two kind of errors, namely $\beta(kD_A)$ and $\alpha(kD_B)$. This fact allows two different relations to be deduced. To do this, firstly, the transmitting coefficients computed on the odd iterations of the algorithm depicted in Fig. 6.16 ($TA_{smn}^{ITER\ odd}$) and the transmitting coefficients obtained on the even iterations of algorithm shown in Fig. 6.17 ($TA_{smn}^{ITER\ even}$) must be related to establish the following relation:

$$\beta(kD_A)\alpha(kD_B) = \frac{TA_{smn}^{ITER\ odd}}{TA_{smn}^{ITER\ even}}. \tag{6.35}$$

Secondly, the computed antenna C transmitting coefficients depicted in Fig. 6.22 must be related to obtain the following expression:

$$\frac{\beta(kD_A)}{\alpha(kD_B)} = \frac{TC_{smn}^{M_{CB}}}{TC_{smn}^{M_{CA}}}. \tag{6.36}$$

Finally, expressions (6.35) and (6.36) must be combined to deduce the following expressions for the computation of the calibration factors:

$$\alpha(kD_B) = \sqrt{\frac{TA_{smn}^{ITER\ odd}TC_{smn}^{M_{CA}}}{TA_{smn}^{ITER\ even}TC_{smn}^{M_{CB}}}}, \tag{6.37}$$

$$\beta(kD_A) = \alpha_{sn}(kD_B)\frac{TC_{smn}^{M_{CB}}}{TC_{smn}^{M_{CA}}}. \tag{6.38}$$

Previous expressions are completely obtainable since all the factors involved in the computation can be obtained as it has been described previously. Hence, the calibrations factors can be determined and, with these, the correct antenna A, B and C transmitting coefficients.

The main drawback of the described technique is the requirement of an additional antenna and the fact of having to take two extra spherical measurements. However, this technique is the most general technique since no

assumptions have been done with regard to the kind of antennas (apart from being first-order probes the antennas A and B) or the knowledge of the gain of the antennas.

Practical results The algorithm described above was tested with the antennas shown in Fig. 6.18 working at 12.1 GHz. Specifically, the antenna of Fig. 6.18(a) was the antenna A, and the antenna of Fig. 6.18(b) was the antenna B. As an additional antenna (antenna C), the RLSA antenna depicted in Fig. 6.23 was used. The measurement distances in the measurements M_A and M_B were the same as in the example of previous section, i.e., $D_A = 3.26$ m and $D_B = 3.15$ m. For the measurements of the antenna C (M_{CA} and M_{CB}), the measurement distances were suitably kept, i.e., $D_{CB} = D_A$ and $D_{CA} = D_B$.

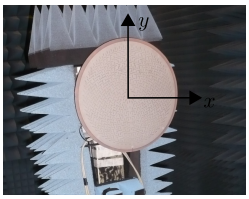

Figure 6.23: Measured RLSA antenna and position with regard to the coordinate system of the AUT.

Firstly, the procedure described above was carried and the calibration factors were obtained. As a result, the computed factors were: $\beta(kD_A) = 0.99 + 3.64j$ and $\alpha(kD_B) = 0.30 - 7.76j$. If the absolute value of $\beta(kD_A)$, i.e., 3.77, is compared to the value obtained with the algorithm proposed in Section 6.4.2.1, i.e., 3.60, it is confirmed that both methods obtain similar results.

Once the calibration factors were obtained, the antenna A, B and C correct transmitting coefficients were obtained. Fig. 6.24 shows the normalized far-field pattern of the antenna C computed from its transmitting coefficients. The normalized far-field pattern of the antennas A and B is the same as the one shown in Fig. 6.20.

Finally, the gain and directivity were determined for the three antennas using the correct transmitting coefficients. Table 6.7 shows the result. Regarding the pyramidal horn, the supplied gain (19.96 dB, from Table 6.5) can be compared to the computed gain. By doing so, it can be observed that the computed gain is quite close to the supplied value.

Unfortunately, the gain of the corrugated horn and the RLSA antenna is not supplied and, therefore, the computed gain of these antennas cannot be verified. However, it is worth to mention that the gain of both antennas is below the directivity and, hence, they are within the valid margin. This fact,

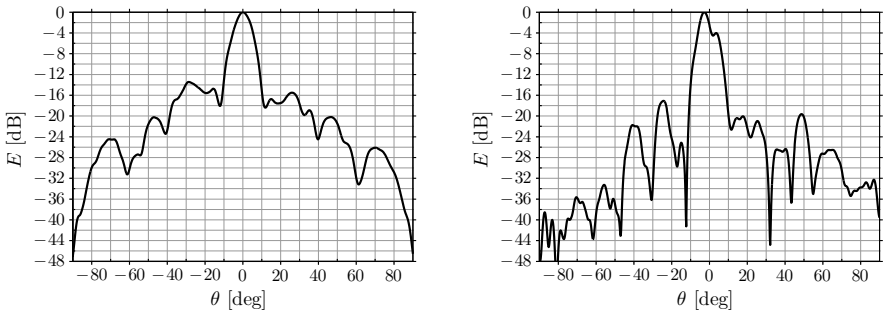

(a) XZ Plane.

(b) YZ Plane.

Figure 6.24: Computed far-field of the RLSA antenna at 12.1 GHz using the correct transmitting coefficients.

in conjunction with the gain of the pyramidal horn, allows to be concluded that the proposed technique obtains accurately the transmitting coefficients.

Antenna	**Measured** S_{11}	**Computed Gain**	**Computed Directivity**
Pyramidal horn	-20.80 dB	**19.37 dB**	20.42 dB
Corrugated horn	-23.92 dB	**13.51 dB**	13.74 dB
RLSA antenna	-18.50 dB	**24.10 dB**	25.31 dB

Table 6.7: Determined parameters of the pyramidal horn, the corrugated horn and the RLSA antenna at 12.1 GHz from the correct transmitting coefficients using the additional antenna technique.

Chapter 7

Conclusions

This thesis has dealt with the diagnosis of antennas by means of the study of the equivalent currents on a surface close to the antenna. These currents have been obtained from spherical measurements which, in general, have been considered to be taken in the near-field region.

Firstly, the vector wave equation was solved in four different coordinate systems. Among these coordinate systems, the most interesting systems for this thesis were the planar and the spherical coordinate systems. The reason of this choice lay in the determination of the equivalent currents on a flat surface and the use of spherical measurements. By using the planar coordinate system, the plane wave spectrum could be used as an intermediate step between the spherical measurements and the desired currents. Chapter 3 presented two different options to perform this transformation by using the modal expansion and the plane wave spectrum. Also, the reconstruction of the equivalent currents was carried out by an integral equation technique and the method of moments.

The above techniques may be divided in two groups: those that apply a direct transformation, from the spherical near-field measurement to the field on the surface of interest and, hence, to the desired equivalent currents (the integral equation technique and the SWE-to-PWE technique), and those that use the far field (the microwave holographic technique). The advantage of the first kind of techniques is the possibility of using the information present in the waves that are present in the near-field region (the evanescent waves) but not in the far field region.

By looking at the results, it is clear that an improvement in resolution is achieved by using the direct transformation. However, in a practical case, this improvement is quite hard to achieve. The reason or this drawback was studied in Chapter 4. Here it was shown how the evanescent waves are strongly attenuated, at short distances. Thus, extremely short measurement distances

must be used to measure these waves, what entails some limitations such as reflections and coupling between AUT and probe.

Assuming that the evanescent waves cannot be normally measured, the only information that can be used normally to reconstruct the equivalent currents is the information present in the far field. Thus, if the field is measured in the far-field region or if the far field is used as an intermediate step, no loss of information is produced in most of situations. In this thesis, this last case (i.e., the microwave holographic technique) has been considered. In Chapter 4 the resolution of the equivalent currents by using this field was studied and it was shown how, in this situation, just the visible plane wave spectrum (i.e., a circle of radius k) is available for the reconstruction. Moreover, in this chapter it was deduced that, with this spectrum, the maximum resolution that can be achieved in the reconstructed currents is 1 λ.

To increase the resolution obtained by using the far field, Chapter 5 proposed several techniques. Firstly the iterative Papoulis-Gerchberg algorithm was proposed, whose aim was to estimate the non-visible spectrum by extrapolating the visible spectrum and using the maximum size of the antenna. As a result, quite accurate equivalent currents were obtained for ideal antennas. The resolution was increased and, by looking at the examples, elements separated 0.8 λ could be clearly distinguished. However, when applying the algorithm to an antenna with elements separated 0.4 λ, the elements could not be distinguished. This fact led to use the periodicity property of the spectrum of antennas formed by discrete elements. This property allowed to clearly distinguish the elements separated 0.4 λ and to exactly determine the amplitude of the elements. Hence, it can be concluded that the proposed technique (the iterative algorithm and the replication of the spectrum) increases the resolution, from 1 λ with the visible spectrum up to 0.4 λ with the proposed technique.

Nevertheless, when applying the algorithm to a real antenna, the results were not as accurate as it was desired. This fact led to apply more restrictive spatial filters (the Papoulis-Gerchberg algorithm just applies a wide filter including all the sources). The equivalent currents were improved, and the currents inside the slots could almost be observed. However, the algorithm was iterative and, hence, not too much iterations could be applied. For this reason, the direct version of the iterative algorithm was also studied in order to improve the reconstructed equivalent currents by using a higher number of iterations but without increasing the computation time.

This direct version was the so-called extrapolation matrix which, in 2-D, could be implemented in two different ways. The first way was the extrapolation matrix by rows and columns, which offered quite good results for linear arrays. The obtained currents were the same as for the iterative algorithm but with a lower computation time. In addition, no increase of this time was produced by increasing the number of iterations so that a high number of iterations

could be applied in the same time. The problems of this technique were its limitations regarding the kind of filters, the shape of the spectrum applied in the extrapolation and the separation of the extrapolation in two different parts, by rows and columns. For these reasons, the second way, the generalized extrapolation matrix was proposed.

This matrix solved the drawbacks of the extrapolation matrix by rows and columns, but involved other problems. The generalized extrapolation matrix required the inversion of an ill-conditioned matrix which, by not fitting in memory, had to be divided into blocks. However, by overcoming these problems, it was shown how the results were quite accurate. In addition, the computation time of this matrix was smaller than the computation time of the iterative algorithm, and the result after an infinite number of iterations could be obtained, i.e., the same result at which the iterative algorithm tends. Nevertheless, in Chapter 5 it was also shown how this technique, though improving the resolution, does not obtains considerably better results than with the iterative algorithm, even though an infinite number of iterations are applied.

In order to improve the obtained currents, another technique, the PDFT (prior discrete Fourier transform), was applied. The aim of this technique is to improve the spatial signal, i.e., the equivalent currents, rather than to extrapolate the visible spectrum. The drawbacks of the PDFT were the same as the drawbacks of the generalized extrapolation matrix, however the equivalent currents obtained by the PDFT were quite better. Whereas the use of a wide filter led to the same results as the iterative algorithm (the same resolution, around $0.7\sim0.8\ \lambda$, was obtained), the use of a restrictive filter improved the results. In this last case, for antennas formed by discrete elements, the resolution was also around $0.3\sim0.4\ \lambda$, as in the iterative algorithm. In addition, the application of a restrictive algorithm to a real antenna allowed the current inside the slot to be determined.

By looking at all the above techniques, it may be concluded that the most interesting techniques are the iterative Papoulis-Gerchberg algorithm and the PDFT. Whereas the PDFT technique allows quite good results to be obtained in a single operation, the iterative algorithm leads also to good results in many cases, but without having to compute the inverse of a large matrix. Furthermore, the resolution achieved by both algorithms is almost the same (around $0.3\sim0.4\ \lambda$ if a restrictive spatial filter is used).

Finally, Chapter 6 proposed several algorithms to carry out the probe calibration for first-order probes. Firstly, the error produced by using the electric Hertzian dipole receiving coefficients instead of the correct receiving coefficients was introduced. Then, three different algorithms for three different situations were described. In the first situation the case in which two identical first-order probes are available was described. For this case, a quite accurate algorithm

was presented which allowed the probe receiving coefficients to be accurately determined.

For the second situation, two different antennas were considered, but the gain of one these antennas was assumed to be known. The algorithm proposed for this case allowed the probe under study to be calibrated by just using one full-sphere measurement. As shown in Chapter 6, the receiving coefficients obtained with this algorithm were also accurate in absolute value.

The third situation involved three different antennas and four different spherical measurements. However, no prior knowledge about the gain of the antennas, nor two identical antennas, were required. The advantage of this algorithm is that it allows the accurate computation of the receiving coefficients of a probe, without applying any additional data, just combining several measurements taken in several set-ups.

Therefore, by using the above algorithms, the accurate receiving coefficients of a first-order probe may be determined. Later, these coefficients may be used to compute the accurate transmitting coefficients of another antenna whose radiated field has been measured with the calibrated probe. One of the most important applications of these transmitting coefficients is the possibility of determining the gain of the antenna easily and with a high accuracy, even though near-field measurements are used. As shown in results of Chapter 6, the gain obtained by applying the computed transmitting coefficients is quite accurate and within the margins offered by the manufacturer.

7.1 Further work

The research around the topics studied in this thesis may be continued beyond the presented here in several ways. First of all, the inverse algorithms may be studied in other coordinate systems, such as the cylindrical coordinate system. These studies may be done either by applying an integral equation technique or by applying a modal expansion technique. Regarding this last case, the research may be also followed on the inverse transformation with the oblate spheroidal wave expansion. In this thesis, this possibility has been pointed out and the keys to carry out this transformation have been described. However, no result has been shown. It would be interesting to implement this transformation in order to be able to compare its results with the results of other techniques.

Secondly, the research may be continued by studying other extrapolation techniques. In this thesis, several techniques have been proposed and other techniques have been just pointed out, e.g. the maximum entropy method. It would be interesting to apply these other techniques, whose criterions differ from the criterions of the Papoulis-Gerchberg algorithm and the PDFT. It

must be taken into account that the change of criterions between these two techniques led to similar results but not identical.

In addition, it may be improved the computation of the inverse of the ill-conditioned matrix required in the generalized extrapolation matrix technique and the PDFT. In this thesis, the use of a couple of methods has been proposed. However, in literature a lot of methods to compute this inverse have been presented. It would be interesting to apply other methods to try to improve the result obtained with these techniques.

Finally, the research may be continued on the probe calibration techniques. In this thesis, three algorithms for first-order probes have been presented, however, these probes are not always available. For this reason, it would be interesting to establish an algorithm for the calibration of odd-order probes or, in general, high-order probes. Thus, the receiving coefficients of any probe might be accurately obtained without approximations. By doing so, the correct transmitting coefficients of an antenna might be computed by using any kind of antenna as a probe.

Appendix A

Bessel functions

In this appendix, the expressions to compute the bessel functions are supplied. The aim of this appendix is not to offer a complete and detailed formulation about the bessel functions, which can be found in [46]. The aim is rather to detail the minimum necessary information to compute the wave functions appeared during this thesis. For this reason, the arguments are treated as a variable (ρ or r) multiplied by a constant (k), as it can be found in previous chapters.

Furthermore, it is worth to mention that, in this appendix, a slight change in notation with regard to the rest of the thesis is done. Until now, the complex variable $\sqrt{-1}$ has been denoted as j. However, in this appendix, in order to avoid confusions with regard to the spherical Bessel function (which is referred as j_n), the complex variable $\sqrt{-1}$ is denoted as i.

A.1 Bessel functions of integer order: Bessel functions

Definition

There are several kinds of Bessel functions with integer order [46]. In this thesis, the functions of interest are those (Z) which are solution to the following differential equation:

$$(k\rho)^2 \frac{d^2 Z}{d(k\rho)^2} + \rho \frac{dZ}{d(k\rho)} + ((k\rho)^2 - n^2)Z = 0. \tag{A.1}$$

Several solutions can be found to (A.1). All of them are normally denoted in an uniform notation as $Z_n^{(c)}(k\rho)$, where n is the order and $k\rho$ the argument.

Depending on the index c, the function solution to (A.1) is one of the following list:

1. $Z_n^{(1)}(k\rho) = J_n(k\rho)$, the Bessel function of first kind
2. $Z_n^{(2)}(k\rho) = N_n(k\rho)$, the Bessel function of second kind or Neumann function
3. $Z_n^{(3)}(k\rho) = H_n^{(1)}(k\rho)$, the Hankel function of first kind
4. $Z_n^{(4)}(k\rho) = H_n^{(2)}(k\rho)$, the Hankel function of second kind

The Hankel functions can be easily computed from the Bessel functions of first and second kind as follows:

$$H_n^{(1)}(k\rho) = J_n(k\rho) + iN_n(k\rho) \tag{A.2}$$

$$H_n^{(2)}(k\rho) = J_n(k\rho) - iN_n(k\rho). \tag{A.3}$$

The behavior of the Bessel functions for short arguments ($k\rho$) is shown in Fig. A.1 and Fig. A.2. In Fig. A.1 the behavior of the first and second kind Bessel functions is shown and in Fig. A.2 this behavior is shown for the absolute value and phase of the Hankel function of first kind. Though not depicted, the second kind Hankel function has the same absolute value and a 90° shifted phase with regard to first kind function.

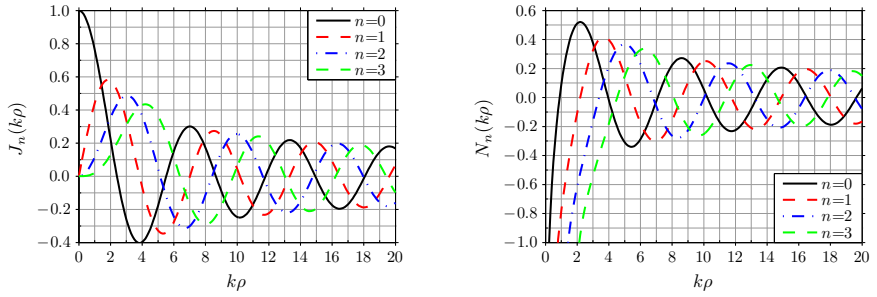

(a) Bessel function of first kind ($J_n(k\rho)$) (b) Bessel function of second kind ($N_n(k\rho)$)

Figure A.1: Low order Bessel functions of first and second kind.

Recurrence relations

The Bessel functions for several orders can be easily computed with the following recurrent relation:

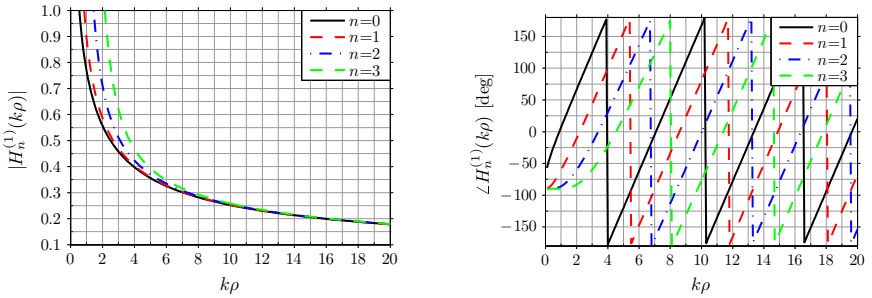

(a) Absolute value of $H_n^{(1)}(k\rho)$

(b) Phase of $H_n^{(1)}(k\rho)$

Figure A.2: Low order Hankel functions of first kind ($H_n^{(1)}(k\rho)$).

$$Z_{n-1}^{(c)}(k\rho) + Z_{n+1}^{(c)}(k\rho) = \frac{2n}{k\rho} Z_n^{(c)}(k\rho). \tag{A.4}$$

In addition, the derivatives of the Bessel functions can be obtained with one of the following recurrent expressions:

$$\frac{dZ_n^{(c)}(k\rho)}{d(k\rho)} = \frac{1}{2}(Z_{n-1}^{(c)}(k\rho) - Z_{n+1}^{(c)}(k\rho)) \tag{A.5a}$$

$$= Z_{n-1}^{(c)}(k\rho) - \frac{n}{k\rho} Z_n^{(c)}(k\rho) \tag{A.5b}$$

$$= -Z_{n+1}^{(c)}(k\rho) + \frac{n}{k\rho} Z_n^{(c)}(k\rho). \tag{A.5c}$$

Graf's Addition theorem

In general, Graf's Addition theorem let us express any Bessel function in one coordinate system ($Z_n^{(c)}(w)$) as a function of the same kind of Bessel function in another coordinate system ($Z_n^{(c)}(u)$) and the Bessel function of first kind in a third coordinate system ($J_n(v)$) as follows:

$$Z_n^{(c)}(w)e^{in\chi} = \sum_{k=-\infty}^{\infty} Z_{n+k}^{(c)}(u) J_k(v) e^{ik\alpha}. \tag{A.6}$$

The previous relation is only valid when $|ve^{\pm j\alpha}| < |u|$ and when variables u, v, w, α and χ are related in the following way:

$$\begin{aligned} w &= \sqrt{u^2 + v^2 - 2uv\cos\alpha} \\ u - v\cos\alpha &= w\cos\chi \\ v\sin\alpha &= w\sin\chi. \end{aligned} \tag{A.7}$$

Graf's addition theorem can be specially useful when dealing with cylindrical wave functions [134]. In this case, this theorem can be applied to translate the Bessel functions of integer order along the y axis from one coordinate system to another. Fig. A.3 the depicts relation between both coordinate systems (primed and unprimed) either for a positive translation (Fig. A.3(a)) or for a negative translation (Fig. A.3(b)).

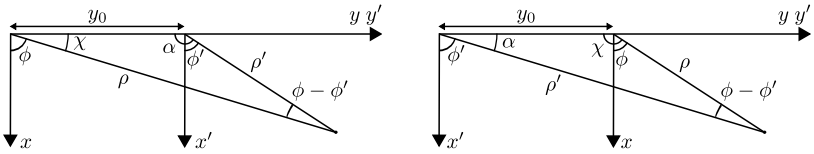

(a) If positive translation ($y_0 > 0$) (b) If negative translation ($y_0 < 0$)

Figure A.3: Diagram for Bessel function translation along y axis.

However, in order to use (A.6), a correspondence must be first stated among the variables of this expression and the cylindrical variables of Fig. A.3. Table A.1 shows this correspondence for both kinds of translations, positive and negative. Once this matching has been carried out, the relation for the Bessel functions expressed in both coordinate systems can be written as follows:

$$Z_n^{(c)}(k\rho)e^{in(\pi/2-\phi)} = \sum_{k=-\infty}^{\infty} Z_{n+k}^{(c)}(|y_0|)J_k(k\rho')e^{ik(\pi/2+\phi')}, \quad if \quad y_0 > 0 \tag{A.8}$$

$$Z_n^{(c)}(k\rho)e^{in(\pi/2+\phi)} = \sum_{k=-\infty}^{\infty} Z_{n+k}^{(c)}(|y_0|)J_k(k\rho')e^{ik(\pi/2-\phi')}, \quad if \quad y_0 < 0 \tag{A.9}$$

Table A.1: Variable correspondence.

Graf's theorem	Cylindrical system if $y_0 > 0$	Cylindrical system if $y_0 < 0$
u	$\|y_0\|$	$\|y_0\|$
v	$k\rho'$	$k\rho'$
w	$k\rho$	$k\rho$
α	$\pi/2 + \phi'$	$\pi/2 - \phi'$
χ	$\pi/2 - \phi$	$\pi/2 + \phi$

A.2 Bessel functions of fractional order: Spherical Bessel functions

Definition

Several kinds of Bessel functions of fractional order can be found in literature [46], e.g. *Riccati-Bessel functions*, *Airy functions*. For this thesis, however, the most interesting functions are the so-called *Spherical Bessel functions*, which is solution of the following differential equation:

$$(kr)^2 \frac{d^2 z}{d(kr)^2} + 2kr \frac{dz}{dkr} + ((kr)^2 - n(n+1))z = 0. \tag{A.10}$$

The solutions to the previous equations are generally denoted as $z_n^{(c)}(kr)$, where n is the order and kr the argument. Depending on the index c, the solution to (A.10) is denoted as as follows:

1. $z_n^{(1)}(kr) = j_n(kr)$, the Spherical Bessel function of first kind
2. $z_n^{(2)}(kr) = n_n(kr)$, the Spherical Bessel function of second kind or Spherical Neumann function
3. $z_n^{(3)}(kr) = h_n^{(1)}(kr)$, the Spherical Hankel function of first kind
4. $z_n^{(4)}(kr) = h_n^{(2)}(kr)$, the Spherical Hankel function of second kind

The Bessel functions of integer order and the spherical Bessel functions are related in the following way:

$$z_n^{(c)}(kr) = \sqrt{\frac{\pi}{2kr}} Z_{n+1/2}^{(c)}(kr) \tag{A.11}$$

As for the Bessel functions of integer order, the spherical Hankel functions and the spherical Bessel functions of first or second kind are related as:

$$h_n^{(1)}(kr) = j_n(kr) + in_n(kr) \tag{A.12}$$

$$h_n^{(2)}(kr) = j_n(kr) - in_n(kr) \tag{A.13}$$

$$j_n(kr) = \frac{h_n^{(1)}(kr) + h_n^{(2)}(kr)}{2} \tag{A.14}$$

$$n_n(kr) = \frac{h_n^{(1)}(kr) - h_n^{(2)}(kr)}{2i} \tag{A.15}$$

Fig. A.4 and Fig. A.5 show the behavior of low order spherical functions for small arguments kr. Specifically, in Fig. A.4(a) the behavior for the spherical Bessel function of first kind is shown and in Fig. A.4(b) for the spherical Bessel function of second kind. Moreover, in Fig. A.5(a) and Fig. A.5(b),the behavior at the same points is depicted for the absolute value and phase, respectively, of the spherical Hankel function of first kind.

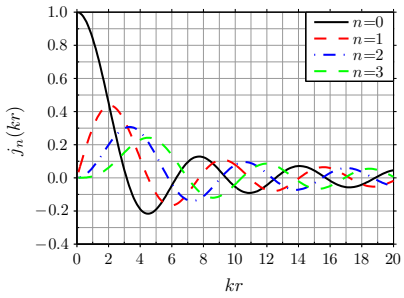

(a) Spherical Bessel function of first kind ($j_n(kr)$)

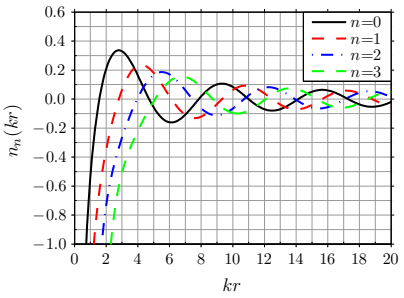

(b) Spherical Bessel function of second kind ($n_n(kr)$)

Figure A.4: Low order spherical Bessel functions of first and second kind.

Recurrence relations

The following recurrent expression can be stated to easily compute the spherical functions of several orders:

$$\frac{1}{kr} z_n^{(c)}(kr) = \frac{1}{2n+1} \left(z_{n-1}^{(c)}(kr) + z_{n+1}^{(c)}(kr) \right). \tag{A.16}$$

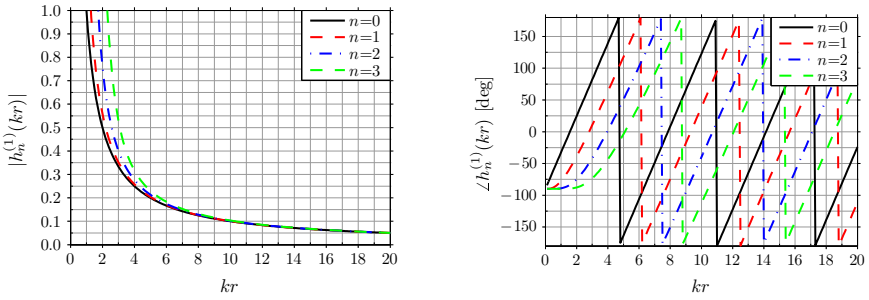

(a) Absolute value of $h_n^{(1)}(kr)$

(b) Phase of $h_n^{(1)}(kr)$

Figure A.5: Low order spherical Hankel functions of first kind ($h_n^{(1)}(kr)$).

In addition, several recurrent relations can be applied to compute the derivatives of the spherical functions. In this case, general expressions are not indicated, but the explicit derivatives needed for the computation of the spherical wave functions required in chapter 2, section 2.2. These expressions, and the way in which they are computed recursively, are:

$$\frac{1}{kr}\frac{d}{d(kr)}\left\{kr z_n^{(c)}(kr)\right\} = z_{n-1}^{(c)}(kr) - n\frac{z_n^{(c)}(kr)}{kr} \tag{A.17a}$$

$$= (n+1)\frac{z_n^{(c)}(kr)}{kr} - z_{n+1}^{(c)}(kr) \tag{A.17b}$$

$$= \frac{1}{2n+1}\left((n+1)z_{n-1}^{(c)}(kr) - n z_{n+1}^{(c)}(kr)\right). \tag{A.17c}$$

Asymptotic behavior

For large kr arguments, both, the spherical Hankel functions and their derivatives, can be approximated by the following simpler expressions valid for $kr \gg n$:

$$h_n^{(1)}(kr) \to (-i)^{n+1}\frac{e^{ikr}}{kr} \qquad kr \to \infty \tag{A.18}$$

$$h_n^{(2)}(kr) \to i^{n+1}\frac{e^{-ikr}}{kr} \qquad kr \to \infty \tag{A.19}$$

$$\frac{1}{kr}\frac{d}{d(kr)}\left\{krh_n^{(1)}(kr)\right\} \to (-i)^n\frac{e^{ikr}}{kr} \qquad kr \to \infty \tag{A.20}$$

$$\frac{1}{kr}\frac{d}{d(kr)}\left\{krh_n^{(2)}(kr)\right\} \to i^n\frac{e^{-ikr}}{kr} \qquad kr \to \infty \tag{A.21}$$

If the spherical Bessel functions of first and second order are the functions that are required for large arguments, the previous expressions in conjunction with (A.14) or (A.15) can be applied for their computation.

Appendix B

Legendre functions

The Legendre functions are used to compute the spherical wave functions (see Chapter 2). In this appendix, these functions are defined and several expressions for their easy computation are shown. In addition, the expressions for the derivatives used in the computation of the spherical wave functions as well as some special values in critical points are indicated.

Nevertheless, as in the Appendix A, a complete study about the Legendre functions is not done. For a detailed information about this kind of functions see [46].

Definition

The Legendre functions are the solution ($L(z)$) to the following differential equation:

$$(1-z^2)\frac{d^2L(z)}{dz^2} - 2z\frac{dL(z)}{dz} + \left(n(n+1) - \frac{m^2}{1-z^2}\right)L(z) = 0 \qquad \text{(B.1)}$$

where $z = x + jy$ (being x and y reals) and x limited to $-1 \leq x \leq 1$. Because of this limitation, when $y = 0$, z may be expressed as $z = \cos\theta$, where $0 \leq \theta \leq \pi$. This case is the one needed for the spherical wave functions computation, hence, just this case will be considered from now on.

The solutions to (B.1) are known as associated Legendre functions of first kind ($P_n^m(\cos\theta)$), and associated Legendre functions of second kind ($Q_n^m(\cos\theta)$), where n is the degree and m is the order. In this thesis, just first the kind functions are employed, hence, just this function is studied in this appendix.

Though not necessary for this thesis, an interesting relation is stated among associated Legendre functions of first kind and Legendre polynomials which, in some cases, may become useful. This relation is:

$$P_n^m(\cos\theta) = (\sin\theta)^m \frac{d^m P_m(\cos\theta)}{d(\cos\theta)^m} \tag{B.2}$$

where the Legendre polynomial $P_m(\cos\theta)$ can be computed as:

$$P_n(\cos\theta) = \frac{1}{2n!} \frac{d^n((\cos\theta)^n - 1)^n}{d(\cos\theta)^n}. \tag{B.3}$$

In Chapter 2, the associated Legendre functions are employed in a normalized form $\bar{P}_n^m(\cos\theta)$. This normalization is carried out as follows:

$$\bar{P}_n^m(\cos\theta) = \sqrt{\frac{2n+1}{2}\frac{(n-m)!}{(n+m)!}} P_n^m(\cos\theta) \tag{B.4}$$

The behavior of the normalized associated Legendre functions for several degrees and orders is shown in Fig. B.1.

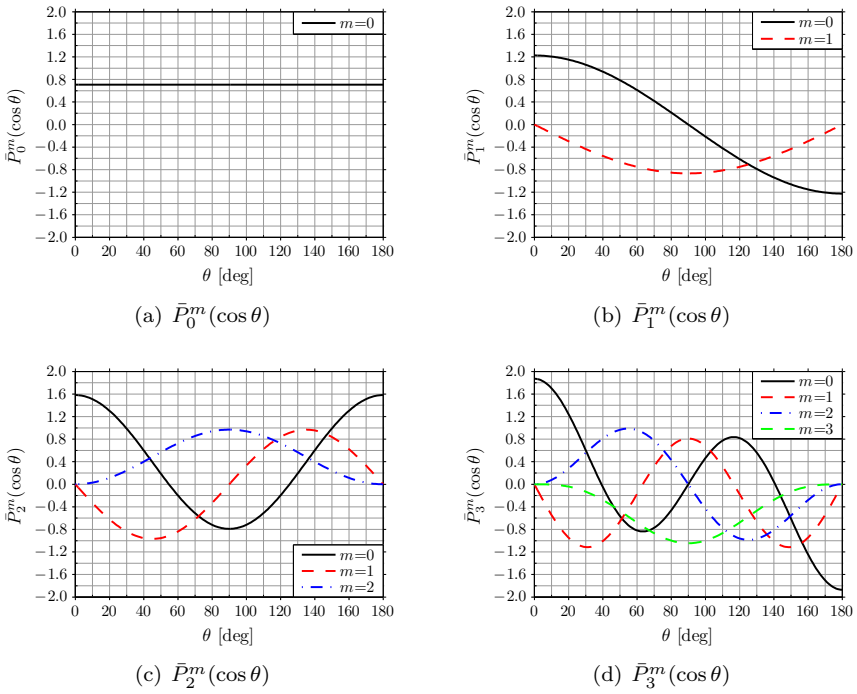

(a) $\bar{P}_0^m(\cos\theta)$ (b) $\bar{P}_1^m(\cos\theta)$

(c) $\bar{P}_2^m(\cos\theta)$ (d) $\bar{P}_3^m(\cos\theta)$

Figure B.1: Normalized associated Legendre functions ($\bar{P}_n^m(\cos\theta)$) for $n = 0 \cdots 3$ and $m = 0 \cdots n$.

Recurrence relations

The associated Legendre functions can be easily computed for several orders or degrees with the following recurrent relations:

$$(n-m+1)P_{n+1}^{m}(\cos\theta) - (2n+1)\cos\theta P_{n}^{m}(\cos\theta) + (n+m)P_{n-1}^{m}(\cos\theta) = 0 \tag{B.5a}$$

$$\sin\theta P_{n}^{m+1}(\cos\theta) - 2m\cos\theta P_{n}^{m}(\cos\theta) + (n+m)(n-m+1)\sin\theta P_{n}^{m-1}(\cos\theta) = 0 \tag{B.5b}$$

$$P_{n}^{n}(\cos\theta) - (2n-1)\sin\theta P_{n-1}^{m-1}(\cos\theta) = 0 \tag{B.5c}$$

The derivative of the associated Legendre functions can also be easily computed with a recursive expression as follows:

$$\frac{dP_{n}^{m}(\cos\theta)}{d\theta} = \begin{cases} -P_{n}^{1}(\cos\theta), & \text{if} \quad m=0 \\ \frac{1}{2}\left[(n-m+1)(n+m)P_{n}^{m-1}(\cos\theta) - P_{n}^{m+1}(\cos\theta)\right], & \text{if} \quad m>0 \end{cases} \tag{B.6}$$

Finally, the spherical wave functions use a relation among associated Legendre functions $P_{n}^{m}(\cos\theta)$, the function $\sin\theta$ and the index m. It is, then, of interest to indicate the following recurrent relation for this special function:

$$\frac{mP_{n}^{m}(\cos\theta)}{\sin\theta} = \begin{cases} 0, & \text{if} \quad m=0 \\ \frac{1}{2}\cos\theta\left[(n-m+1)(n+m)P_{n}^{m-1}(\cos\theta) + P_{n}^{m+1}(\cos\theta)\right] + m\sin\theta P_{n}^{m}(\cos\theta), & \text{if} \quad m>0 \end{cases} \tag{B.7}$$

Special values

The computation of the Legendre functions and its derivative is normally required on the interval from $\theta = 0$ to $\theta = \pi$. Some of these points, however, present singularities and, therefore, must be explicitly indicated.

APPENDIX B. LEGENDRE FUNCTIONS

Since the Legendre functions are involved in the spherical wave functions in three different ways, the special values are indicated on the critical points, namely $\theta = 0$, $\theta = \pi/2$ and $\theta = \pi$, for all ways in which the Legendre functions are employed. Before that, however, in order to reduce notation, the following symbol is defined:

$$n!! = \begin{cases} n \times (n-1) \times \cdots 3 \times 1, & \text{if } n \text{ odd} \\ n \times (n-2) \times \cdots 4 \times 2, & \text{if } n \text{ even} \end{cases} \tag{B.8}$$

With the previous symbol, the special values on critical points are:

$$P_n^{|m|}(\cos\theta)\Big|_{\theta=0} = \begin{cases} 1, & \text{if } |m| = 0 \\ 0, & \text{if } |m| > 0 \end{cases} \tag{B.9a}$$

$$P_n^{|m|}(\cos\theta)\Big|_{\theta=\pi/2} = \begin{cases} (-1)^{(n-|m|)/2} \frac{(n+|m|-1)!!}{(n-|m|)!!}, & \text{if } (n+|m|)\text{even} \\ 0, & \text{if } (n+|m|)\text{odd} \end{cases} \tag{B.9b}$$

$$P_n^{|m|}(\cos\theta)\Big|_{\theta=\pi} = \begin{cases} (-1)^n, & \text{if } |m| = 0 \\ 0, & \text{if } |m| > 0 \end{cases} \tag{B.9c}$$

$$\frac{mP_n^{|m|}(\cos\theta)}{\sin\theta}\Big|_{\theta=0} = \begin{cases} 0, & \text{if } m \neq \pm 1 \\ \pm\frac{n(n+1)}{2}, & \text{if } m = \pm 1 \end{cases} \tag{B.10a}$$

$$\frac{mP_n^{|m|}(\cos\theta)}{\sin\theta}\Big|_{\theta=\pi/2} = \begin{cases} m(-1)^{(n-|m|)/2} \frac{(n+|m|-1)!!}{(n-|m|)!!}, & \text{if } (n+|m|)\text{even} \\ 0, & \text{if } (n+|m|)\text{odd} \end{cases} \tag{B.10b}$$

$$\frac{mP_n^{|m|}(\cos\theta)}{\sin\theta}\Big|_{\theta=\pi} = \begin{cases} 0, & \text{if } m \neq \pm 1 \\ \pm(-1)^{n+1} \frac{n(n+1)}{2}, & \text{if } m = \pm 1 \end{cases} \tag{B.10c}$$

$$\left.\frac{dP_n^{|m|}(\cos\theta)}{d\theta}\right|_{\theta=0} = \begin{cases} 0, & \text{if } |m| \neq 1 \\ \frac{n(n+1)}{2}, & \text{if } |m| = 1 \end{cases} \tag{B.11a}$$

$$\left.\frac{dP_n^{|m|}(\cos\theta)}{d\theta}\right|_{\theta=\pi/2} = \begin{cases} 0, & \text{if } (n+|m|)\text{even} \\ (-1)^{(n-|m|+1)/2}\frac{(n+|m|)!!}{(n-|m|-1)!!}, & \text{if } (n+|m|)\text{odd} \end{cases} \tag{B.11b}$$

$$\left.\frac{dP_n^{|m|}(\cos\theta)}{d\theta}\right|_{\theta=\pi} = \begin{cases} 0, & \text{if } |m| \neq 1 \\ (-1)^n\frac{n(n+1)}{2}, & \text{if } |m| = 1 \end{cases} \tag{B.11c}$$

Appendix C

Rotation and translation coefficients

The expression of the spherical wave functions in one coordinate system (x,y,z) as a function of the spherical wave functions expressed in another coordinate system (x',y',z'), can be divided in two different parts: rotation and translation. This appendix deals with how these both operations are carried out as well as the way the new coefficients, necessary for rotation and translation, are computed. Furthermore some special values and recurrent relations are shown in order to quickly carry out the operations.

C.1 Rotation of spherical waves

C.1.1 Euler angles

An arbitrary rotation of a coordinate system can be performed by the triple rotation depicted in Fig. C.1. As can be observed in this figure, a coordinate system (x,y,z) is transformed into another coordinate system (x',y',z') by means of the following three steps:

1. First a ϕ_0 rotation of (x,y,z) around the z axis is performed. The resulting coordinate system is denoted as (x_1,y_1,z_1)

2. The second step consist of a θ_0 rotation of (x_1,y_1,z_1) around y_1 axis. As a result, the coordinate systems (x_2,y_2,z_2) is obtained.

3. Finally, the last rotation is performed around the z_2 axis the amount indicated by χ_0. With this last rotation, the final coordinate system (x',y',z') is achieved.

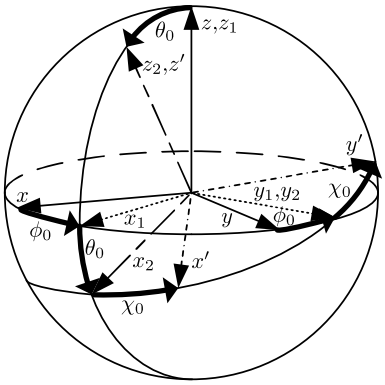

Figure C.1: Triple rotation, from (x,y,z) to (x',y',z') coordinate system: Euler angles.

The angles (χ_0,θ_0,ϕ_0) are the so-called *Euler angles* and are normally used to describe the previous coordinate system rotations. Thus, from now on, these angles will be used to denote the rotation that must be carried out for describing the system (x',y',z') as a function of (x,y,z).

C.1.2 Rotation of spherical wave functions

The spherical wave functions expressed in the unprimed coordinate system (x,y,z) can be expressed as a weighted sum of the wave functions expressed in the primed coordinate system (x',y',z'). If the spherical coordinates (r,θ,ϕ) are used instead of the cartesian coordinates, this relation can be expressed as:

$$\vec{F}^{(c)}_{smn}(r,\theta,\phi) = \sum_{mu=-n}^{n} e^{jm\phi_0} d^n_{\mu m}(\theta_0) e^{j\mu\chi_0} \vec{F}^{(c)}_{s\mu n}(r',\theta',\phi') \qquad \text{(C.1)}$$

where, as can be observed, the rotations around the z axis (χ_0,ϕ_0) are performed by complex exponentials, and the rotation around the y axis (θ_0) is done by means of the so-called *rotation coefficients* $d^n_{\mu m}(\theta_0)$. Since the exponentials are easily computed, the only remaining unknown data are the rotation coefficients. Next section explains the way these coefficients are computed.

C.1.3 Rotation coefficients

The general expression for computing rotation coefficients is the following:

$$d_{\mu m}^{n}(\theta)=\sqrt{\frac{(n+\mu)!(n-\mu)!}{(n+m)!(n-m)!}}\sum_{\sigma}\binom{n+m}{n-\mu-\sigma}\binom{n-m}{\sigma}(-1)^{n-\mu-\sigma}\left(\cos\frac{\theta}{2}\right)^{2\sigma+\mu+m}\left(\sin\frac{\theta}{2}\right)^{2n-2\sigma-\mu-m} \tag{C.2}$$

where the binomial is obtained as:

$$\binom{a}{b}=\frac{a!}{(a-b)!b!} \tag{C.3}$$

Several symmetries and special values for this kind of coefficients can be found in [20]. For instance, in [20], the following recurrence relation is stated among the rotation coefficients that may become very useful:

$$\sqrt{(n+\mu+1)(n-\mu)}\sin\theta d_{\mu+1,m}^{n}(\theta)+\sqrt{(n+\mu)(n-\mu+1)}\sin\theta d_{\mu-1,m}^{n}(\theta)+(2m-2\mu\cos\theta)d_{\mu m}^{n}(\theta)=0 \tag{C.4}$$

Of special interest is the specific value of the rotation coefficients for $\theta=\pi/2$, i.e. $d_{\mu m}^{n}(\pi/2)$. These values are known as *delta constants* and noted as $\Delta_{\mu m}^{n}$. They are employed for the computation of transmitting coefficients (T_{smn}) in Chapter 2. For this reason, next section shows the main expressions to compute these constants.

C.1.4 Delta constants

The delta constants are defined as:

$$\Delta_{\mu m}^{n}=d_{\mu m}^{n}\left(\frac{\pi}{2}\right) \tag{C.5}$$

Therefore, from (C.2), the delta constants can be computed in the following way:

$$\Delta_{\mu m}^{n}=\frac{1}{2^{n}}\sqrt{\frac{(n+\mu)!(n-\mu)!}{(n+m)!(n-m)!}}\sum_{\sigma}\binom{n+m}{n-\mu-\sigma}\binom{n-m}{\sigma}(-1)^{n-\mu-\sigma} \tag{C.6}$$

Several relations can be stated among these new constants. Some of them are shown in the following subsections.

APPENDIX C. ROTATION AND TRANSLATION COEFFICIENTS

Symmetries

$$\Delta^n_{\mu m} = (-1)^{\mu+m}\Delta^n_{m\mu} \tag{C.7a}$$

$$\Delta^n_{\mu m} = (-1)^{n+\mu}\Delta^n_{m,-\mu} \tag{C.7b}$$

$$\Delta^n_{\mu m} = (-1)^{n+m}\Delta^n_{-\mu,m} \tag{C.7c}$$

$$\Delta^n_{\mu m} = (-1)^{\mu+m}\Delta^n_{-\mu,-m} \tag{C.7d}$$

$$\Delta^n_{\mu m} = \Delta^n_{-m,-\mu} \tag{C.7e}$$

$$\Delta^n_{\mu m} = (-1)^{n+m}\Delta^n_{-m,\mu} \tag{C.7f}$$

$$\Delta^n_{\mu m} = (-1)^{n+\mu}\Delta^n_{\mu,-m} \tag{C.7g}$$

Recurrence relations

$$\sqrt{(n+\mu+1)(n-\mu)}\Delta^n_{\mu+1,m} + \sqrt{(n+\mu)(n-\mu+1)}\Delta^n_{\mu-1,m} + 2m\Delta^n_{\mu m} = 0 \tag{C.8a}$$

$$\sqrt{(n+m+1)(n-m)}\Delta^n_{\mu,m+1} + \sqrt{(n+m)(n-m+1)}\Delta^n_{\mu,m-1} - 2\mu\Delta^n_{\mu m} = 0 \tag{C.8b}$$

$$\frac{\sqrt{(n+\mu+1)(n-\mu)}\sqrt{(n+m+1)(n-m)}}{\mu+m+1}\Delta^n_{\mu+1,m+1} + \frac{\sqrt{(n+\mu)(n-\mu+1)}\sqrt{(n+m)(n-m+1)}}{\mu+m-1}\Delta^n_{\mu-1,m-1} = \frac{2(\mu+m)}{(\mu+m)^2-1}\left(n(n+1)-(\mu+m)^2+\mu m+1\right)\Delta^n_{\mu m} \tag{C.8c}$$

Special values

$$\Delta_{\mu 0}^{n} = \begin{cases} 0, & \text{if } (n+\mu)\text{odd} \\ (-1)^{(n-\mu)/2} \frac{1}{2^n} \left[\binom{n+\mu}{\frac{n+\mu}{2}} \binom{n-\mu}{\frac{n-\mu}{2}} \right]^{1/2}, & \text{if } (n+\mu)\text{even} \end{cases} \tag{C.9a}$$

$$\Delta_{0m}^{n} = \begin{cases} 0, & \text{if } (n+\mu)\text{odd} \\ (-1)^{(n-m)/2} \frac{1}{2^n} \left[\binom{n+m}{\frac{n+m}{2}} \binom{n-m}{\frac{n-m}{2}} \right]^{1/2}, & \text{if } (n+\mu)\text{even} \end{cases} \tag{C.9b}$$

$$\Delta_{\mu m}^{n} = (-1)^{n+\mu} \frac{1}{2^n} \sqrt{\binom{2n}{n-\mu}} \tag{C.9c}$$

$$\Delta_{nm}^{n} = \frac{1}{2^n} \sqrt{\binom{2n}{n-m}} \tag{C.9d}$$

$$\Delta_{nn}^{n} = \frac{1}{2^n} \tag{C.9e}$$

C.2 Translation of spherical waves

C.2.1 Translation of spherical wave functions

When two coordinate systems, (x,y,z) and (x',y',z'), are related by means of the translation (A) along the z axis depicted in Fig. C.2, the spherical wave functions defined in both systems can be related as follows:

$$\vec{F}_{s\mu n}^{(c)}(r,\theta,\phi) = \sum_{\sigma=1}^{2} \sum_{\substack{\nu=|\mu| \\ \nu\neq 0}}^{\infty} C_{\sigma\mu\nu}^{sn(c)}(kA) \vec{F}_{\sigma\mu\nu}^{(1)}(r',\theta',\phi') \qquad \text{if } r' < |A| \tag{C.10}$$

and

$$\vec{F}_{s\mu n}^{(c)}(r,\theta,\phi) = \sum_{\sigma=1}^{2} \sum_{\substack{\nu=|\mu| \\ \nu\neq 0}}^{\infty} C_{\sigma\mu\nu}^{sn(1)}(kA) \vec{F}_{\sigma\mu\nu}^{(c)}(r',\theta',\phi') \qquad \text{if } r' > |A| \tag{C.11}$$

where $C_{\sigma\mu\nu}^{sn(c)}(kA)$ are the so-called *translation coefficients* computed as shown in next section.

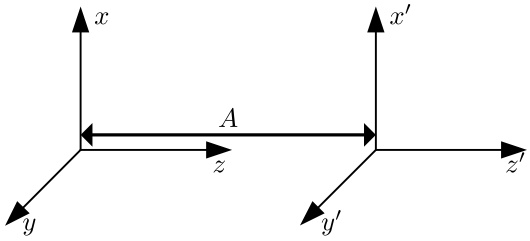

Figure C.2: Translation A along z axis, from (x,y,z) to (x',y',z') coordinate system.

C.2.2 Translation coefficients

The translation coefficients are computed as follow:

$$C_{\sigma\mu\nu}^{sn(c)}(kA) = \frac{j^{n-\nu}}{2}\sqrt{\frac{(2n+1)(2\nu+1)}{n(n+1)\nu(\nu+1)}}\sqrt{\frac{(\nu+\mu)!(n-\mu)!}{(\nu-\mu)!(n+\mu)!}}(-1)^{\mu}$$

$$\sum_{p=|n-\nu|}^{|n+\nu|}\Big[j^{-p}\left\{\delta_{s\sigma}\left(n(n+1)+\nu(\nu+1)-p(p+1)\right)\right. \tag{C.12}$$

$$\left.+\delta_{3-s,\sigma}\left(2j\mu kA\right)\right\}a(\mu,n,-\mu,\nu,p)z_p^{(c)}(kA)\Big]$$

where δ_{nm} is the *Kronecker delta* defined as:

$$\delta_{nm} = \begin{cases} 1, & \text{if } n = m \\ 0, & \text{if } n \neq m \end{cases} \tag{C.13}$$

and $a(\mu,n,-\mu,\nu,p)$ is the so-called *linearization coefficient*. These coefficient scan be computed with the following expression:

$$a(\mu,n,-\mu,\nu,p) = (2p+1)\sqrt{\frac{(n+\mu)!(\nu-\mu)!}{(n-\mu)!(\nu+\mu)!}}\begin{pmatrix} n & \nu & p \\ 0 & 0 & 0 \end{pmatrix}\begin{pmatrix} n & \nu & p \\ \mu & -\mu & 0 \end{pmatrix} \tag{C.14}$$

where $\begin{pmatrix} j_1 & j_2 & j_3 \\ m_1 & m_2 & m_3 \end{pmatrix}$ is the *Wigner 3-j symbol*. The way in which this symbol is computed is detailed in Section C.2.3, however, an important property of this symbol must be pointed out at this moment. This property is the following:

$$\begin{pmatrix} j_1 & j_2 & j_3 \\ 0 & 0 & 0 \end{pmatrix}, \qquad \text{if } (n+\nu+p) \text{ odd} \tag{C.15}$$

This is an important property since it means that only the linearization coefficients satisfying the condition of $(n+\nu+p)$ even are non-zero coefficients. This fact leads to just have to consider the following index p in the sum of (C.12): $p = |n-\nu|, |n-\nu|+2, \cdots, n+\nu-2, n+\nu$, i.e., a step of 2 must be applied.

Symmetries

Some symmetries are stated among the translation coefficients for their easy computation:

$$C_{1\mu\nu}^{1n(c)}(kA) = C_{2\mu\nu}^{2n(c)}(kA) \tag{C.16a}$$

$$C_{2\mu\nu}^{1n(c)}(kA) = C_{1\mu\nu}^{2n(c)}(kA) \tag{C.16b}$$

$$C_{\sigma\mu\nu}^{sn(c)}(kA) = (-1)^{n+\nu} C_{s\mu\nu}^{\sigma n(c)}(kA) \tag{C.16c}$$

$$C_{\sigma\mu\nu}^{sn(c)}(kA) = (-1)^{s+\sigma}(-1)^{n+\nu} C_{s,-\mu,\nu}^{\sigma n(c)}(kA) \tag{C.16d}$$

$$C_{\sigma\mu\nu}^{sn(c)}(kA) = (-1)^{s+\sigma} C_{\sigma,-\mu,\nu}^{sn(c)}(kA) \tag{C.16e}$$

Asymptotic behavior

When the translation distance A tends to ∞, i.e., $kA \to \infty$, the following asymptotic expressions may be applied:

$$C_{\sigma\mu\nu}^{sn(3)}(kA) = \circ\left(\frac{1}{kA}\right), \text{if } \mu \neq \pm 1 \tag{C.17a}$$

$$C_{\sigma 1\nu}^{sn(3)}(kA) = \frac{\sqrt{(2n+1)(2\nu+1)}}{2} j^{\nu-n-1} \frac{e^{jkA}}{kA} + \circ\left(\frac{1}{kA}\right) \tag{C.17b}$$

$$C_{\sigma,-1,\nu}^{sn(3)}(kA) = \frac{\sqrt{(2n+1)(2\nu+1)}}{2} j^{\nu-n-1}(-1)^{s+\sigma} \frac{e^{jkA}}{kA} + \circ\left(\frac{1}{kA}\right) \tag{C.17c}$$

where the symbol $\circ\left(\frac{1}{kA}\right)$ means an error on the order of $(1/kA)$, i.e., the longer the electric distance is, the smaller the error produced by the previous expressions is.

C.2.3 Wigner 3-j symbol

General expression

Wigner 3-j symbols are generally denoted as:

$$\begin{pmatrix} j_1 & j_2 & j_3 \\ m_1 & m_2 & m_3 \end{pmatrix} \tag{C.18}$$

These symbols can be computed, in general, for any combination of indices j_1, j_2, j_3, m_1, m_2 and m_3, as follows:

$$\begin{pmatrix} j_1 & j_2 & j_3 \\ m_1 & m_2 & m_3 \end{pmatrix} =$$

$$\sqrt{(j_1+m_1)!(j_1-m_1)!(j_2+m_2)!(j_2-m_2)!(j_3+m_3)!(j_3-m_3)!}$$

$$\sqrt{\frac{(j_1+j_2-j_3)!(j_1-j_2+j_3)!(-j_1+j_2+j_3)!}{(j_1+j_2+j_3+1)!}} \tag{C.19}$$

$$\sum_z \left[\frac{(-1)^{z+j_1-j_2-m_3}}{z!(j_1+j_2-j_3-z)!(j_1-m_1-z)!(j_2+m_2-z)!} \cdot \right.$$

$$\left. \frac{1}{(j_3-j_2+m_1+z)!(j_3-j_1-m_2+z)!} \right]$$

Special values

Apart from the special value indicated in (C.15), the following other special values may become specially useful when computing wigner 3-j symbols:

$$\begin{pmatrix} j_1 & j_2 & j_1+j_2 \\ m_1 & m_2 & -m_1-m_2 \end{pmatrix} =$$

$$(-1)^{-j_1+j_2-m_1-m_2} \frac{\sqrt{(2j_1)!}\sqrt{(2j_2)!}}{\sqrt{2j_1+2j_2+1}\sqrt{(2j_1+2j_2)!}} \cdot \tag{C.20}$$

$$\frac{\sqrt{(j_1+j_2+m_1+m_2)!}\sqrt{(j_1+j_2-m_1-m_2)!}}{\sqrt{(j_1+m_1)!}\sqrt{(j_1-m_1)!}\sqrt{(j_2+m_2)!}\sqrt{(j_2-m_2)!}}$$

$$\begin{pmatrix} j_1 & j_2 & j_1+j_2-1 \\ m_1 & m_2 & -m_1-m_2 \end{pmatrix} =$$

$$2(j_2 m_1 - j_1 m_2)(-1)^{-j_1+j_2-m_1-m_2} \frac{\sqrt{(2j_1-1)!}\sqrt{(2j_2-1)!}}{\sqrt{(2j_1+2j_2)!}} \cdot \tag{C.21}$$

$$\frac{\sqrt{(j_1+j_2+m_1+m_2-1)!}\sqrt{(j_1+j_2-m_1-m_2-1)!}}{\sqrt{(j_1+m_1)!}\sqrt{(j_1-m_1)!}\sqrt{(j_2+m_2)!}\sqrt{(j_2-m_2)!}}$$

$$\begin{pmatrix} j_1 & j_2 & j_1+j_2 \\ 0 & 0 & 0 \end{pmatrix} = (-1)^{-j_1+j_2} \frac{(j_1+j_2)!\sqrt{(2j_1)!}\sqrt{(2j_2)!}}{j_1!j_2!\sqrt{2j_1+2j_2+1}\sqrt{(2j_1+2j_2)!}} \tag{C.22}$$

Recurrence relation

$$\begin{pmatrix} j_1 & j_2 & j_3 \\ m_1 & m_2 & m_3 \end{pmatrix} =$$

$$\frac{(2j_3+3)\left((j_3+1)(j_3+2)(m_1-m_2)+m_3 j_1(j_1+1)-m_3 j_2(j_2+1)\right)}{(j_3+2)\sqrt{j_3-m_3+1}\sqrt{j_3+m_3+1}\sqrt{-j_1+j_2+j_3+1}\sqrt{j_1-j_2+j_3+1}} \cdot$$

$$\frac{1}{\sqrt{j_1+j_2-j_3}\sqrt{j_1+j_2+j_3+2}} \begin{pmatrix} j_1 & j_2 & j_3+1 \\ m_1 & m_2 & m_3 \end{pmatrix}$$

$$- \frac{(j_3+1)\sqrt{j_3-m_3+2}\sqrt{j_3+m_3+2}\sqrt{-j_1+j_2+j_3+2}\sqrt{j_1-j_2+j_3+2}}{(j_3+2)\sqrt{j_3-m_3+1}\sqrt{j_3+m_3+1}\sqrt{-j_1+j_2+j_3+1}\sqrt{j_1-j_2+j_3+1}} \cdot$$

$$\frac{\sqrt{j_1+j_2-j_3-1}\sqrt{j_1+j_2+j_3+3}}{\sqrt{j_1+j_2-j_3}\sqrt{j_1+j_2+j_3+2}} \begin{pmatrix} j_1 & j_2 & j_3+2 \\ m_1 & m_2 & m_3 \end{pmatrix} \tag{C.23}$$

APPENDIX C. ROTATION AND TRANSLATION COEFFICIENTS

Appendix D

Spheroidal wave functions

The spheroidal coordinate systems are rarely used in electromagnetism. They entail hard formulation and few applications may be found where these coordinate systems present advantages with regard to other coordinate systems. In this thesis, however, in Section 3.5, an interesting application has been presented. This application allows the equivalent currents of an antenna to be determined on a plane surface from spherical measurements. To do this, the spheroidal wave expansion, described in Section 2.2.4, is used, which, in turn, makes use of the spheroidal wave functions.

So far no comments have been done with regard to the way these spheroidal wave functions are obtained. This appendix describes in detail these functions for both, the oblate and prolate spheroidal coordinate system, as well as the special algorithms required for their computation. With this aim, first, the prolate and oblate spheroidal coordinate systems are defined and the relation to the cartesian coordinate system is shown. Then, the spheroidal vector wave functions are reviewed and the expressions for the angular and radial spheroidal functions are described. Finally, the algorithms that must be applied to determine the secondary parameters found in the previous functions are explained.

D.1 Definition

The spheroidal coordinate systems are formed by rotating an ellipse around the z axis. Depending on the position of the foci of the generating ellipse two different spheroidal coordinate systems are formed [47], namely the *prolate spheroidal coordinate system* (if the foci are in the z axis) and the *oblate spheroidal coordinate system* (if the foci are in the XY plane). In both spheroidal systems, coordinates are defined by the following components:

- ξ: Radial component
- η: Angular component
- ϕ: Azimuthal component

For each spheroidal coordinate system, the relation of these components with the cartesian coordinates is different. Next, these relations and the range of variation of each component are described.

Prolate coordinate system

As commented above, the prolate coordinate system is formed by rotating around the z axis an ellipse whose foci are in the z axis. A diagram of the resulting coordinate system can be observed in Fig. D.1, where d is the focal distance.

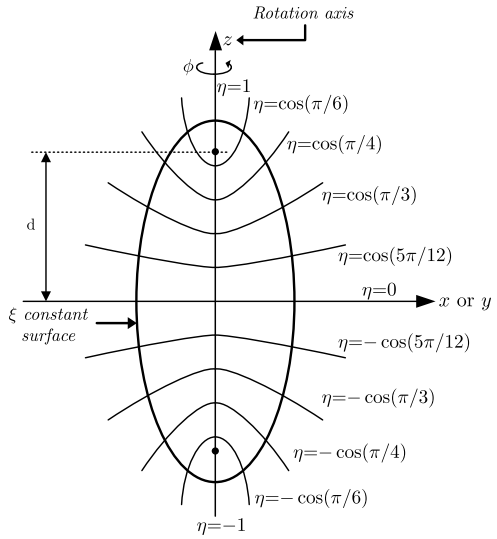

Figure D.1: Prolate spheroidal coordinate system.

The prolate spheroidal components are related to the cartesian components as follows [47]:

$$x = d\sqrt{(1-\eta^2)(\xi^2-1)}\cos\phi \tag{D.1a}$$

$$y = d\sqrt{(1-\eta^2)(\xi^2-1)}\sin\phi \tag{D.1b}$$

$$x = d\eta\xi \tag{D.1c}$$

where

$$-1 \leq \eta \leq 1, \qquad 1 \leq \xi < \infty, \qquad 0 \leq \phi \leq 2\pi \tag{D.2}$$

In this coordinate system, the surface with ξ-component constant forms an ellipsoid with:

- Major axis: 2dξ
- Minor axis: 2d$\sqrt{\xi^2-1}$

Oblate coordinate system

The oblate coordinate system results from the rotation around the z axis of an ellipse whose foci are in the XY plane. Thus, the resulting coordinate system may be depicted as in Fig. D.1, where d is the focal distance of the generating ellipse.

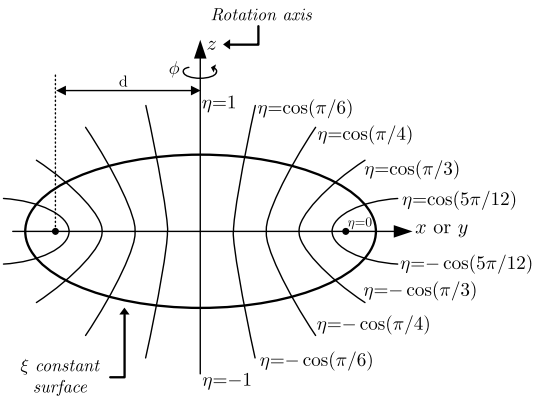

Figure D.2: Oblate spheroidal coordinate system.

In this case, the relation of the oblate spheroidal components with the cartesian components is given by:

$$x = d\sqrt{(1-\eta^2)(\xi^2+1)}\cos\phi \tag{D.3a}$$

$$y = d\sqrt{(1-\eta^2)(\xi^2+1)}\sin\phi \tag{D.3b}$$

$$x = d\eta\xi \tag{D.3c}$$

where

$$-1 \leq \eta \leq 1, \qquad 0 \leq \xi < \infty, \qquad 0 \leq \phi \leq 2\pi \tag{D.4}$$

In addition, it is worth to note that the surface with ξ-component constant is a flattened ellipsoid of revolution [47] whose axes are:

- Major axis: $2\mathrm{d}\sqrt{\xi^2+1}$
- Minor axis: $2\mathrm{d}\xi$

D.2 Spheroidal vector wave functions

The solution in a source-free region of the vector wave equation is deduced in Section 2.2.4 for the oblate spheroidal coordinate system . This solution is expressed in the form of a modal expansion as follows:

$$\vec{E}(\eta,\xi,\phi) = \sum_{smn} \alpha_{smn}\vec{M}_{smn}(\eta,\xi,\phi) \tag{D.5}$$

where α_{smn} are the oblate spheroidal coefficients and $\vec{M}_{smn}(\eta,\xi,\phi)$ are the *spheroidal vector wave functions*, whose expressions are:

$$\begin{aligned}\vec{M}_{1mn}(\eta,\xi,\phi) =& \frac{jm\eta S_{mn}R_{mn}}{\sqrt{(\xi^2+\eta^2)(1+\xi^2)}}e^{jm\phi}\hat{\xi} \\ &+\frac{jm\xi S_{mn}R_{mn}}{\sqrt{(\xi^2+\eta^2)(1-\eta^2)}}e^{jm\phi}\hat{\eta} \\ &-\frac{\sqrt{(1+\xi^2)(1-\eta^2)}}{(\xi^2+\eta^2)}\left[\eta S_{mn}\frac{\partial R_{mn}}{\partial\xi}+\xi R_{mn}\frac{\partial S_{mn}}{\partial\eta}\right]e^{jm\phi}\hat{\phi}\end{aligned} \tag{D.6}$$

$$
\begin{aligned}
&\vec{M}_{2mn}(\eta,\xi,\phi) = \\
&\quad \frac{\sqrt{1+\xi^2}}{kd\sqrt{\xi^2+\eta^2}}\left[\frac{m^2\xi S_{mn}R_{mn}}{(\xi^2+\eta^2)(1-\eta^2)}\right. \\
&\qquad\qquad \left.-\frac{\partial}{\partial\eta}\left(\frac{(1-\eta^2)}{(\xi^2+\eta^2)}\left[\eta S_{mn}\frac{\partial R_{mn}}{\partial\xi}+\xi R_{mn}\frac{\partial S_{mn}}{\partial\eta}\right]\right)\right]e^{jm\phi}\hat{\xi} \\
&\quad + \frac{\sqrt{1-\eta^2}}{kd\sqrt{\xi^2+\eta^2}}\left[-\frac{m^2\eta S_{mn}R_{mn}}{(\xi^2+\eta^2)(1-\eta^2)}\right. \\
&\qquad\qquad \left.+\frac{\partial}{\partial\xi}\left(\frac{(1+\xi^2)}{(\xi^2+\eta^2)}\left[\eta S_{mn}\frac{\partial R_{mn}}{\partial\xi}+\xi R_{mn}\frac{\partial S_{mn}}{\partial\eta}\right]\right)\right]e^{jm\phi}\hat{\eta} \\
&\quad + \frac{jm\sqrt{(1+\xi^2)(1-\eta^2)}}{kd(\xi^2+\eta^2)}\left[\frac{S_{mn}}{(1-\eta^2)}\frac{\partial\xi R_{mn}}{\partial\xi}-\frac{R_{mn}}{(1+\xi^2)}\frac{\partial\eta S_{mn}}{\partial\eta}\right]e^{jm\phi}\hat{\phi}
\end{aligned}
\tag{D.7}
$$

In the above expressions, $S_{mn} = S^{(1)}_{mn}(-jc,\eta)$ (the *spheroidal angular function*) and $R_{mn} = R^{(3)}_{mn}(-jc,j\xi)$ (the *spheroidal radial function*), where the parameter c is the *spheroidicity parameter* [135] obtained, from the wavenumber (k) and the focal distance (d), as:

$$c = kd \tag{D.8}$$

It is worth to mention that, if the vector wave equation were solved in the prolate spheroidal coordinate system, the solution would be expressed as a function of the angular function $S^{(1)}_{mn}(c,\eta)$ and of the radial function $R^{(3)}_{mn}(c,\xi)$.

Next two sections describes the spheroidal angular and radial functions used in the solution of both, the oblate and prolate spheroidal coordinate system, paying special attention on the functions used in the oblate solution (the case of interest for this thesis).

D.2.1 Spheroidal angular functions

The spheroidal angular functions, in general noted as $(S_{mn}(a,\eta))$, are the solution of the following differential equation:

$$\frac{\mathrm{d}}{\mathrm{d}\eta}\left[(1-\eta^2)\frac{\mathrm{d}S_{mn}(a,\eta)}{\mathrm{d}\eta}\right]+\left[\lambda_{mn}(a)-a^2\eta^2-\frac{m^2}{1-\eta^2}\right]S_{mn}(a,\eta)=0 \tag{D.9}$$

where $\lambda_{mn}(a)$ are the *spheroidal eigenvalues*.

The solution may be expressed as a weighted sum of Legendre functions [45],[47]. If just the first kind Legendre functions are considered, and the variable a is substituted by the values of interest (c and $-jc$), the spheroidal angular functions are given by:

$$S_{mn}^{(1)}(c,\eta) = \sum_{k=0,1}^{\infty} d_k^{mn}(c) P_{m+k}^m(\eta) \tag{D.10a}$$

$$S_{mn}^{(1)}(-jc,\eta) = \sum_{k=0,1}^{\infty} d_k^{mn}(-jc) P_{m+k}^m(\eta) \tag{D.10b}$$

where $P_n^m(\eta)$ is the associated Legendre function of degree n and order m (see Appendix B), and $d_k^{mn}(a)$ are the *expansion coefficients*. In the above expressions, the summation is over even values of k for $(n-m)$ even, and over odd values of k for $(n-m)$ odd. Thus, k may be:

- $k = 0, 2, 4, 6, \cdots$ for $(n-m)$ even
- $k = 1, 3, 5, 7, \cdots$ for $(n-m)$ odd

The expansion coefficients are determined by means of the following recurrence relation [46],[47]:

$$\alpha_k^m(a) d_{k+2}^{mn}(a) + \left(\beta_k^m(a) - \lambda_{mn}(a)\right) d_k^{mn}(a) + \gamma_k^m(a) d_{k-2}^{mn}(a) = 0 \tag{D.11}$$

where

$$\alpha_k^m(a) = \frac{(k+2m+1)(k+2m+2)}{(2k+2m+3)(2k+2m+5)} a^2 \tag{D.12a}$$

$$\beta_k^m(a) = (m+k)(m+k+1) + \frac{a^2}{2}\left(1 - \frac{4m^2-1}{(2k+2m-1)(2k+2m+3)}\right) \tag{D.12b}$$

$$\gamma_k^m(a) = \frac{k(k-1)}{(2k+2m-3)(2k+2m-1)} a^2 \tag{D.12c}$$

In the above recurrence relation (D.11), the spheroidal eigenvalues $\lambda_{mn}(a)$ are required to carry out the recursive procedure. In order to obtain these eigenvalues, the following transcendental equation [46],[45],[47] must be solved:

$$U_1(\lambda_{mn}) + U_2(\lambda_{mn}) = 0 \tag{D.13}$$

where

$$U_1(\lambda_{mn}) = \chi^m_{n-m} - \lambda_{mn} - \cfrac{\delta^m_{n-m}}{\chi^m_{n-m-2} - \lambda_{mn} - \cfrac{\delta^m_{n-m-2}}{\chi^m_{n-m-4} - \lambda_{mn} - \cdots}} \tag{D.14a}$$

$$U_2(\lambda_{mn}) = -\cfrac{\delta^m_{n-m+2}}{\chi^m_{n-m+2} - \lambda_{mn} - \cfrac{\delta^m_{n-m+4}}{\chi^m_{n-m+4} - \lambda_{mn} - \cdots}} \tag{D.14b}$$

In the above expressions, the dependence with regard to the parameter a has not been included for simplicity, and the parameters $\chi^m_k = \chi^m_k(a)$ and $\delta^m_k = \delta^m_k(a)$ are computed as follows:

$$\chi^m_k(a) = (m+k)(m+k+1) + \frac{a^2}{2}\left(1 - \frac{4m^2-1}{(2k+2m-1)(2k+2m+3)}\right) \tag{D.15a}$$

$$\delta^m_k(a) = \frac{k(k-1)(k+2m)(k+2m-1)}{(2k+2m-1)(2k+2m-3)(2k+2m+1)}a^4 \tag{D.15b}$$

The computation of the expansion coefficients $d^{mn}_k(a)$ and the spheroidal eigenvalues $\lambda_{mn}(a)$, is efficiently performed by additional algorithms. These algorithms are explained in Section D.3.

In (D.8) and (D.7), not only the spheroidal angular functions are employed, but also the derivatives of these functions. Next section describes how these derivatives may be obtained for the case of oblate spheroidal coordinates.

Derivatives

The first derivatives of the spheroidal angular function can be expressed, from (D.10), as follows:

$$\frac{\partial S^{(1)}_{mn}(a,\eta)}{\partial \eta} = \sum_{k=0,1}^{\infty} d^{mn}_k(a) \frac{\partial P^m_{m+k}(\eta)}{\partial \eta} \tag{D.16}$$

In this expression, since the derivative must be applied with regard to the η component, the derivative just applies on the associated Legendre functions

(the coefficients $d_k^{mn}(a)$ do not depend on η). Hence, the derivative of $S_{mn}^{(1)}(a,\eta)$ must be computed by means of the derivative of $P_k^m(\eta)$ with regard to η. This derivative may be computed by the following recurrence relation [46]:

$$\frac{\partial P_k^m(\eta)}{\partial \eta} = \frac{1}{\eta^2-1}\left(k\eta P_k^m(\eta) - (k+m)P_{k-1}^m(\eta)\right) \tag{D.17}$$

Below, the explicit expressions of the first and second derivatives required in the computation of the spheroidal vector wave functions for the oblate coordinate system are deduced.

First derivative The first derivative can be obtained by substituting (D.17) into (D.16). The resulting expression is:

$$\frac{\partial S_{mn}^{(1)}(-jc,\eta)}{\partial \eta} = \sum_{k=0,1}^{\infty} d_k^{mn}(-jc)\left[\frac{1}{\eta^2-1}\left(k\eta P_k^m(\eta) - (k+m)P_{k-1}^m(\eta)\right)\right] \tag{D.18}$$

Second derivative The expression for second derivative can be deduced in two different ways. The first one consists in deriving the expression (D.18) with regard to η and using the recurrence relation (D.17) again. By doing so, the second derivative may be expressed as follows:

$$\begin{aligned}\frac{\partial^2 S_{mn}^{(1)}(-jc,\eta)}{\partial \eta^2} = \sum_{k=0,1}^{\infty} d_k^{mn}(-jc)\frac{1}{\eta^2-1}\big[&-(m+k)P_{m+k}^m(\eta)\\ &+\eta(2m+k)(1-2(m+k))P_{m+k-1}^m(\eta)\\ &+(2m+k)(2m+k-1)P_{m+k-2}^m(\eta)\big]\end{aligned} \tag{D.19}$$

The second way takes in advantage the presence of the second derivative in the differential equation (D.9). Thus, if the expression for the first derivative (D.18) is inserted in (D.9), the following expression for the second derivative is deduced:

$$\begin{aligned}\frac{\partial^2 S_{mn}^{(1)}(-jc,\eta)}{\partial \eta^2} = \frac{1}{\eta^2-1}\Bigg[&2\eta\frac{\partial S_{mn}^{(1)}(-jc,\eta)}{\partial \eta}\\ &\left(\lambda_{mn}(-jc) + (c\eta)^2 - \frac{m^2}{1-\eta^2}\right)S_{mn}^{(1)}(-jc,\eta)\Bigg]\end{aligned} \tag{D.20}$$

In computing these expressions, it has been found that the results from both expressions agree very well. However, it has also been found that the second option (D.20) is more convenient and faster [47].

D.2.2 Spheroidal radial functions

The spheroidal radial functions, generally noted as $R_{sm}^{(p)}(a,\Psi)$, are the solution of the following differential equation:

$$\frac{\mathrm{d}}{\mathrm{d}\Psi}\left[(\Psi^2-1)\frac{\mathrm{d}R_{mn}^{(p)}(a,\Psi)}{\mathrm{d}\Psi}\right]-\left[\lambda_{mn}(a)-a^2\Psi^2-\frac{m^2}{\Psi^2-1}\right]R_{mn}^{(p)}(a,\Psi)=0 \tag{D.21}$$

where (a,Ψ) are (c,ξ) for the prolate spheroidal coordinate system or $(-jc,j\xi)$ for the oblate spheroidal coordinate system.

The solution may be expressed as a weighted sum of spherical Bessel functions ($z_k^{(p)}(r)$, see Appendix A) for both coordinate systems as follows:

$$R_{mn}^{(p)}(c,\xi)=\frac{1}{\sum\limits_{k=0,1}^{\infty}d_k^{mn}(c)\dfrac{(2m+k)!}{k!}}\left(\frac{\xi^2-1}{\xi^2}\right)^{m/2}\sum_{k=0,1}^{\infty}j^{k+m-n}d_k^{mn}(c)\frac{(2m+k)!}{k!}z_{m+k}^{(p)}(c\xi) \tag{D.22a}$$

$$R_{mn}^{(p)}(-jc,j\xi)=\frac{1}{\sum\limits_{k=0,1}^{\infty}d_k^{mn}(-jc)\dfrac{(2m+k)!}{k!}}\left(\frac{\xi^2+1}{\xi^2}\right)^{m/2}\sum_{k=0,1}^{\infty}j^{k+m-n}d_k^{mn}(-jc)\frac{(2m+k)!}{k!}z_{m+k}^{(p)}(c\xi) \tag{D.22b}$$

where the summation index k behaves with $(n-m)$ as for the spheroidal angular functions (D.10).

The index p in the above expressions determine the kind of waves that are taken into account. The application studied in this thesis just considers outward traveling waves. Thus, assuming the time dependence stated in (2.1), the election must be $p=3$, i.e., the spherical Hankel function of first kind ($z_k^{(3)}(r)=h_k^{(1)}(r)$).

The computation of the spheroidal vector wave equations requires the prior knowledge of the first and second derivatives with regard to the ξ component of the spheroidal radial functions. Next sections explain the way these derivatives may be obtained.

Derivatives

The derivation of the spheroidal radial functions in the oblate coordinate system with regard to the ξ component may be expressed, from (D.22b), as:

$$\frac{\partial R_{mn}^{(3)}(-jc, j\xi)}{\partial \xi} = \frac{1}{\sum\limits_{k=0,1}^{\infty} d_k^{mn}(-jc)\dfrac{(2m+k)!}{k!}} \left(\frac{\xi^2+1}{\xi^2}\right)^{m/2} \sum_{k=0,1}^{\infty} j^{k+m-n} d_k^{mn}(-jc)\frac{(2m+k)!}{k!}\frac{\partial h_{m+k}^{(1)}(c\xi)}{\partial \xi} \tag{D.23}$$

As can be observed, since most of the expression does not depend on the variable ξ, just the derivative of the spherical Hankel function must be computed. This derivative may be determined by the following recurrent relation:

$$\frac{\partial h_n^{(1)}(x)}{\partial x} = h_{n-1}^{(1)}(x) - \frac{n+1}{x} h_n^{(1)}(x) \tag{D.24}$$

Below, the exact expressions for determining the first and second derivatives (obtained from the above equations) are depicted:

First derivative The first derivative can be obtained by substituting (D.24) into (D.23). By doing so, the first derivative is given by:

$$\frac{\partial R_{mn}^{(3)}(-jc, j\xi)}{\partial \xi} = \frac{1}{\sum\limits_{k=0,1}^{\infty} d_k^{mn}(-jc)\dfrac{(2m+k)!}{k!}} \sum_{k=0,1}^{\infty} j^{k+m-n} d_k^{mn}(-jc)\frac{(2m+k)!}{k!} \left(\frac{\xi^2+1}{\xi^2}\right)^{m/2} \left[c h_{m+k-1}^{(1)}(c\xi) - \left\{\left(\frac{m}{\xi(\xi^2+1)} + \frac{m+k+1}{\xi}\right) h_{m+k}^{(1)}(c\xi)\right\}\right] \tag{D.25}$$

Second derivative The second derivative can be deduced in two ways, as for the spheroidal angular functions. The first one consists in deriving with regard to ξ the expression (D.25) and using the recurrence relation (D.24) to determine the resulting derivatives of the Hankel function. As a result, the second derivative is expressed as:

$$\begin{aligned}\frac{\partial^2 R_{mn}^{(3)}(-jc,j\xi)}{\partial\xi^2} =& \frac{1}{\sum\limits_{k=0,1}^{\infty} d_k^{mn}(-jc)\dfrac{(2m+k)!}{k!}} \\ & \sum_{k=0,1}^{\infty} j^{k+m-n} d_k^{mn}(-jc)\frac{(2m+k)!}{k!}\left(\frac{\xi^2+1}{\xi^2}\right)^{m/2} \\ & \left[\left\{\frac{m}{2\xi^2}\left(\frac{2(m-2)}{(\xi^2+1)^2}+\frac{3m+3k+8}{(\xi^2+1)}\right)\right.\right. \\ & \left.+\frac{(m+k+1)+(m+k+1)^2}{\xi^2}\right\} h_{m+k}^{(1)}(c\xi) \\ & -\left\{\frac{m}{\xi(\xi^2+1)}+\frac{2c(m+k+1)-1}{\xi}\right\} h_{m+k-1}^{(1)}(c\xi) \\ & \left.+c^2 h_{m+k-2}^{(1)}(c\xi)\right]\end{aligned} \tag{D.26}$$

The second way consists in using the differential equation (D.21), which contains the second derivative of the spheroidal radial functions. The first derivative of these functions, included in the differential equation, may be determined by (D.25). Thus, substituting (D.25) into (D.21), the second derivative may be obtained as:

$$\begin{aligned}\frac{\partial^2 R_{mn}^{(3)}(-jc,j\xi)}{\partial^2\xi} = \frac{1}{\xi^2+1}\left[\left(\lambda_{mn}(-jc)-\{c\xi\}^2-\frac{m^2}{\xi^2+1}\right) R_{mn}^{(3)}(-jc,j\xi)\right. \\ \left.-2\xi\frac{\partial R_{mn}^{(3)}(-jx,j\xi)}{\partial\xi}\right]\end{aligned} \tag{D.27}$$

As in the derivatives of the spheroidal angular functions, the result of both solutions agree very well. However, it has been found [47] that the second

expression (D.27) is more convenient and faster and, hence, it is recommended to use this second option.

D.3 Secondary parameters

The computation of the spheroidal angular and radial functions requires the prior knowledge of the spheroidal eigenvalues ($\lambda_{mn}(a)$) and the expansion coefficients ($d_k^{mn}(a)$). These both coefficients are computed by the general expressions described in Section D.2.1. However, none of them allow the coefficients to be computed directly. They rather require additional algorithms to compute the coefficients. Next sections describe these algorithms.

D.3.1 Determination of the spheroidal eigenvalues

The spheroidal eigenvalues are determined by solving the transcendental equation (D.13). To do this, the Taylor series expansion technique or the relaxation method may be applied, however they do not converge or lead to non-accurate results when $|c|^2$ is very large [47]. In order to avoid these problems, the transcendental equation can be solved directly for any value of $|c|^2$. This direct solution, however, requires to be achieved in a different way depending on the value of $|c|^2$, for $|c|^2 \leq 10000$ or $|c|^2 > 10000$ [136]. Below, the solution in these two situations is described:

Case I: $|c|^2 \leq 10000$

In this case, the solution can be obtained by employing the Newton's numerical technique [137] to solve for the roots of the equation. This iterative technique works, in general, to find the roots a function $f(x)$, as follows:

$$x^{(p)} = x^{(p-1)} - \frac{f(x^{(p-1)})}{f'(x^{(p-1)})} \tag{D.28}$$

where $x^{(p)}$ are the roots in the iteration p and $f'(x)$ is the derivative of $f(x)$ with regard to the variable x.

Specifically for the transcendental equation, the values of λ_{mn} (the dependence with regard to a is not included for simplicity) on each iteration can be obtained as:

$$\lambda_{mn}^{(p)} = \lambda_{mn}^{(p-1)} - \frac{f(\lambda_{mn}^{(p-1)})}{f'(\lambda_{mn}^{(p-1)})} \tag{D.29}$$

where $f(\lambda_{mn}^{p})$ is the value of the transcendental equation at $\lambda_{mn} = \lambda_{mn}^{p}$. This equation, in a compressed form [46],[138], can expressed as:

$$f(\lambda_{mn}^{(p)}) = N_0^{(p)} - \frac{\delta_{n-m+2}}{M_0^{(p)}} \tag{D.30}$$

where

$$N_k^{(p)} = \chi_{n-m-k}^m - \lambda_{mn}^{(p)} - \frac{\delta_{n-m-k}^m}{N_{k+2}^{(p)}} \tag{D.31}$$

$$M_k^{(p)} = \chi_{n-m+k+2}^m - \lambda_{mn}^{(p)} - \frac{\delta_{n-m+k+4}^m}{M_{k+2}^{(p)}} \tag{D.32}$$

This new expression allows the derivative $f(\lambda_{mn})$ with regard to λ_{mn} ($f'(\lambda_{mn}^p)$) at $\lambda_{mn} = \lambda_{mn}^p$ to be expressed in this way:

$$\begin{aligned} f'(\lambda_{mn}^{(p)}) = \left.\frac{\mathrm{d}(\lambda_{mn})}{\mathrm{d}\lambda_{mn}}\right|_{\lambda_{mn}=\lambda_{mn}^{(p)}} = \\ - \left[1 + \frac{\delta_{n-m}^m}{(N_2^{(p)})^2} + \frac{\delta_{n-m}^m}{(N_2^{(p)})^2}\frac{\delta_{n-m-2}^m}{(N_4^{(p)})^2}\frac{\delta_{n-m}^m}{(N_2^{(p)})^2}\frac{\delta_{n-m-2}^m}{(N_4^{(p)})^2}\frac{\delta_{n-m-4}^m}{(N_6^{(p)})^2} + \cdots\right] \\ - \left[\frac{\delta_{n-m+2}^m}{(M_0^{(p)})^2} + \frac{\delta_{n-m+2}^m}{(M_0^{(p)})^2}\frac{\delta_{n-m+4}^m}{(M_2^{(p)})^2} + \frac{\delta_{n-m+2}^m}{(M_0^{(p)})^2}\frac{\delta_{n-m+4}^m}{(M_2^{(p)})^2}\frac{\delta_{n-m+6}^m}{(M_4^{(p)})^2}\right] \end{aligned} \tag{D.33}$$

In addition, in [136] it is pointed out that the estimated value of λ_{mn} and the starting and end points of the iterative algorithm must be the following to obtain fast an accurate results:

$$\lambda_{mn}^{\text{estimate}} = n(n+1) + \mathbb{R}\left(\frac{c}{2}\right) \tag{D.34}$$

$$\lambda_{mn}^{\text{start}} = n(n+1) - c^2\left(1 - \frac{(2m-1)(2m+1)}{(2n-1)(2n+3)}\right) \tag{D.35}$$

$$\lambda_{mn}^{\text{end}} = n(n+1) + c^2\left(1 - \frac{(2m-1)(2m+1)}{(2n-1)(2n+3)}\right) \tag{D.36}$$

Case II: $|c|^2 > 10000$

In this case the previous Newton's algorithm cannot be applied because exceptionally high accuracy in $\lambda_{mn}^{\text{start}}$ is required for the algorithm to evaluate the correct eigenvalues [136]. This is because there are closed spaced roots in a narrow range and, hence, a very accurate initial guess is required. The expression (D.35) does not fulfills this requirement and, therefore, the Newton's algorithm is not practical in this situation.

Nevertheless, when $|c|^2 > 10000$, the eigenvalues can be determined accurately by the algorithm proposed by Hodge [139]. In this algorithm, the eigenvalues λ_{mn} are the eigenvalues of a tri-diagonal matrix. This matrix is formed as follows:

For $(n-m)$ even

$$A_\lambda^{\text{even}} = \begin{pmatrix} \beta_0 & (\gamma_2\alpha_0)^{1/2} & 0 & 0 & \dots \\ (\gamma_2\alpha_0)^{1/2} & \beta_2 & (\gamma_4\alpha_2)^{1/2} & 0 & \dots \\ 0 & (\gamma_4\alpha_2)^{1/2} & \beta_4 & (\gamma_6\alpha_4)^{1/2} & \dots \\ 0 & 0 & (\gamma_6\alpha_4)^{1/2} & \beta_6 & \dots \\ \vdots & \vdots & \vdots & \vdots & \ddots \end{pmatrix} \tag{D.37}$$

For $(n-m)$ odd

$$A_\lambda^{\text{odd}} = \begin{pmatrix} \beta_1 & (\gamma_3\alpha_1)^{1/2} & 0 & 0 & \dots \\ (\gamma_3\alpha_1)^{1/2} & \beta_3 & (\gamma_5\alpha_3)^{1/2} & 0 & \dots \\ 0 & (\gamma_5\alpha_3)^{1/2} & \beta_5 & (\gamma_7\alpha_5)^{1/2} & \dots \\ 0 & 0 & (\gamma_7\alpha_5)^{1/2} & \beta_7 & \dots \\ \vdots & \vdots & \vdots & \vdots & \ddots \end{pmatrix} \tag{D.38}$$

where, for simplicity, $\alpha_k = \alpha_k^m(a)$, $\beta_k = \beta_k^m(a)$, $\gamma_k = \gamma_k^m(a)$.

One of the most important problems of the Hodge's algorithm is to decide which matrix eigenvalue correspond to each spheroidal eigenvalue $\lambda_{mn}(a)$. In [135] it is proposed several techniques for a real/complex and indices m and n integers/non-integers. In the easiest case, i.e., a real and m and n integers, the eigenvalues are ordered from the lower value to the higher value, and the correspondence is from the lower indices to the higher indices.

D.3.2 Determination of the expansion coefficients

The expansion coefficients $d_k^{mn}(a)$ are determined by the recursive formula (D.11). This formula involves three consecutive expansion coefficients. Hence, the formula requires two initial terms to start the recurrence relation. However, the only available information, apart from (D.11), are the following two relations among the first expansion coefficients [47]:

$$\alpha_0^m d_2^{mn}(a) + (\beta_0^m(a) - \lambda_{mn}(a)) d_0^{mn}(a) = 0, \qquad (k=0) \tag{D.39a}$$

$$\alpha_1^m d_3^{mn}(a) + (\beta_1^m(a) - \lambda_{mn}(a)) d_1^{mn}(a) = 0, \qquad (k=1) \tag{D.39b}$$

Unfortunately these expressions are not enough since they just allow the relations $d_2^{mn}(a)/d_0^{mn}(a)$ and $d_3^{mn}(a)/d_1^{mn}(a)$ to be obtained. By inserting these values into the recursive formula, for $k = 2$ or $k = 3$, one additional term is required. Therefore, the recursive process cannot be started.

In order to obtain this initial term, the following expressions [46] (deduced from the normalization of the spheroidal angular functions) can be applied:

$$\sum_{k=0}^{\infty} \frac{(-1)^{k/2}(k+2m)!}{2^k \left(\frac{k}{2}\right)! \left(\frac{k+2m}{2}\right)!} d_k^{mn}(a) = \frac{(-1)^{(n-m)/2}(n+m)!}{2^{n-m} \left(\frac{n-m}{2}\right)! \left(\frac{n+m}{2}\right)!} \tag{D.40}$$

$$\sum_{k=1}^{\infty} \frac{(-1)^{(k-1)/2}(k+2m+1)!}{2^k \left(\frac{k-1}{2}\right)! \left(\frac{k+2m+1}{2}\right)!} d_k^{mn}(a) = \frac{(-1)^{(n-m-1)/2}(n+m+1)!}{2^{n-m} \left(\frac{n-m-1}{2}\right)! \left(\frac{n+m+1}{2}\right)!} \tag{D.41}$$

where (D.40) is only valid for $(n-m)$ even (being $k = 0, 2, 4, \cdots$); and (D.41) is only valid for $(n-m)$ odd (being $k = 1, 3, 5, \cdots$).

By dividing (D.40) by $d_0^{mn}(a)$, the following relation is derived:

$$d_0^{mn}(a) = \frac{(-1)^{(n-m)/2}(n+m)!}{2^{n-m} \left(\frac{n-m}{2}\right)! \left(\frac{n+m}{2}\right)!} \frac{1}{\sum\limits_{k=0}^{\infty} \frac{(-1)^{k/2}(k+2m)!}{2^k \left(\frac{k}{2}\right)! \left(\frac{k+2m}{2}\right)!} \left[\frac{d_k^{mn}(a)}{d_0^{mn}(a)}\right]} \tag{D.42}$$

Similarly, if (D.41) is divided by $d_1^{mn}(a)$, this other expression is found:

$$d_1^{mn}(a) = \frac{(-1)^{(n-m-1)/2}(n+m+1)!}{2^{n-m} \left(\frac{n-m-1}{2}\right)! \left(\frac{n+m+1}{2}\right)!} \frac{1}{\sum\limits_{k=1}^{\infty} \frac{(-1)^{(k-1)/2}(k+2m+1)!}{2^k \left(\frac{k-1}{2}\right)! \left(\frac{k+2m+1}{2}\right)!} \left[\frac{d_k^{mn}(a)}{d_1^{mn}(a)}\right]} \tag{D.43}$$

The last expressions require the relations $d_k^{mn}(a)/d_0^{mn}(a)$ and $d_k^{mn}(a)/d_1^{mn}(a)$ to compute $d_0^{mn}(a)$ and $d_1^{mn}(a)$, respectively. In order to determine these relations, the recurrent formula (D.11) can be expressed as follows:

$$\frac{d_k^{mn}(c)}{d_{k+2}^{mn}(c)} = -\frac{\alpha_k^m(c)}{(\beta_k^m(c) - \lambda_{mn}(c)) - \gamma_k^m(c)\frac{d_{k-2}^{mn}}{d_k^{mn}(c)}} \tag{D.44}$$

As can be observed, this expression requires a relation of coefficients to start. This relation can be obtained, from (D.39a) and (D.39b), as follows:

$$\frac{d_0^{mn}(c)}{d_2^{mn}(c)} = -\frac{\alpha_0^m(c)}{(\beta_0^m(c) - \lambda_{mn}(c))} \tag{D.45a}$$

$$\frac{d_1^{mn}(c)}{d_3^{mn}(c)} = -\frac{\alpha_1^m(c)}{(\beta_1^m(c) - \lambda_{mn}(c))} \tag{D.45b}$$

By combining the above expressions, all the expansion coefficients may be determined. This combination must be done as described in the following algorithm:

1. The initial relations $d_0^{mn}(a)/d_2^{mn}(a)$ and $d_1^{mn}(a)/d_3^{mn}(a)$ are computed from (D.45a) and (D.45b), respectively.

2. The relations $d_k^{mn}(a)/d_{k+2}^{mn}(a)$ are determined for $0 \leq k \leq k_{max}$ with (D.44).

3. The coefficients $d_0^{mn}(a)$ and $d_1^{mn}(a)$ are obtained by using the values computed in the step 2 and the expressions (D.42) and (D.43), respectively.

4. The expressions (D.45a) and (D.45b) are used to determine $d_2^{mn}(a)$ and $d_3^{mn}(a)$, respectively.

5. Finally, the rest of coefficients since may be determined by either, the recurrent formula (D.11), or the intermediate relations obtained during this algorithm.

The final step is to establish the maximum k (k_{max}) of the previous summations. This index must be chosen high enough so that as much information as possible is included, but considering the computational cost of the algorithm. In [135] it is proposed a formula for the determination of k_{max} from the precision (*prec*) desired on resulting expansion coefficients. This formula is:

$$\frac{d_{k_{max}}^{mn}(c)}{\max\{d_k^{mn}(c),\ 0 \leq k \leq k_{max}\}} \leq 10^{-prec} \tag{D.46}$$

Therefore, by first computing the k_{max} with this expression, the algorithm for the determination of the expansion coefficients can be practically performed with the desired precision in the result.

References

[1] "IEEE standard definitions of terms for antennas." *IEEE Std 145-1993*, pp. i–, Jun 1993.

[2] R. F. Harrington, *Field Computation by Moment Methods*. John Wiley & Sons, 1993.

[3] M. Sadiku, *Numerical Techniques in Electromagnetics*. CRC Press, 2000.

[4] EM Software & Systems S. A. (Pty) Ltd., "FEKO field computations involving bodies of arbitrary shape," July 2008, Suite 5.4, Stellenbosch, South Africa.

[5] A. Corporation, "HFSS (high frequency structural simulator)," 2009, Suite v11, Pittsburg (PA), USA.

[6] C. C. S. Technology, "CST studio suite," 2009, Suite 2009, Germany.

[7] R. Haupt, "An introduction to genetic algorithms for electromagnetics," *Antennas and Propagation Magazine, IEEE*, vol. 37, no. 2, pp. 7–15, Apr 1995.

[8] J. Robinson and Y. Rahmat-Samii, "Particle swarm optimization in electromagnetics," *Antennas and Propagation, IEEE Transactions on*, vol. 52, no. 2, pp. 397–407, Feb. 2004.

[9] M. Baquero, D. Pancorbo, M. Fayos, and D. Sánchez, "Estudio del efecto de las esquinas redondeadas causadas por el fresado en dispositivos en guía de ondas," in *Simposium Nacional de la URSI 2007*, Sep. 2007.

[10] P. Harms, J. Maloney, M. Kesler, E. Kuster, and G. Smith, "A system for unobtrusive measurement of surface currents," *Antennas and Propagation, IEEE Transactions on*, vol. 49, no. 2, pp. 174–184, Feb 2001.

[11] R. E. Collin, *Field Theory of Guided Waves*. John Wiley & Sons, 1991.

[12] C. A. Balanis, *Antenna Theory: Analysis and desing.* John Wiley & Sons, 1997.

[13] C. Cappellin, O. Breinbjerg, and A. Frandsen, "A high-resolution antenna diagnostics technique for spherical near-field measurements," *28th ESA Antenna Workshop, ESTEC*, pp. 889–906, 2005.

[14] D. Sanchez, M. Baquero, V. M. Rodrigo, and B. Bernardo, "Currents reconstruction using a modal expansion of near-field mesurements for synthesis error detection," *Microwave and optical technology letters*, vol. 49, no. 8, pp. 2043–2047, Aug. 2007.

[15] A. Cardama, L. Jofre, J. Rius, J. Romeu, S. Blanch, and M. Ferrando, *Antena.* Edicions UPC, Barcelona, 1998.

[16] J. Bennett, A. Anderson, P. McInnes, and A. Whitaker, "Microwave holographic metrology of large reflector antennas," *Antennas and Propagation, IEEE Transactions on*, vol. 24, no. 3, pp. 295–303, May 1976.

[17] J. Hanfling, G. Borgiotti, and L. Kaplan, "The backward transform of the near field for reconstruction of aperture fields," *Antennas and Propagation Society International Symposium, 1979*, vol. 17, pp. 764–767, Jun 1979.

[18] D. Rochblatt and B. Seidel, "Microwave antenna holography," *Microwave Theory and Techniques, IEEE Transactions on*, vol. 40, no. 6, pp. 1294–1300, Jun 1992.

[19] C. Cappellin, "Antenna diagnostics for spherical near-field antenna measurements," Ph.D. dissertation, Technical University of Denmark (DTU), Lyngby, Denmark, 2007.

[20] J. E. Hansen, *Spherical Near-Field Antenna Measurements.* Peter Peregrinus Ltd., London, United Kingdom, 1988.

[21] F. Xu, W. Hong, and X. Zhu, "A new time domain near field to far field transformation for fdtd in two dimensions," *Microwave Symposium Digest, 2002 IEEE MTT-S International*, vol. 3, pp. 2057–2060, 2002.

[22] T. Sarkar and A. Taaghol, "Near-field to near/far-field transformation for arbitrary near-field geometry utilizing an equivalent electric current and mom," *Antennas and Propagation, IEEE Transactions on*, vol. 47, no. 3, pp. 566–573, Mar 1999.

[23] R. Johnson, H. Ecker, and J. Hollis, "Determination of far-field antenna patterns from near-field measurements," *Proceedings of the IEEE*, vol. 61, no. 12, pp. 1668–1694, Dec. 1973.

[24] A. Yaghjian, "An overview of near-field antenna measurements," *Antennas and Propagation, IEEE Transactions on*, vol. 34, no. 1, pp. 30–45, Jan 1986.

[25] J. A. Souppa, "Minimum weighted norm extrapolation using frequency domain blocking for digital audio," Ph.D. dissertation, University of Miami, 1999.

[26] A. Papoulis, "A new method of image restoration," *Prog. Rep. 39, to Joint Services Technical Advisory Committee*, 1973-1974.

[27] R. W. Gerchberg, "Super resolution through error energy reduction," *Optica Acta*, vol. 21, no. 9, pp. 709–720, 1974.

[28] A. Papoulis, "A new algorithm in spectral analysis and band-limited extrapolation," *Circuits and Systems, IEEE Transactions on*, vol. 22, no. 9, pp. 735–742, Sep 1975.

[29] C. Chamzas and W. Xu, "An improved version of papoulis-gerchberg algorithm on band-limited extrapolation," *Acoustics, Speech and Signal Processing, IEEE Transactions on*, vol. 32, no. 2, pp. 437–440, Apr 1984.

[30] M. Sabri and W. Steenaart, "An approach to band-limited signal extrapolation: The extrapolation matrix," *Circuits and Systems, IEEE Transactions on*, vol. 25, no. 2, pp. 74–78, Feb 1978.

[31] R. J. Marks II, "Gerchberg's extrapolation algorithm in two dimensions," *Applied Optics*, vol. 20, no. 10, pp. 1815–1820, May 1981.

[32] D. Sanchez, M. Baquero, F. Vico, and B. Bernardo, "Currents reconstruction by means of a new 2d extrapolation matrix," in *Antennas and Propagation, 2007. EuCAP 2007. The Second European Conference on*, Nov. 2007, pp. 1–6.

[33] J. Cadzow, "An extrapolation procedure for band-limited signals," *Acoustics, Speech and Signal Processing, IEEE Transactions on*, vol. 27, no. 1, pp. 4–12, Feb 1979.

[34] J. P. Burg, "Maximum entropy spectrum analysis," Ph.D. dissertation, University of Stanford, Palo Alto, CA, 1975.

[35] R. T. Lacoss, "Data adaptive spectral analysis methods," *Geophysics*, vol. 36, no. 4, pp. 661–675, Aug 1975.

[36] C. W. Liao, M. A. Fiddy, and C. L. Byrne, "Imaging from zero locations od far-field intensity data," *Journal of the optical society of America*, vol. 14, no. 12, pp. 3155–3161, Dec 1997.

[37] R. F. Harrington, *Time-Harmonic Electromagnetic Fields.* John Wiley & Sons, 2001.

[38] C. Scott, *Introduction to Optics and Optical Imaging.* John Wiley & Sons, 1998.

[39] J. Stratton, *Electromagnetic theory.* McGraw-Hill, New York, 1941.

[40] P. M. Morse and H. Feshbach, *Methods of Theoretical Physics.* McGraw-Hill, New York, 1953.

[41] P. C. Clemmow, *The Plane Wave Spectrum Representation of Electromagnetic Fields.* John Wiley & Sons, 1996.

[42] W. M. Leach, "Probe compensated near-field measurements on a cylinder," Ph.D. dissertation, Georgia institute of technology, 1972.

[43] W. M. Leach and D. T. Paris, "Probe compensated near-field measurements on a cylinder," *Antennas and Propagation, IEEE Transactions on*, vol. 21, no. 4, pp. 435–445, Jul 1973.

[44] J. Romeu, "Formulación espectral de la radiación. aplicación al caso cilíndrico." Ph.D. dissertation, Departament de teoria de la senyal i comunicacions (UPC), 1991.

[45] C. Flammer, *Spheroidal wave functions.* Stanford university press, Stanford CA, 1957.

[46] M. Abramowitz and I. A. Stegun, *Handbook of mathematical functions.* Dover publications Inc., New ork, 1965.

[47] L. W. Li, X. K. Kang, and M. S. Leong, *Spheroidal wave functions in electromagnetic theory.* Wiley, New York, 2002.

[48] G. Ricciardi and W. Stutzman, "A near-field to far-field transformation for spheroidal geometry utilizing an eigenfunction expansion," *Antennas and Propagation, IEEE Transactions on*, vol. 52, no. 12, pp. 3337–3349, Dec. 2004.

[49] J. Wang, "An examination of the theory and practices of planar near-field measurement," *Antennas and Propagation, IEEE Transactions on*, vol. 36, no. 6, pp. 746–753, Jun 1988.

[50] D. Paris, J. Leach, W., and E. Joy, "Basic theory of probe-compensated near-field measurements," *Antennas and Propagation, IEEE Transactions on*, vol. 26, no. 3, pp. 373–379, May 1978.

[51] F. Larsen, "Probe correction of spherical near-field measurements," *Electronics Letters*, vol. 13, no. 14, pp. 393–395, 7 1977.

[52] F. H. Larsen, "Improved algorithm for probe-corrected spherical near-field/far-field transformation," *Electronics Letters*, vol. 15, no. 19, pp. 588–590, 13 1979.

[53] T. Laitinen, S. Pivnenko, and O. Breinbjerg, "Iterative probe correction technique for spherical near-field antenna measurements," *Antennas and Wireless Propagation Letters, IEEE*, vol. 4, pp. 221–223, 2005.

[54] T. Laitinen and O. Breinbjerg, "A first/third-order probe correction technique for spherical near-field antenna measurements using three probe orientations," *Antennas and Propagation, IEEE Transactions on*, vol. 56, no. 5, pp. 1259–1268, May 2008.

[55] T. Laitinen, S. Pivnenko, and O. Breinbjerg, "Application of the iterative probe correction technique for a high-order probe in spherical near-field antenna measurements," *Antennas and Propagation Magazine, IEEE*, vol. 48, no. 4, pp. 179–185, Aug. 2006.

[56] M. Leibfritz and P. Landstorfer, "Full probe-correction for near-field antenna measurements," *Antennas and Propagation Society International Symposium 2006, IEEE*, pp. 437–440, July 2006.

[57] C. Schmidt, M. Leibfritz, and T. Eibert, "Fully probe-corrected near-field far-field transformation employing plane wave expansion and diagonal translation operators," *Antennas and Propagation, IEEE Transactions on*, vol. 56, no. 3, pp. 737–746, March 2008.

[58] G. Gbur, "Nonradiating sources and the inverse source problem," Ph.D. dissertation, Department of Physics and Astronomy, University of Rochester, Rochester, New York, 2001.

[59] R. P. Porter and A. J. Devaney, "Holography and the inverse source problem," *Journal of the Optical Society of America*, vol. 72, no. 3, pp. 327–330, March 1982.

[60] P. Petre and T. Sarkar, "Planar near-field to far-field transformation using an equivalent magnetic current approach," *Antennas and Propagation, IEEE Transactions on*, vol. 40, no. 11, pp. 1348–1356, Nov 1992.

[61] N.-W. Kang, Y.-S. Chung, C. Cheon, and H.-K. Jung, "A new 2-d image reconstruction algorithm based on fdtd and design sensitivity analysis," *Microwave Theory and Techniques, IEEE Transactions on*, vol. 50, no. 12, pp. 2734–2740, Dec 2002.

[62] P. Petre, T. K. Sarkar, and J. A. Kong, "Differences between modal expansion and integral equation methods for planar near-field to far-field transformation," *Progress in Electromagnetics Research (PIERS)*, vol. 12, pp. 37–56, 1996.

[63] Y. Alvarez, F. Las-Heras, and M. Pino, "On the comparison between the spherical wave expansion and the sources reconstruction method," *Antennas and Propagation, IEEE Transactions on*, vol. 56, no. 10, pp. 3337–3341, Oct. 2008.

[64] C. Cappellin, A. Frandsen, and O. Breinbjerg, "Application of the swe-to-pwe antenna diagnostics technique to an offset reflector antenna," *Antennas and Propagation Magazine, IEEE*, vol. 50, no. 5, pp. 204–213, Oct. 2008.

[65] K. Shlager and G. Smith, "Comparison of two fdtd near-field to near-field transformations applied to pulsed antenna problems," *Electronics Letters*, vol. 31, no. 12, pp. 936–938, Jun 1995.

[66] I. Rekanos, T. Yioultsis, and T. Tsiboukis, "Inverse scattering using the finite-element method and a nonlinear optimization technique," *Microwave Theory and Techniques, IEEE Transactions on*, vol. 47, no. 3, pp. 336–344, Mar 1999.

[67] Y. Alvarez, F. Las-Heras, and M. Pino, "Reconstruction of equivalent currents distribution over arbitrary three-dimensional surfaces based on integral equation algorithms," *Antennas and Propagation, IEEE Transactions on*, vol. 55, no. 12, pp. 3460–3468, Dec. 2007.

[68] A. Taaghol and T. Sarkar, "Near-field to near/far-field transformation for arbitrary near-field geometry, utilizing an equivalent magnetic current," *Electromagnetic Compatibility, IEEE Transactions on*, vol. 38, no. 3, pp. 536–542, Aug 1996.

[69] F. Las-Heras and T. Sarkar, "Radial field retrieval in spherical scanning for current reconstruction and nf-ff transformation," *Antennas and Propagation, IEEE Transactions on*, vol. 50, no. 6, pp. 866–874, Jun 2002.

[70] P. Petre and T. Sarkar, "Planar near-field to far-field transformation using an array of dipole probes," *Antennas and Propagation, IEEE Transactions on*, vol. 42, no. 4, pp. 534–537, Apr 1994.

[71] A. Bjrck, *Numerical Methods for Least Squares Problems.* SIAM: Society for Industrial and Applied Mathematics, 1996.

[72] H. Van der Vost, *Iterative Krylov methods for large linear systems.* Cambridge University Press, 2003.

[73] M. Berry, T. F. Chan, J. Demmel, J. Donato, J. Dongarra, V. Eijkhout, C. Romine, and H. Henk van der Vorst, *Templates for the Solution of Linear Systems: Building Blocks for Iterative Methods.* Society for Industrial Mathematics, 1987.

[74] J. Colinas, Y. Goussard, and J.-J. Laurin, "Application of the tikhonov regularization technique to the equivalent magnetic currents near-field technique," *Antennas and Propagation, IEEE Transactions on*, vol. 52, no. 11, pp. 3122–3132, Nov. 2004.

[75] P. C. Hansen, "Numerical tools for analysis and solution of fredholm integral equations of the first kind," *Inverse problems*, vol. 8, pp. 849–872, Dec. 1992.

[76] M. E. Kilmer and D. P. O'leary, "Choosing regularization parameters in iterative methods for ill-posed problems," *SIAM Journal on Matrix Analysis and Applications (SIMAX)*, vol. 22, no. 4, pp. 1204–1221, 2001.

[77] Y. Rahmat-Samii and J. Lemanczyk, "Application of spherical near-field measurements to microwave holographic diagnosis of antennas," *Antennas and Propagation, IEEE Transactions on*, vol. 36, no. 6, pp. 869–878, Jun 1988.

[78] J. Lee, E. Ferren, D. Woollen, and K. Lee, "Near-field probe used as a diagnostic tool to locate defective elements in an array antenna," *Antennas and Propagation, IEEE Transactions on*, vol. 36, no. 6, pp. 884–889, Jun 1988.

[79] A. V. Oppenheim, *Discrete-Time Signal Processing.* Prentice-Hall, 1999.

[80] Q. Liu and N. Nguyen, "An accurate algorithm for nonuniform fast fourier transforms (nufft's)," *Microwave and Guided Wave Letters, IEEE*, vol. 8, no. 1, pp. 18–20, Jan 1998.

[81] Q. H. Liu, X. M. Xu, B. Tian, and Z. Q. Zhang, "Applications of nonuniform fast transform algorithms in numerical solutions of differential and integral equations," *Geoscience and Remote Sensing, IEEE Transactions on*, vol. 38, no. 4, pp. 1551–1560, Jul 2000.

[82] A. J. Devaney and E. Wolf, "Multipole expansions and plane wave representations of the electromagnetic field," *Journal of Mathematical Physics*, vol. 15, no. 2, pp. 234–244, Feb 1974.

[83] C. Cappellin, O. Breinbjerg, and A. Frandsen, "Properties of the transformation from the spherical wave expansion to the plane wave expansion," *Radio Science*, vol. 43, 2008.

[84] J.-E. Sten and E. Marengo, "Inverse source problem in an oblate spheroidal geometry," *Antennas and Propagation, IEEE Transactions on*, vol. 54, no. 11, pp. 3418–3428, Nov. 2006.

[85] ——, "Inverse source problem in the spheroidal geometry: Vector formulation," *Antennas and Propagation, IEEE Transactions on*, vol. 56, no. 4, pp. 961–969, April 2008.

[86] "Transformation formulas for spherical and spheroidal multipole fields," *AEU - International Journal of Electronics and Communications*, vol. 61, no. 4, pp. 262–269, 2007.

[87] A. J. Devaney, "Nonradiating surface sources," *Journal of the Optical Society of America A*, vol. 21, no. 11, pp. 2216–2222, 2004.

[88] A. J. Devaney and E. Wolf, "Radiating and nonradiating classical current distributions and the fields they generate," *Phys. Rev. D*, vol. 8, no. 4, pp. 1044–1047, Aug 1973.

[89] A. Gamliel, K. Kim, A. I. Nachman, and E. Wolf, "A new method for specifying nonradiating, monochromatic, scalar sources and their fields," *Journal of the Optical Society of America A*, vol. 6, no. 9, pp. 1388–1393, 1989.

[90] A. J. Devaney and E. A. Marengo, "A method for specifying nonradiating, monochromatic, scalar sources and their fields," *Pure Appl. Opt.*, no. 7, pp. 12 313–1220, 1998.

[91] S. Kay and J. Marple, S.L., "Spectrum analysisa modern perspective," *Proceedings of the IEEE*, vol. 69, no. 11, pp. 1380–1419, Nov. 1981.

[92] T. B. Hansen and A. D. Yaghjian, *Plane-Wave Theory of Time-Domain Fields: Near-Field Scanning Applications.* Wiley-IEEE Press, 1999.

[93] E. Martini, O. Breinbjerg, and S. Maci, "Reduction of truncation errors in planar near-field aperture antenna measurements using the method of alternating orthogonal projections," in *Antennas and Propagation, 2006. EuCAP 2006. First European Conference on*, Nov. 2006, pp. 1–6.

[94] ——, "Reduction of truncation errors in planar near-field aperture antenna measurements using the gerchberg-papoulis algorithm," *Antennas and Propagation, IEEE Transactions on*, vol. 56, no. 11, pp. 3485–3493, Nov. 2008.

[95] Y. Rahmat-Samii, "Microwave holography of large reflector antennas–simulation algorithms," *Antennas and Propagation, IEEE Transactions on*, vol. 33, no. 11, pp. 1194–1203, Nov 1985.

[96] D. Sanchez-Escuderos, M. Baquero-Escudero, E. Antonino-Daviu, and J. Herranz-Herruzo, "Resolution enhancement in equivalent currents reconstruction by means of prior discrete fourier transform," *Electronics Letters*, vol. 45, no. 5, pp. 248–249, 26 2009.

[97] C. L. Byrne, R. M. Fitzgerald, M. A. Fiddy, T. J. Hall, and A. M. Darling, "Data adaptive spectral analysis methods," *Journal of the Optical Society of America*, vol. 73, no. 11, pp. 1481–1487, Nov 1983.

[98] E. Martini, O. Breinbjerg, and S. Maci, "A convergence criterion for the iterative gerchberg-papoulis algorithm applied to truncation error reduction in planar near-field measurements," in *Antennas and Propagation, 2007. EuCAP 2007. The Second European Conference on*, Nov. 2007, pp. 1–7.

[99] D. Sánchez Escuderos, "Algoritmos de reconstrucción de corrientes de alta resolución," Master's thesis, Polytechnic Unversity of Valencia, Dept. of communications, 2007.

[100] D. Youla, "Generalized image restoration by the method of alternating orthogonal projections," *Circuits and Systems, IEEE Transactions on*, vol. 25, no. 9, pp. 694–702, Sep 1978.

[101] M. Sabri and W. Steenaart, "Comments on "an extrapolation procedure for band-limited signals"," *Acoustics, Speech and Signal Processing, IEEE Transactions on*, vol. 28, no. 2, pp. 254–254, Apr 1980.

[102] J. Cadzow, "Observations on the extrapolation of a band-limited signal problem," *Acoustics, Speech and Signal Processing, IEEE Transactions on*, vol. 29, no. 6, pp. 1208–1209, Dec 1981.

[103] M. Sabri and W. Steenaart, "Rebuttal to "observations on the extrapolation of a band-limited signal problem"," *Acoustics, Speech and Signal Processing, IEEE Transactions on*, vol. 29, no. 6, pp. 1209–1209, Dec 1981.

[104] A. Jain and S. Ranganath, "Extrapolation algorithms for discrete signals with application in spectral estimation," *Acoustics, Speech and Signal Processing, IEEE Transactions on*, vol. 29, no. 4, pp. 830–845, Aug 1981.

[105] D. Kolba and T. Parks, "Optimal estimation for band-limited signals including time domain considerations," *Acoustics, Speech and Signal Processing, IEEE Transactions on*, vol. 31, no. 1, pp. 113–122, Feb 1983.

[106] S. Dharanipragada and K. Arun, "Bandlimited extrapolation using time-bandwidth dimension," *Signal Processing, IEEE Transactions on*, vol. 45, no. 12, pp. 2951–2966, Dec 1997.

[107] L. Potter and K. Arun, "Energy concentration in band-limited extrapolation," *Acoustics, Speech and Signal Processing, IEEE Transactions on*, vol. 37, no. 7, pp. 1027–1041, Jul 1989.

[108] S. Cabrera and T. Parks, "Extrapolation and spectral estimation with iterative weighted norm modification," *Signal Processing, IEEE Transactions on*, vol. 39, no. 4, pp. 842–851, Apr 1991.

[109] W. Xu and C. Chamzas, "On the extrapolation of band-limited functions with energy constraints," *Acoustics, Speech and Signal Processing, IEEE Transactions on*, vol. 31, no. 5, pp. 1222–1234, Oct 1983.

[110] X.-W. Zhou and X.-G. Xia, "The extrapolation of high-dimensional band-limited functions," *Acoustics, Speech and Signal Processing, IEEE Transactions on*, vol. 37, no. 10, pp. 1576–1580, Oct 1989.

[111] A. Papoulis, *The Fourier integral and its applications.* McGraw-Hill, New York, 1962.

[112] D. Sanchez, M. Baquero, E. Alfonso, and F. Vico, "Currents reconstruction with high resolution using the fft iterative method and spectrum replies," in *Antennas and Propagation, 2006. EuCAP 2006. The First European Conference on*, Nov. 2006, pp. 1–6.

[113] D. Sanchez, M. Baquero, D. Gonzalez, and E. Alfonso, "Improvement of resolution in equivalent currents reconstruction using papoulis-gerchberg algorithm and replicas of the spectrum," *Electronics Letters*, vol. 43, no. 19, pp. 1010–1012, 13 2007.

[114] D. Sanchez-Escuderos, M. Baquero-Escudero, F. Vico-Bondia, and V.-M. Rodrigo-Penarrocha, "Algorithm for currents reconstruction using the fft iterative method and a lattice of the spectrum," in *Antennas and Propagation Society International Symposium 2006, IEEE*, July 2006, pp. 1379–1382.

[115] D. Sánchez Escuderos, M. Baquero Escudero, V. M. Rodrigo Peñarrocha, and F. Vico Bondía, "Mejora de la velocidad de convergencia en un método iterativo aplicado a la reconstrucciń de corrientes," in *Simposium Nacional de la URSI 2006*, Sep. 2006.

[116] M. Sabri and W. Steenaart, "Discrete hilbert transform filtering," *Acoustics, Speech and Signal Processing, IEEE Transactions on*, vol. 25, no. 5, pp. 452–454, Oct 1977.

[117] F. Burris, "Matrix formulation of the discrete hilbert transform," *Circuits and Systems, IEEE Transactions on*, vol. 22, no. 10, pp. 836–838, Oct 1975.

[118] S. Roy and A. Agrawal, "Digital low-pass filtering using the discrete hilbert transform," *Acoustics, Speech and Signal Processing, IEEE Transactions on*, vol. 26, no. 5, pp. 465–467, Oct 1978.

[119] D. Sanchez, M. Baquero, J. Herranz, and E. Antonino, "High resolution in currents reconstruction applying the extrapolation matrix and spectrum replies," in *Antennas and Propagation Society International Symposium, 2007 IEEE*, June 2007, pp. 417–420.

[120] Y. Saad, *Iterative methods for sparse linear system.* Boston, MA: PWS, 1996.

[121] M. Vajtersic and M. Becka, "Block-svd algorithms and their adaptation to hypercubes and rings," in *Parallel Algorithms/Architecture Synthesis, 1997. Proceedings. Second Aizu International Symposium*, Mar 1997, pp. 175–181.

[122] P. Arbenz and M. Oettli, "Block implementations of the symmetric qr and jacobi algorithms," in *ONPAR '92/ VAPP V: Proceedings of the Second Joint International Conference on Vector and Parallel Processing*, 1992, pp. 827–828.

[123] A. Heldring, J. Rius, and L. Ligthart, "New block ilu preconditioner scheme for numerical analysis of very large electromagnetic problems," *Magnetics, IEEE Transactions on*, vol. 38, no. 2, pp. 337–340, Mar 2002.

[124] A. Heldring, J. Rius, J.-M. Tamayo, J. Parron, and E. Ubeda, "Fast direct solution of method of moments linear system," *Antennas and Propagation, IEEE Transactions on*, vol. 55, no. 11, pp. 3220–3228, Nov. 2007.

[125] H. M. Shieh, C. L. Byrne, and M. A. Fiddy, "Image reconstruction: a unifying model for resolution enhancement and data extrapolation. tutorial," *Journal of the optical society of America*, vol. 23, no. 2, pp. 258–266, Feb 2006.

[126] H. M. Shieh, C. L. Byrne, M. E. Testorf, and M. A. Fiddy, "Iterative image reconstruction using prior knowledge," *Journal of the optical society of America*, vol. 23, no. 6, pp. 1292–1300, Jun 2006.

[127] H. M. Shieh and M. A. Fiddy, "Accuracy of extrapolates data as a function of prior knowledge and regularization," *Applied optics*, vol. 45, no. 14, pp. 3283–3288, May 2006.

[128] P. Hansen, "Analysis of discrete ill-posed problems by means of the l-curve," *SIAM Rev.*, vol. 34, pp. 561–580, 1992.

[129] G. Golub, M. Heath, and G. Wahba, "Generalized cross-validation as a method for choosing a good ridge parameter." *Technometrics*, vol. 21, pp. 215–223, May 1979.

[130] J. Shi, M. Cracraft, K. Slattery, M. Yamaguchi, and R. DuBroff, "Calibration and compensation of near-field scan measurements," *Electromagnetic Compatibility, IEEE Transactions on*, vol. 47, no. 3, pp. 642–650, Aug. 2005.

[131] S. Burgos, S. Pivnenko, O. Breinbjerg, and M. Sierra-Castaer, "Comparative investigation of four antenna gain determination techniques," *Antennas and Propagation, 2007. EuCAP 2007. The Second European Conference on*, pp. 1–6, Nov. 2007.

[132] ——, "Standard gain horn calibration: pattern integration versus three-antenna technique," *Antennas and Propagation, 2007. EuCAP 2007. The Second European Conference on*, pp. 1–6, Nov. 2007.

[133] D. Sánchez-Escuderos, M. Baquero-Escudero, B. Bernardo-Clemente, and V. M. Rodrigo-Peñarrocha, "Determination of probe receiving coefficients for near-field to far-field transformation," *Microwave and optical technology letters*, Accepted for publication.

[134] M. Baquero, "Transformaciones espectrales y aplicación a síntesis de ondas, medida de antenas y difracción," Ph.D. dissertation, Departamento de comunicaciones (UPV), 1994.

[135] P. E. Falloon, P. C. Abbott, and J. B. Wang, "Theory and computation of spheroidal wave functions," *Journal of Physics A: Mathematical and General,*, vol. 36, no. 20, pp. 5477–5495, 2003.

[136] L. W. Li, T. S. Yeo, P. S. Kooi, M. S. Leong, and K. Y. Tan, "Computations of spheroidal harmonics with complex arguments: A review with an algorithm," *Physical review. E, Statistical physics, plasmas, fluids, and related interdisciplinary topics*, vol. 58, no. 5, pp. 6792–6806, 1998.

[137] W. H. Press, B. P. Flannery, W. T. Teukolsky, and W. T. Vetterling, *Numerical recipes in C, the art of scientific computing.* Cambridge University Press, New York, 1988.

[138] P. Falloon, "Theory and computation of spheroidal harmonics with general arguments," Ph.D. dissertation, University of Western Australia, 2001.

[139] D. B. Hodge, "Eigenvalues and eigenfunctions of the spheroidal wave equation," *J. Math. Phys.*, vol. 11, pp. 2308–2312, 1970.

Related Publications

JCR indexed journals

1. D. Sanchez, M. Baquero, V. M. Rodrigo, and B. Bernardo, "Currents reconstruction using a modal expansion of near-field mesurements for synthesis error detection," *Microwave and optical technology letters*, vol. 49, no. 8, pp. 2043–2047, Aug. 2007.

2. D. Sanchez, M. Baquero, D. Gonzalez, and E. Alfonso, "Improvement of resolution in equivalent currents reconstruction using papoulis-gerchberg algorithm and replicas of the spectrum," *Electronics Letters*, vol. 43, no. 19, pp. 1010–1012, 13 2007.

3. D. Sanchez-Escuderos, M. Baquero-Escudero, E. Antonino-Daviu, and J. Herranz-Herruzo, "Resolution enhancement in equivalent currents reconstruction by means of prior discrete fourier transform," *Electronics Letters*, vol. 45, no. 5, pp. 248–249, 26 2009.

4. D. Sánchez-Escuderos, M. Baquero-Escudero, B. Bernardo-Clemente, and V. M. Rodrigo-Peñarrocha, "Determination of probe receiving coefficients for near-field to far-field transformation," *Microwave and optical technology letters*, Accepted for publication.

Other journals

1. D. Sánchez-Escuderos, M. Baquero-Escudero, E. Alfonso-Alós, and E. Antonino Daviu, "Improvement on equivalent current reconstruction by means of new information addition," *Revista ITECKNE*, vol. 5, no. 1, pp. 28–36, July 2008.

2. D. Sánchez-Escuderos, M. Baquero-Escudero, E. Alfonso-Alós, B. Bernardo Clemente, V. M. Rodrigo-Peñarrocha, and A. Vila-Jiménez, "Antenna diagnostics using near-field measurements with coupling reduc-

tion," *Accepted for publication in ITEAM Magazine (Revista del Instituto de telecomunicaciones y aplicaciones multimedia)*, 2009.

International conferences

1. D. Sanchez-Escuderos, M. Baquero-Escudero, F. Vico-Bondia, and V.-M. Rodrigo-Penarrocha, "Algorithm for currents reconstruction using the fft iterative method and a lattice of the spectrum," in *Antennas and Propagation Society International Symposium 2006, IEEE*, July 2006, pp. 1379–1382.

2. D. Sanchez, M. Baquero, E. Alfonso, and F. Vico, "Currents reconstruction with high resolution using the fft iterative method and spectrum replies," in *Antennas and Propagation, 2006. EuCAP 2006. The First European Conference on*, Nov. 2006, pp. 1–6.

3. D. Sanchez, M. Baquero, J. Herranz, and E. Antonino, "High resolution in currents reconstruction applying the extrapolation matrix and spectrum replies," in *Antennas and Propagation Society International Symposium, 2007 IEEE*, June 2007, pp. 417–420.

4. D. Sanchez, M. Baquero, F. Vico, and B. Bernardo, "Detection of defective elements in an x band array antenna from its near field measurements," in *Antennas and Propagation Society International Symposium, 2007 IEEE*, June 2007, pp. 1637–1640.

5. D. Sanchez, M. Baquero, F. Vico, and B. Bernardo, "Currents reconstruction by means of a new 2D extrapolation matrix," in *Antennas and Propagation, 2007. EuCAP 2007. The Second European Conference on*, Nov. 2007, pp. 1–6.

6. D. Sanchez, M. Baquero, F. Vico, and B. Bernardo, "Near field retrieval from far field using PDFT," in *Antennas and Propagation Society International Symposium, 2008. AP-S 2008. IEEE*, July 2008, pp. 1–4.

National conferences

1. D. Sánchez, M. Baquero, M. Simón, and F. Vico, "Reconstrucción de las corrientes equivalentes de una antena sobre un plano a partir de medidas en una geometría esférica," in *Simposium Nacional de la URSI 2005*, Sep. 2005.

2. D. Sánchez Escuderos, V. M. Baquero Escudero, Rodrigo Peñarrocha, and F. Vico Bondía, "Mejora de la velocidad de convergencia en un método iterativo aplicado a la reconstrucciń de corrientes," in *Simposium Nacional de la URSI 2006*, Sep. 2006.

3. D. Sánchez Escuderos, D. Baquero Escudero, González Ovejero, and F. Vico Bondía, "Mejora de la reconstrucción de corrientes mediante la matriz de extrapolación 2D," in *Simposium Nacional de la URSI 2007*, Sep. 2007.

4. D. Sánchez-Escuderos, M. Baquero-Escudero, J. I. Herranz-Herruzo, and F. Vico Bondía, "Algoritmo iterativo para calibración de sondas en medidas esféricas," in *Accepted for publication in Simposium Nacional de la URSI 2009, Santander (Cantabria).*